

Investigations of Certain Novel Aspects of the Structure and Properties of Transition Metal Oxides

A Thesis
Submitted for the Degree of
Doctor of Philosophy
in the Faculty of Science

by
Rana Saha



Chemistry and Physics of Materials Unit
Jawaharlal Nehru Centre for Advanced Scientific Research
(A Deemed University)
Bangalore-560064

July 2016

*Dedicated to my
parents & teachers*

DECLARATION

I hereby declare that the matter embodied in this thesis entitled “**Investigations of Certain Novel Aspects of the Structure and Properties of Transition Metal Oxides**” is the result of investigations carried out by me at the Chemistry and Physics of Materials Unit, Jawaharlal Nehru Centre for Advanced Scientific Research, Bangalore, India, under the supervision of Prof. C. N. R. Rao and Prof. A. Sundaresan and it has not been submitted elsewhere for the award of any degree or diploma.

In keeping with the general practice in reporting scientific observations, due acknowledgement has been made whenever the work described is based on the findings of other investigators. Any omission that might have occurred by oversight or error of judgment is regretted.

Bangalore

30/07/2016



Rana Saha

CERTIFICATE

We hereby certify that the matter embodied in this thesis entitled “**Investigations of Certain Novel Aspects of the Structure and Properties of Transition Metal Oxides**” has been carried out by Mr. Rana Saha at the Chemistry and Physics of Materials Unit, Jawaharlal Nehru Centre for Advanced Scientific Research, Bangalore, India, under our supervision and that has not been submitted elsewhere for the award of any degree or diploma.



Bangalore

30/07/2016

Prof. C. N. R. Rao and Prof. A. Sundaresan

(Research Supervisors)

ACKNOWLEDGEMENTS

I express my sincere gratitude to my advisors Prof. C. N. R. Rao and Prof. A. Sundaresan for enormous freedom, constant motivation and excellent guidance throughout my Ph.D. Working with them has been a thoroughly enjoyable experience. Contagious enthusiasm and vision of Prof. Rao for science has motivated me at various times. His valuable comments and instructions on various scientific projects and writing papers have helped me immensely. I am extremely grateful for his kindness, endless support and encouragement during my stay at JNC. I am thankful to Prof. Sundaresan for useful scientific discussion on various projects. Working with him has been very inspiring. I greatly appreciate his approach towards research and I have learnt this lesson for my life-long. I also convey my heartfelt gratitude to them for excellent experimental resources they have provided for the group. My time with them has been the most valuable period of my academic development and personal refinement. I shall always cherish fond memories of my association with them.

I thank Prof. U. V. Waghmare (JNCASR), Prof. A. K. Sood (IISc), Prof. S. M. Yusuf (BARC), Prof. C. Narayana (JNCASR), Prof. M. K. Sanyal (SINP), Prof. Sean Langridge and Dr. Pascal Manuel (STFC Rutherford Appleton Laboratory, UK), Prof. R. Datta, Dr. S. N. Shirodkar (JNCASR), Dr. P. Kumar (IISc), Dr. A. K. Bera (BARC), Dr. R. Dhanya, Mr. D. S. Negi and Mr. V. I. Hegde (JNCASR) for fruitful collaborations and insightful discussions.

I would also like to thank Dr. N. V. Ter-Oganessian (SFedU, Russia), Prof. K. H. Kim and Mr. D. H. Jang (SNU, Korea), Prof. B. J. Kennedy (University of Sydney), Dr. Emmanuelle Suard and Prof. J. R. Carvajal (ILL, France), Dr. Francois Fauth (ALBA, Spain), Dr. Maxim Avdeev (ANSTO, Australia) for the interesting and fruitful scientific collaborations. I have been greatly benefited from their expertise, and learned a lot in this process.

I extend my sincere thanks to Dr. A. Govindaraj who has been kind and cooperative whenever I approached him for any help.

I owe my sincere thanks to my present lab mates Somnath, Chandan, Avijit, Amit, Premkumar, Ravishankar, Pavitra, Gopal, Sunita, Ram, Pramoda, Anand, Lingampalli, Uttam, Manjeet, Sreedhara, Manoj, Rajesh, Magesh, Deepa, Pratap, Manjunath and Manaswee for their wonderful company and scientific discussions.

I am grateful to my past labmates Dr. Pranab Mandal, Dr. Nitesh Kumar, Mrs. Ajmala Shireen, Mr. Srikanth Revoju, Ms. Monali Moirangthem, Dr. Nandakumar Kalarikkal, Dr. K. Vasu, Dr. Angshuman Nag, Dr. C. R. Serrao, Dr. Y. Sundarayya, Dr. Barun Das, Dr. Kanishka Biswas, Dr. Urmimala Maitra for their help and guidance during my initial period of Ph.D.

I thank all the technical staff of JNCASR, especially Mr. Anil, Mr. Vasu, Mr. Srinath, Mr. Mahesh, Mrs. Selvi, Dr. Jay Ghatak and Mrs. Usha. I thank Mrs. Shashi, Mr. Gowda and Mr. Victor for their help on various occasions.

I would like to thank all my Integrated Ph.D. course instructors, Prof. S. Balasubramanian, Prof A. Sundaresan, Prof. T. K. Maji, Prof. Swapan K. Pati, Prof. N. S. Vidhyadhiraja, Prof. K. S. Narayan, Prof. M. Eswaramoorthy, Prof. Shobhana Narasimhan, Prof. Umesh V. Waghmare, Prof. Amitabh Joshi, Prof. G.U. Kulkarni, Prof. Chandrabhas Narayana, Prof. Ranjan Datta, Prof. S. M. Shivaprasad, Prof. S. Ranganathan (IISc), Prof. T. N. Guru Row (IISc), Mrs. Shobha Narayana for the courses they provided and stimulating scientific interactions.

I would like to thank JNCASR for providing me an Integrated Ph.D scholarship. I also acknowledge the RAK-CAM fellowship.

I extend my sincere thanks to the entire Academic and Administrative staff of JNCASR for their efficiency and helpfulness. Special thanks are due to the members of computer laboratory and library.

I would also like to thank the Hostel staff, Mess workers and Chandraiah canteen for keeping me well fed. Not to forget, Sharanappa and Shivuanna for the hot cup of coffee, and Raju for the utility service.

I wish to thank my Integrated Ph. D. batch mates Varun, Dileep, Sharma, Pandeewar, Chidambar, Arpan, Gayatri and Sudeshna for their company and help.

I thank all my friends in JNC and IISc: Sudipta, Sasmita, Partha, Sachi, Debu, Sudip, Prakash, Pralok, Ritesh, Bivas, Arun, Suman, Parikshit, Somnath, Asutosh, Soumik, Gautam, Dibyajyoti, Kaushik, Sisir, Anirban, Dheeraj, Rajib, Mohini, Krishnendu, Sumanta, Satyanarayan, Rajkumar, Sujoy, Abhiroop, Ananya, Sohini, Soumyabrata, Syamantak, Tarak, Nivedita, Anindita, Papri, Pallabi, Monodeep, Ranjan, Swagatam, Aritra, Saurav, Shreya, Shreyan, Anindita Pal, Niloyendu, Satya, Manisha, Subhajit, and many more. I especially thank Prabhas for the technical help during writing the thesis. My stay in JNC would not have been as wonderful and enjoyable without their presence.

I express my deep gratitude to all the professors of Department of Chemistry, Ramakrishna Mission Vivekananda Centenary College, Rahara, for their guidance and encouragements towards research. I would like to express my deepest gratitude from the core of my heart to Dr. Arunavo Sen who has made me passionate about science.

I would like to express my sincere thanks and regards to Mrs. Indumati Rao and Mr. Sanjay Rao for their love, affection and warm hospitality extended to all of us during the course of my association with them.

Finally, I express my sincere gratitude to all those who helped me directly or indirectly.

Last but not the least, my parents for their unending support and encouragement during my up and downs. They have always believed in me, and never tied me down in any of my endeavors. I would like to thank Swastika for her constant support in my academic and non-academic affairs.

Rana Saha

PREFACE

Transition metal oxides constitute one of the most important classes of solids, exhibiting a wide range of structures and fascinating properties such as high T_C superconductivity, colossal magnetoresistance, metal-insulator transition, magnetoelectric multiferroicity. While the nature of metal-oxygen bond varies between ionic to highly covalent, the intriguing macroscopic properties of transition metal oxides result from a strong coupling among spin, orbital, charge and lattice degrees of freedom. The strong interactions among valence electrons lead to localization of electrons in the d -orbital, while the orbital degree of freedom gives rise to anisotropy in the electronic interactions.

In order to understand the correlation among various degrees of freedom, investigations on magnetic, dielectric, magnetoelectric and optical properties of various transition metal oxides crystallizing in AlFeO_3 -type, perovskite, spinel, and wurtzite structures have been carried out in this thesis. In addition, a detailed study on crystallographic and magnetic symmetry has also been performed by means of synchrotron x-ray and neutron diffraction techniques to establish the structure-property relationship. The thesis consists of eight chapters.

Chapter 1 gives a brief overview of a few important aspects such as orbital ordering, charge ordering, spin ordering and magnetoelectric properties of transition metal oxides. Further, the magnetic symmetry governing the magnetoelectric interaction in transition metal oxides has been discussed briefly. A brief description on the experimental techniques used for the present investigations are also given in this chapter.

Chapter 2 describes the role of cation disorder in controlling the structure and magnetic properties of $\text{Al}_{1-x}\text{Ga}_x\text{FeO}_3$ ($x = 0, 0.5, 1$) family of oxides. To understand the structure-property correlation, a detailed investigation has been carried out by employing x-ray, neutron diffraction, Mössbauer, and Raman spectroscopy. The study has revealed the occurrence of several interesting features related to unit cell parameters, site disorder, and ionic size correlating with the observed properties. The origin and tendency of cations to disorder and the associated properties are traced to the local structure and ionic sizes. In this chapter, metastable structural phases of $\text{Al}_{1-x}\text{Ga}_x\text{FeO}_3$ ($x = 0, 0.5, 1$) family of oxides realized by mechanochemical chemistry have also been studied. The metastable structures exhibit different magnetic properties from the original structure thereby correlating the structure-property relationship.

Chapter 3 focuses on the importance of magnetic symmetry analysis to understand the nature of magnetoelectric coupling in orthorhombic perovskite EuZrO_3 . Magnetic symmetry analysis requires proper knowledge on magnetic easy axis or magnetic anisotropy which arises due to strong spin-orbit coupling. To determine the magnetic easy axis, temperature dependent high-resolution neutron powder diffraction experiments were performed on polycrystalline EuZrO_3 . In addition, synchrotron x-ray diffraction was carried out to know the crystallographic symmetry. From the analysis of neutron diffraction data, the easy axis and the Shubnikov group which supports linear magnetoelectric effect were determined.

Chapter 4 dwells on the structural aspects of YVO_3 which undergoes a change in the lattice symmetry upon an orbital order-disorder transition due to strong coupling between the orbitals and the lattice. Since orbital ordering is the driving force for anisotropic electronic interactions which in turn control the physical properties of orthovanadates, it is essential to understand the orbital states of YVO_3 as a function of temperature. Temperature dependent synchrotron x-ray diffraction experiment was performed on

polycrystalline YVO_3 showing the occurrence of structural phase co-existence of G - and C -type orbital ordered states in a narrow temperature range ($T_{\text{Structural}} \leq T \leq T_{\text{Néel}}$).

Chapter 5 discusses the magnetic exchange anisotropy across the interface of two magnetically different transition metal oxides, namely, ferromagnetic $\text{La}_{0.7}\text{Sr}_{0.3}\text{MnO}_3$ (LSMO) and charge-ordered antiferromagnetic $\text{Y}_{0.5}\text{Ca}_{0.5}\text{MnO}_3$ (YCMO). For this purpose, several bilayers of LSMO-YCMO were grown and their magnetic properties were investigated. The present investigation also throws light on the structure of bilayer grown under strong biaxial tension imposed by SrTiO_3 (STO) substrate. In this chapter, the observation of exchange bias after cooling the sample in the presence of a low remnant magnetic field of a superconducting magnet has been discussed.

Chapter 6 deals with the discovery of linear magnetoelectric effect in a family of A -site magnetic spinel oxides, MnX_2O_4 ($X = \text{Al}, \text{Ga}$) exhibiting simple collinear spin structure. The observed linear magnetoelectricity is associated with the single-ion effects of magnetic ion (Mn^{2+}) located in the noncentrosymmetric tetrahedral environment. In the absence of a neutron diffraction experiment, magnetic easy axis was determined from the magnetic and magnetoelectric measurements on a single crystal. The obtained magnetic space group based on the knowledge on magnetic easy axis supports linear magnetoelectric effect in these A -site magnetic spinel oxides.

Chapter 7 introduces the effect of A -site cation ordering on the structure and properties of strongly frustrated B -site magnetic spinel oxides as well as spinel with magnetic ions at both A and B sites, LiMCr_4O_8 ($M = \text{Ga}, \text{In}, \text{Fe}$). These compounds undergo a structural phase transition at the antiferromagnetic transition from a highly symmetric cubic structure to relieve the magnetic frustration. The presence of two inequivalent cations at the A -site leads to a modulation of the Cr-Cr distance in the pyrochlore lattice thereby creating a breathing distortion, which is absent in the conventional isotropic pyrochlore, ZnCr_2O_4 . The stronger breathing distortion in In and Fe

compound gives rise to a spin-gap state which is associated with a sharp dielectric anomaly. On the other hand, a relatively weaker breathing distortion in the Ga compound leads to a short-range ordering without any gapped state, analogous to ZnCr_2O_4 .

Chapter 8 describes the effect of aliovalent anion (N, F) substitution on the optical properties of ZnO. It has been a common trend for a long time to substitute the cations in metal oxides to modify the electronic structure thereby tuning the related physical properties. However, such efforts show marginal changes in the electronic structure and hence exhibit a limited effect on the optical properties. A unique strategy of co-substitution of aliovalent anions in metal oxides has been demonstrated to change the electronic structure of ZnO remarkably thereby giving rise to new absorption features in the visible range as compared to unsubstituted ZnO, which is in the UV region. The effect of co-substitution of anions in transition metal oxides is driven by the combined action of electrostatic and covalent effects.

CONTENTS

Declaration	iii
Certificate	v
Acknowledgements	vii
Preface	xi
Contents	xv

1. A brief overview of some aspects of transition metal oxides and their properties

Summary	1
1.1 Introduction	3
1.2 Jahn-Teller distortion and orbital ordering	6
1.2.1 Second-order Jahn-Teller effect:	11
1.3 Charge ordering	12
1.4 Magnetic exchange interaction	15
1.4.1 Direct exchange:	16
1.4.2 Indirect exchange:	16
1.4.3 Superexchange:	17
1.4.4 Anisotropic exchange interaction:	20
1.5 Magnetic anisotropy	20
1.5.1 Magnetocrystalline anisotropy:	21
1.5.1.1 Anisotropy in antiferromagnet	22
1.5.2 Exchange anisotropy:	24
1.6 Magnetoelectric effect	27
1.6.1 Symmetry constraints	29
1.6.2 Magnitude constraints	32
1.7 X-ray and neutron diffraction	32
1.7.1 X-ray diffraction	34

1.7.2 Neutron diffraction	34
1.8 Rietveld refinement	35
1.8.1 Peak-profile function:	36
1.8.2 Profile fitting:	37
1.8.3 Full structure refinement:	37
1.8.4 Magnetic structure determination from refinement:	39
1.8.5 <i>R</i> -factors:	42
1.9 Magnetic properties	43
1.9.1 DC magnetometry:	43
1.9.2 AC magnetometry:	46
1.10 Dielectric properties	49
1.10.1 Capacitance and dielectric loss:	49
1.10.2 Pyroelectric current measurement:	52
Bibliography	55

2. Structure and magnetic properties of $\text{Al}_{1-x}\text{Ga}_x\text{FeO}_3$ family of oxides

Summary.....	59
2.1 Introduction	61
2.2 Scope of the present investigation	62
2.3 Experimental details	63
2.4 Results and discussion.....	65
2.4.1 Structure and magnetic properties of $\text{Al}_{1-x}\text{Ga}_x\text{FeO}_3$:	65
2.4.1.1 Structure	65
2.4.1.1.1 X-ray diffraction of AlFeO_3 and GaFeO_3	65
2.4.1.1.2 Neutron diffraction of AlFeO_3	67
2.4.1.1.3 Neutron diffraction of GaFeO_3	75
2.4.1.1.4 Raman spectroscopy of AlFeO_3	80
2.4.1.2 Magnetic properties	83
2.4.1.2.1 DC magnetization.....	83
2.4.1.2.2 Mössbauer spectra of AlFeO_3 and GaFeO_3	85
2.4.1.3 Theoretical understanding of cation disorder and related properties	86

2.4.2 Effect of Cr substitution on the structural and magnetic properties of GaFeO ₃ :	90
2.4.2.1 Theoretical understanding of site-specific cation substitution	96
2.4.3 Ball-milling induced structural transitions in Al _{1-x} Ga _x FeO ₃ (x = 0, 0.5, 1):	99
2.4.3.1 AlFeO ₃	99
2.4.3.1.1 X-ray diffraction study	99
2.4.3.1.2 Raman spectroscopic study	100
2.4.3.1.3 Magnetic property	101
2.4.3.2 GaFeO ₃	102
2.4.3.2.1 X-ray diffraction study	102
2.4.3.2.2 Raman spectroscopic study	104
2.4.3.2.3 Magnetic property	104
2.5 Conclusions	108
Bibliography	109
3. Crystallographic and magnetic structures of the magnetoelectric EuZrO₃	
Summary	113
3.1 Introduction.....	115
3.2 Scope of the present investigation	117
3.3 Experimental details	118
3.4 Results and discussion	119
3.4.1 Crystal structure:	119
3.4.2 Magnetic properties:.....	120
3.4.3 Magnetic structure:.....	122
3.4.4 Magnetic symmetry analysis:.....	126
3.5 Conclusions	127
Bibliography	128

4. Temperature effects on the structural aspects of YVO₃

Summary.....	131
4.1 Introduction	133
4.2 Scope of the present investigation	135
4.3 Experimental details	136
4.4 Results and discussion.....	137
4.4.1 Ambient condition X-ray diffraction study in RVO ₃ (R = Y, Sm, Eu, Gd, Tb):	137
4.4.2 Low-temperature X-ray diffraction study in YVO ₃ :	143
4.5 Conclusions	151
Bibliography	151

5. Exchange bias at the interface between ferromagnetic La_{0.7}Sr_{0.3}MnO₃ and charge-ordered antiferromagnetic Y_{0.5}Ca_{0.5}MnO₃

Summary.....	155
5.1 Introduction	157
5.2 Scope of the present investigation	158
5.3 Experimental details	159
5.4 Results and discussion.....	160
5.4.1 Structure characterization of LSMO - YCMO bilayer:	160
5.4.2 DC Magnetization as a function of temperature [M (T)] and time [M (t)]:	163
5.4.3 DC Magnetization as a function of magnetic field, M (H):	167
5.4.3.1 Field - Cooled (FC) exchange bias	167
5.4.3.2 Training effect.....	172
5.4.3.3 Remnant - Field - Cooled (RFC) exchange bias	173
5.4.3.4 Temperature-dependent Field - Cooled (FC) exchange bias	175
5.5 Conclusions	176
Bibliography	176

6. Magnetoelectric effect in *A*-site magnetic spinel oxides, MnX_2O_4 ($\text{X} = \text{Al, Ga}$)

Summary	179
6.1 Introduction	181
6.2 Scope of the present investigation	183
6.3 Experimental details	184
6.4 Results and discussion	185
6.4.1 Structure:	185
6.4.1.1 X-ray diffraction of MnX_2O_4 ($\text{X} = \text{Al, Ga}$)	185
6.4.1.2 Neutron diffraction of MnGa_2O_4	188
6.4.2 Magnetic properties of MnX_2O_4 ($\text{X} = \text{Al, Ga}$):	191
6.4.3 Dielectric properties of MnX_2O_4 ($\text{X} = \text{Al, Ga}$):	194
6.4.4 Magnetic anisotropy dependent magnetoelectric interaction in MnGa_2O_4 :	198
6.4.4.1 Magnetic measurements on single crystal of MnGa_2O_4	199
6.4.4.2 Magnetoelectric measurements on single crystal of MnGa_2O_4	201
6.5 Conclusions	204
Bibliography	205

7. Magnetostructural coupling and magnetodielectric effect in *A*-site cation-ordered spinel oxides, LiMCr_4O_8 ($\text{M} = \text{Ga, In, Fe}$)

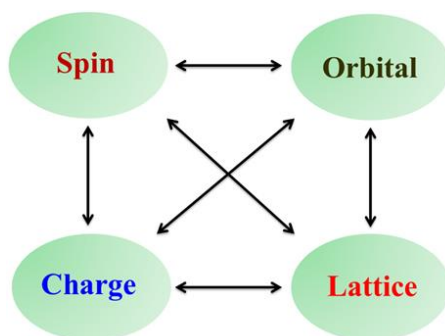
Summary	207
7.1 Introduction	209
7.2 Scope of the present investigation	211
7.3 Experimental details	212
7.4 Results and discussion	214
7.4.1 Structure:	214
7.4.1.1 X-ray diffraction study of $\text{LiGaCr}_4\text{O}_8$ and $\text{LiInCr}_4\text{O}_8$	214
7.4.1.2 X-ray diffraction study of $\text{LiFeCr}_4\text{O}_8$	215
7.4.1.3 Neutron diffraction study of $\text{LiGaCr}_4\text{O}_8$	217
7.4.1.4 Neutron diffraction study of $\text{LiFeCr}_4\text{O}_8$	221

7.4.2 Magnetic properties of LiMCr_4O_8 (M = Ga, In, Fe):	223
7.4.2.1 Magnetization and heat capacity study of $\text{LiGaCr}_4\text{O}_8$ and $\text{LiInCr}_4\text{O}_8$	223
7.4.2.2 Magnetization and heat capacity study of $\text{LiFeCr}_4\text{O}_8$	232
7.4.3 Dielectric properties of LiMCr_4O_8 (M = Ga, In, Fe):.....	234
7.4.3.1 Dielectric study of $\text{LiGaCr}_4\text{O}_8$ and $\text{LiInCr}_4\text{O}_8$	234
7.4.3.2 Dielectric study of $\text{LiFeCr}_4\text{O}_8$	238
7.4.4 Raman spectroscopic study of $\text{LiFeCr}_4\text{O}_8$	243
7.5 Conclusions	245
Bibliography	245
8. Effect of aliovalent anion (N, F) substitution on the properties of ZnO	
Summary.....	249
8.1 Introduction	251
8.2 Scope of the present investigation.....	252
8.3 Experimental details	253
8.4 Results and discussion.....	254
8.4.1 X-ray diffraction:	254
8.4.2 X-ray photoelectron and IR spectroscopy:	255
8.4.3 Raman spectroscopy:.....	258
8.4.4 UV-Visible, Photoluminescence and Electron Energy Loss Spectroscopy:.....	258
8.4.5 Isothermal magnetization data:.....	261
8.4.6 Important interpretations from first-principles calculations:.....	263
8.5 Conclusions	264
Bibliography	265
List of publications	269

A brief overview of some aspects of transition metal oxides and * their properties

Summary

Transition metal oxides constitute one of the most important classes of solids, exhibiting a wide range of structures and fascinating properties originating from a strong coupling among spin, orbital, charge and lattice degrees of freedom. Here, we discuss the intriguing aspects of strong electron correlation effect and orbital degrees of freedom in transition metal oxides. The strong interactions among valence electrons lead to localization of electrons in the *d*-orbital, while the orbital degree of freedom gives rise to anisotropy in the electronic interactions. A description has been given of the magnetic exchange interaction and anisotropy which is essential to understand the magnetic properties of various oxides. The cross coupling between magnetism and electricity known as the magnetoelectric effect is another important property exhibited by transition metal oxides which has been explored. In addition, a brief discussion on the diffraction techniques essential to study the variety of crystal and magnetic structures are presented. Finally, we discuss the experimental techniques employed to study the magnetic and dielectric properties of various oxides.



*This chapter also briefly describes about the experimental techniques.

1.1 Introduction

Since ancient times, transition metal oxides have been one of the most important families of solid which exhibit a plethora of structure and physical properties [1,2]. The crystal structures of oxides vary from cubic to the triclinic structure. Simple binary oxides of chemical formula MO generally crystallize in the rock-salt or nickel-arsenide as well as wurtzite structure while dioxides crystallize in the fluorite, rutile (tetragonal), distorted rutile or some other complex structures. Many sesquioxides, M_2O_3 possess the corundum (rhombohedral) structure. On the other hand, some of the ternary oxides are found to crystallize in the perovskite structure (ABO_3), spinel structure (AB_2O_4), bronze structure (A_xBO_3), pyrochlore structure ($A_2B_2O_7$) and garnet structure ($A_3B_5O_{12}$). Many of the transition metal oxides are not truly three-dimensional but have low-dimensional features. For example, La_2CuO_4 and La_2NiO_4 with the K_2NiF_4 structure are two-dimensional compared to $LaCuO_3$ and $LaNiO_3$ which are three-dimensional perovskites. In addition, several other structural types are also known. Interestingly, in oxides, the nature of chemical bonding between metal and oxygen varies from nearly ionic to highly covalent to metallic. Besides this structural diversity in transition metal oxides, they exhibit a wide range of electronic and magnetic properties [3,4]. They show metallic properties (e.g. ReO_3 , RuO_2 , $LaNiO_3$) at one end, while oxides with highly insulating behavior ($BaTiO_3$) are found at the other end. There are oxides which traverse from insulating to the metallic regime as a function of temperature, pressure and chemical composition (e.g. V_2O_3 , $La_{1-x}Sr_xVO_3$). In addition, these oxides exhibit various interesting electronic phenomena arising from charge density waves (e.g. $K_{0.3}MoO_3$), charge ordering (e.g. $La_{0.5}Ca_{0.5}MnO_3$, Fe_3O_4) and oxygen vacancy ordering (e.g. $Ca_2Fe_2O_5$, $Ca_2Mn_2O_5$). Oxides are also known to show interesting magnetic properties starting from ferromagnetism in CrO_2 and $La_{0.7}Sr_{0.3}MnO_3$, ferrimagnetism in $GaFeO_3$ and Fe_3O_4 and finally antiferromagnetism in NiO and $LaCrO_3$. The temperature-induced spin-state transition has been realized in $LaCoO_3$, where the Co^{3+} ion undergoes low-spin to intermediate spin to high-spin state transitions. Analogous to ferromagnetic hysteresis i.e. phase transition and domain switching has also been realized in the electrical property of metal oxides, e.g. $BaTiO_3$ shows switchable spontaneous ferroelectric polarization. The magnetoelectric

properties where magnetization can be controlled by an electric field or vice versa was discovered in rhombohedral Cr_2O_3 [5-7].

The fascination in transition metal oxides research reached a milestone following the discovery of high-temperature superconductivity in $\text{La}_{2-x}\text{Ba}_x\text{CuO}_4$ [8]. The increasing interest in the field of metal oxides gave birth to exciting colossal magnetoresistance phenomena in perovskite manganites ($\text{La}_{1-x}\text{Ca}_x\text{MnO}_3$) [9,10]. Although the effect of magnetic field on the electrical resistivity of ordinary metal is not significant but the effect of magnetic field on the electrical resistance of metallic $\text{La}_{1-x}\text{Ca}_x\text{MnO}_3$ becomes “colossal”. With the advent of modern technological advancement, another exciting phenomenon was discovered in transition metal oxides, BiFeO_3 where magnetism and ferroelectricity coexist- termed as multiferroics [11,12]. Although the phenomenon of magnetism and ferroelectricity is mutually exclusive, there are certain materials (e.g. TbMnO_3 , CoCr_2O_4) where ferroelectricity originates from particular spin configurations thereby allowing the possibility of controlling the magnetic properties with an electrical field or electrical properties with a magnetic field [13]. Although the bottleneck for the efficient magnetoelectric-multiferroic material is the operational temperature as well as the strength of magnetoelectric coupling there has been constant effort to realize it in practice. The room temperature magnetoelectric operation has been realized in BiFeO_3 [14] and *Z*-type hexaferrite ($\text{Sr}_3\text{Co}_2\text{Fe}_{24}\text{O}_{41}$) [15].

In transition metal oxides, both the ionic size and the electronegativity of the anion and cation are considerably different. As a result, there would be a small overlap between the metal *d* and oxygen *p* orbitals resulting in narrow electronic bands with bandwidths typically of the order of 1-2 eV. In these materials the outer *s*- and *p*-orbitals form a filled valence band and an empty conduction band separated by an energy gap of ~ 5 to 10 eV [2]. The *d*-band which is present in the vicinity of Fermi level would be narrow due to the fact that in the metal oxides metal ions are farther apart and have a smaller spatial extension. It is, therefore, reasonable that to understand the fascinating properties of transition metal oxides we need to focus on the outer *d*-electrons. The intriguing macroscopic properties (e.g. electrical, magnetic and optical) of transition metal oxides originate from the following two important aspects of *d*-electrons.

(1) The valence d -electrons in these materials interact very strongly thereby tending to localize or to bind to a specific atomic site. In the case of localized electron situation i.e. the on-site Coulomb energy, U (the cost of putting two electrons on the same lattice site) is so strong that electrons cannot move freely through the crystal and therefore they cannot be treated anymore as free particles and are rather termed as correlated electrons. The latter aspect of d -electrons - a feature associated with the way electrons have to avoid each other if the Coulomb effects are large, become significant in controlling the properties of transition metal oxides. The competition between metallic behavior [parameterized by the transfer integrals (t) in the tight binding model, or the size of the electronic bandwidth (W)] and Coulomb energy (Hubbard- U) is expressed by the Hubbard model. Therefore, in the stable ground state ($U = \infty$), each lattice site would be occupied by one electron without any movement thereby minimizing the on-site Coulomb energy. Now another situation can arise when U is large but not infinite ($U > W$) for a singly occupied lattice site, where the spins of nearest-neighbour sites are antiparallel but the spins of next-nearest-neighbor sites are parallel. Then it is possible for an electron to hop to the nearest- neighbor site to save the kinetic energy but not to the next-nearest-neighbor site due to the Pauli exclusion principle. Therefore the system becomes an insulator. Such an antiferromagnetic insulator with a large U and one electron per site is known as a Mott insulator. When $U < W$, the metallic behavior is observed. The crossover occurs when $U \sim W$ where there is a metal-insulator transition. The outer s and p electrons interact strongly with neighboring atoms and are described by the collective-electron model (band theory) while the outer f electrons which are tightly bound to the nuclei and well screened from the neighboring atoms are described by the localized electron model. Outer d -electrons have an intermediate character, as they are not screened from the neighboring atoms by outer core electrons. Because of this intermediate nature of d -electrons transition metal oxides exhibit itinerant as well as localized electron properties.

(2) Another important microscopic phenomenon is the orbital degree of freedom. Once the valence d -electron is localized to a specific atomic site now there is a possibility of electrons to choose several types of energetically equivalent or degenerate electronic orbitals around the atoms. The orbital degree of freedom

ensures that the electrons can choose from a manifold of possible electronic states. For example, the valence electrons of $\text{La}_{1-x}\text{Ca}_x\text{MnO}_3$ are located on the Mn^{3+} ions, where they can occupy either of two d -orbitals, $d_{x^2-y^2}$ or d_{z^2} . At low temperature, each electron can occupy one of the two orbitals (or a linear combination of the two). However, their choices of occupying a particular orbital are not independent. Once a valence electron localizes in a definite Mn d -orbital, the charge distribution around this ion is distorted and the adjacent oxygen ligands are dislodged. This results in spontaneous formation of an ordered pattern of occupied orbitals throughout the crystal lattice. It can be easily understood from the schematic [Figure 1.1] of two possible orbital patterns for Mn^{3+} ions on a square lattice. From this figure, it is seen that the uniform arrangement of occupied orbitals give rise to antiferromagnetic interactions, while the alternate arrangement of occupied orbitals favors ferromagnetic interactions [16]. In the presence of an external magnetic field, it is possible to switch from one orbital state to another state thereby changing the magnetic ground state. A similar model can be employed to understand the colossal magnetoresistance in $\text{La}_{1-x}\text{Ca}_x\text{MnO}_3$, where a small change in the magnetic field gives rise to a large change in electrical conductivity.

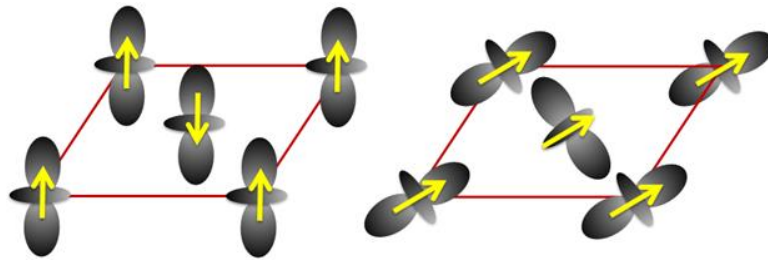


Figure 1.1: The schematic representation of two-dimensional orbital ordered states of Mn^{3+} d -orbitals on a square lattice. The corresponding spin configurations are indicated by yellow arrows.

1.2 Jahn-Teller distortion and orbital ordering

The fascinating physical properties of transition metal oxides depend on whether the valence electrons are localized on individual atomic sites or delocalized throughout the solid. In this context, transition metal ions in the orbitally degenerate state are of particular interest because the preferential occupation of specific d -orbitals can lead to the development of a long-range ordered pattern. This phenomenon termed as orbital ordering, makes the bonding between the cations in the oxides strongly directional depending on the kind of the occupied orbitals and their mutual orientation, which

further influences magnetic interactions and electron transport [17]. Prototypical system for perovskite oxides is LaVO_3 [$\text{V}^{3+} 3d^2(t_{2g}^2 e_g^0)$] and LaMnO_3 [$3d^4(t_{2g}^3 e_g^1)$] [18].

In some $3d$ transition metal oxides (e.g. LaMnO_3 , YVO_3 , KCuF_3) orbital ordering and concomitant Jahn-Teller (JT) distortion has been realized. Jahn-Teller theorem states that “any non-linear molecular system in a degenerate electronic state will be unstable and will undergo distortion to form a system of lower symmetry and lower energy thereby removing the degeneracy” [19]. The JT distortion is observed for high-spin $\text{Mn}^{3+} 3d^4(t_{2g}^3 e_g^1)$, $\text{Cu}^{2+} 3d^9(t_{2g}^6 e_g^3)$, $\text{V}^{3+} 3d^2(t_{2g}^2 e_g^0)$ and low-spin $\text{Ni}^{3+} 3d^7(t_{2g}^6 e_g^1)$. The electronic configuration indicates that JT ions are orbitally degenerate. Let us consider the example of LaMnO_3 where Mn^{3+} is a Jahn-Teller ion and located in the octahedral environment. Now in the presence of octahedral crystal field the five-fold degeneracy of the d -orbital will be lifted. This will form a three-fold degenerate t_{2g} and two-fold degenerate e_g level. The e_g orbital will undergo further splitting and this will result in the distortion of the octahedron as shown in Figure 1.2. This process is energetically favorable because the energy cost of increased elastic energy is balanced by a resultant electronic energy lowering due to distortion.

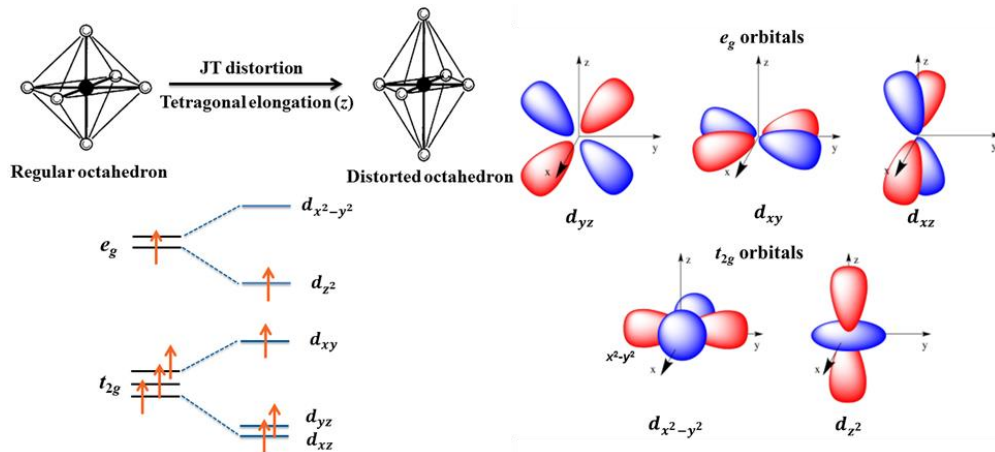


Figure 1.2: The electronic configuration of Jahn-Teller Mn^{3+} ion. A regular octahedron becomes distorted resulting in the splitting of the t_{2g} and e_g levels. The distortion lowers the energy because the singly occupied e_g level is lowered in energy. The right panel shows the anisotropic-shaped five d orbitals in the cubic crystal field.

In the case of the static Jahn-Teller effect [20,21] the distortion which occurs spontaneously is fixed on a particular axis of an octahedron. Below a certain critical temperature, if each of the Jahn-Teller distorted sites interact with each other, cooperatively throughout the crystal, then there will be an ordering of the local

distortions which will result in the change in the macroscopic crystallographic symmetry. This kind of structural phase transitions arising from the correlation or ordering of the Jahn-Teller distorted lattice sites is termed as cooperative Jahn-Teller effect [22,23]. Such temperature-induced cooperative Jahn-Teller distortion and associated structural phase transitions have been observed in tetragonal zircon structure (DyVO_4), spinel structure (FeCr_2O_4 , NiCr_2O_4 , FeV_2O_4) and perovskite (KCuF_3 , KMnF_3). In the case of LaMnO_3 , cooperative pseudo-Jahn-Teller effect has been observed around $T_{PJT} \sim 750$ K, where the compound undergoes a transition from the Jahn-Teller distorted orthorhombic phase to a high temperature orthorhombic phase which is nearly cubic [24-26]. In addition to the pseudo static and cooperative Jahn-Teller effects, another kind of averaged Jahn-Teller effect has been observed which involves rapid hopping of the distortion from one site to another site giving rise to dynamic Jahn-Teller effect [27]. It has been realized in hole doped manganites which contain a mixture of Mn^{3+} and Mn^{4+} ions. Apart from the double exchange interactions, this kind of dynamic JT distortion can also arise when thermal fluctuations (kT) are higher than the energy gained by the system due to distortion. In this case, there will be rapid, thermally induced fluctuations between the two JT distorted states. Therefore it becomes difficult to understand whether the system is orbital ordered or disordered.

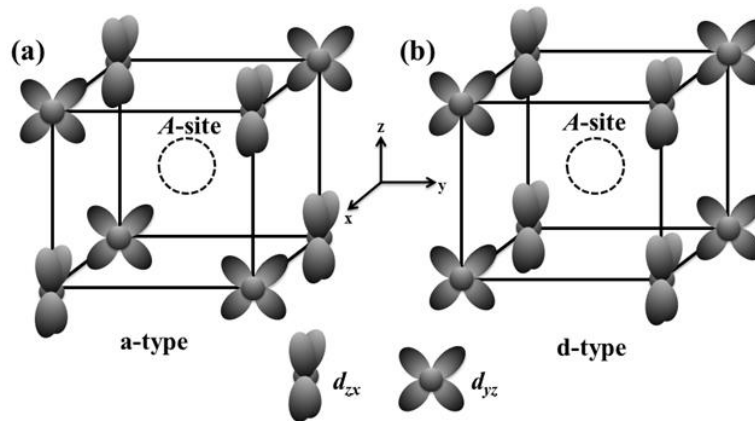


Figure 1.3: Two types of orbital ordering with the *a*-type and *d*-type JT distortions.

In the perovskite-type transition metal compounds, there are two possible JT distortions depending on the stacking of the elongated octahedra along the *c*-axis, *d*-type, and *a*-type JT distortion respectively [Figure 1.3] [17]. In the *d*-type JT distortion, the elongated axes of octahedra are parallel along the *c* axis and in the case of *a*-type distortion; the elongated axes are rotated by 90° along the *c* axis [17,28]. In

LaMnO₃(d^4), YVO₃ (d^2), YTiO₃ (d^1) d -type JT distorted state is the stable ground state, while in LaVO₃ (d^2) a -type JT-distortion is the stable ground state. In KCuF₃, both the d -type and a -type JT distorted states are found as the ground state. In addition to that, it has been shown from Hartree-Fock calculations that in perovskite-type transition metal oxides GdFeO₃-type octahedral distortion or octahedral tilt also plays an important role in stabilizing the particular type of JT distorted state. In the presence of large GdFeO₃-type distortion, the covalency between the A -site cations and oxygen makes the d -type JT distortion (same orbital along the c axis) energetically favorable than the a -type JT distortion (alternating orbitals along the c direction). As a result, the orbital-ordered states compatible with the d -type JT distortions are favored in LaMnO₃, YVO₃, and YTiO₃ which have the relatively large GdFeO₃ type distortion. In the case of less distorted LaVO₃, the orbital ordering compatible with the a -type JT distortion is favored because of the pure superexchange effect.

In RVO_3 (R = rare-earth and Y) family of orthorhombic perovskites, two types of JT distortion with the corresponding types of orbital ordering are shown in Figure 1.4 [28]. In the G -type orbital ordered state, the $d_{xy}d_{yz}$ and $d_{xy}d_{zx}$ orbitals are occupied alternatively along the orthogonal directions resulting in “out of phase” arrangement of V-O distances between successive ab planes (a -type JT distortion). In the case of C -type orbital ordered state, the $d_{xy}d_{yz}$ and $d_{xy}d_{zx}$ orbitals are occupied alternately in the ab plane while the same orbitals are arranged along the c direction leading to an “in phase” arrangement of V-O distances between successive ab planes (d -type JT distortion).

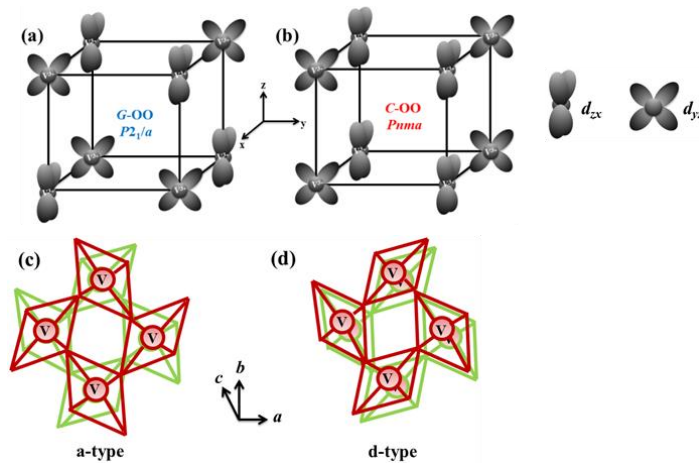


Figure 1.4: Schematic representation of (a) G -type and (b) C -type orbital-ordered states along with associated (c) a -type and (d) d -type JT effects reflected on the distortion of VO₆ octahedra.

The orbital ordering plays an active role in controlling the anisotropic electron-transfer interaction [29]. Based on the orbital direction-dependent arrangement of occupied orbitals throughout the crystal, it favors or disfavors the double-exchange interaction and the superexchange (ferromagnetic or antiferromagnetic) interaction giving rise to complex spin-orbital coupled state. Therefore, different orbital ordered states can give rise to different macroscopic properties. For example, in LaMnO_3 , alternate ordering of $(3x^2 - r^2)$ and $(3y^2 - r^2)$ orbitals on neighboring Mn^{3+} ions gives rise to an in-plane ferromagnetic exchange interaction while the magnetic coupling between two successive ab planes is antiferromagnetic in nature. This type of magnetic interactions is termed as A -type antiferromagnetic state [Figure 1.5] which is the manifestation of anisotropic superexchange interaction resulting from the particular type orbital ordered state. In addition to that, rod-type arrangement of $(3z^2 - r^2)$ orbitals along the c axis give rise to ferromagnetic interaction while the in plane magnetic interactions is antiferromagnetic in nature [Figure 1.5].

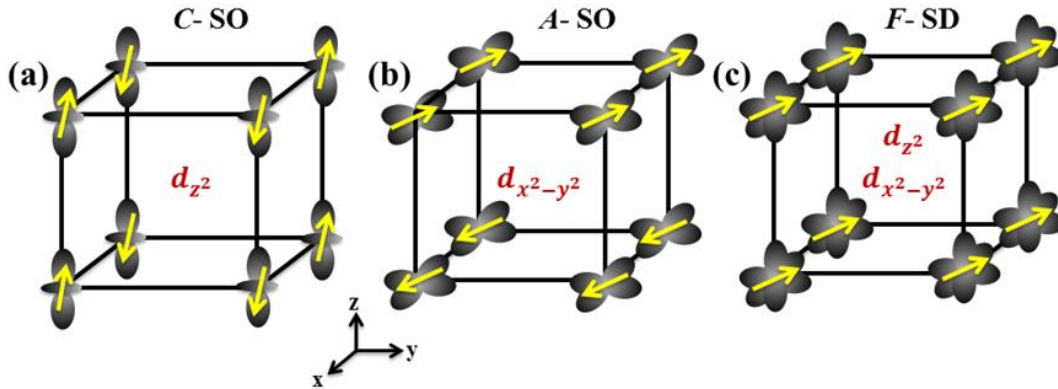


Figure 1.5: Different types of orbital and spin ordered states in perovskite manganites. SO and SD stands for spin order and spin-disorder respectively.

In the hole-doped manganese oxides (e.g. $\text{Nd}_{1-x}\text{Sr}_x\text{MnO}_3$, $\text{La}_{0.5}\text{Sr}_{0.5}\text{MnO}_3$) in which double-exchange interaction emerges depending on the strength of doping or strain, (by growing a thin film on a suitable substrate) various orbital ordered and disordered states emerge followed by respective spin ordered states. In general, the decrease of hole doping enhances the F (orbital-disordered) region, whereas the increase (or decrease) in the c/a ratio (the ratio of apical to equatorial Mn-O bond length) favors the C (A) states [29]. In the case of $R\text{VO}_3$ compounds, the G -type orbital ordering favors C -type antiferromagnetic (ferromagnetic interactions along the c direction and antiferromagnetic interaction in the ab plane) ordering, while the C -type

orbital ordering favors G -type antiferromagnetic ordering (antiferromagnetic interactions along the orthogonal directions).

1.2.1 Second-order Jahn-Teller effect:

It has been observed that, in transition metal oxides, in the presence of orbitally degenerate d electrons, the system undergoes cooperative Jahn-Teller distortion with concomitant orbital ordering. Interestingly, in the absence of d electrons, another type of Jahn-Teller distortion is realized in these oxides giving rise to the phenomenon of ferroelectricity [30]. The ferroelectric material possesses switchable macroscopic electric polarization as a result of spontaneous ordering of electric dipoles originating from the non-centrosymmetric arrangement of anions and cations. The net polarization (\vec{P}) is defined as the total dipole moment ($\vec{\mu}$) per unit volume (V), such that $\vec{P} = \sum \vec{\mu}/V$ and $\vec{\mu} = q\vec{r}$, where charges ($+q$, $-q$) of opposite polarity are separated by a distance, \vec{r} . Ferroelectric materials undergo a phase transition from the high temperature centrosymmetric paraelectric phase to the low temperature spontaneously polarized state with broken inversion symmetry across the transition temperature known as Curie-temperature (T_C). The ferroelectric instability is driven by the second-order JT effect [31] which lowers the energy of a system by hybridizing the empty d orbital of transition metal ion with the p orbital of oxygen ion. This particular JT effect is called second order because it involves the second-order terms in the perturbative expansion of total energy with respect to distortions from a centrosymmetric high temperature paraelectric phase, expanded as a function of polar distortion (Q), about the centrosymmetric phase with energy $E^{(0)}$ as [32],

$$E = E^{(0)} + \langle 0|H^{(1)}|0\rangle Q + \frac{1}{2} \left[\langle 0|H^{(2)}|0\rangle - 2 \sum_n \frac{|\langle 0|H^{(1)}|n\rangle|^2}{E^{(n)} - E^{(0)}} \right] Q^2 + \dots \quad (1.1)$$

where $|0\rangle$ is the lowest energy solution of $H^{(0)}$ and $E^{(n)}$ are the energies associated with the excited states $|n\rangle$. The first order term, $\langle 0|H^{(1)}|0\rangle Q$ describes the first-order JT distortion and it does not give rise to ferroelectricity because it only survives for the d orbitals when the distortion (Q) is centrosymmetric. The second-order term which is the sole source of non-centrosymmetric off-centering contains two opposing terms, the first term is due to the short-range repulsive forces raising the energy of the system and

the second term is associated with the covalent bond formation stabilizing the ionic displacements (this term is always negative unless it is zero by symmetry). Therefore, when the second term is larger than the first term of second-order terms (e.g. in the case of d^0 electronic configuration where repulsive force is absent) the total energy is negative favouring ferroelectric instability. From the expression of second term of second-order terms it is clear that if the ground and lowest excited states are of different parity (e.g. if the valence and conduction bands are made of p^n and d^0 orbitals respectively) to keep the polar distortion (Q) odd as well as the energy states are closely separated, the second term will be highly positive thereby making the overall energy largely negative which supports spontaneous polar distortion. This second-order JT distortion explains the observation of proper ferroelectricity defined as the structural instability towards the polar state associated with electronic pairing, e.g. in the case of BaTiO_3 , where hybridization between Ti ($3d$) and O ($2p$) orbitals stabilizes the ferroelectricity. The second-order JT distortion is also visible in the case of elements containing inert-pair of electrons, e.g. in PbTiO_3 hybridization between the Pb ($6s$) and O ($2p$) electrons gives rise to large Pb polarizability and hence ferroelectricity.

1.3 Charge ordering

The parent undoped compound, LaMnO_3 where Mn is present in +3 state, shows spin, orbital and lattice orders. Now doping of manganites with alkaline-earth ions such as Ca^{2+} and Sr^{2+} results in a fraction of Mn ions occurring in the +4 state, thereby resulting in a new electronic order, charge order (CO) [33]. In the charge-ordered state, electrons become localized due to the ordering of +3 and +4 charges of the Mn ions on specific lattice site giving rise to long-range order throughout the crystal structure. The charge-ordered phases are originating from the interaction between the charge carriers and phonons wherein the Jahn-Teller distortions play a significant role. Accompanying the charge ordering, the Mn^{3+} (e_g) orbitals ($3d_{z^2}$) and the associated lattice distortions (long Mn-O bonds) also develop long-range order, giving rise to orbital-ordered state. The ordered arrangement of occupied orbital following the concomitant charge-ordering gives rise to complex CE-type spin-ordering [29]. This kind of spin structure is characterized by the alternate ordering of Mn^{3+} and Mn^{4+} ions in a checkerboard fashion as shown in Figure 1.6. The spin ordering in the ab plane is somewhat complex

and it stacks antiferromagnetically along the c axis. In contrast, A -type antiferromagnetic ordering lacks charge ordering. Orbital and spin ordering accompanied by charge ordering shows the CE-type antiferromagnetic ordering, while in the presence of only orbital and spin ordering A -type antiferromagnetic ordering is realized.

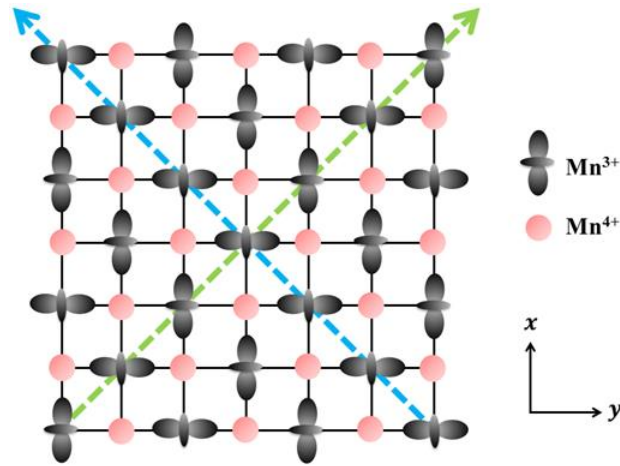


Figure 1.6: CE-type charge ordering and associated orbital ordering of the $3x^2-r^2 / 3y^2-r^2$ orbitals in the ab plane of half-doped manganates.

The occurrence of charge-ordering has been studied in great detail in the perovskite mixed valent rare-earth manganites of the general composition $R_{1-x}A_x\text{MnO}_3$ (R = rare earth, Y; A = alkaline earth). The charge ordering has also been realized in Fe_3O_4 which undergoes charge-ordered to disordered state at 120 K, known as Verwey transition [34]. In half-doped rare-earth manganites ($x = 0.5$) the charge-ordering phenomenon is found to be favorable due to the presence of equal proportions of the Mn^{3+} and Mn^{4+} states. In addition, depending on the R and A ions, charge-ordering has also been observed in various compositions in the range $0.3 < x < 0.75$. The mean A -site cation radius (r_A) significantly controls the bandwidth of the e_g electrons of Mn ions through a change in Mn $3d$ and O $2p$ hybridization. With increasing size of r_A , Mn-O-Mn bond angle and consequently the bandwidth increases due to increased hydrostatic pressure. As a result, electrons of the Mn^{3+} hop to the Mn^{4+} by the double-exchange (DE) mechanism which plays a crucial role in the occurrence of ferromagnetism and metallicity in these manganites. Therefore, it is inferred that on the one hand, the double-exchange mechanism prefers the ferromagnetism, while at the other end CO state prefers antiferromagnetic insulating state by localizing the electrons. Manganites with very large r_A tend to be FM and metallic, with a Curie temperature T_c that

increases with r_A . For example, $\text{La}_{0.7}\text{Ca}_{0.3}\text{MnO}_3$ and $\text{La}_{0.7}\text{Sr}_{0.3}\text{MnO}_3$ with larger r_A shows ferromagnetic metallic behavior, while $\text{Pr}_{0.7}\text{Ca}_{0.3}\text{MnO}_3$ with relatively smaller r_A shows charge-ordering at 230 K followed by antiferromagnetic ordering at 170 K, where both antiferromagnetism and charge order coexists. The later observation is consistent with the general observation that manganites with smaller r_A have predominating charge-ordered state. The presence charge and orbital orders distorts the Mn^{3+}O_6 octahedron locally, which undergoes long range ordering. For example, the charge-ordered structure of $\text{Nd}_{0.5}\text{Sr}_{0.5}\text{MnO}_3$ consists of distorted oxygen octahedra containing zigzag chains with alternate long Mn-O bonds, 1.921 and 2.021 Å along [110] and short Mn-O bonds 1.881 and 2.020 Å along [-110] as seen from Figure 1.7 [35,36].

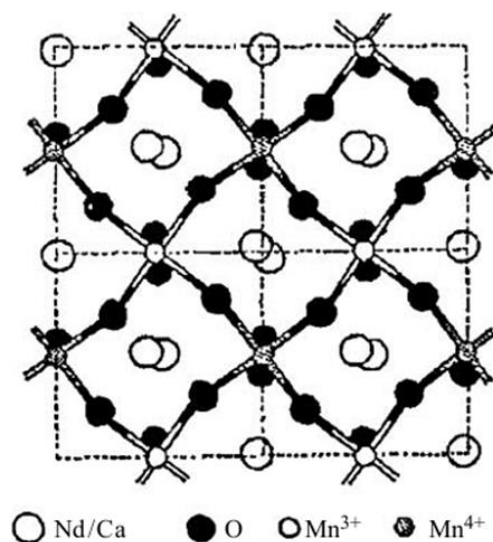


Figure 1.7: The structure of charge-ordered ($T = 10$ K) $\text{Nd}_{0.5}\text{Sr}_{0.5}\text{MnO}_3$ in the ab plane containing zigzag chains with alternating long and short Mn-O bonds. Mn^{4+} ions are located at $(\frac{1}{2} 0 0)$ and Mn^{3+} ions are present at $(0 \frac{1}{2} 0)$ [adapted with permission from ref. 35, © (2008) by the Royal Society of Chemistry].

There are two types of charge/orbital/spin phase diagram. In the case of type-I, there occurs concomitant orbital, charge and spin transitions only for the half-doped manganites i.e. $T_{\text{CO}} = T_{\text{N}}$. In a relatively wide-bandwidth system, $\text{Nd}_{0.5}\text{Sr}_{0.5}\text{MnO}_3$, while cooling the ferromagnetic ordering occurs first followed by orbital, charge and spin (AF) ordering at a lower temperature. In the case of type-II, first, the orbital and charge-ordered state appear concomitantly at a higher temperature followed by antiferromagnetic transitions at a lower temperature, as realized in the smaller bandwidth system, $\text{Pr}_{0.5}\text{Ca}_{0.5}\text{MnO}_3$. In these materials, the ferromagnetic metallic state is realized only in the presence of an external magnetic field. The field required to melt

the CO state to metallic state varies with r_A and the manganites with smaller r_A remains charge-ordered even in the presence of very high magnetic fields. Thus $\text{Y}_{0.5}\text{Ca}_{0.5}\text{MnO}_3$ ($r_A = 1.13 \text{ \AA}$) has a very robust CO state which remains unaffected by high magnetic field ($> 15 \text{ T}$). On the other hand, CO state of manganites with relatively larger average A-site cation radius, e.g. in $\text{Nd}_{0.5}\text{Sr}_{0.5}\text{MnO}_3$ ($r_A = 1.24 \text{ \AA}$) and $\text{Pr}_{0.6}\text{Ca}_{0.4}\text{MnO}_3$ ($r_A = 1.17 \text{ \AA}$) the charge-ordered state can be melted to ferromagnetic metallic state in the presence of smaller magnetic fields.

Interestingly, in the chemically phase-pure, mixed valent, rare-earth manganites the coexistence of charge-ordered antiferromagnetic and the ferromagnetic metallic state has also been observed below a critical temperature leading to the phenomenon of electronic phase separation [35]. For example, in $\text{Nd}_{0.5}\text{Ca}_{0.5}\text{MnO}_3$ below 150 K, ferromagnetic phase, A-type AFM phase and charge-ordered CE-type AFM phase coexists [37]. Moreover, it is shown that in the presence of magnetic field FM phase grows at the expense of AFM phase. $\text{Pr}_{0.7}\text{Ca}_{0.3}\text{MnO}_3$ also shows the occurrence of electronic phase separation between CO-AFM state and FM state below 80 K. Since the sizes of these electronic inhomogeneities are of the order of hundreds of nanometer or more, therefore those are experimentally identified by diffraction and many other techniques. Since the fractions of these electronic inhomogeneities are sensitive to the external magnetic (or electric) field, therefore the phenomenon of colossal magnetoresistance in $\text{La}_{0.5}\text{Ca}_{0.5}\text{MnO}_3$ can be understood based on the competition between DE mechanism and CO states and various other mechanisms, the details of which are beyond the scope of present discussion.

1.4 Magnetic exchange interaction

Here we discuss the important concepts of magnetic exchange interactions between two magnetic ions with net magnetic moments [38]. Exchange interactions are the driving forces for long range magnetic order. The magnetic exchange force is quantum-mechanical in nature and usually expressed by the Heisenberg spin Hamiltonian as $\hat{H} = -\sum_{ij} J_{ij} S_i \cdot S_j$, where J_{ij} is the exchange constant between the neighboring i^{th} and j^{th} spins. The factor of 2 is omitted because the summation includes each pair of spins twice. The exchange force is fundamentally electrostatic (Coulomb) in nature, because spins of similar orientation cost energy when they are close together and save energy

when they are apart. There are three types of exchange interactions, (1) direct exchange, (2) indirect exchange and (3) superexchange.

1.4.1 Direct exchange:

If the magnetic moments on neighboring magnetic ions interact through an exchange interaction without the involvement of an intermediary then it is termed as a direct exchange. In the case of a direct exchange, the electronic wave functions of the interacting atoms will overlap. Therefore direct exchange will experience both electrostatic attractive and repulsive forces. According to Pauli exclusion principle, the electrons with parallel spins will stay far from each other to reduce the repulsive forces. As a result, direct exchange interaction would favor the antiferromagnetic coupling between neighboring magnetic atoms. Since the radial distribution function of d and f electron wave functions decay exponentially with distance from the nucleus, the direct exchange can operate within a short distance and will decrease as the distance between interacting magnetic atom increases. For this reason, in oxides and other insulating compounds, the direct exchange is usually not an important medium to establish magnetic long-range order.

1.4.2 Indirect exchange:

When the magnetic ions are too far apart to overlap directly, then the exchange between the magnetic moments occur through an intermediary and therefore it is known as an indirect exchange. In the case of transition metal oxides, the p orbital of an oxygen atom bridges the neighboring d orbitals to establish a long-range magnetic order. In the case of magnetic materials containing rare-earth ion which contains $4f$ electrons and shielded by the $5s$ and $5p$ electrons also cannot make direct exchange interaction. In this case, the indirect exchange takes place by invoking the partially filled $5d$ states [39]. This process can be imagined as an electron from $4f$ orbital is excited to the partially filled $5d$ orbital, experiencing an exchange interaction with the electron located on a nearest neighbor $4f$ orbital and then returns to the initial state. Such an indirect exchange interaction generally gives rise to a ferromagnetic coupling of the magnetic moments.

In metals, the indirect exchange interaction is known as RKKY (Ruderman, Kittel, Kasuya and Yoshida) interaction or itinerant exchange, where the intermediary is the conduction electrons [40-42]. A localized magnetic moment spin-polarizes the conduction electrons and this polarization in turn couples to a neighboring localized magnetic moment a distance r away and the exchange interaction $J_{RKKY}(r)$ is given by, $J_{RKKY}(r) \propto \frac{\cos(2k_F r)}{r^3}$, where k_F is the Fermi wave vector. The interaction is long range and has an oscillatory dependence on the distance between the magnetic moments. Therefore, depending on the separation the coupling may be either ferromagnetic or antiferromagnetic. The coupling is oscillatory with wavelength π/k_F . In Figure 1.8, a schematic representation of metal-oxygen bonding has been depicted comparing between the direct and indirect or superexchange.

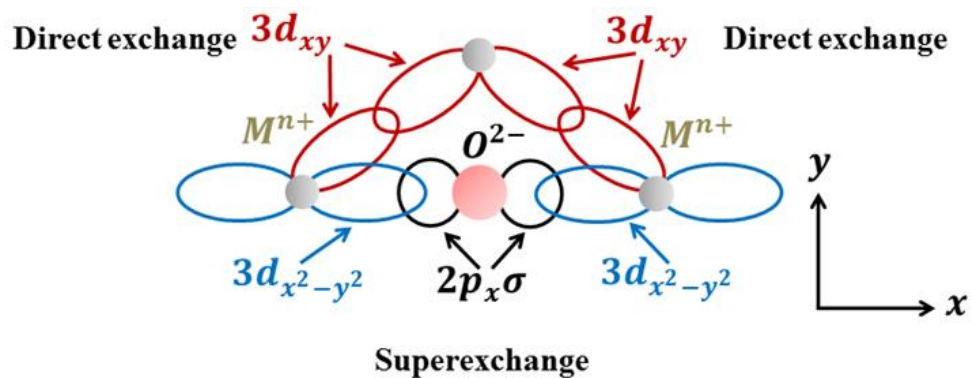


Figure 1.8: Comparison of direct exchange and superexchange in terms of orbital overlap

1.4.3 Superexchange:

Superexchange mechanism is also an indirect exchange interaction between non-neighboring magnetic ions mediated by a non-magnetic ion located between the magnetic ions [43,44]. Figure 1.9 illustrates the superexchange interaction between two Mn^{2+} ions via an intermediate O^{2-} ion in an antiferromagnetic insulator MnO .

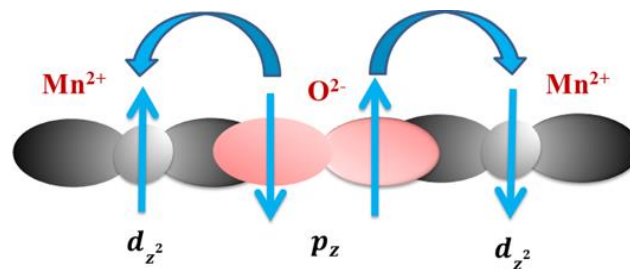


Figure 1.9: Superexchange in MnO

From this figure, it is viewed that O^{2-} transfers a $2p$ electron to the neighboring Mn^{2+} ion. The $3d$ electron spin on Mn^{2+} ion is aligned parallel to the $2p$ electron spin of O^{2-} due to the covalent mixing of the p and d wave functions. Since the direction of spins on O^{2-} is opposite to each other, therefore according to the Pauli exclusion principle, the $3d$ spins on the two Mn^{2+} ions must be antiparallel. This antiferromagnetic coupling between the Mn^{2+} ions results in delocalization of electrons over the whole structure thereby lowering the kinetic energy of the system. For this superexchange process $J \sim -t^2/U$, where t is the hopping integral which is proportional to the energy width of the conduction band and U is the Coulomb energy. The strength of antiferromagnetic coupling between the metal ions depends on the degree of overlap of orbitals and thus superexchange strongly depends on the M-O-M bond angle. Generally the exchange is maximum when this angle is 180° .

Besides the antiferromagnetic superexchange, it is possible to have a ferromagnetic superexchange interaction as observed in mixed valent transition metal oxides and this process is termed as a double exchange [45-47]. For example, in the compound $La_{1-x}Sr_xMnO_3$ ($0 \leq x \leq 1$), a fraction x of the Mn ions are Mn^{4+} and $1-x$ are Mn^{3+} . Now the singly occupied e_g orbital of Mn^{3+} is connected to the neighboring empty e_g orbital of Mn^{4+} via an O^{2-} ion. Therefore the e_g electron of Mn^{3+} ion can hop to the next unoccupied orbital of Mn^{4+} ion, if when it arrives its spin is aligned with the spin of the t_{2g} electrons due to Hund's rule. That means hopping is energetically favorable without spin-flip of the hopping electron as illustrated in Figure 1.10(a). On the other hand, this hopping process would be energetically unfavorable for an e_g electron to hop to a neighboring ion in which the t_{2g} spins are antiparallel to the incoming e_g electron as shown in Figure 1.10(b). Therefore, ferromagnetic alignment of both the donating and receiving ions are essential to maintaining the high-spin configuration of neighboring magnetic ions. The hopping process also saves the kinetic energy. As a result of this ferromagnetic spin arrangement the e_g electrons can hop through the crystal rendering the material to be metallic.

A similar double exchange process has been realized in magnetite (Fe_3O_4), where a double exchange mechanism aligns the Fe^{2+} and Fe^{3+} ions on the octahedral sites, while the Fe^{3+} ions on the tetrahedral sites do not take part in this process but remains

antiferromagnetically coupled with the Fe^{3+} ions on the octahedral sites via superexchange interaction. As a result, the net magnetic moments ($4 \mu_B$) arise due to only Fe^{2+} ions alone.

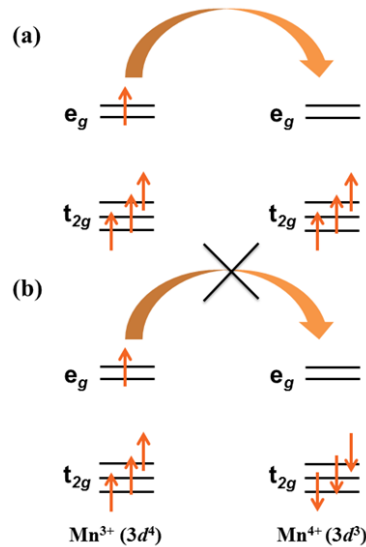


Figure 1.10: Schematic representation of double exchange mechanism giving rise to a ferromagnetic coupling between Mn^{3+} and Mn^{4+} ions. Exchange interaction favors hopping if (a) neighboring ions are aligned ferromagnetically and not if (b) neighboring ions are antiferromagnetically aligned.

Although both superexchange and double exchange process are an indirect exchange interaction, there is a difference in terms of spin-transfer other than the nature of magnetic coupling arises as a result of exchange interaction. In the case of superexchange, the electron transfer process is actually virtual i.e. electrons do not actually move between the two neighboring magnetic ions, the occupancy of the d orbital is always same or differs by two. However, in double exchange, the itinerant d electrons move from one metal site to the next site through intermediate non-magnetic ligand. The difference between the two processes is illustrated in Figure 1.11.

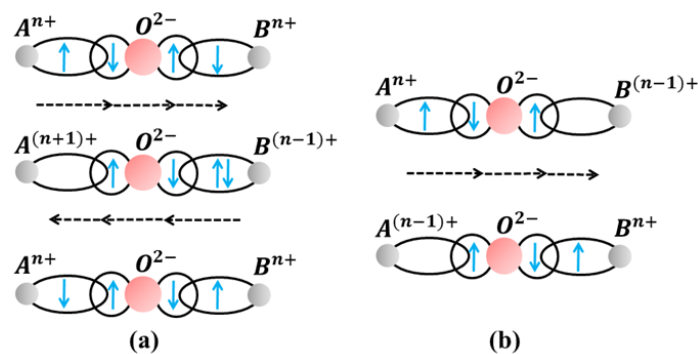


Figure 1.11: Schematic illustration of (a) virtual spin transfer in the superexchange process giving rise to antiferromagnetism and (b) real spin transfer in the double exchange interaction resulting in ferromagnetism. A and B are the metal ions, the dotted arrow indicates the direction of electron transfer.

Now we briefly summarize the Goodenough-Kanamori rules which qualitatively rationalize the magnetic properties of various magnetic insulators, where magnetic ions interact through superexchange interaction and M-O-M bond angle is 180° .

- The superexchange interactions will be antiferromagnetic when the virtual electron transfer occurs between overlapping orbitals where each of them is half-filled.
- The superexchange interactions will be ferromagnetic when the virtual electron transfer takes place from a half-filled to an empty orbital or from a filled to a half-filled orbital.

In this context, it is important to mention that if the orbitals are orthogonal then there would be no overlap and hence no electron transfer. As a result, exchange interaction between spins in orthogonal orbitals is a ferromagnetic potential exchange which represents the electron repulsion (provided the magnetic ions are not far apart).

1.4.4 Anisotropic exchange interaction:

So far we have discussed the isotropic exchange interaction. In the presence of spin-orbit coupling, there is an exchange interaction between the excited state of one magnetic ion (it has a similar role to that of oxygen atom in superexchange) and the ground state of the other magnetic ion resulting in anisotropic exchange interaction or Dzyaloshinsky-Moriya (DM) interaction [48,49]. The Hamiltonian for the DM interaction can be expressed as, $\hat{H} = \vec{D} \cdot \vec{S}_1 \times \vec{S}_2$, where \vec{S}_1 and \vec{S}_2 are the two neighboring spins and \vec{D} is the constant. The effect of DM interaction is to cant the spins leading to the generation of weak ferromagnetism in an antiferromagnetic material (e.g. $\alpha\text{-Fe}_2\text{O}_3$).

1.5 Magnetic anisotropy

The term magnetic anisotropy suggests that the magnetic properties depend on the crystallographic direction in which they are measured. Therefore it can also be termed as magnetocrystalline anisotropy which is an intrinsic property of any magnetic material. However, anisotropy can also originate from the shape and size of the sample and stresses. In the case of multilayer thin films, the existence of interface or exchange anisotropy has also been realized. The later examples are of extrinsic or induced

anisotropy because those are not associated with the crystallographic symmetry but can be tuned or modified externally. Here we will discuss only the magnetocrystalline and exchange anisotropy. In addition, we shall briefly discuss the effect of external magnetic field in controlling the anisotropy in the antiferromagnetic material.

1.5.1 Magnetocrystalline anisotropy:

Magnetocrystalline anisotropy can be defined as a force which binds the magnetization in certain equivalent crystallographic axes in a crystal. The preferential or energetically favorable direction for the alignment of the magnetization of a magnetic material is known as the easy axis. On the other hand, the energetically unfavorable direction is called as hard axis. In Figure 1.12 $M(H)$ curves for single crystals of cubic iron (BCC) and nickel (FCC) are shown measured in different crystallographic directions [50]. From this figure it is observed that magnetic saturation can be achieved with a low magnetic field along [100] and [111] direction in the case of iron and nickel respectively, indicating that those directions are the easy direction of magnetization for those elements.

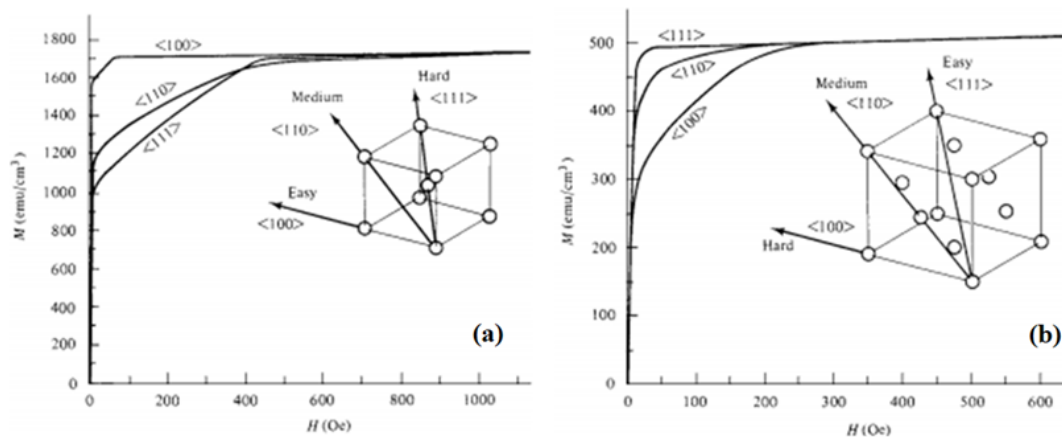


Figure 1.12: Magnetic field dependent isothermal magnetization data, $M(H)$ for (a) iron and (b) nickel [adapted with permission from ref. 50, © (2008) by John Wiley and Sons].

In the presence of fairly high magnetic fields along the hard axis (as shown in the above figure), domain rotation occurs by overcoming the crystal anisotropy resulting in the saturation of magnetization along the direction of magnetic field. Therefore, stronger the magnetic anisotropy of a particular magnetic material, higher the magnitude of the magnetic field required to rotate the magnetization direction away from its easy axis. The amount of energy stored in a cubic crystal to shift the direction of saturation magnetization vector (M_s) from an easy to a hard axis can be expressed in

terms of a series expansion of the direction cosines of M_s with respect to the crystal axes. In a cubic crystal, if M_s makes angles a, b, c with the crystal axes and $\alpha_1, \alpha_2, \alpha_3$ are the cosines of these angles then [50],

$$E = K_0 + K_1(\alpha_1^2\alpha_2^2 + \alpha_2^2\alpha_3^2 + \alpha_3^2\alpha_1^2) + K_2(\alpha_1^2\alpha_2^2\alpha_3^2) + \dots \quad (1.2)$$

where K_0, K_1, K_2, \dots are the anisotropy constants for a particular material at a fixed temperature and therefore temperature dependent. With increasing temperature the anisotropy decreases and hence the coercive field. From the above expression, it is clear that anisotropy energy is strongly dependent on the direction cosines. The strength of anisotropy is determined by the magnitude of the anisotropy constants.

Also one can have a uniaxial anisotropy i.e. the crystal (e.g. elemental cobalt, barium ferrite) contains single easy axis along which the magnetization can point either up or down. In this case, the anisotropy energy depends on a single angle, θ , between the M_s vector and a single axis (in the case of cobalt this axis is the stacking direction of hexagonally close-packed planes, c direction). The anisotropy energy of hexagonal cobalt takes the form [50],

$$E = K_0 + K_1\text{Sin}^2\theta + K_2\text{Sin}^4\theta + \dots \quad (1.3)$$

The magnetocrystalline anisotropy mainly arises due to spin-orbit coupling. In the presence of an external magnetic field, when it tries to reorient the spin direction of an electron, the orbit of that electron also tends to be reoriented due to a coupling between the spin and orbital motion of electrons. Now the strong coupling between orbit and lattice inhibits the rotation of the spin axis. Therefore, the amount of energy required to rotate the spin axis is equivalent to the amount of energy needed to overcome the spin-orbit coupling. The magnetocrystalline anisotropy remains unaffected by the nearest neighbor spin-spin coupling because the associated isotropic exchange energy depends only on the angle between adjacent spins and does not depend on the direction of spin axis relative to the crystal lattice.

1.5.1.1 Anisotropy in antiferromagnet

Now we discuss a few interesting aspects of magnetocrystalline anisotropy in an antiferromagnetic material in the presence of an external magnetic field. Depending on

the direction of applied magnetic field with respect to the initial direction of sublattice magnetization two transitions are realized in antiferromagnetic material such as, (1) spin-flop transition and (2) spin-flip (metamagnetic) transition, which will be discussed with the help of schematics as shown in Figure 1.13.

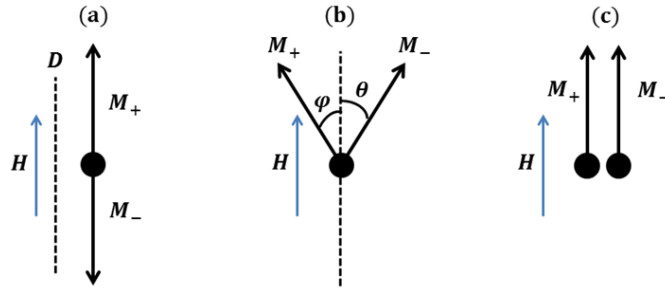


Figure 1.13: Schematics of spin-flop and spin-flip transitions.

Let us first look at the antiferromagnetic state (a) where the spins of two sublattices are parallel in zero or small applied magnetic field along the crystallographic axis (D). Now with increasing the strength of magnetic field along D -axis, there is a possibility of the spin directions to rotate into the configuration (b), while the magnetocrystalline anisotropy will try to keep the spin in the original direction. However, at a critical magnetic field when the strength of magnetic field overcomes the crystal anisotropy, the spins suddenly snaps into a configuration (b) causing a sudden increase in magnetization. This process is known as spin-flop transition. Further increase of magnetic field rotates the moments until saturation is achieved in a similar way when a magnetic field is applied perpendicular to the magnetization direction of the sublattice. In Figure 1.14(a) such spin-flop transition observed in MnF_2 is shown [50,51].

Now another situation occurs when the crystal anisotropy is very strong and the magnetic field is applied parallel to the crystallographic axis (D). In this case, magnetization will first increase due to increase in the magnitude of one sublattice magnetization along the field direction at the expense of other sublattice magnetization oriented opposite to the field direction. At a high critical value of magnetic field, the spin configurations will transform from the antiparallel spin state (a) to parallel spin state (c) in a single step without going through the spin-flop transition. This phenomenon is known as a spin-flip transition or metamagnetic transition. This particular behavior shows a magnetic-field-induced phase transition from an

antiferromagnetic to a ferromagnetic state at a constant temperature. The term ‘meta’ is used to contract the temperature induced antiferromagnetic to a ferromagnetic phase transition. In Figure 1.14(b) such spin-flip or metamagnetic transition observed in FeCl_2 is shown [50,52]. From Figure 1.14 it is clear that in the case of spin-flop transition the saturation magnetization is reached in two steps, while for the spin-flip transition saturation is reached in a single step.

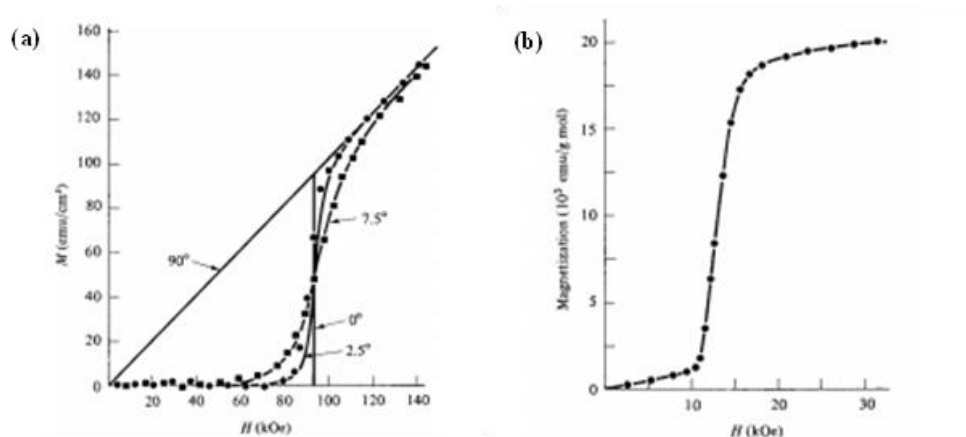


Figure 1.14: Isothermal magnetization data as a function of magnetic field, $M(H)$ showing (a) two steps spin-flop transition in a single crystal of MnF_2 and (b) single step spin-flip transition in powdered FeCl_2 which has a very high degree of preferred orientation. Therefore the field direction was almost parallel to the crystallographic axis [adapted with permission from ref. 50, © (2008) by John Wiley and Sons].

1.5.2 Exchange anisotropy:

Exchange anisotropy is the interfacial anisotropy which was first observed at the interface between a ferromagnet (FM) and an antiferromagnet (AFM), e.g. at the interface between single domain particles of ferromagnetic cobalt surrounded by antiferromagnetic cobalt oxide [53,54]. If the combined magnetic system is cooled through the Néel temperature (T_N) of the AFM in the presence of an external magnetic field, the anisotropy developed at the interface below T_N will be manifested by an asymmetric shift of the magnetization hysteresis loop of the ferromagnet towards the field axis as well as increase in coercivity and wide hysteresis loop. The Curie temperature, T_C , of FM should be higher than the Néel temperature, T_N , of AFM to ensure that the moments of the ferromagnetic layer are already aligned along the direction of the cooling field. The role of the cooling magnetic field is to provide the combined system as a whole a single easy direction. In the absence of the magnetic-field-cooling-process, exchange interactions occur at all interfaces, resulting in a random distribution of easy axis. It is easier to magnetize the ferromagnetic layer along

the direction of cooling magnetic field than the antiferromagnetic layer due to the weaker anisotropy of the former. Therefore it can be viewed as if the ferromagnetic layer is exchange biased by a unidirectional exchange field, H_{ex} , of the antiferromagnetic layer. From the shift of hysteresis loop, it also appears that there exists an additional biasing magnetic field resulting in unidirectional exchange anisotropy. When H and H_{ex} are in the same direction, there will be a shift of the hysteresis loop. When both fields are acting at a right angle then a hard axis response will be realized. The total energy of the combined system can be expressed as [55],

$$E = -HMt_{FM}\cos(\theta - \beta) + Kt_{AFM}\sin^2\alpha - J_{int}\cos(\beta - \alpha) \quad (1.4)$$

where M is the magnetization of the ferromagnet, K is the anisotropy constant of the antiferromagnet, t_{FM} and t_{AFM} are the thickness of the ferromagnet and antiferromagnet. The angle θ describes the angle between the applied field and the FM anisotropy axis, β describes the angle between the magnetization and the FM anisotropy axis and α is the angle between AFM sublattice magnetization and AFM anisotropy axis. In the above expression, the first term arises due to the interaction of the ferromagnet with the applied field, H , the second term is associated with the anisotropy energy in the antiferromagnet and the third term takes care of interfacial exchange interaction between the ferromagnet and antiferromagnet.

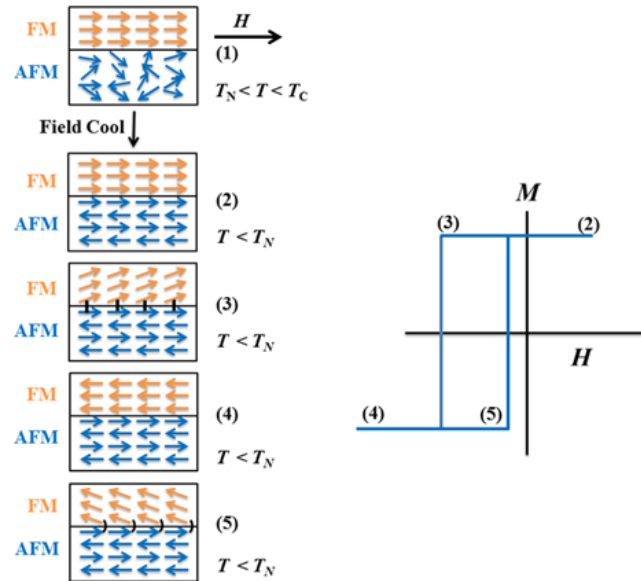


Figure 1.15: Schematic representation of spin configurations of exchange-biased FM-AFM bilayer at different stages of the shifted hysteresis loop. In the cartoon model, compensated antiferromagnetic layer which contains an equal number of oppositely oriented spins has been considered. The antiferromagnetic layer can also be uncompensated with an unequal number of opposite spins.

Now we discuss the mechanism of hysteresis loop shift in a bilayer of FM-AFM through an intuitive sketch as shown in Figure 1.15 [56]. On application of a magnetic field in the range $T_N < T < T_C$, the spins in the ferromagnetic layer align along the direction of the cooling magnetic field while the spins in the antiferromagnetic layer remain random as shown in state (1) of Figure 1.15. Upon cooling the bilayer below the Néel temperature ($T < T_N$) in the presence of a magnetic field the spins of the first layer of AFM are forced to align parallel to the adjoining spins in the FM due to the positive exchange interaction and the other interior spins in the AFM are arranged antiparallel fashion to produce net-zero magnetization as depicted in state (2) of Figure 1.15. This spin arrangement below T_N will be retained even after removal of the magnetic field. If now the magnetic field direction is reversed the ferromagnetic spins start to rotate, and at the same time exchange force at the interface will try to reverse the direction of spins in AFM. However, strong crystal anisotropy of the AFM will resist the rotation of spins in the AFM layer as shown in state (3) of Figure 1.15 and it appears that the AFM spins at the interface exert a microscopic torque on the FM spins to keep them aligned parallel. Therefore, an extra field is required to overcome the microscopic torque for a complete reversal of ferromagnetic spins when it is in contact with the antiferromagnetic layer thereby increasing the coercive field (state 4). Since the AFM layer binds the direction of FM spins in one preferred orientation or easy direction of magnetization, it is called as unidirectional anisotropy and it has to be contrasted with respect to uniaxial anisotropy where two equivalent easy axes in opposite directions are possible. After that when the magnetic field is restored to the original direction, the FM layer will rotate at a smaller field due to the favorable parallel interaction with the AFM spins which exert a torque in the same direction. This reduces the coercive field for restoring the initial configuration (state 5). During the whole process, it appears that the exchange interaction at the interface is being effected by an internal biasing field (in addition to the external field) which shifts the hysteresis loop (right panel of Figure 1.15) thereby giving rise to exchange bias phenomenon. Although this simple model qualitatively explains the behavior of exchange bias but it is unable to explain the phenomena quantitatively. To understand this interfacial phenomenon properly the roles of several other parameters e.g. interface impurity, disorder, roughness, interfacial spin configuration or orientation of magnetic domains needs to be understood.

Exchange-bias finds tremendous application in spin-valves which is a giant magnetoresistive sensor. It consists of two FM layers separated by a non-magnetic (NM) spacer and one of the FM layers is in contact with AFM layer which pins the magnetization of that FM along a particular direction thereby setting a reference magnetization [Figure 1.16]. Now the spins of the second FM layer can be aligned with an applied magnetic field with respect to the reference FM layer. The angle between the magnetic moments in the two ferromagnetic layers controls the resistance of the device. Therefore depending on the relative orientation of spins with applied magnetic field changes the resistance which is used for sensing or storage applications. The thickness of the non-magnetic spacer layer controls the relative orientation of spins in the absence of an external magnetic field.

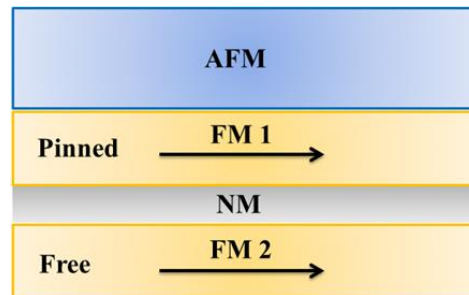


Figure 1.16: Schematic of a spin valve

1.6 Magnetoelectric effect

Transition metal oxides exhibit an interesting coupling between magnetization and electric polarization which is known as magnetoelectric coupling. In other words, it can be defined as the induced magnetization in the presence of an electric field or induced electric polarization in the presence of magnetic field. The magnetoelectric effect (ME) was first predicted by Curie in 1894 on the basis of symmetry considerations [57]. Later, based on the theoretical prediction of Dzyaloshinskii in 1960 [5], Astrov experimentally demonstrated the occurrence of linear magnetoelectric effect in the antiferromagnetically ordered state of Cr_2O_3 [6,7]. Although the coupling between the order parameters was small in terms of practical application, since then there has been a continuous effort to improve the coupling between the magnetization and electric polarization. Besides this, there have been parallel attempts to study new microscopic mechanisms which can lead to the discovery of materials with better functionality. The interest in studying the magnetoelectric effect received renewed attention after the

discovery of multiferroics where both ferromagnetism and ferroelectricity coexists. Magnetolectric multiferroics are the promising materials for application in devices for ME data storage and switching, spin-wave generation, modulation of amplitudes, polarizations and phases of optical waves etc.

The magnetolectric effect is described in Landau theory by writing the free energy F under the Einstein summation convention in S.I. units as [11],

$$\begin{aligned}
 -F(E, H) = & -F_0 + \frac{1}{2}\epsilon_0\epsilon_{ij}E_iE_j + \frac{1}{2}\mu_0\mu_{ij}H_iH_j + \alpha_{ij}E_iH_j + \frac{\beta_{ijk}}{2}E_iH_jH_k \\
 & + \frac{\gamma_{ijk}}{2}H_iE_jE_k + \frac{\delta_{ijkl}}{2}E_iE_jH_kH_l + \dots
 \end{aligned} \tag{1.5}$$

The first term is the free energy in the absence of magnetic and electric fields. The second and third term results from the electrical and magnetic response to an electric and magnetic fields respectively. Here, ϵ_0 is the permittivity of free space and ϵ_{ij} (second-rank tensor) is the relative permittivity which is temperature dependent but independent of E_i in non-ferroic material; μ_0 is the permeability of free space and μ_{ij} (second-rank tensor) is the relative permeability which is also temperature dependent. In the above expression the fourth term describes the first-order bilinear, EH , magnetolectric coupling with coefficient α_{ij} (second-rank tensor) which is temperature dependent. The fifth and sixth terms represent second order electrobimagnetic EH^2 and magnetobielectric HE^2 coupling with coefficients β_{ijk} and γ_{ijk} (third-rank tensor), respectively, which also depend on temperature. The last term is associated with third order bielectrobimagnetic E^2H^2 effect with coefficient δ_{ijkl} which is a fourth-rank tensor.

We obtain the linear magnetolectric coefficient (α_{ij}) by differentiating F with respect to E_i and then putting $E_i = 0$ or differentiating F with respect to H_j and then putting $H_j = 0$ (ignoring the higher order terms). This establishes the linear relationship between electric polarization and magnetic field or magnetization and electric field.

$$P_i = \frac{\partial F}{\partial E_i} = \alpha_{ij}H_j; \quad M_j = \frac{\partial F}{\partial H_j} = \alpha_{ij}E_i \tag{1.6}$$

To observe the linear magnetoelectric effect in any insulating magnetic materials there are two essential constraints, (1) symmetry and (a) magnitude restrictions.

1.6.1 Symmetry constraints

We have seen that the thermodynamic potential associated with linear magnetoelectric effect is linear in both E_i and H_j . Since E_i is a polar vector and H_j is an axial vector, α_{ij} must be odd under both space inversion and time reversal, and also symmetric under the product of two operations to keep the free energy invariant. In a magnetic material, time-reversal symmetry adds 90 magnetic point groups [58] in addition to the already existing 32 crystallographic point groups. The magnetoelectric effect is allowed only in 58 of the 90 magnetic point groups and among them there are only 11 possible forms for the second-rank tensor α_{ij} . The different forms of the tensor α_{ij} associated with allowed magnetoelectric effect are shown in Table 1.1 [59].

Table 1.1: Magnetoelectric point groups and non-zero components of linear magnetoelectric tensor, α_{ij}

Magnetic point group	Symmetry allowed linear coefficient (α_{ij})
1, $\bar{1}$ '	α_{ij} , where $ij = 1, 2, 3$
2, m' , $2/m'$	$\alpha_{11}, \alpha_{13}, \alpha_{22}, \alpha_{31}, \alpha_{33}$
2', m , $2'/m$	$\alpha_{12}, \alpha_{21}, \alpha_{23}, \alpha_{32}$
222, $m'm'2$, $m'm'm'$	$\alpha_{11}, \alpha_{22}, \alpha_{33}$
22'2', $2mm$, $m'm2'$, $m'mm$	α_{23}, α_{32}
3, $\bar{3}$ ', 4, $\bar{4}$ ', $4/m'$, 6, $\bar{6}$ ', $6/m'$, ∞ , $\infty m'$	$\alpha_{11} = \alpha_{22}, \alpha_{12} = -\alpha_{21}, \alpha_{33}$
4', $\bar{4}$ ', $4'/m'$	$\alpha_{11} = -\alpha_{22}, \alpha_{12} = \alpha_{21}$
32, $3m'$, $\bar{3}'m'$, 422, $4m'm'$, $\bar{4}'2m'$, 4/ $m'm'm'$, 622, $6m'm'$, $\bar{6}'m'2$, 6/ $m'm'm'$, $\infty 2$, $\infty/m'm'$, ∞/m'	$\alpha_{11} = \alpha_{22}, \alpha_{33}$
4'22, 4' mm' , $\bar{4}2m$, $\bar{4}2'm'$, 4'/ $m'mm'$	$\alpha_{11} = -\alpha_{22}$
32', $3m$, $\bar{3}'m$, 42'2', 4 mm , $\bar{4}'2'm$, 4/ $m'mm$, 62'2', 6 mm , $\bar{6}'m2'$, 6/ $m'mm$, $\infty 2'$, $\infty/m'm$	$\alpha_{12} = -\alpha_{21}$
23, $m'3$, 432, $\bar{4}'3m'$, $m'3m'$, $\infty\infty$, $\infty\infty m'$	$\alpha_{11} = \alpha_{22} = \alpha_{33}$

The general form of the second-rank magnetoelectric tensor, α_{ij} , mentioned in the above table is,

$$\begin{bmatrix} \alpha_{11} & \alpha_{12} & \alpha_{13} \\ \alpha_{21} & \alpha_{22} & \alpha_{23} \\ \alpha_{31} & \alpha_{32} & \alpha_{33} \end{bmatrix}$$

To have knowledge on the time reversal symmetry we need to know the magnetic symmetry associated with the periodic arrangement of magnetic dipoles in the magnetically ordered state of a material. Time-reversal symmetry causes the reversal of the direction of magnetic moments (up spin becomes down or vice-versa). Though we depict the atomic magnetic moment with an arrow but it is somewhat confusing. Classically, magnetization arises from moving electric charge tracing a current loop. Therefore, reversing time actually reverses the direction of current flow and hence the direction of magnetization.

Magnetic symmetry guides the magnetoelectric behavior of a material because the magnetoelectric coefficients contain the symmetry of the material. Interestingly, the symmetry of the crystal structure is modified depending on the arrangement of magnetic dipoles in the magnetically ordered state. Let us take the example of Fe_2O_3 and Cr_2O_3 , both of them crystallize in the corundum structure (α - Al_2O_3 , $R\bar{3}c$) which belongs to the point group $\bar{3}m1'$. In the antiferromagnetically ordered state, the arrangement of atomic magnetic moments along the $[001]$ direction of the rhombohedral unit cell is different for Fe_2O_3 and Cr_2O_3 as shown in Figure 1.17 [60].

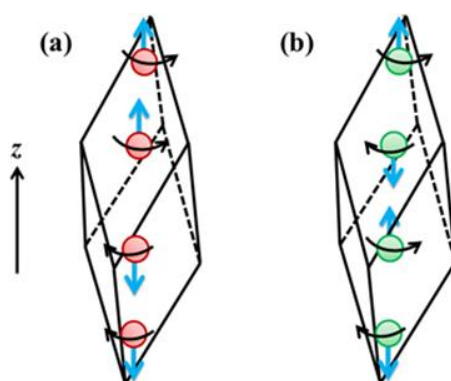


Figure 1.17: Spin configurations of antiferromagnetic (a) Fe_2O_3 and (b) Cr_2O_3 . The arrows denote the atomic magnetic moment of respective metal ions generated from the moving electric charge in a loop shown as a curved arrow.

Depending on the direction of magnetic moments, the magnetic point groups for Fe_2O_3 and Cr_2O_3 are $\bar{3}m$ and $\bar{3}'m'$, where the former magnetic point group is centrosymmetric

and the later is non-centrosymmetric possessing the element $\bar{1}'$. Therefore the linear magnetoelectric effect is symmetry forbidden in Fe_2O_3 and it is symmetry allowed in Cr_2O_3 .

Although the magnetic symmetry broadly indicates the possibility of a linear magnetoelectric effect but the strength of coupling (in terms of magnitude) depends on a specific microscopic mechanism which is highly material-dependent. The microscopic origin of electrically induced magnetoelectric effect in the antiferromagnetic state is understood based on the cationic displacements with respect to the anions thereby modifying the electronic wave functions and changing the magnetic interactions through spin-orbit coupling [60]. From the schematics, as shown in Figure 1.18, it is evident that in the presence of an applied electric field, the positive ions move in the applied field direction and negative ions in the opposite direction, generating electric polarization. In the presence of an electric field, the cation and anion comes closer in one pair and goes further in another pair resulting in increase or decrease in electron overlap which will affect the electron orbital motion of cation. Therefore up spins are differently affected than the down spins giving rise to a net magnetization. Hence the material becomes magnetoelectric. It is important to mention that in the absence of an electric field both the net magnetization and the electric polarization is zero.

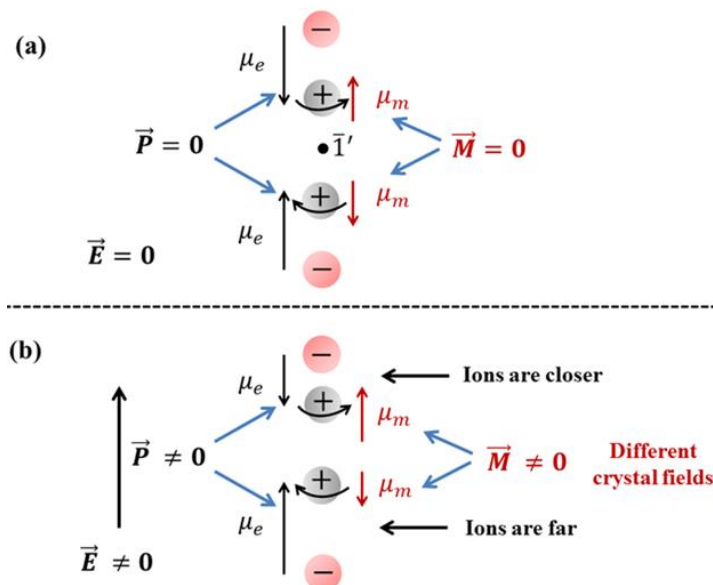


Figure 1.18: Microscopic origin of magnetoelectric effect in an antiferromagnet, where μ_e and μ_m correspond to the electric and magnetic dipoles, respectively. The gray and red circle represents the magnetic cation and non-magnetic anion respectively.

1.6.2 Magnitude constraints

The upper limit of linear magnetoelectric coefficient, α_{ij} is restricted by the geometric mean of the diagonalized tensors ϵ_{ii} and μ_{jj} such that, $\alpha_{ij}^2 \leq \epsilon_0 \mu_0 \epsilon_{ii} \mu_{jj}$ [61]. Therefore, to achieve larger magnetoelectric coupling the material should be simultaneously ferromagnetic and ferroelectric due to the fact that the magnetic and electric susceptibility would be high in those material. Although it is not always true that a ferroelectric or ferromagnetic material would have a higher value of electric or magnetic susceptibility, but in multiferroic materials improved magnetoelectric susceptibility can be achieved. Such magnitude restriction does not apply to the higher-order coefficients. For example, in the piezoelectric paramagnet, $\text{NiSO}_4 \cdot 6\text{H}_2\text{O}$, the second-order term, $\beta_{ijk}H_jH_k$ dominates over the first-order term $\alpha_{ij}H_j$. To improve the magnetoelectric coupling significantly, strain also plays an important role as demonstrated in the composite material, e.g. $\text{BaTiO}_3\text{-CoFe}_2\text{O}_4$. In this biphasic material, poled BaTiO_3 (ferroelectric) in the presence of an electric field changes shape (through piezoelectric effect) which distorts the magnetic domains of ferrimagnetic CoFe_2O_4 via electrostriction effect. In the presence of a magnetic field the magnetoelectric effect occurs via piezomagnetism and magnetostriction.

1.7 X-ray and neutron diffraction

In this thesis, both x-ray and neutron diffraction techniques which are complementary for the determination of different information of structure and symmetry have been used [62-64]. In addition to the nuclear information, from the analysis of neutron diffraction data both the direction and magnitude of the magnetic moment and hence magnetic symmetry was determined. This is due to the fact that neutron has a magnetic moment ($-1.91 \mu_N$) which can interact with the scattering atom having a net magnetic moment. In contrast, x-rays being an electromagnetic radiation are diffracted by the electrons of atom only and hence insensitive to magnetic ordering. Both x-ray and neutron diffraction obey the Bragg law which states that constructive interference would occur if the path difference between the x-rays or neutron beams scattered from parallel planes is an integer number of the wavelength of radiation. If the planes of atoms which are separated by a distance d make an angle θ with the incident beam as shown in the Figure 1.19, then the path difference would be $2d\sin\theta$. Therefore, for

constructive interference, the equation known as Bragg's Law must be satisfied, $n\lambda = 2d\sin\theta$, where n is an integer called the order of reflection.

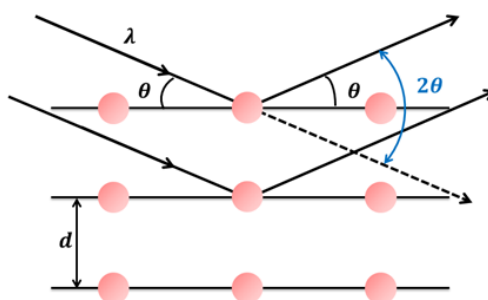


Figure 1.19: Bragg diffraction geometry.

In Table 1.2, a brief comparison regarding the strength and weakness of both x-ray and neutron diffraction methods are described.

Table 1.2: Comparison between x-ray and neutron diffraction.

X-ray diffraction	Neutron diffraction
scattered by the electrons of an atom	being uncharged, scattered only by the nucleus (in the case of magnetic material additional scattering occurs from the magnetic moments of an atom)
scattering intensity is proportional to atomic number (Z)	neutron scattering length does not vary linearly with Z
atomic scattering factor decreases with scattering angle	atomic scattering factor is independent of scattering angle atomic coordinates, and thermal parameters are obtained with high accuracy for the high-angular-resolution data
cannot probe the light elements such as oxygen	precise determination of light elements is possible in the presence of heavy atoms
does not give information of magnetic moments	direction and magnitude of magnetic moment can be determined
absorption problem is severe especially for the heavier atoms	absorption coefficients are roughly four orders of magnitude lower than the corresponding x-ray absorption coefficients
a small amount of sample is sufficient to collect a diffraction pattern	requires a larger amount of sample because neutron sources are much weaker than x-ray, hence powder average structural information would be better

1.7.1 X-ray diffraction

X-rays used for the diffraction experiment are most commonly generated by two methods, the x-ray tube method, and synchrotron x-ray. The x-ray tube method is used to produce x-ray in the laboratory x-ray diffractometer. In this method, the filament is heated to produce electrons which are then accelerated in a vacuum by a high electric field of ~ 40 kV and then allowed to collide with the metal target, Cu (in many cases Mo is also used as a metal target) thereby producing both bremsstrahlung and x-rays. The generated x-rays have wavelengths $K\alpha_1$ (1.5406 Å), $K\alpha_2$ (1.5444 Å), $K\beta_{1,3}$ (1.3922 Å) and $K\beta_3$ (1.3926 Å) [65]. Cu- $K\beta$ radiation is filtered out by using a Ni filter, but it is difficult to remove Cu- $K\alpha_2$. Therefore the conventional laboratory x-ray diffractometer contains $K\alpha_1$ and $K\alpha_2$ which produce relatively broad diffraction peaks with asymmetric peak shapes rendering the profile analysis complicated. Furthermore, laboratory x-ray filtering process leads to reduction in intensity. In addition it is difficult to distinguish peak splitting when peaks appear closely in the diffraction pattern in the case of compound with small lattice parameter difference. All these limitations could be overcome by using high-angular resolution monochromatic synchrotron x-ray radiation with a tuneable wavelength. Therefore, a particular wavelength can be used based on the requirement of experiment and intensity of radiation is also significantly higher than laboratory x-ray. Moreover, with synchrotron radiation, improved signal-to-noise discrimination could be achieved.

1.7.2 Neutron diffraction

For the present thesis constant-wavelength (CW) and time-of-flight (TOF) neutron diffraction data were collected by using neutrons generated at reactors and spallation sources, respectively. In the case of nuclear research reactor based source, neutrons are generated from the fission of heavy nucleus, ^{235}U . For spallation source, a heavy metal target is bombarded with high energy protons generated by a particle accelerator. As a result of this collision high energy is imparted to the target thereby generating spallation neutrons. The spallation neutrons occur in pulses because the protons are produced in bursts by particle accelerators. In both the process, since the produced neutrons have very high energy, so they are passed through a moderator, heavy water, to reduce their energy before using for the diffraction experiment.

In the case of the constant-wavelength experiment, usually, Debye-Scherrer diffractometer geometry is used. During the diffraction experiment, usually an array of detectors is allowed to move about the cylindrical sample. The neutron wavelength is chosen by an appropriate monochromator. In contrast, in the case of TOF neutron diffraction experiment, the detectors are located at fixed scattering angles and diffraction pattern is recorded as a function of time delay from the start of a neutron burst at the source. The repetition frequency of the source together with neutron flight path will set the range of neutron wavelengths arriving at the diffractometer, which in turn dictates the range of d spacing accessible by a particular detector. The detectors are fixed because different neutron wavelengths would be diffracted by the different atomic planes with different d -spacing.

1.8 Rietveld refinement

Rietveld refinement is the most useful method for the analysis of x-ray and neutron powder diffraction data to determine the crystal and magnetic structure [66,67]. It is the least squares fitting procedure that minimizes the difference between the observed and calculated diffraction profiles. The form of function that is minimized is expressed by the equation:

$$y_{ic} = y_{ib} + \sum_p \sum_{k=k_1^p}^{k_2^p} G_{ik}^p I_k \quad (1.7)$$

where y_{ic} is the calculated intensity at point i in the diffraction pattern, y_{ib} is the background intensity, G_{ik} is a normalized peak profile function and I_k is the intensity of the k^{th} Bragg reflection, $k_1 \dots k_2$ are the reflections contributing intensity to point i . The superscript p corresponds to the possible phase present in the sample. The intensity (I_k), of the k^{th} Bragg reflection is expressed as:

$$I_k = SM_K L_K |F_K|^2 P_K A_K E_K \quad (1.8)$$

where S is the scale factor such that $y(calc) = S \times y(obs)$, M_K is the multiplicity, L_K is the Lorentz-Polarization factor. F_K is the structure factor which is expressed as,

$F_K = \sum_{j=1}^n f_j \exp[2\pi i (hx_j + ky_j + lz_j)]$, where h, k, l are miller indices; x_j, y_j, z_j are the atomic coordinates of atom j ; f_j is the atomic scattering factor of atom j , which is defined as $f = f_0 \exp \left[\frac{-B \sin^2 \theta}{\lambda^2} \right]$. In this expression, B is the Debye-Waller temperature factor ($B = 8\pi^2 U^2$), which is proportional to the mean squared displacements (U^2) of scattering matter. In the expression of intensity, I_k , the term P_K corresponds to the effects of preferred orientation, the factor A_K is the absorption correction, and E_K is the extinction correction factor which is usually dominating in single crystal.

The least-squares parameters involved in the refinement can be divided into two categories such as instrumental parameters and structural parameters. The instrumental parameters include the zero offset, the background parameters, the peak shape parameters, absorption correction and asymmetry correction. The crystallographic parameter includes a scale factor, lattice parameters of the unit cell, the atomic coordinates and thermal parameters of each atom forming the asymmetric unit. Now we discuss the refinement of above-mentioned parameters using a whole pattern or Rietveld method to analyze the structural information from the powder diffraction data.

1.8.1 Peak-profile function:

For x-ray and constant-wavelength neutron data, the peak profile is described by pseudo-Voigt (pV) approximation of the Voigt function. The pseudo-Voigt function is a linear combination of Lorentzian (L) and Gaussian components (G) as expressed by the equation [68],

$$pV = \eta L + (1 - \eta)G \quad (1.9)$$

where η is the pseudo-Voigt mixing parameter. The angular (2θ) dependence of the full width at half maximum (FWHM) of Gaussian and Lorentzian component of the peak shape is modelled with the following equation [69]:

$$(\text{FWHM})_G^2 = U \tan^2 \theta + V \tan \theta + W \quad (1.10)$$

$$(\text{FWHM})_L = X \tan \theta + Y / \cos \theta \quad (1.11)$$

where U, V and W are the Gaussian FWHM parameters, and X, Y are the Lorentzian FWHM parameters. In addition to the instrumental broadening effects, these parameters reveal important information about the microstructure with respect to the size and strain effects [70,71]. In the case of high-resolution synchrotron x-ray diffraction pattern, asymmetric peak broadening (Lorentzian) at low angles is prominent due to the extremely narrow peak widths. In this case X, Y can be refined accurately but U, V and W needs to be fixed at the instrumental values. The θ dependence of aforementioned FWHM functions of peak shape cannot be used to model the hkl -dependent anisotropic peak broadening [72]. In contrast to x-ray data, in the case of CW neutron data peak shapes are more Gaussian due to dominating instrument contribution and hence U, V and W can be determined accurately. On the other hand, for TOF neutron data, complex peak-shape functions (Von Dreele), which depend on a number of instrument-dependent coefficients, are used to perform Rietveld refinement due to the fact that neutron-pulse nature gives rise to additional and asymmetric peak broadening effect.

1.8.2 Profile fitting:

Before performing the refinements of structural parameters we need to subtract the background (the background was estimated by linear interpolation between selected points between peaks and then subtracted) and then refine the profile parameters e.g. 2θ correction, unit-cell parameters, variation of FWHM and peak asymmetry with scattering angle (2θ). Another important condition is that, the peak positions of the observed and calculated peaks must match fairly well, otherwise refinement will not work. For that reason 2θ correction and unit-cell parameters needs to be refined first and then rest of the profile parameters. In this structure-free approach (Le Bail refinement) intensities of the reflections are simply adjusted to fit the observed intensities, to extract initial values of the profile parameters. If the profile parameters are incorrect then it would be reflected in the characteristics difference profile, then from the careful inspection of the profile plot it needs to be deciding which parameter requires further refinement.

1.8.3 Full structure refinement:

Once we have the information on background contribution and correct profile parameters, the very next step is to refine the structural parameters using a correct

structural model. In this case, the calculated pattern must first be scaled to the observed one. The next step is to refine the atomic coordinates of the heavier atoms followed by lighter atoms. If this sequence of refinement converges then all atomic coordinates can be refined simultaneously or otherwise constraint refinement needs to be performed. The changes in atomic coordinates will affect the structure factor and hence in the relative peak intensities.

In the case of refinement of thermal parameters (B) with XRD data, the thermal parameters of heavier atoms are only refined while constraining the thermal parameters of lighter similar atoms to be equal. Refinement of thermal parameters with neutron data is much reliable because the atomic scattering cross sections with neutrons are independent of $\sin\theta/\lambda$. Thermal parameter refinement is quite tricky because all measurement and modelling errors finally enter into B . Sometime the value of B goes to negative (not physical) and as a result the high angle reflections have increasingly higher calculated intensities than the observed one. Similarly, overestimating the value of B would lead to a reduction in calculated intensities at high scattering angle. The overestimation of B sometimes arises by refining the background, when the peaks are strongly overlapping at high angles. The value of B could be negative either due to the fact that the density of scattering matter has been considered to be underestimated for that site or the absorption correction has not been accounted properly. It has been observed that high absorption leads to weakening of low angle data or conversely that the high angle data appear stronger than they should be. Among the structural parameters, the scale, the occupancy parameters and the thermal parameters are highly correlated with one another and very much sensitive to the background correction than the atomic coordinates. For this reason occupancy parameters are difficult to refine with x-ray diffraction data and therefore sometime chemical constraint are applied. With neutron diffraction data chemical occupancy can be refined much more reliably because of the reliability of determination of B parameter. To minimize the problem of parameter correlation, refinement of two different data sets (e.g. one x-ray and one neutron data or two different XRD patterns recorded with different wavelengths under same experimental conditions) which contains complementary information is considered. Finally, the initial profile parameters can also be refined along with the structural parameters to convergence or obtain reliable R (agreement indices) values.

1.8.4 Magnetic structure determination from refinement:

A particular magnetic structure is described by the magnitude and direction of the magnetic moment of a magnetic atom and magnetic propagation vector (\vec{k}). The magnetic propagation vector describes how the moment magnitude and direction of a magnetic atom located at the zeroth unit cell is related to the other magnetic atoms on the symmetry related sites within the nuclear unit cell [73]. It is analogous to the translational symmetry used to describe the periodicity of crystal structure. There are two ways to describe a magnetic structure. The most close to conventional crystallography is the use of magnetic space group (Shubnikov groups) and the other way is the formalism of propagation vectors used together with the representation analysis. Now we briefly discuss the formalism of magnetic propagation vectors. Any type of magnetic structure (e.g. collinear, non-collinear, spiral, conical, and cycloidal) in a crystal can be represented by the Fourier series:

$$m_{lj} = \sum_k S_{kj} \exp(-2\pi i k R_l) \quad (1.12)$$

This expression is similar to Bloch waves which describe the atomic moments (m_{lj}) of any atom j in unit-cell l by relating it to that of the related atom in the zeroth unit cell using a phase relation defined by a propagation vector, \vec{k} and lattice translational separation R_l of the two atoms. The Fourier coefficients S_{kj} are complex vectors. The necessary condition for real m_{lj} is $S_{-kj} = S_{kj}^*$. According to the fundamental hypothesis of the magnetic symmetry analysis, Fourier coefficients S_{kj} that describe the magnetic structures with propagation vector \vec{k} must be a linear combination of the basis vectors (atomic components) of the irreducible representations of G_k as described below:

$$S_{kj} = \sum_{n\lambda} C_{n\lambda}^{kv} S_{n\lambda}^{kv}(j) \quad (1.13)$$

where ν labels the active irreducible representation, Γ^ν , of the propagation vector group G_k , λ labels the component corresponding to the dimension of the representation Γ^ν , n is an additional index running between one and the number of times ($n = 1 \dots n_\nu$) the

representation Γ^ν is contained in the global magnetic representation Γ_{Mag} . The magnetic representation [74-76] describes the effect of symmetry operators of the little group (G_k) on the position of atoms (permutation representation, Γ_{Perm}) and magnetic moments (axial vector representation Γ_{Axial}), usually expressed by $\Gamma_{\text{Mag}} = \Gamma_{\text{Perm}} \times \Gamma_{\text{Axial}}$. The magnetic representation for an atomic site can be decomposed into contributions from the irreducible representations of the little group, $\Gamma_{\text{Mag}} = \sum_\nu n_\nu \Gamma^\nu$ and n_ν is given by [77],

$$n_\nu = \frac{1}{n(G_k)} \sum_{g \in G_k} \chi_{\Gamma_{\text{Mag}}}(g) \chi_{\Gamma^\nu}(g)^* \quad (1.14)$$

where $\chi_{\Gamma_{\text{Mag}}}(g)$ is the character of the magnetic representation and $\chi_{\Gamma^\nu}(g)^*$ is the complex conjugate of the character of the irreducible representation with index ν for symmetry element g . The decomposition of Γ_{Mag} into the irreducible representations of the little group G_k gives the number of basis vectors that contribute to Γ_{Mag} from each irreducible representation. In the Eq. 1.13, the quantities $S_{n\lambda}^{k\nu}(j)$ are constant vectors and $C_{n\lambda}^{k\nu}$ are the mixing coefficients which are the free parameters of the magnetic structure. Though both $S_{n\lambda}^{k\nu}(j)$ and $C_{n\lambda}^{k\nu}$ could be complex, the condition $S_{-kj} = S_{kj}^*$ ensures the reality of the magnetic moments. Usually the total number of $C_{n\lambda}^{k\nu}$ is lower than the number of Fourier components of each magnetic atom in the unit cell. The number of free coefficients to describe a magnetic structure corresponding to a single representation of G_k is related to the number of independent basis vectors $n_f \propto n_\nu \times \dim(\Gamma^\nu)$.

According to the above discussion, it is evident that determination of correct magnetic structure requires three important information, space group of the crystal structure, propagation vector and Fourier components for each magnetic atom. We briefly discuss them below.

1. At first, we need to know the crystallographic symmetry or space group (as obtained from the structural parameter refinement discussed in section 1.8.3) of the material in the paramagnetic state. Using this profile and structural parameters one can refine the low temperature (magnetically ordered state) crystal structure, if the

space group is similar to the paramagnetic state. In case, there is a structural change at low temperature then we need to find out the symmetry of that structure.

2. Next we need to determine the magnetic propagation vector(s), \vec{k} , from the indexing of magnetic Bragg peak (it could be a new peak or increased intensity of existing Bragg peak which could not be accounted by the structural model) at lower scattering angles in the low temperature (magnetically ordered state) neutron diffraction data. Usually, the appearance of new Bragg peak indicate antiferromagnetic ordering which could be commensurate (e.g. $\vec{k} = \frac{1}{2} \frac{1}{2} 0$); incommensurate (e.g. $\vec{k} = 0 \frac{1}{2} 0.21$) and spin configurations with ($\vec{k} = 0 0 0$), where magnetic and chemical unit cells are of same dimension. On the other hand, in the case of ferromagnetic or ferrimagnetic ordering, magnetic intensity is usually found be added to the existing nuclear Bragg peaks.

3. The final step is to determine the n coefficients ($C_{n\lambda}^{kv}$) for n basis vectors, $S_{n\lambda}^{kv}(j)$, for spin on atom j , because linear combination of n basis vectors give the Fourier coefficients (see Eq. 1.13), which in turn gives the magnitude and direction of magnetic moment according to the Eq. 1.12. This step is performed using the magnetic symmetry analysis developed by E. F. Bertaut [74]. Magnetic symmetry analysis facilitates to find out the irreducible representations of the little group (G_k), which consists of only those symmetry elements of the space group which leaves the propagation vector invariant. The irreducible representations contain the information of possible magnetic structures which also satisfies the symmetry constraints imposed by the crystal structure. From the refinement (using computer program, e.g. FULLPROF) one can determine which irreducible representation among all the possibilities actually fits the magnetic Bragg peak properly [78]. Once we find the correct model from the refinement, it would be easier to obtain the coefficients of basis vectors of that irreducible representation and hence the magnitude and direction of magnetic moment. After the determination of magnetic structure we can find out the Shubnikov group (only for the commensurate magnetic structure), which actually helps to visualize the magnetic symmetry among the moments.

1.8.5 R-factors:

The progress of a Rietveld refinement is usually monitored by looking at the difference profile plot. In addition quantitative agreement between the observed data and calculated pattern is obtained through agreement indices or *R*-factors which are defined as follows [79]:

$$R_p \text{ (profile)} = \frac{\sum_i |y_i(\text{obs}) - y_i(\text{calc})|}{\sum_i y_i(\text{obs})} \quad (1.15)$$

$$R_{wp} \text{ (weighed - profile)} = \left\{ \frac{\sum_i w_i [y_i(\text{obs}) - y_i(\text{calc})]^2}{\sum_i w_i [y_i(\text{obs})]^2} \right\}^{1/2} \quad (1.16)$$

where $y_i(\text{obs})$ and $y_i(\text{calc})$ is the observed and calculated intensity at step i , respectively and w_i is the weight assigned to the individual step intensity. During the Rietveld refinement, the expression in the numerator of R_{wp} gets minimized. In the case of background subtracted diffraction data, $y_i(\text{obs})$ is the net intensity after subtraction. On the other hand, if the background is refined then $y_i(\text{obs})$ and $y_i(\text{calc})$ includes the background contribution, as a result R_{wp} becomes small because a considerable amount of intensity is accounted for by the background function. For the present thesis, all the refinement was carried out without refining the background (only subtracted). The R_{wp} value should approach the statistically expected *R* value, R_{exp} , which reflects the quality of the data or counting statistics.

$$R_{exp} \text{ (expected)} = \left[\frac{(N - P)}{\sum_i^N w_i y_i(\text{obs})^2} \right]^{1/2} \quad (1.17)$$

where N is the number of observations and P is the number of refinable parameters. The ratio of R_{wp} to R_{exp} is known as goodness-of-fit (*GOF*) and it should ideally approach 1.

$$\chi^2 = \frac{R_{wp}}{R_{exp}} \quad (1.18)$$

Depending on the counting statistics, the value of χ^2 can be greater (high counting statistics) or smaller (small counting statistics) than 1. Finally, if the R_{wp} value of structural refinement approaches R_{wp} value of Le Bail fitting (structure-free), then it is considered to be a good refinement.

The reliability of a structural model used for the refinement is often quantified based on the agreement between observed and calculated structure factors, F_{hkl} . The value of R_F decrease during the refinement with the gradual improvement in the structural model.

$$R_F (\text{Structure factors}) = \frac{\sum_{hkl} |F_{hkl}(\text{obs}) - F_{hkl}(\text{calc})|}{\sum_{hkl} |F_{hkl}(\text{obs})|} \quad (1.19)$$

Similar to R_F , another quantity Bragg intensity R value, R_B , is also used to monitor the improvement in the structural model shown below:

$$R_B (\text{Bragg}) = \frac{\sum_{hkl} |I_{hkl}(\text{obs}) - I_{hkl}(\text{calc})|}{\sum_{hkl} |I_{hkl}(\text{obs})|} \quad (1.20)$$

where $I_{hkl} = mF_{hkl}^2$ (m = multiplicity), $I_{hkl}(\text{obs})$ is the observed integrated intensity of reflection hkl calculated at the end of the refinement after distributing each $y_i(\text{obs})$ between the contributing peaks according to the calculated intensities $I_{hkl}(\text{calc})$. At the end the quality of refinement needs to be verified from a careful inspection of the atomic parameters, which should be chemically realizable.

1.9 Magnetic properties

1.9.1 DC magnetometry:

The principle of magnetization (net magnetic moment per unit volume) measurement is based on the magnetic flux change in a coil, governed by the Faraday's law of electromagnetic induction. This law states that the induced electromotive force (e.m.f.) in a closed circuit is equal to the rate of change of magnetic flux enclosed by the circuit. This law is expressed by the following equation:

$$V = -N \frac{d\phi}{dt} = -NA \frac{dB}{dt} \quad (1.21)$$

where V is the induced e.m.f., ϕ is the magnetic flux passing through a coil of N turns and A is the cross-sectional area of the coil, B is the magnetic induction = $\left(\frac{\phi}{A}\right)$, $\frac{d\phi}{dt}$ is the rate of change of magnetic flux.

The magnetic measurements of all samples are carried out using a SQUID (Superconducting Quantum interference Device) - VSM (Vibrating Sample Magnetometer) Magnetic Property Measurement System (MPMS3). The SQUID magnetometer consists of (1) a superconducting magnet which is used to generate magnetic fields, (2) a second-order gradiometer superconducting detection coil which senses the change in the external magnetic field and transforms them into an electrical current, (3) an input transformer that transforms the resulting current into a magnetic flux in the direct current (dc) SQUID device, (4) electronics which transform the applied flux into a room temperature voltage output and acquisition hardware and software for recording, storing and analyzing the data. To maintain the superconducting state of detection coil and dc SQUID device liquid helium is used as a refrigerant. In Figure 1.20 the important components of MPMS3 SQUID system are shown.

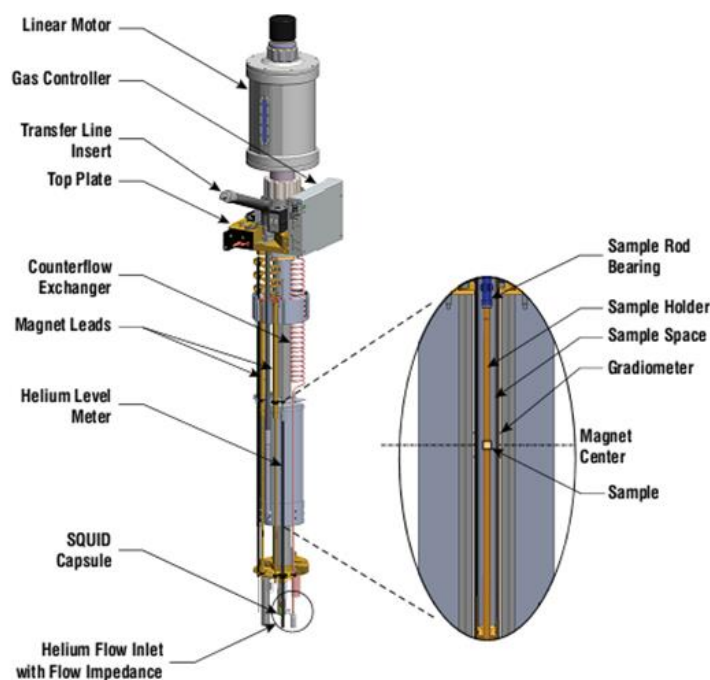


Figure 1.20: The schematic diagram of different components of MPMS3 SQUID system [adapted from the Quantum Design, Inc.].

The magnetometer vibrates a magnetized sample sinusoidally up and down inside a stationary superconducting detection (or pick-up) coils, which are located outside the sample chamber within a 4 K environment and at the center of the superconducting magnet. The detection coil is a single superconducting wire which is wound into three coils configured as a balanced second order gradiometer. They have been arranged in such a way those voltages due to changes in the applied field are canceled out and only the signal from the sample remains. The sample is ideally located in the center of the detection coil. Due to the movement of the sample through the detection coils, the magnetic moment of the sample induces a change in magnetic flux which in turn results in a change in an electric current in the coils (Faraday's law). The induced signal in the detection coil is proportional to the magnetic moment as well as to the amplitude and frequency of the vibration, as evident from the following expression,

$$V_{coil} = 2\pi f C m A \sin(2\pi f t) \quad (1.22)$$

where, m is the magnetic moment of the sample, A and f is the amplitude and frequency of the vibration, C is the coupling constant. Because the detection coils are connected to the SQUID device (located below the magnet inside a superconducting shield) forming a closed superconducting loop, the induced current from the detection coil couples inductively to the SQUID device.

The SQUID device is very sensitive to extremely subtle magnetic fields and it is based on the tunneling of superconducting electrons across a very narrow insulating gap, known as Josephson junction between two superconductors forming a ring. According to Faraday's law, a changing magnetic flux through the ring would induce a voltage and current in the ring. This induced current would add to the measuring current in one junction and subtracts in the other resulting in a periodic appearance of resistance in the superconducting circuit and a voltage between the junctions due to the wave nature of superconducting current. Each voltage step across the boundary of the ring corresponds to the passage of a single flux quantum. SQUID uses this change in flux quantum to detect the small magnetic field. Because SQUID devices are very sensitive to fluctuations in a magnetic field, they are kept under superconducting

shielding to prevent magnetic flux from the superconducting magnet and laboratory environment.

Since SQUID is an extremely sensitive highly linear current-to-voltage converter, the variations in the current in the detection coils generate corresponding variations in the SQUID output voltage which are proportional to the magnetic moment of the sample. Hence, in MPMS3 from the measurement of voltage variations in the SQUID sensor as the sample is moved through the superconducting detection coils provides a highly accurate measurement of sample magnetic moment. The sensitivity of SQUID-VSM is 10^{-8} emu, two orders of magnitude higher than VSM.

1.9.2 AC magnetometry:

AC magnetic measurements give important information about the magnetization dynamics because the induced magnetic moment is time-dependent, while DC magnetic measurements determine the equilibrium value of the magnetization in a sample because the sample moment is constant during the measurement time. In AC magnetic measurements, a small AC field ($H_{AC} = H_0 \sin \omega t$) applied to a sample, either in the absence or presence of small DC magnetic field, resulting in time-dependent moment in the sample. In contrast to DC magnetization measurements, AC magnetometry does not require any sample motion in the detection coil because the field of the time-dependent moment induces a current in the coil. The detection circuitry is configured to detect only in a narrow frequency band, usually at the fundamental frequency to that of the AC drive field.

In AC magnetometry, we measure the susceptibility, (χ), defined as, $\chi = dM/dH$, which is the slope of the $M(H)$ curve in DC magnetometry, where $\chi = M/H$. Therefore the AC susceptibility can be considered as the slope of the $M(H)$ curve in DC measurements. In fact at very low frequencies, the AC magnetic moment of the sample follows the $M(H)$ curve which is measured in the DC magnetometry. The induced AC moment in the presence of small AC field is expressed by,

$$M_{AC} = (dM/dH) \cdot H_{AC} \sin(\omega t) \quad (1.23)$$

where H_{AC} is the amplitude of the driving field, ω is the driving frequency and $\chi = dM/dH$, is the slope of the $M(H)$ curve. Therefore, with changing DC magnetic field, different parts of the $M(H)$ curve are accessed giving rise to different susceptibility. The main advantage of AC magnetometry is that the small magnetic shifts can be detected even when the absolute moment is large, because this measurement is sensitive to a small change in $M(H)$ curve and not to the absolute value.

In the presence of dynamic effects in the sample, the AC moment at high frequencies does not follow the DC magnetization curve. At higher frequencies, AC-magnetization of the sample lags behind the AC drive field. For this reason, AC magnetic susceptibility measurement gives rise to two parameters, the magnitude of the susceptibility, (χ), and the phase shift, (φ) relative to the drive signal. The AC susceptibility, χ , can also be expressed as,

$$\chi = \chi' + j\chi'' \quad (1.24)$$

where χ' is the in-phase, or real component and χ'' is the out-of-phase, or imaginary component. Furthermore they can be expressed as,

$$\chi' = \chi \cos\varphi; \quad \chi'' = \chi \sin\varphi \quad (1.25)$$

$$\chi = \sqrt{\chi'^2 + \chi''^2}; \quad \varphi = \tan^{-1}(\chi''/\chi') \quad (1.26)$$

In the low-frequency AC magnetic measurement, χ' corresponds to the slope of DC, $M(H)$ curve and χ'' indicates the dissipation in the sample. In conducting materials, dissipation occurs due to eddy currents. A non-zero χ'' arises in spin-glasses due to relaxation and irreversibility.

The magnetometer used for measuring AC susceptibility consists of three coils, a primary coil, and two secondary coils as shown in the schematic representation [Figure 1.21]. The sample is placed at the center of one of the secondary coil. The coils are wound in such way that in the absence of the sample, the signal generated from both the secondary coils cancel each other. The primary coil which surrounds (in most cases), produces an AC magnetic field. The two components of susceptibility (χ' and χ'') are

extracted using a circuit consisting of a lock-in amplifier. During the susceptibility measurement in the Physical Property Measurement System (PPMS), the sample undergoes a five point measurement process. The sample is successively moved to center of bottom detection coil, center of top detection coil and again center of bottom detection coil. The signals are modified and digitized by an analog to digital (A/D) converter and then saved as response waveform. After these measurements, two more readings are obtained with sample placed at the center between the two coil arrays with opposite polarities of the calibration coil detection circuit. The real (χ') and imaginary (χ'') parts are calculated for each response waveform by fitting and comparing to the driving signal.

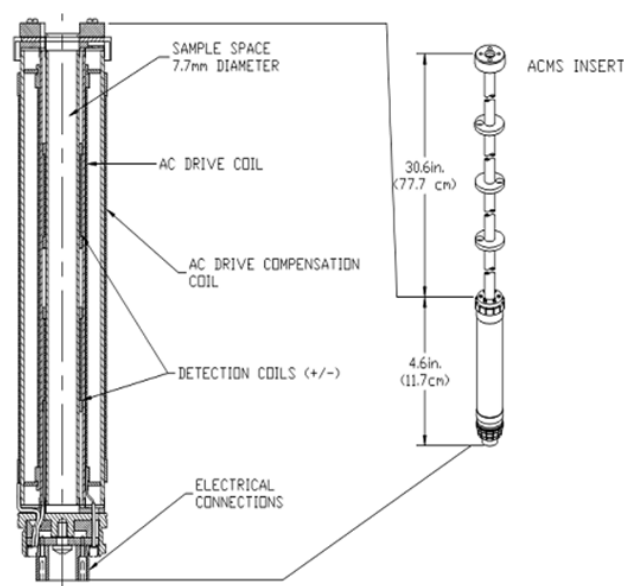


Figure 1.21: The schematic diagram of different components of PPMS system used for AC susceptibility measurement [adapted from the Quantum Design, Inc.].

In this thesis, AC magnetometry has been employed to study the spin-glass state of the magnetic material. This is defined as a random, mixed-interacting magnetic system characterized by a random, yet cooperative, freezing of spins at a well-defined temperature T_f (freezing temperature) below which a highly irreversible, metastable frozen state appears without the usual long range magnetic ordering [38]. The AC susceptibility measurement is particularly useful in determining the freezing temperature of spin-glasses and it cannot be extracted from specific heat [80]. The freezing temperature (T_f) is determined by measuring the temperature dependence of χ' , which reveals a cusp at the freezing temperature and the position of cusp is dependent on the frequency of AC magnetic field. This feature is unique for the

characterization of spin-glass phases. In many cases it is observed that, the combination of AC and DC magnetometry gives complementary information which helps in better understanding of glassy behavior in the magnetic material [81,82]. In addition, the dynamic susceptibility can also be used to study the nature of magnetic phase transition, e.g. ferromagnetic transitions. Usually, χ diverges at the critical temperature of a phase transition. Critical exponents characterize the nature of the divergence as a function of temperature and DC magnetic field. From the critical exponents it is possible to distinguish between various models of magnetic interactions, e.g. 3-d Heisenberg, Ising model [83].

1.10 Dielectric properties

1.10.1 Capacitance and dielectric loss:

From the study of temperature and frequency dependent capacitance, we obtain information about dielectric properties of insulating metal oxides. The capacitance (C) can be defined as the amount of electric charge (Q) stored for an applied electric potential (V), expressed as,

$$C = \frac{Q}{V} \quad (1.27)$$

The capacitance of a parallel-plate capacitor made of two parallel plane electrodes of area A and separated by a distance d can be expressed as,

$$C = \varepsilon \frac{A}{d} = \varepsilon_0 \varepsilon_r \frac{A}{d} \quad (1.28)$$

where ε is the absolute complex permittivity of the material expressed as $\varepsilon = \varepsilon' - j\varepsilon''$ [84], ε_0 is the permittivity of free space and the value is constant (8.854×10^{-12} F m⁻¹), ε_r is the dimensionless relative complex permittivity ($\varepsilon_r = \varepsilon_r' - j\varepsilon_r''$) which is defined as, $\varepsilon_r = \varepsilon/\varepsilon_0$. The components ε_r' (ε') and ε_r'' (ε'') are the real and imaginary part of the permittivity respectively. The induced polarization in a polar material is given by,

$$P = D - \varepsilon_0 E = \varepsilon E - \varepsilon_0 E = \varepsilon_r \varepsilon_0 E - \varepsilon_0 E \quad (1.29)$$

$$P = (\varepsilon_r - 1)\varepsilon_0 E \quad (1.30)$$

where $D = \varepsilon E$, is the electric displacement. Both real and imaginary component of permittivity vary with frequency ($f = \omega/2\pi$) as well as temperature. Although the real and imaginary component depends on the frequency but they cannot vary independently with frequency due to the fact that their frequency dependencies are connected to each other through the Kramers-Krönig relationship,

$$\varepsilon_r'(\omega) = \frac{1}{\pi} \int_{-\infty}^{+\infty} \frac{\varepsilon_r''(\omega_0)}{\omega_0 - \omega} d\omega_0 \quad (1.31)$$

which indicates that a drop in ε_r' with increasing frequency would be associated with a peak in ε_r'' . It is evident that at low frequencies the dipoles can follow the AC signal, but at very high frequencies they are unable to follow the signal and thus relax. ε_r' has contributions from the ionic, dipolar, atomic and electronic polarizability which depends on the frequency as illustrated in Figure 1.22. Other than ferroelectric material, the relative permittivity of a dielectric material is independent of magnitude of applied electric field, provided the dielectric material can withstand that voltage.

In addition to the energy storing (represented by ε_r') in a dielectric material when an AC voltage ($V_0 \sin \omega t$) is applied it also leads to energy dissipation (represented by ε_r'') in terms of heat. The dissipation of energy per unit volume at each point is,

$$W = 2\pi f E^2 \varepsilon_r'' \quad (1.32)$$

where f is the frequency of sinusoidal electric field and E is the root mean square value of electric field. For this reason ε_r'' is considered as a measure of the energy loss per period. The complex conjugate of relative complex permittivity (ε_r^*) is represented in the Argand plane, where ε_r' is the abscissa and ε_r'' as the ordinate, drawing a curve with frequency ($f = \omega/2\pi$), where $\varepsilon_r^* = \varepsilon_r' + j\varepsilon_r''$. The segment to the origin makes an angle δ with the abscissa, so that, $\tan \delta = \varepsilon_r''/\varepsilon_r'$. Therefore, Eq. 1.32 becomes, $W = 2\pi f E^2 \varepsilon_r' \tan \delta$, where $\tan \delta$ is known as loss tangent and δ as the loss angle. Dielectric loss is an important quantity which dictates about the amount of

leakage present in a particular material. For practical application this loss parameter should be as small as possible. An ideal capacitor would have $\tan\delta$ less than 0.1.

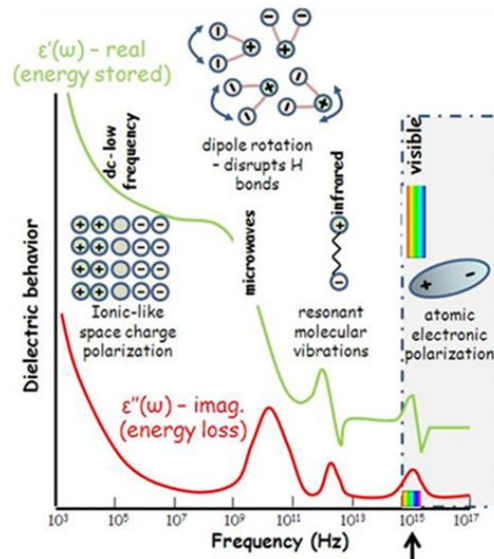


Figure 1.22: Frequency dependence of real and imaginary component of relative permittivity [adapted from the nanoHUB.org]

To measure the temperature and frequency dependent capacitance we have used a parallel plate geometry for the capacitor which was mounted in a custom made multifunctional probe and then inserted in the PPMS (Physical Property Measurement System) chamber which has been used to access the low temperature and magnetic fields. The capacitance was measured using programs written with the software Labview and an LCR meter (Agilent E4980A). In Figure 1.23 the experimental set-up used for the measurement is shown.

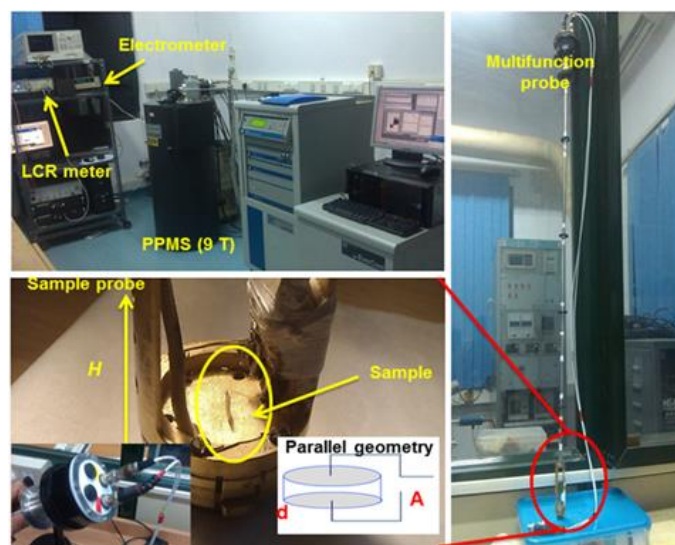


Figure 1.23: Experimental set-up for capacitance and pyroelectric measurements

1.10.2 Pyroelectric current measurement:

The phenomenon of generation of spontaneous polarization in a material in response to a change in temperature is known as pyroelectricity. The temporary voltage created due to the change in temperature is the source of small current in the pyroelectric circuit. The pyroelectric effect can be quantified as [60],

$$\Delta \vec{P}_S = \vec{P} \Delta T \quad (1.33)$$

where, \vec{P} is the pyroelectric coefficient and $\Delta \vec{P}_S$ is the change in spontaneous polarization in response to a change in temperature ΔT . It was first observed by the Greek philosopher Theophrastus, in the mineral Tourmaline which attracted straw and bits of wood when heated [85]. The pyroelectric effect has been realized in those materials which have polar point symmetry such as 1, 2, m , $mm2$, 3, $3m$, 4, $4mm$, 6 and $6mm$. There are two types of pyroelectric effects. The first one is primary pyroelectric effect which is observed in the polar material where permanent dipole moment (where electric charges are present in the asymmetric environment) of the structure changes with temperature. The other one is secondary pyroelectric effect as observed in the piezoelectric material where it arises as a result of heating process that changes the mechanical stress, resulting in the changes in the surface charge density.

Based on the crystallographic symmetry and origin of pyroelectricity, it is evident that all pyroelectric materials are piezoelectric and they would be ferroelectric if the spontaneous polarization can be reversed with the application of an external electric field. Therefore, in the case of ferroelectric material where it is difficult to apply a very high electric field to measure P - E hysteresis loop, in that case, paraelectric to ferroelectric phase transition can be characterized by the observation of primary pyroelectric effect which is reversible with the polarity of the electric field. Since the pyroelectric current is measured while warming at zero bias voltage, therefore it would be beneficial to use this method to separate the current that is due to a sole change of the ferroelectric polarization. As we know that the electrical current (i) between the two electrodes attached in a parallel plate dielectric has three contributions such as, capacitive, resistive and ferroelectric which is expressed by the following equation,

$$i = C \frac{dV}{dt} + \frac{V}{R} + A \frac{dP}{dt} \quad (1.34)$$

where the first term is capacitive, the second term is resistive, the third term is associated with ferroelectric polarization, C is the capacitance, V is the voltage, R is the resistance, A is the area of electrode and t is the data recording time. The third term which is voltage independent is obtained from the pyroelectric measurement at zero bias.

To measure the pyroelectric current of a ferroelectric material, first, the sample is poled in the presence of a direct current (dc) voltage from a temperature above the Curie temperature to the lowest possible temperature to align the ferroelectric domains into a mono-domain state, though complete conversion may not occur. In a polycrystalline material, with the application of external poling electric field the polar axes of the crystallites will be reoriented in such a way that those polar axes would have a component parallel to the direction of electric field, thereby producing a net polarization. Because in the presence of an electric field, \vec{E} , a polarized material with polarization, \vec{P} , will be stabilized by an amount of energy equal to $-\vec{P} \cdot \vec{E}$. Therefore, crystallites with a less perfect ferroelectric domain or polar axes would cause the macroscopic polarization (\vec{P}_S) to be smaller than that achieved for a mono-domain of single crystal. After reaching the lowest temperature, the external electric field is removed and the circuit shorted for some time (~ 30 min) to remove the stray charges or reduce the leakage contribution, so that signal-to-noise ratio could be better. Next, the current would be recorded at zero bias as a function of temperature while warming the sample across the Curie temperature. For a magnetoelectric material, similar poling protocol would be followed but there will be a constant magnetic field during poling as well as during the time of data collection. The magnetic field should be kept on even during shorting the electrodes. Usually, for a ferroelectric or magnetoelectric material the profile of temperature dependent pyroelectric current gives rise to an asymmetric peak. From the integration of measured pyroelectric (or magnetoelectric) current (I) with time (t) followed by the division with the area of the electrode (A) we obtain the ferroelectric (or magnetoelectric) polarization (P) and the formula to obtain polarization is given by, $P = \int I dt/A$. The warming rate can be varied e.g. for a

material with small magnitude of ferroelectric polarization the pyroelectric current can be recorded with a temperature ramping rate of 15-20 K/min and for strong magnitude of ferroelectric polarization the data can be recorded at the rate of 4-8 K/min. In this context, it is important to mention that for a real ferroelectric material the position of pyroelectric peak should not vary with the ramping rate used for recording the current.

Though this is a very simple and widely used method for establishing a ferroelectric state in a material, it suffers from various drawbacks associated with leakage that can also lead to a pyroelectric profile similar to that obtained for a ferroelectric material thereby misleading the interpretation. Therefore careful measurements are very important. The problem of leakage arises from the finite conductivity of the sample due to the trapped charge at the electrode contact-sample interface, in the bulk of the medium e.g. at the grain boundary as well as in the form of intrinsic oxygen defects giving rise to multiple valences. In the material the existence of electret, where the presence of a strongly inhomogeneous distribution of trapped charges can give rise to pyroelectric effect, because they also possess permanent dipole moment and exhibits piezoelectricity due to electrostriction [86]. The background current can also arise from the usage of the cable of long length and improper shielding. In the case of improper shielding, the electromagnetic radiation or stray field of the laboratory environment can induce a constant background current in the pyroelectric circuit. Therefore, the cable connecting the sample probe and electrometer should be as small as possible and also it must be properly shielded and should have low resistance (to reduce resistive current). To avoid the sample related leakage component, the sample should be stoichiometric and highly sintered.

We have recorded the temperature dependent pyroelectric current of our samples using the programs written with the help of software Labview and Keithley 6517A electrometer. For this measurement, we have used similar experimental set-up and PPMS as shown in Figure 1.23. DC voltage was applied to the samples by using a Radiant Technologies, Inc. precision workstation.

Bibliography

- [1] C. N. R. Rao and B. Raveau, Transition metal oxides, VCH Publishers Inc. (1995).
- [2] C. N. R. Rao and G. V. Subba Rao, Phys. Status Solidi A **1**, 597 (1970).
- [3] C. N. R. Rao, Annu. Rev. Phys. Chem. **40**, 291 (1989).
- [4] P. A. Cox, Transition metal oxides: an introduction to their electronic structure and properties, Oxford University Press, Vol 27 (2010).
- [5] I. E. Dzyaloshinskii, Zh. Exp. Teor. Fiz. **37**, 881 (1959) [Sov. Phys. JETP **10**, 628 (1960)].
- [6] D. N. Astrov, Sov. Phys. JETP **13**, 729 (1961).
- [7] D. N. Astrov, Sov. Phys. JETP **11**, 708 (1960).
- [8] J. G. Bednorz and K. A. Müller, Z. Phys. B Condens. Matter **64**, 189 (1986).
- [9] A. Ramirez, J. Phys.: Condens. Matter **9**, 8171 (1997).
- [10] C. N. R. Rao and B. Raveau, Colossal magnetoresistance, charge ordering and related properties of manganese oxides, World Scientific (1998).
- [11] W. Eerenstein, N. Mathur, and J. F. Scott, Nature **442**, 759 (2006).
- [12] C. N. R. Rao, A. Sundaresan, and R. Saha, J. Phys. Chem. Lett. **3**, 2237 (2012).
- [13] Y. Tokura and S. Seki, Adv. Mater. **22**, 1554 (2010).
- [14] J. Wang *et al.*, Science **299**, 1719 (2003).
- [15] Y. Kitagawa, Y. Hiraoka, T. Honda, T. Ishikura, H. Nakamura, and T. Kimura, Nat. Mater. **9**, 797 (2010).
- [16] B. Keimer, Nat. Mater. **5**, 933 (2006).
- [17] T. Mizokawa, D. Khomskii, and G. Sawatzky, Phys. Rev. B **60**, 7309 (1999).
- [18] J. B. Goodenough and J.-S. Zhou, J. Mater. Chem. **17**, 2394 (2007).
- [19] H. A. Jahn and E. Teller, Proc. R. Soc. A161, 220 (1937).
- [20] I. B. Bersuker, Chem. Rev. **101**, 1067 (2001).
- [21] U. Opik and M. Pryce, Proc. Roy. Soc. A 238, 425 (1957).
- [22] I. B. Bersuker, The Jahn-Teller effect and Vibronic Interactions in Modern Chemistry, Plenum Press, New-York (1984); I. B. Bersuker, The Jahn-Teller effect: A Bibliographic Review, IFI/Plenum, New-York (1984); I. B. Bersuker and V. Z. Polinger, Vibronic Interactions in Molecules and Crystals, Springer-

- Verlag, Berlin (1989); I. B. Bersuker, *Electronic Structure and Properties of Transition Metal Compounds*, Wiley-Interscience Publication (1996)
- [23] G. A. Gehring and K. A. Gehring, Co-operative Jahn-Teller effects in *Reports on Progress in Physics*, Vol. 38, part I, Edited by J. M. Ziman, Institute of Physics (1975).
- [24] T. Chatterji, F. Fauth, B. Ouladdiaf, P. Mandal, and B. Ghosh, *Phys. Rev. B* **68**, 052406 (2003).
- [25] J. Rodriguez-Carvajal, M. Hennion, F. Moussa, A. Moudden, L. Pinsard, and A. Revcolevschi, *Phys. Rev. B* **57**, R3189 (1998).
- [26] L. Martín-Carrón and A. De Andrés, *Eur. Phys. J. B* **22**, 11 (2001).
- [27] A. Millis, B. I. Shraiman, and R. Mueller, *Phys. Rev. Lett.* **77**, 175 (1996).
- [28] M. Sage, G. Blake, C. Marquina, and T. Palstra, *Phys. Rev. B* **76**, 195102 (2007).
- [29] Y. Tokura and N. Nagaosa, *Science* **288**, 462 (2000).
- [30] J. M. Rondinelli, A. S. Eidelson, and N. A. Spaldin, *Phys. Rev. B* **79**, 205119 (2009).
- [31] R. G. Pearson, *J. Mol. Struct.* **103**, 25 (1983).
- [32] J. K. Burdett, *Inorg. Chem.* **20**, 1959 (1981).
- [33] C. N. R. Rao, A. Arulraj, A. K. Cheetham, and B. Raveau, *J. Phys.: Condens. Matter* **12**, R83 (2000).
- [34] E. J. Verwey, *Nature* **144**, 327 (1939).
- [35] V. B. Shenoy and C. N. R. Rao, *Phil. Trans. R. Soc. A* **366**, 63 (2008).
- [36] T. Vogt, A. Cheetham, R. Mahendiran, A. Raychaudhuri, R. Mahesh, and C. N. R. Rao, *Phys. Rev. B* **54**, 15303 (1996).
- [37] C. Ritter, R. Mahendiran, M. Ibarra, L. Morellon, A. Maignan, B. Raveau, and C. N. R. Rao, *Phys. Rev. B* **61**, R9229 (2000).
- [38] S. Blundell, *Magnetism in condensed matter*, Oxford University Press, New York (2001).
- [39] T. McGuire, M. Shafer, R. Joenk, H. Alperin, and S. Pickart, *J. Appl. Phys.* **37**, 981 (1966).
- [40] M. A. Ruderman and C. Kittel, *Phys. Rev.* **96**, 99 (1954).
- [41] T. Kasuya, *Prog. Theor. Phys.* **16**, 45 (1956).
- [42] K. Yoshida, *Phys. Rev.* **106**, 893 (1957).
- [43] J. Kanamori, *J. Phys. Chem. Solids* **10**, 87 (1959).

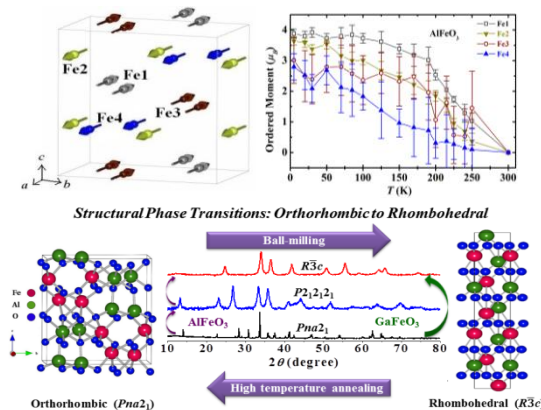
- [44] P. Anderson, Phys. Rev. **79**, 350 (1950).
- [45] C. Zener, Phys. Rev. **82**, 403 (1951).
- [46] P. W. Anderson and H. Hasegawa, Phys. Rev. **100**, 675 (1955).
- [47] P.-G. De Gennes, Phys. Rev. **118**, 141 (1960).
- [48] T. Moriya, Phys. Rev. **120**, 91 (1960).
- [49] T. Moriya, Phys. Rev. Lett. **4**, 228 (1960).
- [50] B. D. Cullity and C. D. Graham, Introduction to magnetic materials, John Wiley & Sons (2011).
- [51] I. Jacobs, J. Appl. Phys. **32**, 61 (1961).
- [52] C. Starr, F. Bitter, and A. Kaufmann, Phys. Rev. **58**, 977 (1940).
- [53] W. H. Meiklejohn and C. P. Bean, Phys. Rev. **102**, 1413 (1956).
- [54] W. H. Meiklejohn and C. P. Bean, Phys. Rev. **105**, 904 (1957).
- [55] N. A. Spaldin, Magnetic materials: fundamentals and applications, Cambridge University Press (2010).
- [56] J. Nogués and I. K. Schuller, J. Magn. Magn. Mater. **192**, 203 (1999).
- [57] P. Curie, Journal de physique **3**, 393 (1894).
- [58] D. B. Litvin, IUCr e-book, <http://www.iucr.org/publ/978-0-9553602-2-0> (2013).
- [59] International Tables for Crystallography, Vol. D, Physical Properties of crystals, Edited by A. Authier, Kluwer Academic Publishers (2003).
- [60] R. E. Newnham, Properties of materials: anisotropy, symmetry, structure, Oxford University Press, (2005).
- [61] W. Brown Jr, R. Hornreich, and S. Shtrikman, Phys. Rev. **168**, 574 (1968).
- [62] B. D. Cullity, Elements of X-ray diffraction, 2nd Edition, Addison Wesley Publishing Company Inc. (1977).
- [63] T. Chatterji, Neutron scattering from magnetic materials, Gulf Professional Publishing (2005).
- [64] G. E. Bacon, Monographs on the physics and chemistry of materials, 2nd Edition, Oxford University Press, London (1962).
- [65] J. A. Bearden, Rev. Mod. Phys. **39**, 78 (1967).
- [66] H. M. Rietveld, J. Appl. Crystallogr. **2**, 65 (1969).
- [67] H. M. Rietveld, Acta Crystallogr. **22**, 151 (1967).
- [68] P. Thompson, D. Cox, and J. Hastings, J. Appl. Crystallogr. **20**, 79 (1987).
- [69] G. Caglioti, A. t. Paoletti, and F. Ricci, Nuclear Instrum. **3**, 223 (1958).

-
- [70] J. Rodríguez-Carvajal, Laboratoire Léon Brillouin (CEA-CNRS), CEA/Saclay **91191** (2003).
- [71] J. Rodriguez-Carvajal, M. Fernandez-Diaz, and J. Martinez, *J. Phys.: Condens. Matter* **3**, 3215 (1991).
- [72] P. W. Stephens, *J. Appl. Crystallogr.* **32**, 281 (1999).
- [73] E. F. Bertaut, *J. Appl. Phys.* **33**, 1138 (1962).
- [74] E. F. Bertaut, *Acta Crystallogra. A* **24**, 217 (1968).
- [75] E. F. Bertaut, *J. Magn. Magn. Mater.* **24**, 267 (1981).
- [76] O. V. Kovalev, Representations of the crystallographic space groups: irreducible representations, induced representations, and corepresentations, 2nd Edition, Edited by H. T. Stokes, and D. M. Hatch, Gordon and Breach Science (1993).
- [77] A. S. Wills, *Phys. Rev. B* **63**, 064430 (2001).
- [78] J. Rodríguez-Carvajal, Program included in the FullProf Suite, version July-2010, ILL (2010).
- [79] L. McCusker, R. Von Dreele, D. E. Cox, D. Louer, and P. Scardi, *J. Appl. Crystallogr.* **32**, 36 (1999).
- [80] J. Mydosh, *J. Magn. Magn. Mater.* **157**, 606 (1996).
- [81] R. Mathieu, P. Jönsson, P. Nordblad, H. A. Katori, and A. Ito, *Phys. Rev. B* **65**, 012411 (2001).
- [82] T. Jonsson, K. Jonason, P. Jönsson, and P. Nordblad, *Phys. Rev. B* **59**, 8770 (1999).
- [83] A. G. Berndt, X. Chen, H. Kunkel, and G. Williams, *Phys. Rev. B* **52**, 10160 (1995).
- [84] A. K. Jonscher, Dielectric relaxation in solids, Chelsea Dielectrics Press (1983).
- [85] S. B. Lang, *Ferroelectrics* **230**, 99 (1999).
- [86] I. Lubomirsky and O. Stafsudd, *Rev. Sci. Instrum.* **83**, 051101 (2012).

Structure and magnetic properties of $\text{Al}_{1-x}\text{Ga}_x\text{FeO}_3$ family of oxides*

Summary

$\text{Al}_{1-x}\text{Ga}_x\text{FeO}_3$ family of oxides crystallizing in a non-centrosymmetric polar space group ($Pna2_1$) show interesting structure - magnetic property relationship which was investigated in detail by employing x-ray, neutron diffraction, Mössbauer and Raman spectroscopy. The study has revealed the occurrence of several interesting features related to unit cell parameters, site disorder and ionic size correlating with the observed magnetic properties. Site-specific substitution of isovalent Cr^{3+} in Fe site reduces the Néel temperature while it increases to a small extent on substituting Cr^{3+} in the Ga site of GaFeO_3 . Interestingly, upon ball-milling $\text{Al}_{1-x}\text{Ga}_x\text{FeO}_3$ undergoes reversible structural phase transformations. AlFeO_3 transforms to an orthorhombic $P2_12_12_1$ structure followed by its transformation to the $R\bar{3}c$ structure while GaFeO_3 and $\text{Al}_{0.5}\text{Ga}_{0.5}\text{FeO}_3$ directly go to the $R\bar{3}c$ structure. Magnetic properties of the $Pna2_1$ and the transformed phases show significant differences. Also, first-principles simulations throw light on the structure-property relationships.



*Papers based on this chapter are published in: J. Solid State Chem. 184, 494 (2011), © (2011) by Elsevier; J. Solid State Chem. 184, 2353 (2011), © (2011) by Elsevier; Inorg. Chem. 50, 9527 (2011), © (2011) by the American Chemical Society and Phys. Rev. B 85, 134449 (2012), © (2012) by the American Physical Society.

2.1 Introduction

Magnetoelectric oxides are a fundamentally as well as technologically important class of materials where the application of an external magnetic field generates electric polarization, or electric field produces magnetization [1,2]. Therefore, the cross coupling between magnetization and electric polarization provides additional degrees of freedom in the strongly correlated oxides. However, there are only a few materials, e.g., TbMnO_3 [3], CoCr_2O_4 [4] which show strong coupling between magnetization and polarization. The origin of electric polarization in these materials is due to the non-collinear spin configurations which arise as a result of strong magnetic frustration at low temperature [5]. Remeika synthesized orthorhombic non-perovskite GaFeO_3 , which shows ferrimagnetic ordering at very high temperature and also piezoelectric [6]. Later the existence of magnetoelectric coupling was demonstrated by Arima *et al.* on a single crystalline sample of GaFeO_3 [7]. Interestingly, GaFeO_3 contains anti-site cation disorder thereby strongly influencing the magnetic and related properties. A similar compound, AlFeO_3 which is comparatively less studied is also found to adopt the same crystallographic structure. GaFeO_3 belongs to the Shubnikov point group $m'2'm$ which supports linear magnetoelectric effect [7]. Given the unusual properties of AlFeO_3 and GaFeO_3 , we have carried out temperature dependent neutron diffraction study, along with magnetic and Mössbauer measurements to establish the detailed nature of magnetic properties and their relation to the structure [8]. Raman spectroscopic studies have been used to understand the phonon modes of AlFeO_3 and their coupling with the spin configuration [9].

There has been some interest in investigating phase transitions of these oxides. Both $\alpha\text{-Al}_2\text{O}_3$ and $\alpha\text{-Fe}_2\text{O}_3$ crystallize in the rhombohedral structure ($R\bar{3}c$) while $\beta\text{-Ga}_2\text{O}_3$ has a monoclinic structure ($C2/m$). Metastable orthorhombic phases ($Pna2_1$) of these materials are also known [10]. Studies of AlFeO_3 and GaFeO_3 at high pressures and high temperatures seem to indicate the occurrence of decomposition while there are also reports of a transition to perovskite phase at high pressure [11,12]. Studies of Nagai *et al.* [13], although not entirely clear, seem to suggest that the structure of AlFeO_3 transforms to another form of orthorhombic structure at high pressures and comes back to the trigonal phase on the release of pressure.

2.2 Scope of the present investigation

GaFeO₃ and AlFeO₃, which are derived from Fe₂O₃ by the substitution of one Fe³⁺ by Ga³⁺ or Al³⁺, show ferrimagnetic properties [14], unlike the parent binary oxides, Fe₂O₃. Moreover, investigation of magnetic properties of Al_{1-x}Ga_xFeO₃ was carried out to understand the magnetic ordering and associated properties which depend sensitively on anti-site cation disorder. The origin and tendency of cations to disorder and the associated properties are strongly related to the local structure and ionic sizes [8]. The effect of isovalent cation (Cr³⁺) substitution on GaFeO₃ was studied, and it showed interesting changes in magnetic properties depending on the site of cation substitution [12].

There has been interest in investigating the phase transitions of AlFeO₃ and GaFeO₃ because of their unique structures and properties, especially to find out whether the orthorhombic structures of these oxides transform to other structures when subjected to grinding or ball-milling. To our surprise, we find ball-milling transform these oxides from the orthorhombic structure (*Pna2*₁) to the rhombohedral structure (*R* $\bar{3}c$) with significant differences between AlFeO₃ and GaFeO₃ concerning the nature of the transformation [15]. On the other hand, solid solution of the end members, Al_{0.5}Ga_{0.5}FeO₃ upon ball-milling directly transforms from the initial orthorhombic structure (*Pna2*₁) to the rhombohedral structure (*R* $\bar{3}c$). Interestingly, on annealing all these compounds at very high temperature, the starting structural phase is restored indicating that the phase transition is reversible in nature. Besides characterizing the phase transitions by x-ray diffraction and Raman spectroscopy, we have studied the magnetic properties of the different phases. First-principles density functional theory calculations have been carried out to understand the properties of these materials relating to their structures, and also, it throws light on the nature of the phase transitions. The present study also indicates that how cation disorder which is inherent to these material controls the physical properties of the material. The results on structural phase transitions suggest that such mechanochemical chemistry would be an excellent tool to synthesize materials with metastable structures and study their crystallographic details in response to high pressure.

2.3 Experimental details

AlFeO_3 and GaFeO_3 were prepared by the co-precipitation method [16] starting from stoichiometric amounts of Fe_2O_3 (99.9%) and Al (Ga_2O_3) (99.9%) powder. The powders were dissolved separately in concentrated hydrochloric acid to prepare the respective metal chlorides and then mixed followed by stirring for half an hour. After that, NH_4OH solution was added drop by drop with continuous stirring until rich precipitation was achieved. Then the precipitate was filtered, washed with distilled water to remove the residual ammonium chloride salt till neutral pH and dried at 80°C in an air oven for 24 hrs. The dried powders were ground, pelletized and sintered at 1350°C for 2 hours in the air with a heating rate of $3^\circ\text{C}/\text{min}$. These oxides were also prepared by the ceramic method by heating mixtures of the component oxides at 1400°C with a repeated grinding, pelletizing and heating. Other compositions of $\text{Al}_{1-x}\text{Ga}_x\text{FeO}_3$ were synthesized by the conventional solid state reaction. Polycrystalline samples of $\text{GaFe}_{1-x}\text{Cr}_x\text{O}_3$ ($x = 0.05, 0.1$ and 0.2) and $\text{Ga}_{1-x}\text{Cr}_x\text{FeO}_3$ ($x = 0.05$ and 0.1) were prepared by solid state reaction method. First, appropriate amounts of Cr_2O_3 (99.9%) was substituted to Fe_2O_3 (or Ga_2O_3) (99.9%) by grinding followed by heating at 1000°C and then mixed with Ga_2O_3 (or Fe_2O_3) maintaining the 1:1 ratio. This mixture was reground thoroughly, pelletized and sintered at 1300°C for 12 h.

To confirm the phase purity of these oxides, x-ray diffraction patterns were recorded with a Bruker D8 Advance x-ray diffractometer, and all of them were found to crystallize in orthorhombic structure (space group $Pna2_1$). A software package FULLPROF suite [17] was used to perform Rietveld refinement on the diffraction data. Neutron diffraction experiments on polycrystalline $\text{Al}_{1-x}\text{Ga}_x\text{FeO}_3$ ($x = 0, 1$) samples were carried out at Dhruva research reactor, Trombay, INDIA, over the temperature range of 5-300 K using five linear positions sensitive detector (PSD) based powder diffractometer ($\lambda = 1.2443 \text{ \AA}$). Cylindrical vanadium container has been used to pack the powdered sample and a commercial closed cycle helium refrigerator to perform the low-temperature measurements.

DC magnetization measurements were carried out using a vibrating sample magnetometer in Physical Property Measurement System (PPMS) under Zero-Field-Cooled (ZFC) and Field-Cooled (FC) conditions in the temperature range 10 to 330 K

in the presence of 100 Oe magnetic field. Magnetic hysteresis curves were recorded at 5 K in the magnetic field range of ± 60 kOe. Mössbauer spectra were recorded in transmission mode using ^{57}Co γ -ray source in a Rhodium matrix and multi-channel analyzer. The sample thickness was adjusted so that the Fe content was approximately 10 mg/cm^2 . Calibrations of velocity and isomer shift were performed using α -iron (Fe) foil. Measurements at low temperatures were carried out using a helium closed cycle cooler system attached to the sample chamber. Unpolarized micro-Raman measurements were carried out on a polycrystalline pellet of AlFeO_3 in backscattering geometry using the 514.5-nm line of an Ar-ion laser (Coherent Innova 300) and Raman spectrometer (Dilor XY) coupled to a liquid nitrogen-cooled charge-coupled device detector. Temperature dependent experiments were performed in the temperature range of 5 to 315 K, with an accuracy of temperature ± 0.1 K using a continuous-flow He cryostat (Oxford Instruments).

These oxides were subjected to ball-milling using a planetary mono mill (Fritsch Pulverisette-6, Germany) to study the phase transitions. A batch of 2 g of the each sample was taken separately in an 80 ml capacity agate (99.9% SiO_2) bowl containing 10-15 agate balls of 10 mm diameter. Ball-milling was carried out without any additives (dry ball-milling) at a speed of 400 rpm for 12-24 hrs. The ambient temperature during ball-milling is around 400°C . It is important to note that we did not find any contamination in the ball-milled samples from the ball-mill vessel. The ball-milled samples have been characterized by various methods. The ball-milled samples were annealed in air at 700°C and characterized similarly. Then, the samples were also heated in the range of 1000 - 1350°C in air for 24 h. X-ray diffraction patterns of the powdered samples were recorded with a Bruker D8 Advance x-ray diffractometer to confirm the phase purities of these oxides. A software package FULLPROF suite [17] was used to analyze the structural data. Raman spectra of powdered samples were recorded at room temperature with a LabRAM HR 800 high-resolution Raman spectrometer (HORIBA-JobinYvon) using a He-Ne laser ($\lambda = 632.8 \text{ nm}$). Magnetic properties of the samples were measured using a vibrating sample magnetometer in Physical Property Measurement System (PPMS).

2.4 Results and discussion

First, the detailed results on the structure and magnetic properties of $\text{Al}_{1-x}\text{Ga}_x\text{FeO}_3$ family of oxides obtained from x-ray, neutron diffraction, Mössbauer, dc-magnetization measurements and Raman spectroscopic investigations will be discussed followed by a brief theoretical interpretation of the experimental findings. Next, the experimental results on ball-milling induced structural phase transformations in these compounds and the magnetic properties of corresponding compounds will be discussed.

2.4.1 Structure and magnetic properties of $\text{Al}_{1-x}\text{Ga}_x\text{FeO}_3$:

2.4.1.1 Structure

To investigate the crystallographic and magnetic structures of $\text{Al}_{1-x}\text{Ga}_x\text{FeO}_3$ family of oxides, x-ray as well as neutron diffraction experiments have been carried out.

2.4.1.1.1 X-ray diffraction of AlFeO_3 and GaFeO_3

In Figure 2.1, x-ray diffraction patterns of AlFeO_3 and GaFeO_3 are shown along with profile fits and difference patterns to show how they possess the same structure. In this chapter throughout standard setting $Pna2_1$ has been used instead of non-conventional setting $Pc2_1n$.

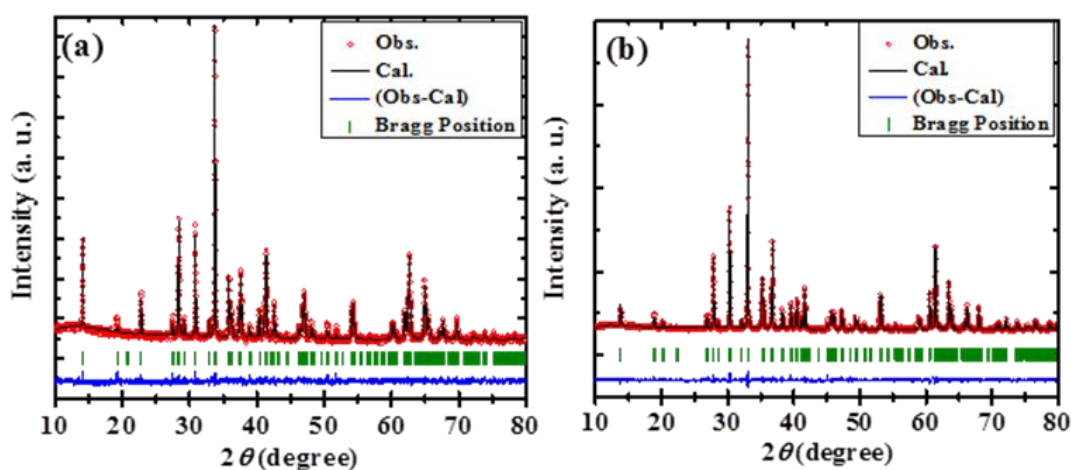


Figure 2.1: XRD patterns of (a) AlFeO_3 and (b) GaFeO_3 along with profile fits, difference patterns and Bragg positions ($T = 298$ K).

X-ray diffraction measurements on AlFeO_3 and GaFeO_3 done by us gave the following lattice parameters: $a = 4.9806$ (3) Å, $b = 8.5511$ (6) Å and $c = 9.2403$ (6) Å for AlFeO_3 ; $a = 5.0814$ (2) Å, $b = 8.7436$ (3) Å and $c = 9.3910$ (2) Å for GaFeO_3 . The

space group of both these oxides is $Pna2_1$. X-ray Diffraction measurements showed that $Al_{0.5}Ga_{0.5}FeO_3$ also crystallizes in the $Pna2_1$ space group with the lattice parameters, $a = 5.0306$ (1) Å, $b = 8.6461$ (2) Å, and $c = 9.3175$ (2) Å. These values lie in between those of $AlFeO_3$ and $GaFeO_3$. A series of polycrystalline compounds of $Al_{1-x}Ga_xFeO_3$ ($x = 0.3, 0.7, 0.9$) made by solid state reaction were studied using XRD. All these compounds crystallize in the orthorhombic structure with the non-centrosymmetric $Pna2_1$ space group. In Figure 2.2, x-ray diffraction patterns of $Al_{1-x}Ga_xFeO_3$ compositions are shown along with profile fits and difference patterns. The structural parameters of the $Al_{1-x}Ga_xFeO_3$ ($x = 0.3, 0.7, 0.9$) compositions are shown in Table 2.1.

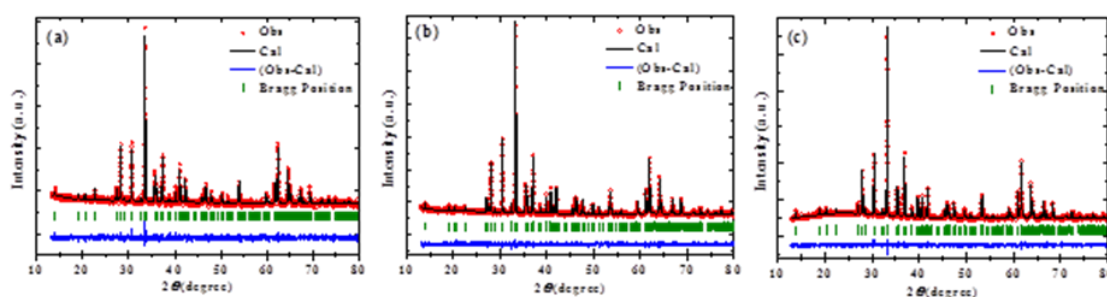


Figure 2.2: XRD patterns of (a) $Al_{0.7}Ga_{0.3}FeO_3$, (b) $Al_{0.3}Ga_{0.7}FeO_3$ and (c) $Al_{0.1}Ga_{0.9}FeO_3$ along with profile fits, difference patterns and Bragg positions ($T = 298$ K).

Table 2.1: Lattice parameters and unit cell volume of $Al_{1-x}Ga_xFeO_3$ ($x = 0, 0.3, 0.7, 0.9, 1$) at 298 K

Compound formula	a (Å)	b (Å)	c (Å)	Volume (Å ³)
$AlFeO_3$	4.9806 (3)	8.5511 (6)	9.2403 (6)	393
$Al_{0.7}Ga_{0.3}FeO_3$	5.0049 (3)	8.5998 (5)	9.2848 (5)	400
$Al_{0.3}Ga_{0.7}FeO_3$	5.0443 (1)	8.6728 (3)	9.3395 (3)	409
$Al_{0.1}Ga_{0.9}FeO_3$	5.0688 (2)	8.7165 (3)	9.3705 (3)	414
$GaFeO_3$	5.0814 (2)	8.7436 (3)	9.3910 (2)	417

In Figures 2.3 (a) and (b) we have plotted the unit cell parameters and volume with the Ga content which show that there is a linear increase in the structural parameters with increasing concentration of Ga. This behavior is associated with the larger ionic radii of Ga^{3+} as compared to Al^{3+} .

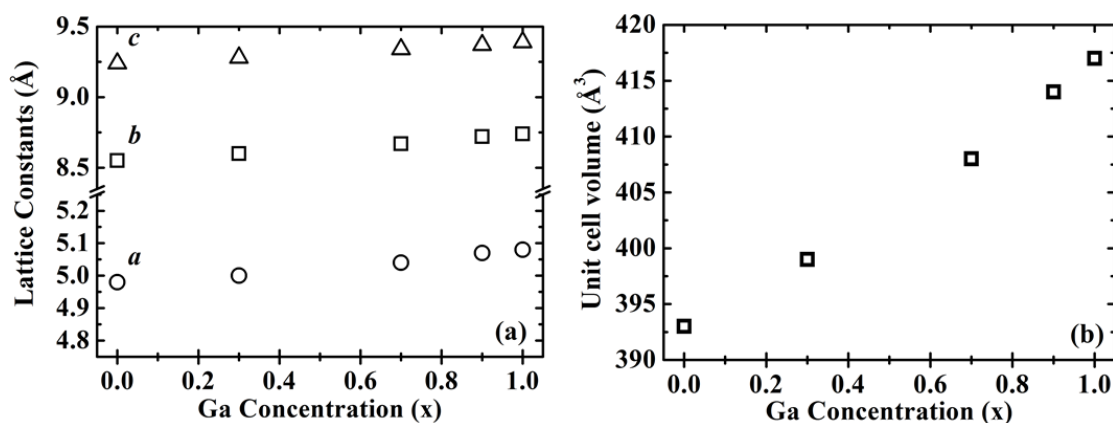


Figure 2.3: Variation of (a) lattice constants and (b) unit cell volume in $\text{Al}_{1-x}\text{Ga}_x\text{FeO}_3$ as a function of Ga content at 298 K.

2.4.1.1.2 Neutron diffraction of AlFeO_3

A detailed neutron diffraction study was carried out on AlFeO_3 . Figure 2.4 shows the Rietveld refined neutron diffraction patterns for AlFeO_3 at 298, 250, 150, 50 and 5 K. The Rietveld analysis of the neutron diffraction pattern at 298 K confirms the single phase formation of the compound with the orthorhombic crystal structure ($Pna2_1$). The temperature dependent neutron diffraction data indicates that there is no structural phase transition down to lowest temperature. At 298 K, the observed diffraction pattern could be fitted with only nuclear intensities confirming the paramagnetic nature of the sample. Distinct, coherent nuclear scattering lengths of 0.9450×10^{-12} , 0.3449×10^{-12} , and 0.5803×10^{-12} cm for Al, Fe, and O, respectively, allows precise determination of oxygen coordinates of the sample. We show the refined lattice parameters and other structural parameters in Table 2.2. The values of the lattice parameters are in good agreement with the earlier reported values for the same compound [18]. Under the space group $Pna2_1$, all atoms (both anions and cations) are in general position, and thus we vary the fractional atomic coordinates during the refinement except for the z coordinate of the Al1 site. Here, the z value of the Al1 site was kept fixed at zero to define the origin of the unit cell. We have varied the isotropic thermal parameters, and the occupancy factors of all cations during the refinement. The occupancy factors of the oxygen atoms were kept fixed at 1.0 (fully occupied). In Tables 2.3 and 2.4 we summarize the refined values of the bond angles and bond distances obtained from the refinement of room temperature neutron data.

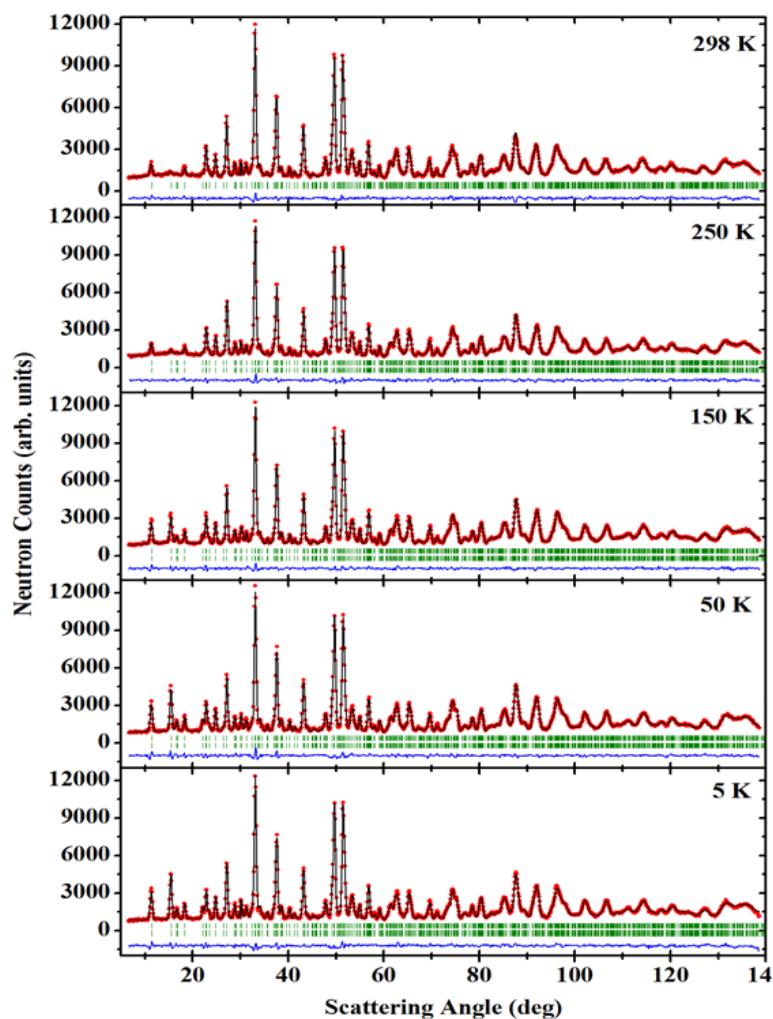


Figure 2.4: Observed (red solid circles) and calculated (solid lines) neutron diffraction patterns of AlFeO_3 at 298, 250, 150, 50, and 5 K. Solid line at the bottom in each panel shows the difference between observed and calculated patterns. Vertical lines show the position of Bragg peaks.

Table 2.2: Atomic coordinates of AlFeO_3 at 298 K

Space Group: $Pna2_1$ (Orthorhombic), $a = 4.9806$ (3) Å, $b = 8.5511$ (6) Å, and $c = 9.2403$ (6) Å					
Atoms	x	y	z	B_{iso}	Occ.
Fe1/Al	0.1876 (6)	0.1502 (4)	0.5827 (9)	0.20 (2)	0.83 (2) / 0.17 (2)
Fe2/Al	0.6646 (3)	0.0320 (3)	0.7998 (9)	0.38 (3)	0.81 (1) / 0.19 (1)
Al1/Fe	0.1686 (2)	0.1545 (3)	0	0.56 (2)	0.85 (1) / 0.14 (1)
Al2/Fe	0.8164 (7)	0.1613 (3)	0.3098 (4)	0.56 (4)	0.74 (2) / 0.26 (2)
O1	0.8164 (7)	0.1613 (3)	0.3098 (4)	0.53 (5)	1.0
O2	0.9824 (5)	0.3218 (9)	0.4201 (2)	0.53 (3)	1.0
O3	0.5073 (2)	0.4905 (7)	0.4331 (5)	0.80 (2)	1.0
O4	0.6620 (9)	0.0047 (9)	0.2040 (8)	0.50 (1)	1.0
O5	0.1418 (5)	0.1630 (7)	0.1984 (6)	0.66 (2)	1.0
O6	0.8372 (5)	0.1652 (6)	0.6767 (1)	0.50 (3)	1.0

$$R_p = 5.49\%, R_{\text{wp}} = 6.42\%, R_{\text{exp}} = 4.40\%, R_{\text{Bragg}} = 2.04\%, \chi^2 = 2.13\%$$

Table 2.3: Bond lengths and bond angles for the AlFeO₃ sample at 298 K

Site	Bond Length		Bond Angles	
Fe1	Fe1-O1 ₁ *	2.337 (11)	O1 ₂ -Fe1-O3	174.4 (8)
	Fe1-O1 ₂ *	2.115 (12)	O1 ₁ -Fe1-O5 ₂	158.2 (8)
	Fe1-O2	2.041 (14)	O2-Fe1-O5 ₁	161.3 (10)
	Fe1-O3	1.890 (11)		
	Fe1-O5 ₁	1.954 (11)		
	Fe1-O5 ₂	1.950 (11)		
Fe2	Fe2-O1	2.236 (10)	O1-Fe2-O5	165.0 (8)
	Fe2-O2	2.076 (14)	O2-Fe2-O3	158.8 (10)
	Fe2-O3	1.879 (11)	O4-Fe2-O6	163.8 (9)
	Fe2-O4	2.142 (11)		
	Fe2-O5	1.824 (11)		
	Fe2-O6	1.960 (13)		
Al1	Al1-O2	1.767 (15)	O2-Al1-O4	110.1 (10)
	Al1-O4	1.840 (10)	O2-Al1-O6 ₁	115.7 (10)
	Al1-O6 ₁	1.743 (14)	O2-Al1-O6 ₂	108.3 (9)
	Al1-O6 ₂	1.780 (14)	O4-Al1-O6 ₁	112.0 (10)
			O4-Al1-O6 ₂	103.7 (9)
			O6 ₁ -Al1-O6 ₂	106.0 (10)
Al2	Al2-O1 ₁	1.900 (14)	O1 ₁ -Al2-O3	179.0 (10)
	Al2-O1 ₂	1.956 (14)	O1 ₂ -Al2-O4 ₁	175.3 (9)
	Al2-O2	1.972 (16)	O2-Al2-O4 ₂	173.0 (10)
	Al2-O3	1.827 (14)		
	Al2-O4 ₁	1.920 (13)		
	Al2-O4 ₂	2.018 (14)		

* The equivalent oxygen atoms in a given polyhedra are labeled by suffix 1 and 2.

Table 2.4: Cation-oxygen-cation bond angles for different sites and the corresponding cation-cation distances for the AlFeO_3 at 298 K

Bond Angles		Cation-Cation Distance	
Fe1-O1 ₂ -Fe2	165.5 (6)	Fe1-Fe2	4.539 (6)
Fe1-O1 ₁ -Al2	162.3 (9)	Fe1-Al2	4.018 (8)
Fe1-O2-Al1	116.7 (9)	Fe1-Al1	3.246 (12)
Fe2-O2-Al1	117.6 (8)	Fe2-Al1	3.291 (11)
Al1-O2-Al2	119.0 (10)	Al1-Al2	3.224 (15)
Fe1-O3-Fe2	120.3 (7)	Fe1-Fe2	3.269 (10)
Fe1-O3-Al2	131.6 (9)	Fe1-Al2	3.390 (12)
Al1-O4-Al2	126.6 (8)	Al1-Al2	3.359 (12)
Al1-O4-Al2	120.4 (8)	Al1-Al2	3.348 (12)
Fe1-O5-Fe2	131.1 (7)	Fe1-Fe2	3.439 (10)
Fe1-O5-Fe2	127.1 (7)	Fe1-Fe2	3.379 (9)
Fe2-O6-Al1	123.2 (8)	Fe2-Al1	3.258 (11)
Fe2-O6-Al1	121.0 (9)	Fe2-Al1	3.256 (12)

Based on the Rietveld analysis of neutron diffraction data, we arrive at the crystal structure as shown in Figure 2.5. The crystal structure of these compounds is made up of alternate layers of cations and oxygen ions stacked along the crystallographic c direction. There are four different cation sites (Fe/Al), labeled as Fe1, Fe2, Al1 and Al2 occupying the Wyckoff position $4a$. Fe ions predominantly occupy the Fe1 and Fe2 sites whereas, Al ions mainly present at the Al1 and Al2 sites. Fe1, Fe2, and Al2 ions are present in octahedral surroundings while Al1 site is in a tetrahedral environment [Figure 2.5]. The octahedra share the edges, whereas the tetrahedron shares oxygen ions at the corners. No edge sharing occurs between the octahedra and tetrahedra. There are eight formula units (40 atoms) per unit cell, in agreement with the earlier reports. From the derived values of bond lengths and bond angles, given in Tables 2.3 and 2.4, a distortion in $(\text{Fe/Al})\text{O}_6$ octahedra, as well as Al1O_4 tetrahedra, is evident. The observed distortion in the polyhedra is due to the significant difference between ionic

radii of Fe^{3+} (0.645 Å for coordination number VI) and Al^{3+} (0.535 Å for coordination number VI) along with the site disorder caused by Fe and Al mixed occupation [6].

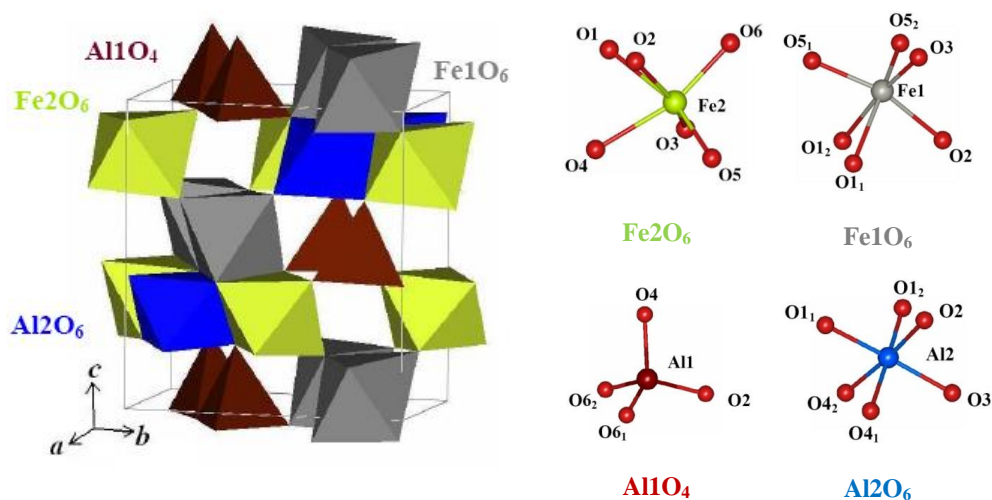


Figure 2.5: The crystal structure (unit cell) of the AlFeO_3 . A schematic view of the $(\text{Fe}/\text{Al})\text{O}_6$ octahedra and Al1O_4 tetrahedra embedded in the unit cell. The right part of the unit cell shows the orientation of Fe1, Fe2, Al1, Al2 polyhedra.

Magnetic structure of AlFeO_3 has been identified based on the indexing of the magnetic Bragg peaks in the low angle neutron diffraction pattern [Figure 2.4]. The determination of magnetic structure was accomplished following the representation analysis technique of group theory described by Bertaut [19,20]. FULLPROF suite package [17] has been used to obtain the basis vectors associated with each possible magnetic model. We have summarized the irreducible representations and the basis vectors in Table 2.5.

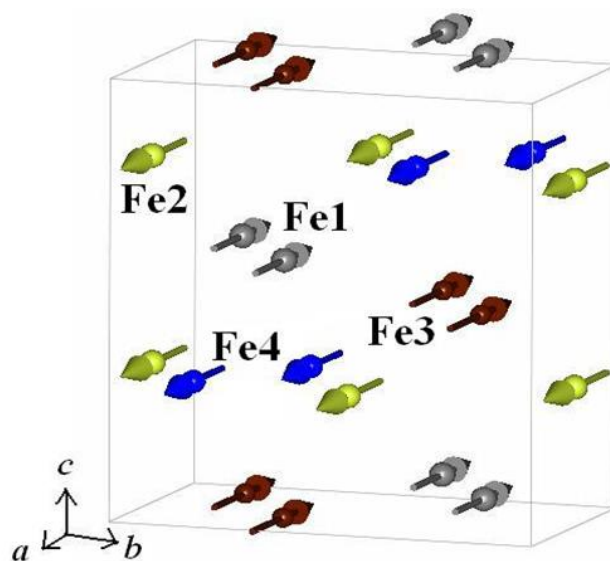


Figure 2.6: The magnetic structure (unit cell) of AlFeO_3 .

Table 2.5: Basis vectors for $\vec{k} = (000)$ and position $4a$ for representation $\Gamma_1, \Gamma_2, \Gamma_3,$ and Γ_4 for AlFeO_3

IR		Basis vectors			
		(x, y, z)	$(-x, -y, z+1/2)$	$(x+1/2, -y+1/2, z)$	$(-x+1/2, y+1/2, z+1/2)$
Γ_1	Ψ_1	(1 0 0)	(-1 0 0)	(-1 0 0)	(1 0 0)
	Ψ_2	(0 1 0)	(0 -1 0)	(0 1 0)	(0 -1 0)
	Ψ_3	(0 0 1)	(0 0 1)	(0 0 -1)	(0 0 -1)
Γ_2	Ψ_1	(1 0 0)	(-1 0 0)	(1 0 0)	(-1 0 0)
	Ψ_2	(0 1 0)	(0 -1 0)	(0 -1 0)	(0 1 0)
	Ψ_3	(0 0 1)	(0 0 1)	(0 0 1)	(0 0 1)
Γ_3	Ψ_1	(1 0 0)	(1 0 0)	(-1 0 0)	(-1 0 0)
	Ψ_2	(0 1 0)	(0 1 0)	(0 1 0)	(0 1 0)
	Ψ_3	(0 0 1)	(0 0 -1)	(0 0 -1)	(0 0 1)
Γ_4	Ψ_1	(1 0 0)	(1 0 0)	(1 0 0)	(1 0 0)
	Ψ_2	(0 1 0)	(0 1 0)	(0 -1 0)	(0 -1 0)
	Ψ_3	(0 0 1)	(0 0 -1)	(0 0 1)	(0 0 -1)

A propagation vector, $\vec{k} = (0\ 0\ 0)$, accounts the magnetic reflections. The magnetic reducible representation Γ for the $4a$ site can be decomposed as a direct sum of irreducible representations as, $\Gamma_{\text{mag}} = 3\ \Gamma_1 + 3\ \Gamma_2 + 3\ \Gamma_3 + 3\ \Gamma_4$. The refinement of the magnetic structure by considering the representation Γ_3 (among all four representations) gives the best fit to the observed diffraction patterns at $T \leq 250$ K, i.e., below the magnetic ordering temperature. We show the fitted data in Figure 2.4, and the corresponding magnetic structure in Figure 2.6. We describe the magnetic structure as the collinear ferrimagnetic spin configurations with the ordered magnetic moment aligned along the crystallographic a direction.

The site occupancies were found not to vary with lowering of temperature. Therefore, the values of the site occupancies as derived from the analysis of the diffraction pattern at 298 K (paramagnetic state) were used for the magnetic structure refinement. The averaged ordered magnetic moments are found to be 3.88 (15), 3.64 (14), 3.01 (75), and 2.79 (43) μ_B/Fe ion at Fe1, Fe2, Fe3 (Al1), and Fe4 (Al2) sites respectively. Here, the moments at Fe1 and Fe3 sites are parallel to each other and

aligned antiparallel to the parallelly aligned moments at Fe2 and Fe4 sites. The magnetic moments are calculated from the Fourier coefficients using the general formula, $m_{lj} = \sum_k S_{kj} \exp(-2\pi i k R_l)$, as discussed in chapter 1 (section 1.8.4).

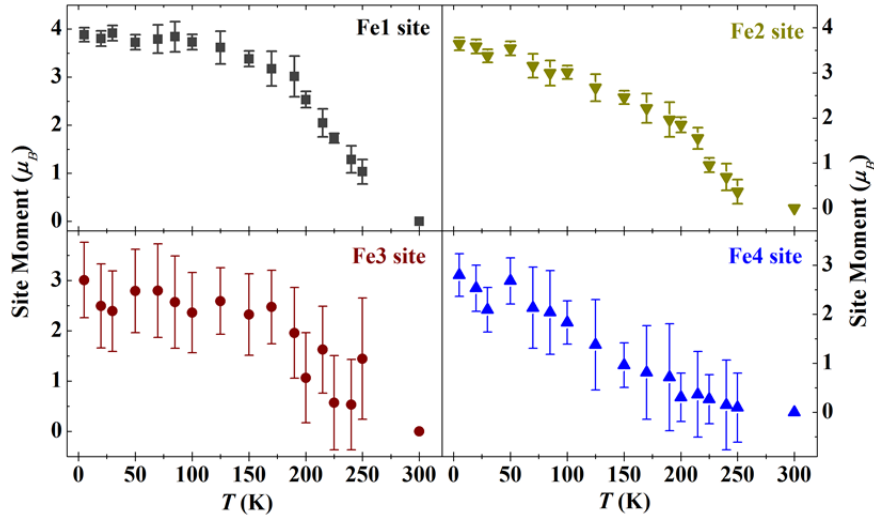


Figure 2.7: The temperature dependence of the ordered site moments per Fe ion at Fe1, Fe2, Fe3 and Fe4 sites in AlFeO_3 .

In Figure 2.7, the temperature dependence of the ordered moments for all four cation sites is shown. The moments of the Fe1, Fe2, and Fe3 sites show almost a normal Brillouin function like temperature dependence, whereas we observe a clear deviation from a normal Brillouin function temperature dependence for the ordered moment of the Fe4 site. The magnetic ordering temperature for all four sites is found to be ~ 270 K (T_N).

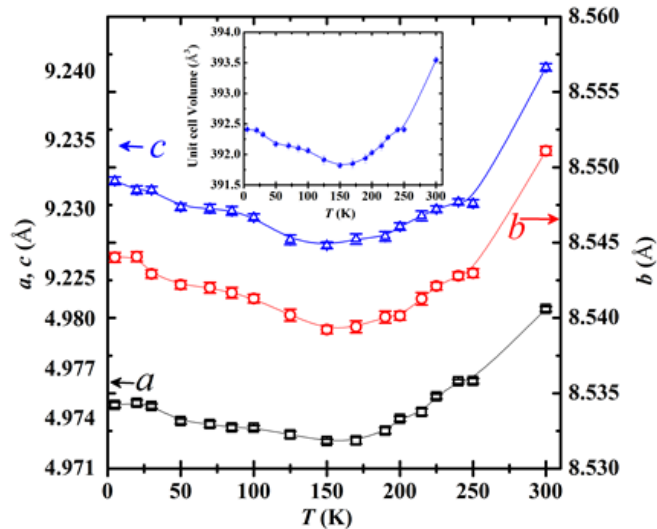


Figure 2.8: The temperature dependence of lattice parameters of AlFeO_3 . The inset shows the temperature dependence of the unit cell volume.

Temperature dependence of the lattice parameters (subsequently, the unit cell volume), depicted in Figure 2.8, shows a unique nature with a dip at $T \sim 150$ K. The expansion of the lattice at lower temperatures is a very uncommon and an interesting phenomenon of negative thermal expansion. In the present compound, the magnetic ordering occurs due to the cation-oxygen-cation superexchange antiferromagnetic interactions where the strength of the interaction strongly depends on the bond angles and bond lengths. The exchange interaction is strongest for the 180° cation-oxygen-cation bond angle and weakens with the deviation of the bond angle from 180° . In Table 2.4 we have shown the $A-O-A'$ ($A, A' = \text{Fe}/\text{Al}$) bond angles which are greater than 115 degrees, as well as the corresponding cation-cation distances. The most important pathways for the antiferromagnetic superexchange interactions are $\text{Fe1}-[O1/O3/O5]-\text{Fe2}$ and $\text{Fe1}-[O1/O3]-\text{Al2}$ (Fe ions have occupied 26 at. % of the Al2 site). In all other cases, the Al1 site is involved which is less populated by Fe ions (~ 14 at. %).

In Figure 2.9 we show the temperature dependence of Fe1-O5-Fe2 bond angles (a representative case) and corresponding Fe1-Fe2 distances. Interestingly, the $\text{Fe1-O5}_1\text{-Fe2}$ bond angle starts to decrease below ~ 150 K, where the unit cell volume expands [inset of Figure 2.8], whereas the $\text{Fe1-O5}_2\text{-Fe2}$ bond angle starts increasing below this temperature. Besides, an anomaly in the Fe1-Fe2 distances around the same temperature has been found.

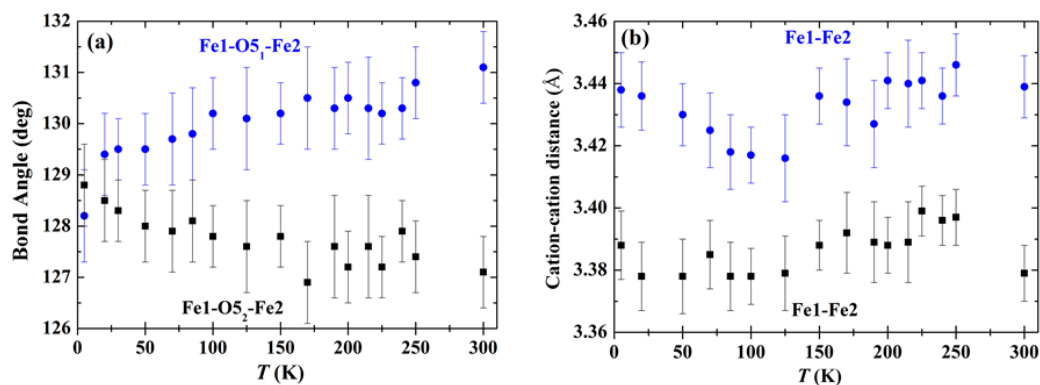


Figure 2.9: (a) The temperature dependence of Fe1-O5-Fe2 bond angles of AlFeO_3 and (b) Corresponding Fe1-Fe2 distances as a function of the temperature of AlFeO_3 .

We have also quantified the distortion in the polyhedra in the following way. The distortion parameter (Δ) of a coordination polyhedron AO_N ($A: \text{Fe1}, \text{Fe2}, \text{Al1}, \text{and Al2}$) with an average value of the $A-O$ bond length, \bar{d} , is defined in Eq. 2.1 as:

$$\Delta = \frac{1}{N} \sum_1^N \{(d_N - \bar{d})/\bar{d}\}^2 \quad (2.1)$$

The temperature dependent values of Δ for all three octahedral and Al tetrahedral sites shown in Figure 2.10 indicate that the AlO_4 tetrahedra are almost regular in nature while Fe1 and Fe2 ions are present in the distorted octahedral environment. Although the octahedral (Al_2O_6) site, relatively less distorted; however, the temperature dependence of Δ shows a peak around 150 K, and we correlate this behavior with the observed temperature dependence of unit cell volume which is a mirror image of the Δ versus T curve [Figure 2.8].

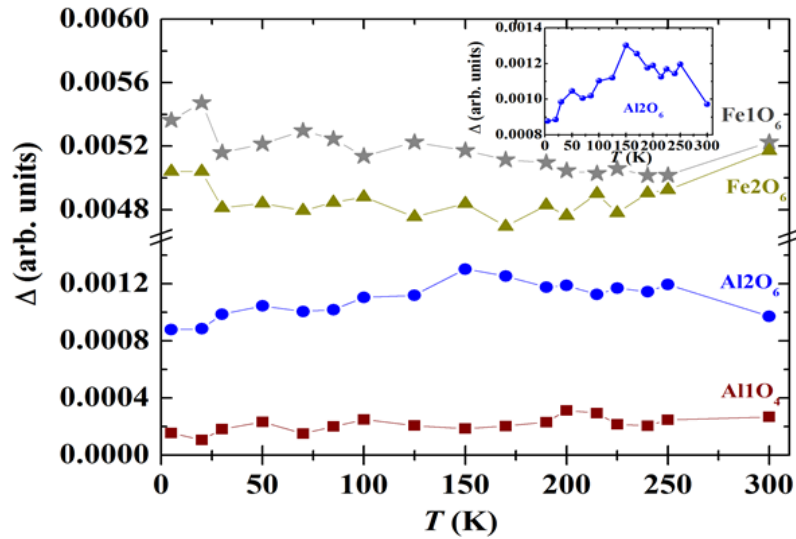


Figure 2.10: The distortion parameter (Δ) as a function of temperature for Fe/Al polyhedral in AlFeO_3 . An enlarged view of the temperature dependence of Δ for Al_2O_6 octahedra is shown in inset.

2.4.1.1.3 Neutron diffraction of GaFeO_3

Neutron diffraction experiment followed by Rietveld refined pattern at 298 K reveals that GaFeO_3 also crystallizes in the non-centrosymmetric space group $Pna2_1$. In Figure 2.11 neutron diffraction patterns of GaFeO_3 at 298 and 5 K are shown indicating that down to the lowest temperature there is no structural transition. Similar to AlFeO_3 in the case of GaFeO_3 , at lower temperatures, an increase in the intensity of the nuclear Bragg peaks at lower scattering angles suggest a ferromagnetic or ferrimagnetic ordering [Figures 2.4 and 2.11]. We show the Rietveld refined lattice parameters and other structural parameters in Tables 2.6 (298 K) and 2.7 (5 K). In the Rietveld refinement, the coherent nuclear scattering lengths of 0.9450×10^{-12} , 0.7288×10^{-12} , and

0.5803×10^{-12} cm for Fe, Ga, and O, respectively, allow accurate determination of atomic coordinates. The site occupancies were found not to vary with lowering of temperature. Therefore, the values of the site occupancies as derived from the analysis of the diffraction pattern at 298 K (paramagnetic state) were used for the magnetic structure refinement.

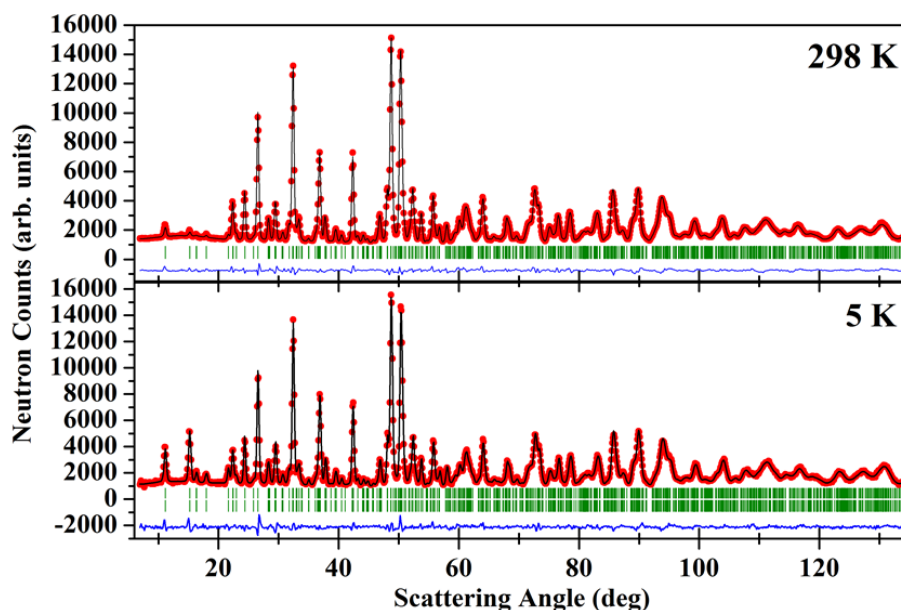


Figure 2.11: Observed (solid red circles) and calculated (solid lines) neutron diffraction patterns of the GaFeO_3 at 298 and 5 K. Solid line at the bottom of each panel shows the difference between observed and calculated patterns. Vertical lines indicate the position of Bragg peaks.

Table 2.6: Atomic coordinates of GaFeO_3 at 298 K

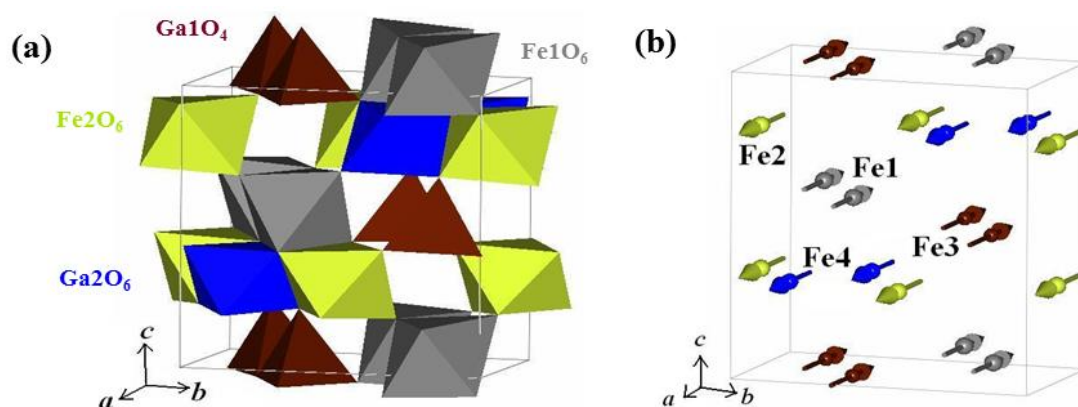
Space Group: $Pna2_1$ (Orthorhombic), $a = 5.0814$ (2) Å, $b = 8.7436$ (3) Å, and $c = 9.3910$ (2) Å					
Atoms	x	y	z	B_{iso}	Occ.
Fe1/Ga	0.1895 (5)	0.1531 (5)	0.5842 (4)	0.21 (3)	0.65 (2) / 0.35 (2)
Fe2/Ga	0.6705 (9)	0.0327 (4)	0.7995 (6)	0.64 (2)	0.70 (1) / 0.30 (1)
Ga1/Fe	0.1755 (2)	0.1491 (5)	0	0.36 (4)	0.91 (3) / 0.09 (3)
Ga2/Fe	0.8053 (8)	0.1575 (7)	0.3073 (6)	0.40 (1)	0.46 (1) / 0.54 (1)
O1	0.9771 (9)	0.3269 (7)	0.4230 (6)	0.87 (5)	1.0
O2	0.5171 (4)	0.4921 (9)	0.4403 (5)	0.84 (3)	1.0
O3	0.6538 (9)	-0.0009 (8)	0.2005 (9)	0.60 (4)	1.0
O4	0.1492 (8)	0.1605 (8)	0.1957 (5)	0.68 (5)	1.0
O5	0.8401 (7)	0.1744 (7)	0.6688 (7)	0.58 (3)	1.0
O6	0.5093 (3)	0.1676 (10)	0.9405 (8)	0.65 (4)	1.0

$R_p = 4.93\%$, $R_{wp} = 5.76\%$, $R_{exp} = 3.80\%$, $R_{Bragg} = 2.74\%$, $\chi^2 = 2.3\%$

Table 2.7: Atomic coordinates of GaFeO₃ at 5 K

Space Group: $Pna2_1$ (Orthorhombic), $a = 5.0814(2) \text{ \AA}$, $b = 8.7436(3) \text{ \AA}$, and $c = 9.391(2) \text{ \AA}$					
Atoms	x	y	z	B_{iso}	Occ.
Fe1/Ga	0.1931 (2)	0.1537 (6)	0.5850 (5)	0.05 (3)	0.65 (2) / 0.35 (2)
Fe2/Ga	0.6741 (1)	0.0308 (5)	0.7987 (8)	0.48 (1)	0.70 (1) / 0.30 (1)
Ga1/Fe	0.1821 (8)	0.1479 (8)	0	0.10 (2)	0.91 (3) / 0.09 (3)
Ga2/Fe	0.8138 (3)	0.1586 (6)	0.3084 (7)	0.14 (4)	0.46 (1) / 0.54 (1)
O1	0.9764 (2)	0.3266 (5)	0.4256 (9)	0.61 (5)	1.0
O2	0.5187 (9)	0.4906 (6)	0.4376 (4)	0.59 (2)	1.0
O3	0.6508 (8)	0.0007 (6)	0.2025 (1)	0.45 (3)	1.0
O4	0.1550 (9)	0.1630 (1)	0.1976 (3)	0.42 (4)	1.0
O5	0.8448 (8)	0.1716 (1)	0.6719 (4)	0.31 (2)	1.0
O6	0.5113 (2)	0.1655 (3)	0.9412 (2)	0.49 (3)	1.0
μ_{Fe1}	-4.41 (25)			χ^2 %	3.57
μ_{Fe2}	3.45 (22)			R_p %	5.61
μ_{Fe3}	-2.81 (77)			R_{wp} %	6.67
μ_{Fe4}	2.99 (52)			R_{exp} %	3.53
				R_{Bragg} %	2.5
				R_{Mag} %	6.92

GaFeO₃ has a crystal structure similar to that of AlFeO₃ with a non-centrosymmetric space group. In GaFeO₃, there are four different cation sites Fe1, Fe2, Ga1 and Ga2, of which Fe1, Fe2, and Ga2 have an octahedral oxygen environment. The cation in the Ga1 site is in the tetrahedral oxygen environment. The crystal structure of this compound is made up of alternative layers of cations and oxygen ions along the crystallographic c direction. The octahedra share edges between themselves, whereas the tetrahedron shares oxygen ions at the corners. No edge sharing occurs between the octahedra and tetrahedra. There are eight formula units (40 atoms) per unit cell, and the crystal structure remains same down to 5 K.

**Figure 2.12:** (a) Crystal and (b) magnetic structure (unit cell) of GaFeO₃.

The magnetic unit cell dimension of GaFeO_3 is the same as the nuclear one [Figures 2.12 (a) and (b)]. The magnetic structure is collinear ferrimagnetic with the ordered magnetic moment aligned along the crystallographic a direction. The Néel sublattices are $A = \text{Fe1} + \text{Ga1}$ and $B = \text{Fe2} + \text{Ga2}$. Here, the moments at Fe1 and Fe3 (Ga1) sites are parallel to each other and aligned antiparallel to the moments at Fe2 and Fe4 (Ga2) sites which are aligned parallel among themselves. In Figure 2.13 the temperature dependence of the ordered site moments for all four cation sites is shown indicating a T_N around 220 K.

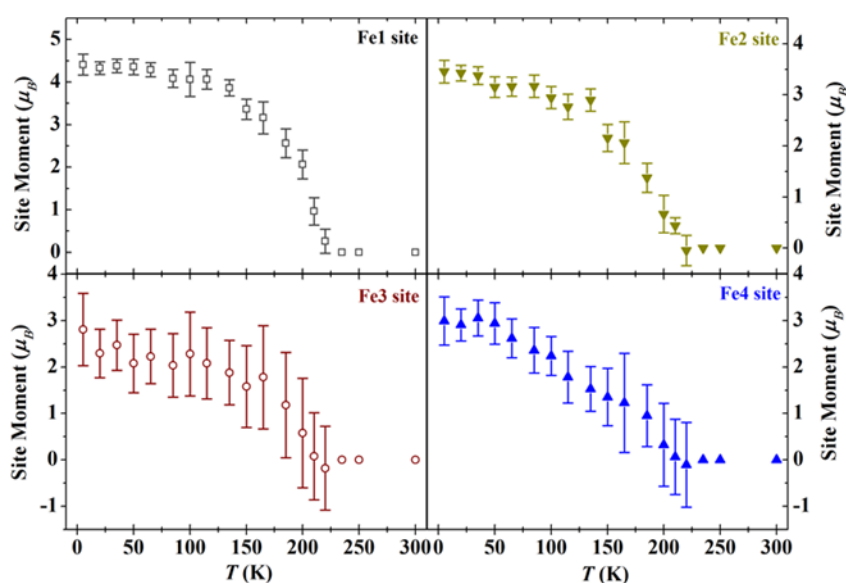


Figure 2.13: The temperature dependence of the ordered moments per Fe ion at Fe1, Fe2, Fe3, and Fe4 sites in GaFeO_3 .

Temperature dependence of the lattice parameters (subsequently, the unit cell volume), depicted in Figure 2.14, shows a unique nature with a dip at $T \sim 150$ K similar to that found in AlFeO_3 . In both AlFeO_3 and GaFeO_3 the increase in the parameters becoming even more marked in the 200-250 K range. It is noteworthy that the T_N values of $\text{Al}_{1-x}\text{Ga}_x\text{FeO}_3$ are in the 200-250 K range as will be seen later. In Figure 2.15 we show the temperature dependent values of Δ for all three octahedral and Ga1 tetrahedral sites. Strongly distorted nature of the octahedral environment of both Fe1 and Fe2 sites and relatively less distorted octahedral site (Ga2O_6) is evident from Tables 2.8 and 2.9. The temperature dependence of Δ was found to be negligible for the Ga1O_4 tetrahedron. Moreover, it was found that (Fe/Ga) polyhedra are more distorted in comparison with (Fe/Al) polyhedra, which could be due to a larger amount of site disorder associated with relatively better size matching between Fe^{+3} and Ga^{+3} .

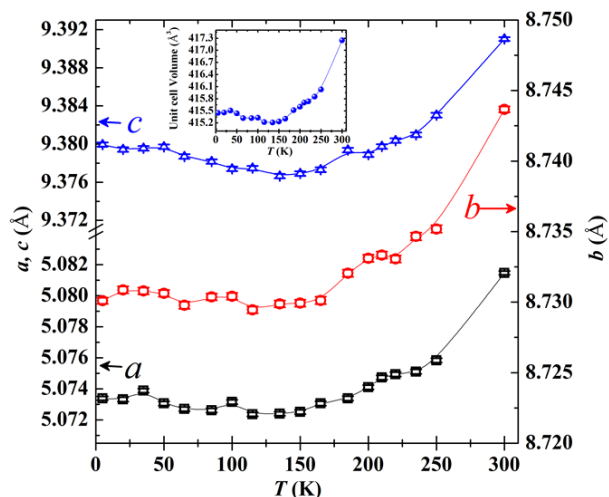


Figure 2.14: The temperature dependence of lattice parameters of GaFeO_3 . The inset shows the variation of unit cell volume as a function of temperature.

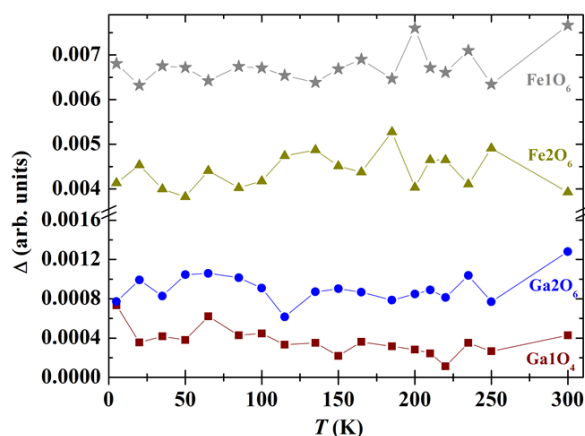
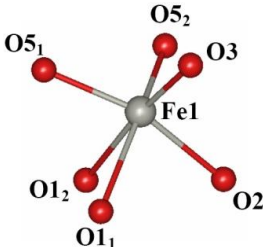
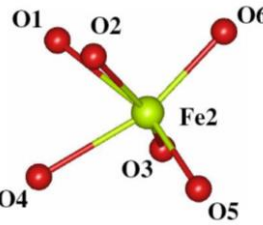
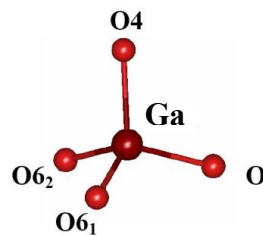
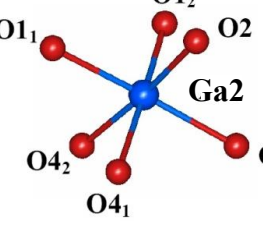


Figure 2.15: The distortion parameter (Δ) as a function of temperature for Fe/Ga polyhedral in GaFeO_3 .

Table 2.8: Cation-oxygen-cation bond angles for different sites and the corresponding cation-cation distances for GaFeO_3 sample

Bond Angles		Cation-Cation Distance	
Fe1-O1 ₂ -Fe2	166.7 (5)	Fe1-Fe2	4.637 (7)
Fe1-O1 ₁ -Ga2	164.5 (6)	Fe1-Ga2	4.068 (7)
Fe1-O2-Ga1	120.5 (5)	Fe1-Ga1	3.325 (7)
Fe2-O2-Ga1	119.0 (5)	Fe2-Ga1	3.342 (7)
Ga1-O2-Ga2	112.7 (5)	Ga1-Ga2	3.237 (6)
Fe1-O3-Fe2	122.6 (6)	Fe1-Fe2	3.342 (7)
Fe1-O3-Ga2	130.9 (5)	Fe1-Ga2	3.432 (7)
Ga1-O4-Ga2	121.3 (4)	Ga1-Ga2	3.409 (6)
Ga1-O4-Ga2	125.0 (4)	Ga1-Ga2	3.446 (6)
Fe1-O5-Fe2	126.8 (5)	Fe1-Fe2	3.486 (7)
Fe1-O5-Fe2	127.0 (5)	Fe1-Fe2	3.412 (7)
Fe2-O6-Ga1	123.6 (6)	Fe2-Ga1	3.303 (7)
Fe2-O6-Ga1	121.6 (5)	Fe2-Ga1	3.359 (6)

Table 2.9: Bond lengths & Bond Angles of GaFeO₃ ($T = 298$ K)

Site	Bond Length		Bond Angles	
Fe1 	Fe1-O1 ₁	2.401 (9)	O1 ₂ -Fe1-O3	174.7 (7)
	Fe1-O1 ₂	2.112 (9)	O1 ₁ -Fe1-O5 ₂	155.9 (7)
	Fe1-O2	2.051 (10)	O2-Fe1-O5 ₁	162.8 (7)
	Fe1-O3	1.897 (9)		
	Fe1-O5 ₁	1.954 (10)		
	Fe1-O5 ₂	1.868 (9)		
	Fe2 	Fe2-O1	2.268 (9)	O1-Fe2-O5
Fe2-O2		2.097 (10)	O2-Fe2-O3	159.2 (8)
Fe2-O3		1.913 (9)	O4-Fe2-O6	163.4 (7)
Fe2-O4		2.155 (9)		
Fe2-O5		1.945 (9)		
Fe2-O6		1.954 (10)		
Ga1 		Ga1-O2	1.776 (9)	O2-Ga1-O4
	Ga1-O4	1.845 (6)	O2-Ga1-O6 ₁	119.5 (8)
	Ga1-O6 ₁	1.793 (11)	O2-Ga1-O6 ₂	108.3 (7)
	Ga1-O6 ₂	1.894 (10)	O4-Ga1-O6 ₁	111.9 (7)
			O4-Ga1-O6 ₂	102.5 (6)
			O6 ₁ -Ga1-O6 ₂	104.7 (8)
	Ga2 	Ga2-O1 ₁	2.034 (9)	O1 ₁ -Ga2-O3
Ga2-O1 ₂		1.994 (10)	O1 ₂ -Ga2-O4 ₁	175.0 (7)
Ga2-O2		2.106 (10)	O2-Ga2-O4 ₂	167.8 (7)
Ga2-O3		1.876 (9)		
Ga2-O4 ₁		2.039 (9)		
Ga2-O4 ₂		2.064 (9)		

2.4.1.1.4 Raman spectroscopy of AlFeO₃

Temperature dependent Raman study of AlFeO₃ was carried out by Sood *et. al.* [9] to shed light on the vibrational properties which bear signatures of structure and magnetic order, central to the magnetoelectric interaction. AlFeO₃ crystallizing in the

orthorhombic $Pna2_1$ space group containing eight formula units i.e. 40 atoms in a unit cell, giving rise to 120 normal modes, namely $\Gamma_{\text{Fe}} = 6A_1 + 6A_2 + 6B_1 + 6B_2$, $\Gamma_{\text{Al}} = 6A_1 + 6A_2 + 6B_1 + 6B_2$; $\Gamma_{\text{O}} = 18A_1 + 18A_2 + 18B_1 + 18B_2$ [21]. Since the inversion symmetry is lacking, Raman modes are also infrared active. Of the 117 Raman modes, A_1 , B_1 , and B_2 are acoustic modes. Figure 2.16 shows the Raman spectrum at 5 K, revealing 18 modes labeled as S1 to S18 in the range of 100-2200 cm^{-1} . Table 2.10 lists the experimental (at 5 K) and the calculated frequencies for disordered ferrimagnetic state close to the experimental values.

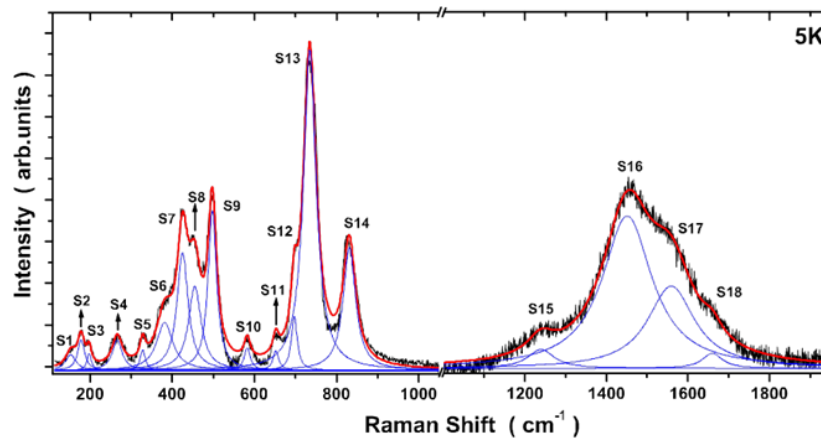


Figure 2.16: Unpolarized Raman spectra of AlFeO_3 at 5 K. Solid (thin) lines are a fit of individual modes with a sum of Lorentzian functions, and the thick solid line shows the total fit to the experimental data.

Table 2.10: List of the experimentally observed frequencies at 5 K and calculated frequencies in AlFeO_3 for the disordered ferrimagnetic ($\text{Fe}_2\text{-Al}_2$ anti-site disorder) state.

Mode Assignment	Experimental ω (cm^{-1})	Calculated ω (cm^{-1})
S1	156	154
S2	178	179
S3	198	197
S4	268	270
S5	328	331
S6	380	379
S7	425	425
S8	453	453
S9	498	499
S10	587	581
S11	650	654
S12	698	691
S13	738	733
S14	826	807
S15 (Two-magnon)	1240	
S16 (Overtone)	1450	
S17 (Second order)	1560	
S18 (Overtone)	1660	

First principles density functional calculations suggest that the first-order Raman phonons occur below $\sim 810 \text{ cm}^{-1}$. Since the intensity of S15 mode is zero above Néel temperature, it is attributed to the two-magnon Raman scattering. We attribute the modes S16 to S18 to second-order Raman scattering coupled with magnetic degrees of freedom. Figure 2.17 shows the temperature-dependent mode frequencies of some of the prominent first-order phonon modes S4, S7 to S10, S13, and S14. We summarize the following observations: (1) The frequencies of S4, S7, S8, S9, S10 and S13 modes show a sharp change at T_N . The temperature derivative of S4 and S10 mode frequencies ($\partial\omega/\partial T$) change sign at T_N . (2) The frequency of mode S13 shows a jump by $\sim 4 \text{ cm}^{-1}$ near T_N . (3) The slope of ω with respect to temperature for the S4, S8, S9, S10 and S14 modes show changes near 100 K. In this context it is important to mention that temperature dependent unit cell volume of AlFeO_3 obtained from neutron diffraction experiment exhibits a broad minima in the 100 K range [see Figure 2.8] where slope change in few first order phonon modes have been observed.

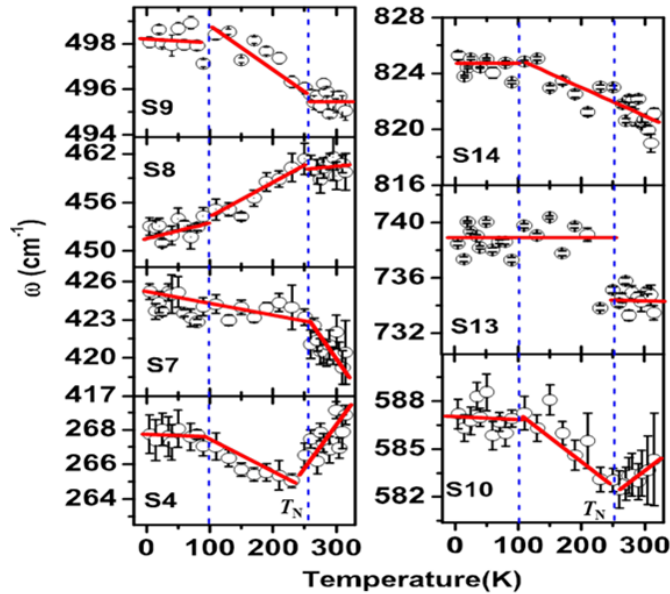


Figure 2.17: Temperature dependence of the first-order phonon modes S4, S7, S8, S9, S10, S13, and S14. The linear fits shown in solid lines (red) are indicative of sharp changes in the three temperature regions.

The solid lines in panels are linear fits in three regions i.e. 300 to 250 K, 250 to 100 K and 100 to 5 K. The temperature dependence of the mode S8 is anomalous below T_N , i.e., frequency decreases on lowering the temperature. The anomalous hardening of the S8 mode with increasing temperature is attributed to the strong spin-phonon coupling at the second order (J_2). First-principles analysis points out that the anomaly

in S8 mode is primarily influenced by Fe₂-Al₂ disorder, while S4 mode is additionally influenced by Fe₁-Al₂ disorder [9]. The anomalies in the temperature dependence of the phonon modes S4, S7, S8, S9 and S10 near T_N are similar to those in $RMnO_3$ ($R = Pr, Nd, Sm, Tb, Dy, La$) [22] and $GaFeO_3$ [21]. The sharp change in the frequency of S13 mode at T_N can arise from subtle local structural change. Following manganites and theoretical calculations, the sharp changes in mode frequencies of S4, S7, S8, S9, and S10 indicates the strong spin-phonon coupling in the magnetic phase below T_N leading to strong first-order phonon renormalization.

2.4.1.2 Magnetic properties

2.4.1.2.1 DC magnetization

$AlFeO_3$ is ferrimagnetic with a T_N of 250 K while $GaFeO_3$ exhibits a ferrimagnetic T_N of 210 K as evident from Figure 2.18. We observe magnetic hysteresis at low temperatures [see insets of Figure 2.18]. The value of saturation magnetization, remnant magnetization, and coercive field in the case of $AlFeO_3$ ($GaFeO_3$) are 13.9 (19.9) emu/g, 7.9 (10.1) emu/g and 12.9 (7.7) kOe respectively. Thus, both magnetic phase transition and unit cell parameters vary systematically with the cation size or Ga content. Both the compounds show a divergence between the zero-field-cooled and field-cooled magnetization data. The ferrimagnetic magnetization of $Al_{1-x}Ga_xFeO_3$ ($x = 0, 1$) mainly originates from the difference in Fe occupation at the four inequivalent cation sites. Low-temperature magnetic ordering in these oxides is due to the cation-oxygen-cation superexchange antiferromagnetic interaction.

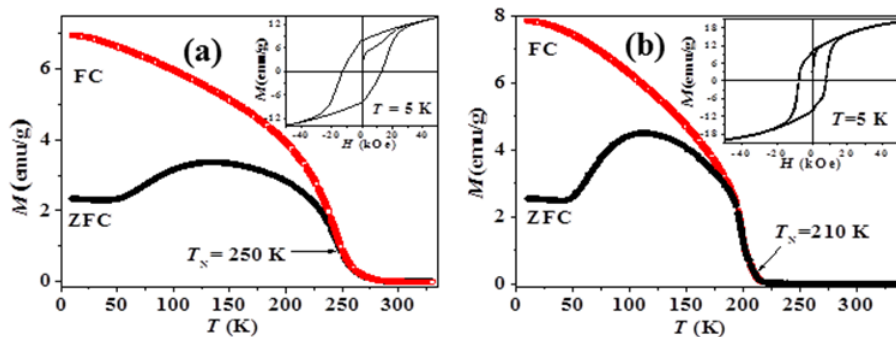


Figure 2.18: Temperature dependent dc magnetization of (a) $AlFeO_3$ and (b) $GaFeO_3$ under field - cooled (FC) and zero - field - cooled (ZFC) conditions. Insets show the magnetic hysteresis at 5 K.

In general, the bifurcation of ZFC and FC data is considered to be an indication of a spin-glass-like state. Very often by measuring temperature dependent ac susceptibility

where the maximum temperature of χ' , corresponding to the spin freezing temperature usually varies with the measuring frequency indicative of spin-glass systems. Temperature dependent ac susceptibility measurements on AlFeO_3 exhibits a maximum in χ' around the ferrimagnetic transition shifting to higher temperature with increasing frequency as shown in Figure 2.19 indicating that the origin of divergence is associated with a conventional spin-glass state.

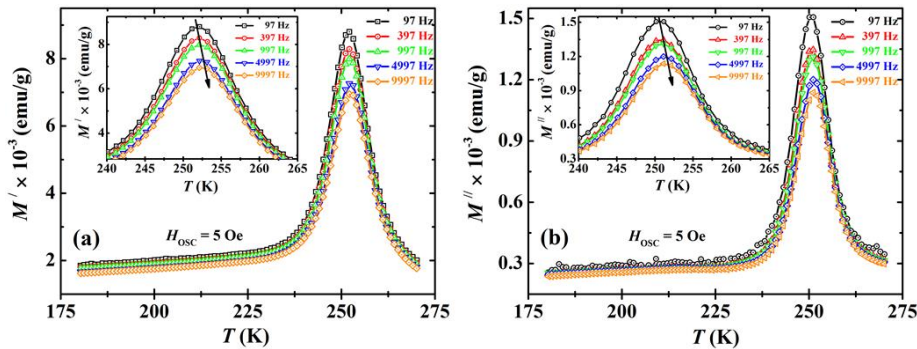


Figure 2.19: Temperature dependent (a) real and (b) imaginary part of ac magnetic susceptibility data of AlFeO_3 measured at various frequencies in the presence of an ac magnetic field of 5 Oe. Inset of (a) and (b) shows the enlarged region across the peak maxima which shows frequency dependence.

To study the glassy dynamics, we have examined the time-dependent magnetic relaxation [23] effect at constant temperature and magnetic field on AlFeO_3 . After cooling the sample under ZFC or FC mode to the desired measurement temperature we have applied the magnetic field for ZFC mode, or retain the cooling magnetic field in the case of FC mode. After that, time dependent magnetization growth is recorded at the measurement temperature in the presence of a constant magnetic field. In Figure 2.20 we compare the normalized magnetization data (M_t/M_0) as a function of time (t) at 200 K in both ZFC and FC conditions performed in the presence of a magnetic field of 100 Oe.

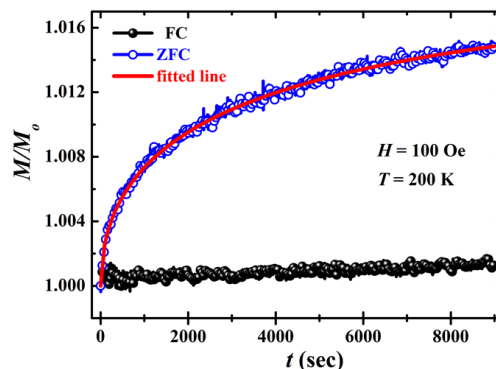


Figure 2.20: Time-dependent dc magnetization data of AlFeO_3 at 200 K after zero-field-cooled (ZFC) and field-cooled (FC) conditions in the presence of a magnetic field of 100 Oe.

From Figure 2.20, we observe that there is an increase in magnetization with time in the presence of a magnetic field of 100 Oe under ZFC conditions while the magnetization data remains almost unchanged with time in the FC conditions. We have fitted the time-dependent ZFC magnetization data with the stretched exponential function of the type, $M_t(H) = M_0(H) + [M_\infty(H) - M_0(H)] [1 - \exp\{- (t/\tau)^\alpha\}]$ [24] as shown in Figure 2.20. From the fit we obtain stretching parameter, $\alpha = 0.63$ and the characteristic relaxation time, $\tau = 4410$ sec. These experimental results confirm the existence of the glassy state.

2.4.1.2.2 Mössbauer spectra of AlFeO_3 and GaFeO_3

Mössbauer spectra were recorded by Y. Sundarayya on both oxides and it appeared as doublets. An analysis of this doublet reveals the paramagnetic nature of the randomly oriented Fe^{3+} ions with no exchange interactions. The isomer shift values obtained for this doublet also confirms the presence of iron in the oxidation state of III. To determine the distribution of Fe at different cation sites, Mössbauer spectra was recorded on the samples at low temperatures using a helium closed cycle cooler system attached to the sample chamber. In Figure 2.21, Mössbauer spectra of AlFeO_3 and GaFeO_3 at 10 K is shown. The spectra were analyzed using the WinNormos-for-Igor Mössbauer spectra fitting software sold by WissEl GmbH, Starnberg, Germany. The hyperfine parameters were obtained by fitting theoretical subspectral curves to experimental data with Lorentzian line shapes to deconvolute Fe sites in the spectra. The areas of the lines in the hyperfine spectra were constrained to be in the ratio 3:2:1:1:2:3. In Table 2.11 refined parameters are shown. The isomer shifts obtained at 10 K are found to be 0.2–0.35 mm/s for the three samples compared to α -iron, consistent with the ferric state in oxide materials [23,25,26].

The site occupancies of the three octahedral sites Fe1, Fe2, (Al/Ga)2 and one tetrahedral sites (Al/Ga)1 was determined from the respective areas of different Fe sites by the method described in the literature [27]. From this analysis, the Fe site occupancies of the Fe1, Fe2, A2 and A1 sites in AlFeO_3 are found to be 50, 26, 17 and 7 respectively. The Fe site occupancy values for GaFeO_3 are respectively 50, 23, 17, 10. The magnetic hyperfine field values in these oxides correspond to the ferric state and the hyperfine fields at the Fe1, Fe2, (Al/Ga)2, and (Al/Ga)1 sites decreases with the Ga content in $\text{Al}_{1-x}\text{Ga}_x\text{FeO}_3$ ($x = 0, 1$).

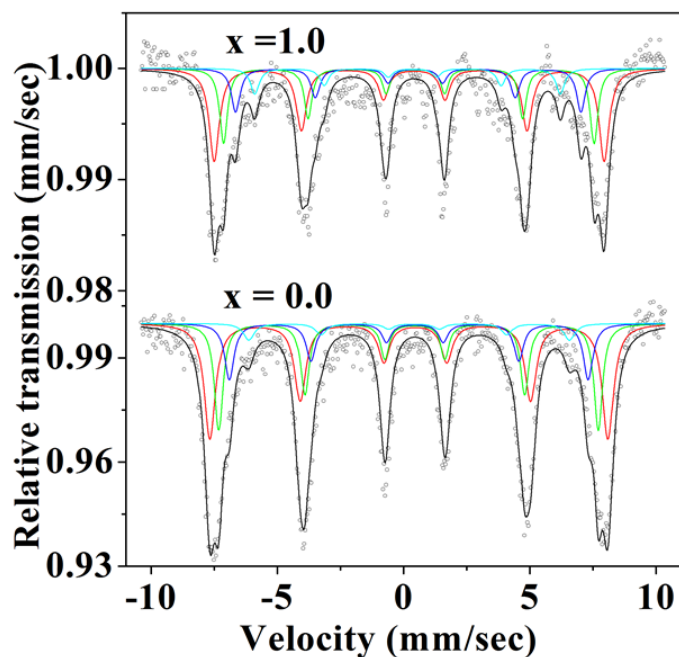


Figure 2.21: Mössbauer spectra of $\text{Al}_{1-x}\text{Ga}_x\text{FeO}_3$ ($x = 0, 1$) recorded at 10K.

Table 2.11: Mössbauer parameters for $\text{Al}_{1-x}\text{Ga}_x\text{FeO}_3$ ($x = 0, 1$) system at 10K

Compound	Site	δ (mm/sec)	ΔE_Q (mm/sec)	B_{hf} (kOe)	Fe Occupancy (%)
AlFeO_3	Fe1	0.34 (3)	-0.26 (5)	489 (1)	50
	Fe2	0.32 (4)	-0.25 (7)	466 (1)	26
	Al2	0.33 (7)	-0.24 (1)	441 (1)	17
	Al1	0.32 (2)	-0.19 (4)	394 (1)	7
GaFeO_3	Fe1	0.32 (1)	-0.20 (3)	479 (1)	50
	Fe2	0.34 (7)	-0.26 (3)	455 (1)	23
	Ga2	0.33 (2)	-0.28 (5)	424 (2)	17
	Ga1	0.25 (2)	-0.20 (7)	375 (1)	10

2.4.1.3 Theoretical understanding of cation disorder and related properties

Disorder, magnetic ordering and stability of AlFeO_3 have been studied theoretically by Waghmare *et al.* [8] and the main results are shown below. Cation site disorder here means the occupation of Fe site by an Al (or Ga) cation or vice versa, arising from an interchange of Al and Fe atoms in the perfectly ordered structure. From the observed data of occupancies of cation sites [Table 2.2] at low temperature, disorder arises with the highest probability through interchange in the positions of Fe and Al cations at Fe2 and Al2 sites.

(1) From the energies of the ferromagnetically and antiferromagnetically ordered states of AlFeO_3 [Table 2.12], it becomes clear that the antiferromagnetic state (AFM) is more stable than the ferromagnetic (FM) one in the chemically ordered case. Magnetic moments of the various Fe ions change significantly [Table 2.13] with a change in their ordering, resulting in Fe^{3+} in the low-spin state in the FM-ordered state. As the low-spin state of Fe^{3+} is known to be rare in nature, FM state of AlFeO_3 is indeed much higher in energy than the AFM one.

Table 2.12: Energetics of magnetic configuration in AlFeO_3

order/ disorder	Total energy of magnetic configuration (eV)		
	$\text{AlFeO}_3\text{-FM}$	$\text{AlFeO}_3\text{-AFM}$	$\text{GaFeO}_3\text{-AFM}$
ordered	-297.02	-300.67	-270.75
disordered	-298.59	-300.09	-270.64

Table 2.13: Magnetic moments of individual Fe ions (μ_B) in AlFeO_3

Atom no.	Cation site	Magnetic moment (μ_B)			
		FM		AFM	
		order	disorder	order	disorder
1	Fe1	1.26	3.85	3.59	3.69
2	Fe1	1.26	-3.20	3.59	3.40
3	Fe1	1.26	3.12	3.59	3.71
4	Fe1	1.26	3.77	3.59	3.58
5	Fe2/Al2	0.50	1.27	-3.57	-3.72
6	Fe2	0.50	3.70	-3.57	-3.59
7	Fe2	0.50	3.66	-3.57	-3.58
8	Fe2	0.50	3.81	-3.57	-3.54

(2) On introducing the anti-site disorder between Fe2 and Al2, it was found that FM ordering in the disordered state is lower in energy than the FM ordering in the chemically ordered state. Secondly, the magnetic moments (Table 2.13) change significantly only of the Fe ion located at the Al2 site indicating that Fe is in the low-spin state in the FM ordering and the magnetic moment on each Fe^{3+} ion varies with the location in both the AFM and FM states. In this sense, the system is ferrimagnetic with a rather small effective magnetic moment, consistent with experimental observation.

(3) Finally, larger exchange energy E_{xc} in the disordered FM state than that in the ordered FM state is responsible for its high-spin state and its greater stability [Figure 2.22].

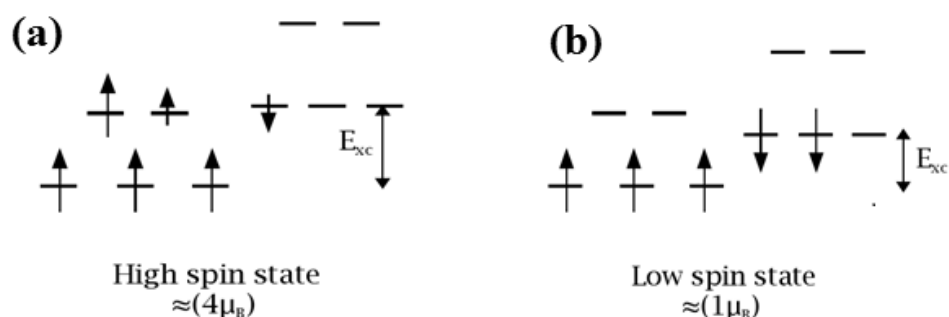


Figure 2.22: (a) High-spin and (b) low-spin states.

(4) From the study of the relation between structure and magnetic ordering as well as anti-site disorder it is observed that Fe2 site prefers dichotomous (bi-modal distribution) of bond lengths while the Al2 site exhibits uniformity in bond lengths. In the relaxed structures, the bond lengths change considerably with the change in magnetic ordering [Tables 2.14 and 2.15] implying a strong spin-phonon coupling consistent with the findings of temperature dependent Raman spectroscopy. It indicates that (a) a high-spin state of Fe^{3+} is energetically favorable (lower) than the low-spin state. (b) Fe-O bonds are longer when Fe^{3+} is in the high-spin state, a feature intimately linked with the disorder since the Shannon-Prewitt radius of Fe^{3+} in the low-spin state is close to that of Al^{3+} in octahedral coordination. (c) FM state in the disordered case is significantly lower in energy because only Fe^{3+} at the Al2-site takes the low-spin state, and Fe^{3+} at other sites are in the high-spin state. Therefore, in the high-spin configuration, Fe-O bond lengths are longer reflecting in the Fe-O bonds in the AFM state with Fe^{3+} taking the high-spin state.

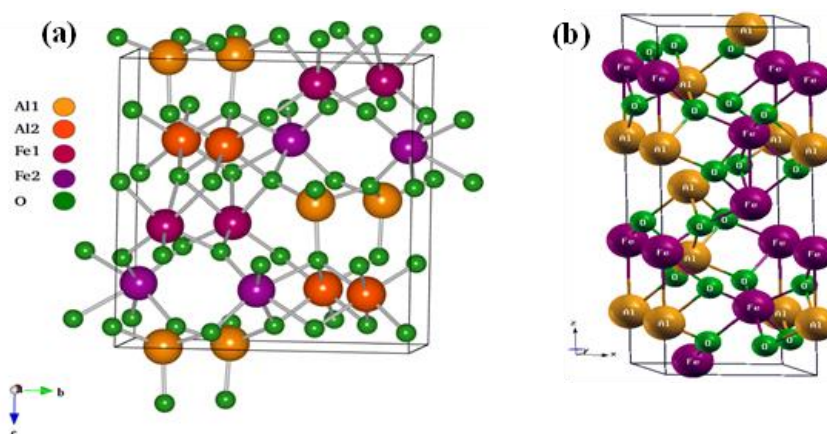
Table 2.14: Total magnetic moments in $AlFeO_3$

order/ disorder	Total magnetic moment (μ_B)	
	FM	AFM
Ordered	7.80	0.058
Disordered	22.87	-0.002

Table 2.15: Fe-O and Al-O bond lengths (Å) in AlFeO_3

state	Chemically ordered		Chemically disordered	
	L(Fe-O)	L(Al-O)	L(Fe-O)	L(Al-O)
FM	1.87	1.90	1.85	1.86
	1.87	1.92	1.93	1.87
	1.97	1.93	1.95	1.91
	2.04	1.96	1.97	1.95
	2.06	1.96	1.97	2.02
	2.11	2.02	1.99	2.05
AFM	1.83	1.88	1.90	1.85
	1.89	1.90	2.02	1.86
	1.99	1.92	2.02	1.90
	2.10	1.94	2.03	1.95
	2.18	1.95	2.05	2.05
	2.24	1.97	2.09	2.07

(5) The energetics of AlFeO_3 in perovskite and corundum structures [see Figure 2.23] has been determined. While Fe is found to prefer *A*-site with a high-spin state and *G*-type AFM ordering, the energy of the cubic perovskite is almost 3 eV higher than the observed one. Secondly, Fe^{3+} randomly occupying Al sites in the corundum structure takes the low spin state (due to size mismatch), and hence AlFeO_3 in the corundum structure is higher in energy by about 84 meV/formula unit. Thus, the stability of the observed structure is partly due to the distinct sites associated with Al and Fe.

**Figure 2.23:** Structure of AlFeO_3 in (a) orthorhombic and (b) corundum structures.

(6) From the examination of disorder, magnetic ordering, and stability of GaFeO₃ we found a greater degree of anti-site disorder in GaFeO₃. It is understandable from the fact that the radius of Fe³⁺ in the high-spin state ($R = 0.62 \text{ \AA}$) is close to that of Ga³⁺ in octahedral coordination while the radius of Fe³⁺ in the high-spin state does not match with that of Al³⁺ in octahedral coordination. The interesting results are outlined below:

(a) The antiferromagnetic state is lower in energy than the FM one in both the ordered and disordered cases with a slightly larger magnetic moment in the latter.

(b) In the antiferromagnetic state, magnetic moments at Fe1 and Fe2 sites are not of the same magnitude giving a weak magnetic moment effectively.

(c) The energy difference between the AFM states in the disordered and ordered cases be only 36 meV/formula unit (as opposed to 73 meV/formula unit of AlFeO₃). Thus, an anti-site disorder in GaFeO₃ is expected to be more prominent than in AlFeO₃.

2.4.2 Effect of Cr substitution on the structural and magnetic properties of GaFeO₃:

GaFeO₃ crystallizes in an orthorhombic crystal structure (space group $Pna2_1$) with four different cation sites labeled Ga1, Ga2 (mostly occupied by gallium) and Fe1, Fe2 (mostly occupied by iron). Ga2, Fe1, Fe2 are present in the octahedral environment, and Ga1 is present in the tetrahedral site respectively. GaFeO₃ exhibits a ferrimagnetic T_N of 210 K, which results from the unequal distribution of Fe spins of nearly equal magnitude on the sublattice. GaFeO₃ contains only trivalent metals in the structure like rare earth orthoferrites, making them attractive systems for investigations by substituting cations of similar charges. In LaFeO₃, partial substitution of Fe by Cr leads to a reduction in the Néel temperature from 750 K in LaFeO₃ to 280K in LaCrO₃ [11]. Moreover, Cr doping is one of the most adopted strategies to tune the dielectric and piezoelectric properties of ferroelectrics for practical applications. Cr is effective in decreasing the aging effect and the dielectric loss; thus, the effect of doping of Cr³⁺ is that of stabilizing the piezoelectric and dielectric properties [28,29]. In this work the effect of Cr substitution on magnetic properties of GaFeO₃ have been investigated by synthesizing GaFe_{1-x}Cr_xO₃ ($x = 0.05, 0.1$ and 0.2) and Ga_{1-x}Cr_xFeO₃ ($x = 0.05$ and 0.1) and examining their magnetic properties. In addition to that, we have also tried to

understand how the crystallographic site-specific substitution of Cr either in Ga or Fe sites of GaFeO_3 manifest itself and the resulting magnetic properties can be differentiated based on the substitution site of Cr.

All these oxides were found to crystallize in the orthorhombic structure (space group $Pna2_1$) as parent compound GaFeO_3 as evident from the XRD pattern shown in Figures 2.24 and 2.25.

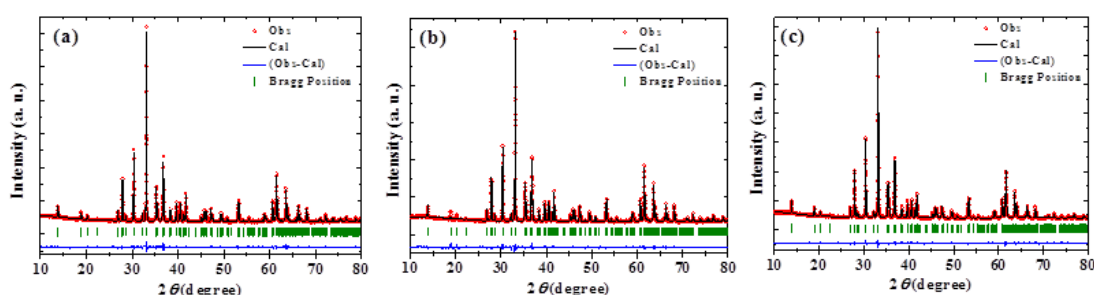


Figure 2.24: XRD patterns of (a) $\text{GaFe}_{0.95}\text{Cr}_{0.05}\text{O}_3$, (b) $\text{GaFe}_{0.9}\text{Cr}_{0.1}\text{O}_3$ and (c) $\text{GaFe}_{0.8}\text{Cr}_{0.2}\text{O}_3$ along with profile fits, difference patterns and Bragg positions ($T = 298\text{ K}$).

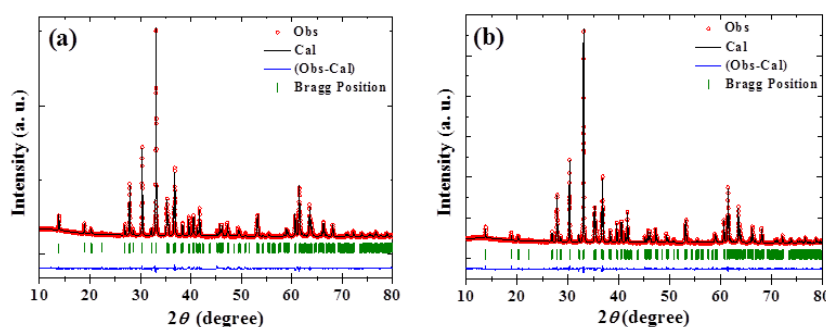


Figure 2.25: XRD patterns of (a) $\text{Ga}_{0.95}\text{Cr}_{0.05}\text{FeO}_3$ and (b) $\text{Ga}_{0.9}\text{Cr}_{0.1}\text{FeO}_3$ along with profile fits, difference patterns and Bragg positions ($T = 298\text{ K}$).

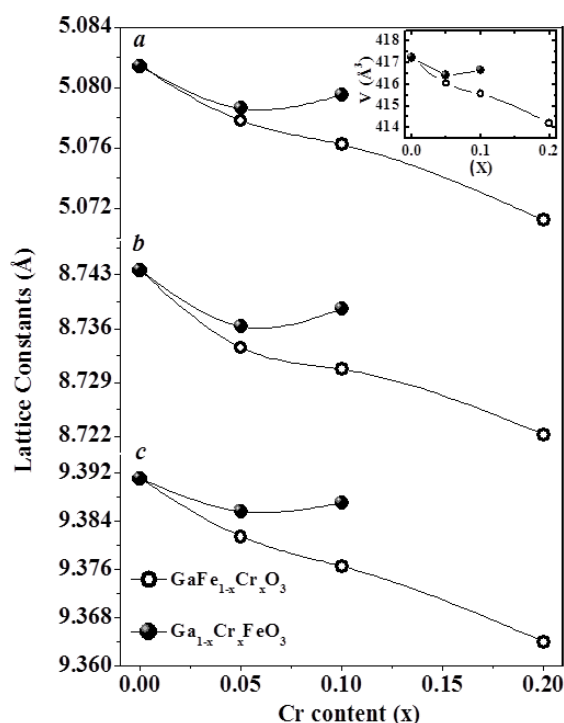
The crystallographic data of precursor oxides and Cr-substituted GaFeO_3 is shown in Tables 2.16 and 2.17, respectively. In Figure 2.26 the variation of lattice parameters in $\text{GaFe}_{1-x}\text{Cr}_x\text{O}_3$ and $\text{Ga}_{1-x}\text{Cr}_x\text{FeO}_3$ with composition have been plotted.

Table 2.16: Crystallographic data of precursor oxides

$(\text{Fe}_{1-x}\text{Cr}_x)_2\text{O}_3$ (Space Group: $R\bar{3}c$, Rhombohedral)						
	% substitution	a (Å)	b (Å)	c (Å)	χ^2 (%)	R_{Bragg} (%)
x (Cr)	10	5.0309 (4)		13.7167 (13)	2.41	1.71
$(\text{Ga}_{1-y}\text{Cr}_y)_2\text{O}_3$ (Space Group: $C2/m$, Monoclinic)						
y (Cr)	10	12.2459 (7)	3.0410 (2)	5.8114 (3)	3.57	0.62

Table 2.17: Crystallographic data of $\text{GaFe}_{1-x}\text{Cr}_x\text{O}_3$ and $\text{Ga}_{1-y}\text{Cr}_y\text{FeO}_3$

GaFe _{1-x} Cr _x O ₃ (Space Group: <i>Pna</i> 2 ₁ , Orthorhombic)						
	% substitution	<i>a</i> (Å)	<i>b</i> (Å)	<i>c</i> (Å)	χ^2 (%)	<i>R</i> _{Bragg} (%)
<i>x</i> (Cr)	0	5.0814 (2)	8.7436 (3)	9.3910 (2)	2.30	2.74
	5	5.0778 (0)	8.7335 (1)	9.3814 (1)	2.11	1.50
	10	5.0762 (1)	8.7307 (1)	9.3765 (1)	2.72	1.74
	20	5.0712 (1)	8.7222 (1)	9.3640 (1)	2.93	1.67
Ga _{1-y} Cr _y FeO ₃ (Space Group: <i>Pna</i> 2 ₁ , Orthorhombic)						
<i>y</i> (Cr)	5	5.0786 (1)	8.7363 (1)	9.3856 (1)	2.73	1.58
	10	5.0795 (1)	8.7386 (1)	9.3870 (1)	2.07	1.58

**Figure 2.26:** Variation of lattice constants in $\text{GaFe}_{1-x}\text{Cr}_x\text{O}_3$ ($x = 0.05, 0.1$ and 0.2) and $\text{Ga}_{1-x}\text{Cr}_x\text{FeO}_3$ ($x = 0.05$ and 0.1) with Cr content at 298 K obtained from XRD. Variation of unit cell volume is shown in the inset.

From Figure 2.26, it is observed that the change in lattice constants is more marked when Cr is substituted in the Fe site of GaFeO_3 while the effect in lattice constants and unit cell volume is marginal when substituted Cr is present in the Ga site of GaFeO_3 . The unit cell volume of $\text{GaFe}_{1-x}\text{Cr}_x\text{O}_3$ decreases from 417 ($x = 0.0$) to 414 Å³ ($x = 0.2$) compared to $\text{Ga}_{1-x}\text{Cr}_x\text{FeO}_3$ which has a unit cell volume close to that of GaFeO_3 . These changes are consistent with the radius of octahedral Cr^{3+} (0.615 Å) compared to Fe^{3+} (0.645 Å, High Spin) and Ga^{3+} (0.62 Å), the radius of Cr^{3+} being considerably smaller than that of Fe^{3+} . To establish that Cr^{3+} has gone into the

octahedral Ga2 site (Cr^{3+} cannot occupy the tetrahedral Ga1 site) in the $\text{Ga}_{1-x}\text{Cr}_x\text{FeO}_3$ series of compounds a detailed analysis of the XRD data for the $x = 0.1$ composition have been carried out. For this purpose, all the occupancies have been fixed because x-rays cannot differentiate elements of close atomic numbers. The occupancies were fixed based on neutron diffraction results as shown in Table 2.6. We refined the thermal parameters while placing the substituent atoms at different (Ga and Fe) sites and found large thermal parameters when the atoms are present at Fe sites. The results of the refinement are shown in Table 2.18 to indicate that the proposed cation distribution is consistent with the diffraction data, but due to the similar scattering powers of the cations, the diffraction data is not very sensitive to the cation distribution. The differences observed in the structural parameters and magnetic properties of $\text{GaFe}_{1-x}\text{Cr}_x\text{O}_3$ and $\text{Ga}_{1-x}\text{Cr}_x\text{FeO}_3$ also show that we have achieved Cr substitution at different sites.

Table 2.18: Results of structure refinement of $\text{Ga}_{0.9}\text{Cr}_{0.1}\text{FeO}_3$ at 298 K

$\text{Ga}_{0.9}\text{Cr}_{0.1}\text{FeO}_3$					
Space Group: $Pna2_1$ (Orthorhombic), $a = 5.0795$ (1) Å, $b = 8.7386$ (1) Å, and $c = 9.3870$ (1) Å					
Atoms	x	y	z	B_{iso}	Occ.
Fe1/Ga3	0.1968 (10)	0.1507 (8)	0.5857 (4)	0.95 (11)	0.65 (0) / 0.35 (0)
Fe2/Ga4	0.6741 (6)	0.0335 (3)	0.7939 (7)	0.75 (6)	0.70 (0) / 0.30 (0)
Ga1/Fe3	0.1742 (8)	0.1543 (8)	0.0000 (0)	1.60 (10)	0.91 (0) / 0.09 (0)
Ga2/Fe4/Cr	0.8148 (6)	0.1632 (4)	0.3090 (5)	0.25 (7)	0.25 (0) / 0.55 (0) / 0.20 (0)
O1	0.984 (3)	0.324 (2)	0.423 (1)	0.51 (8)	1.0
O2	0.531 (2)	0.485 (2)	0.428 (1)	0.51 (8)	1.0
O3	0.655 (3)	0.005 (1)	0.208 (1)	0.51 (8)	1.0
O4	0.156 (3)	0.156 (2)	0.200 (0)	0.51 (8)	1.0
O5	0.867 (3)	0.160 (2)	0.671 (1)	0.51 (8)	1.0
O6	0.526 (3)	0.163 (2)	0.941 (1)	0.51 (8)	1.0

$R_{\text{Bragg}} = 8.09\%$, $\chi^2 = 2.20\%$

$\text{GaFe}_{1-x}\text{Cr}_x\text{O}_3$ exhibits ferrimagnetic T_N values of 192 K, 170 K and 110 K for $x = 0.05$, 0.1 and 0.2 respectively, compared with a T_N of 210 K in the case of GaFeO_3 . On the other hand $\text{Ga}_{1-x}\text{Cr}_x\text{FeO}_3$ for $x = 0.05$, 0.1 shows T_N of 215 and 220 K respectively, indicating that the substitution of Cr at the Ga site has a negligible effect on ferrimagnetic transition. Typical magnetization plots of $\text{GaFe}_{1-x}\text{Cr}_x\text{O}_3$ and $\text{Ga}_{1-x}\text{Cr}_x\text{FeO}_3$ are shown in Figures 2.27 and 2.28 respectively. From Figure 2.28 (a) it is observed that T_N decreases significantly with increase in x in $\text{GaFe}_{1-x}\text{Cr}_x\text{O}_3$. A magnetic hysteresis has been observed at low temperature (see insets of Figures 2.27 and 2.28).

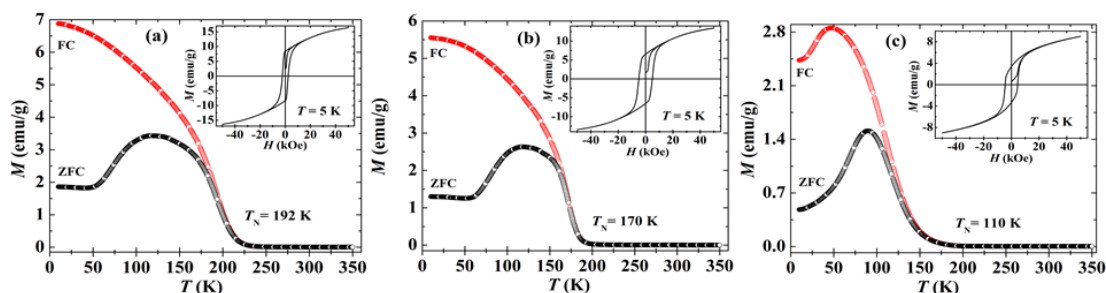


Figure 2.27: Temperature dependent magnetization of (a) $\text{GaFe}_{0.95}\text{Cr}_{0.05}\text{O}_3$, (b) $\text{GaFe}_{0.9}\text{Cr}_{0.1}\text{O}_3$ and (c) $\text{GaFe}_{0.8}\text{Cr}_{0.2}\text{O}_3$ under field-cooled (FC) and zero-field-cooled (ZFC) conditions. Magnetic hysteresis at 5 K is shown in the inset.

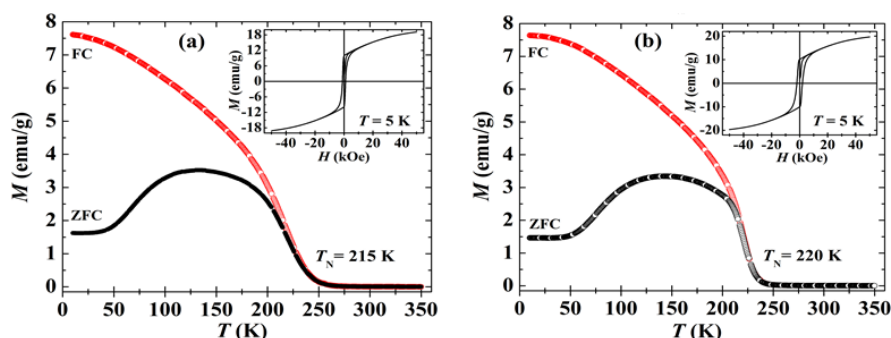


Figure 2.28: Temperature dependent magnetization of (a) $\text{Ga}_{0.95}\text{Cr}_{0.05}\text{FeO}_3$ and (b) $\text{Ga}_{0.9}\text{Cr}_{0.1}\text{FeO}_3$ under field-cooled (FC) and zero-field-cooled (ZFC) conditions. Magnetic hysteresis at 5 K is shown in the inset.

In Table 2.19 the values of saturation magnetization (M_S), remanent magnetization (M_R), and coercive field (H_C) are shown. The divergence between the field-cooled (FC) and zero-field-cooled (ZFC) magnetization data was observed just as in GaFeO_3 .

Table 2.19: Magnetic data from the hysteresis of $\text{GaFe}_{1-x}\text{Cr}_x\text{O}_3$ and $\text{Ga}_{1-x}\text{Cr}_x\text{FeO}_3$ (two component mixture)

Compound	M_S (emu/g)	M_R (emu/g)	H_C (kOe)	T_N (K)
$\text{GaFe}_{0.8}\text{Cr}_{0.2}\text{O}_3$	9.01	3.4	4.4	110
$\text{GaFe}_{0.9}\text{Cr}_{0.1}\text{O}_3$	13.5	6.5	5	170
$\text{GaFe}_{0.95}\text{Cr}_{0.05}\text{O}_3$	16.4	8.4	2.3	192
GaFeO_3	19.9	10.1	7.7	210
$\text{Ga}_{0.95}\text{Cr}_{0.05}\text{FeO}_3$	19.1	9.8	1.1	215
$\text{Ga}_{0.9}\text{Cr}_{0.1}\text{FeO}_3$	19.7	10	1.9	220

Although a decreasing trend has been found in M_S and M_R with x in $\text{GaFe}_{1-x}\text{Cr}_x\text{O}_3$, it is negligible with x in $\text{Ga}_{1-x}\text{Cr}_x\text{FeO}_3$. The important result from the study of

Cr substitution in GaFeO_3 is that Cr substitution in the Fe site in $\text{GaFe}_{1-x}\text{Cr}_x\text{O}_3$ markedly affects the structural parameters as well as the magnetic properties while substitution of Cr at the Ga site has marginal effects as illustrated in Figure 2.29. The weak interaction between $\text{Cr}^{3+}(3\mu_B)\text{--O--Cr}^{3+}(3\mu_B)$ and $\text{Fe}^{3+}(5\mu_B)\text{--O--Cr}^{3+}(3\mu_B)$ [30] as compared with $\text{Fe}^{3+}(5\mu_B)\text{--O--Fe}^{3+}(5\mu_B)$ interaction may be related to the lowering of T_N . If the spin of the substituting Cr^{3+} ion aligns with the Fe^{3+} ion, spin magnetic moment (SMM) of $\text{Cr}^{3+}(d^3)$ ion is $3\mu_B$; thus, the net SMM is expected to be reduced by $2\mu_B$ per formula unit [22].

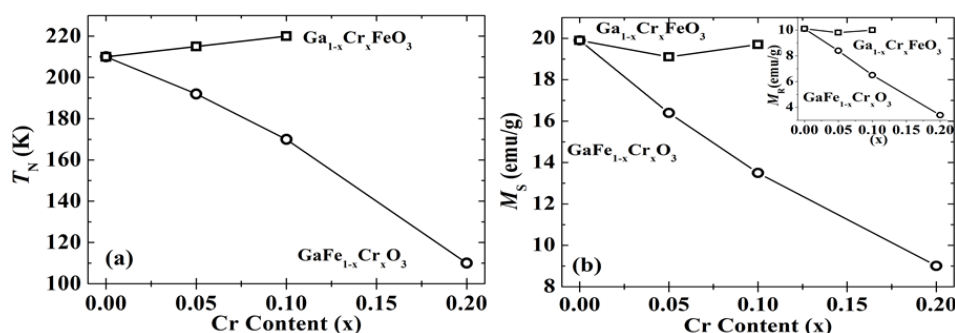


Figure 2.29: Variation of (a) Néel temperature (T_N) and (b) M_S (in the inset M_R) with Cr concentration for $\text{GaFe}_{1-x}\text{Cr}_x\text{O}_3$ ($x = 0.05, 0.1$ and 0.2) and $\text{Ga}_{1-x}\text{Cr}_x\text{FeO}_3$ ($x = 0.05$ and 0.1) respectively.

Table 2.20: Magnetic data from the hysteresis of $\text{GaFe}_{1-x}\text{Cr}_x\text{O}_3$ and $\text{Ga}_{1-x}\text{Cr}_x\text{FeO}_3$ (three component mixture)

Compound formula	M_S (emu/g)	M_R (emu/g)	H_C (kOe)	T_N (K)
$\text{GaFe}_{0.9}\text{Cr}_{0.1}\text{O}_3$	14.2	6.8	4.2	168
$\text{GaFe}_{0.95}\text{Cr}_{0.05}\text{O}_3$	16.8	8.5	7.1	201
GaFeO_3	19.9	10.1	7.7	210
$\text{Ga}_{0.95}\text{Cr}_{0.05}\text{FeO}_3$	19.9	10.4	7.7	222
$\text{Ga}_{0.9}\text{Cr}_{0.1}\text{FeO}_3$	18.4	9.1	5.7	201

It is important to note that the magnetization data of Cr-substituted GaFeO_3 prepared from a three-component mixture of Ga_2O_3 , Fe_2O_3 and Cr_2O_3 are entirely different [Table 2.20]. The Néel temperatures, as well as unit cell parameters, are also different [11]. Thus, there is negligible change in the unit cell volume even when $x = 0.15$, and the T_N values are much lower than those observed here. These results observed on Cr substituted GaFeO_3 establish that the method of preparation employed

has enabled site-selective substitution. The changes in structural parameters and magnetic properties with x corroborate the occurrence of specific site effects. The decrease in T_N and other properties of $\text{GaFe}_{1-x}\text{Cr}_x\text{O}_3$ with an increase in x parallels the reduction in unit cell volume. Rare-earth orthochromates show such a decline in T_N with unit cell volume.

2.4.2.1 Theoretical understanding of site-specific cation substitution

Theoretical understandings on the above experimental findings developed by Waghmare *et al.* [12] through first-principles calculations show that substitution at the Ga2 and Fe1 sites would have different effects on the structural parameters and magnetic properties of GaFeO_3 . The effect of Cr doping at Fe1, Fe2, Ga1 and Ga2 sites have been studied, taking the concentration of substituent to be one Cr per unit cell (i.e. 12.5 %).

In simulations of Cr substitution at the cation sites, both antiferromagnetic (AFM) (note that this forms a ferrimagnetic (FiM) state with a nonzero moment) and ferromagnetic (FM) configurations have been considered, i.e., magnetic moments on transition metals aligned anti-parallel or parallel to each other [8]. From the cohesive energies of these configurations, it was observed that Cr substitution at Ga2 site with the antiferromagnetic ordering of spins is favorable (-6.94 eV/atom). Since both Fe1 and Fe2 sites have octahedral coordination, energies of Cr substitution at these two locations is almost the same (-6.85 eV/atom). Ga1 being a tetrahedral site, Cr^{3+} cannot occupy it. The bond-valence sums, V , was calculated by Eq. (2.2),

$$V = e^{R_0/B} \sum e^{R_i/B} \quad (2.2)$$

where, R_0 is the length of a bond of unit valence, R_i is the bond length of bond i the ion connected to, and B is a parameter, approximately equal to 0.37 \AA for most bonds. Knowledge of the bond valence sums against the oxidation state of each atom allows one to assess if a given structure obeys the normal rules of structural chemistry. If the bond valence sum differs by more than 0.1 valence unit from the oxidation state of the ion, it suggests that the structure may not be stable. The Bond-valence sums for the Cr ion at the Fe1, Fe2, Ga1 and Ga2 sites are shown in Table 2.21. Since Cr is in the +III oxidation state, according to the criterion for stability of the structure discussed above,

Cr substitution at Ga2 (both AFM and FM states) and Fe1 (both AFM and FM) sites is favored. On the other hand, Cr is relatively weakly bonded to the lattice when substituted at Fe2 and Ga1 sites. It is important to note that the overall energetics would have contributions from all the ions and bonds giving rise to the reasonable stability of all the configurations. From the bond-valence analysis, we infer that the structure is not locally stable, particularly at the substituted Cr-site.

Table 2.21: Bond valence sum of Cr-O bonds

Cation site	Magnetic ordering	
	FM	AFM
Fe1	2.98	3.07
Fe2	3.12	3.22
Ga1	3.30	3.36
Ga2	3.03	3.06 (AFM)* 3.003 (FM)*

*AFM: Fe1-O-Cr AFM interaction; FM: Fe1-O-Cr FM interaction

Noting that Fe1-O-Fe1 and Fe2-O-Fe2 bond angles are quite smaller than 150° and Fe1-O-Fe2 bond angles are close to 180° , we have focused on magnetic configurations with moments/spins at all Fe1 sites aligned up and those at all Fe2 sites aligned down. Even in the AFM configurations, there is an overall magnetic moment [Table 2.22] in the system reflecting the asymmetry in the electronic density of states with up and down spins [Figure 2.30]. This asymmetry, prominent near the Fermi energy, is stronger in the case of Cr substitution at Ga2 site correlating with its larger total magnetic moment. Also, the pseudogap at the Fermi energy in the Ga2-AFM configuration reaffirms its greater relative stability inferred from bond-valence analysis. Although we have initialized the spins of magnetic ions at all the sites with the up state, these magnetic moments relax to slightly different spin configurations, particularly the one at Cr-site [Table 2.22] in the self-consistent solution. We find that the magnetic moment of Cr ion in the AFM (*i.e.* FiM) case is the largest for doping at the Ga2 site. Cr at the Ga2 site is connected to 4 Fe1 sites via oxygen with (Fe1-O-Cr) bond angles of 165° , 130° , 104° , and 99° . Cr³⁺ and Fe³⁺ ions being in the d^3 and d^5 states respectively, super-exchange between Cr and Fe1 connected with a bond angle of 165° is FM in nature, while it is AFM for the remaining Fe1 sites with bond angles of $< 150^\circ$. Therefore, the orientation of spin at the Cr substituted at Ga2 site parallel to that

of the spins on the Fe1 site (opposite to the Fe2 site) in the former and anti-parallel to the spins on the Fe1 site (parallel to the Fe2 site) in the latter. These competing interactions lead to nearly the same energies of configurations with the spin of Cr^{3+} (a) parallel and (b) antiparallel to the spins at the Fe1 sites. Thus, the AFM (FiM) state and associated transition are not affected much by Cr substitution at the Ga2 site, while maintaining a sizeable magnetic moment of Cr^{3+} [Table 2.22]. In contrast, substitution of Cr at the Fe1 site results in the reduction of the total magnetic moment.

Table 2.22: Total magnetic moment and magnetic moments of Cr^{3+}

Cation site	Total magnetic moment (μ_B)		Magnetic moment on Cr (μ_B)	
	FM	AFM	FM	AFM
Fe1	23.20	-1.87	2.66	2.39
Fe2	26.01	1.99	2.52	-2.29
Ga1	22.00	1.91	-1.79	1.69
Ga2	20.03	-2.79 (AFM)* 2.8 (FM)*	2.66	-2.57 (AFM)* 2.68 (FM)*

*AFM: Fe1-O-Cr AFM interaction; FM: Fe1-O-Cr FM interaction

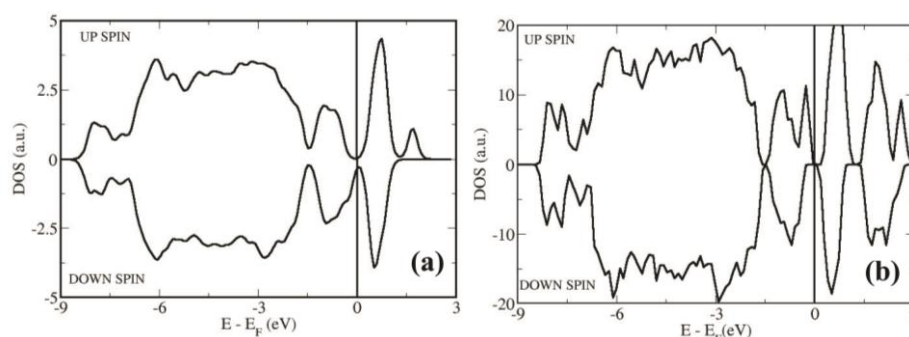


Figure 2.30: Electronic density of states for (a) Cr at Ga2 site with AFM ordering and (b) for Cr at Fe1 site with AFM ordering.

To understand the observed change in T_N with Cr-substitution in GaFeO_3 requires the inclusion of the effects of the disorder. Unsubstituted GaFeO_3 has anti-site disorder between Ga2 and Fe sites [8]. This disorder is promoted further when Cr is substituted at the Fe1 site while it reduces upon substituting Cr at the Ga2 site. As disorder results in the reduction of the strength of magnetic interactions [8], we expect a decrease in T_N when Cr substitution occurs at the Fe1 site. On the other hand, disorder is supposed to be weaker when Cr substitution takes the Ga2 sites, and the strength of AFM superexchange, therefore, remains roughly the same (while increasing the overall

magnetic moment). We, therefore, expect T_N to remain nearly the same for Cr-substitution at Ga2 sites as observed in our experiments. Note that in the octahedral coordination, Cr^{3+} ion has an ionic radius of 0.615 Å, whereas Fe^{3+} has an ionic radius of 0.645 Å in the high spin state and 0.55 Å in the low spin state in an octahedral oxygen environment. Ga^{3+} in octahedral (Ga2) and tetrahedral (Ga1) coordination has ionic radii of 0.62 Å and 0.47 Å ionic radii respectively. The difference in ionic radii is the least for Cr at Ga2 site as compared to that of Fe1 or Fe2 sites. We expect compressive stress on the crystal upon substitution of Cr at the Fe1 site and hence a reduction in unit cell volume and subsequent decrease in the strength of AFM interactions and T_N . In contrast, simulations reveal no significant stress when Cr is substituted at the Fe2 site (AFM ordering), correlating with essentially no change in T_N in this case.

2.4.3 Ball-milling induced structural transitions in $\text{Al}_{1-x}\text{Ga}_x\text{FeO}_3$ ($x = 0, 0.5, 1$):

2.4.3.1 AlFeO_3

2.4.3.1.1 X-ray diffraction study

X-ray diffraction data was recorded on AlFeO_3 subjected to ball milling for 12 h at room temperature. The XRD patterns of the starting material and the ball-milled samples are shown in Figure 2.31(a) and 2.31(b) respectively. The ball-milled sample shows completely different diffraction pattern as compared with the starting pattern. The ball-milled sample shows line broadening and the crystallite size calculated from line broadening employing the Scherrer formula was found to be around 20 nm. Annealing the ball-milled sample at 700 °C showed no changes in the positions of the reflections as can be seen from Figure 2.31(c). The XRD pattern of the ball-milled AlFeO_3 does not match with that of $\alpha\text{-Fe}_2\text{O}_3$. Furthermore, XRD pattern of a 1:1 mixture of $\alpha\text{-Fe}_2\text{O}_3$ and $\alpha\text{-Al}_2\text{O}_3$ [Figure 2.31(d)] is entirely different from that of ball-milled AlFeO_3 confirming that the ball-milling does not decompose AlFeO_3 into the constituent oxides. Interestingly, we observe that ball-milling for extended periods of 24 h at 298 K gives rise to different diffraction pattern which is similar to the XRD pattern of $\alpha\text{-Fe}_2\text{O}_3$ ($R\bar{3}c$) as shown in Figure 2.31(e). Moreover upon heating the 24 h ball-milled sample to 1350 °C, we observe that the XRD pattern [Figure 2.31(f)] of AlFeO_3 looks similar to the starting pattern of the compound indicating that the

structure retraces to the original one. Profile fitting using FULLPROF suite [Figure 2.31(g)] showed that the structure of 12 h ball-milled AlFeO_3 was akin to $\delta\text{-Al}_2\text{O}_3$ with the $P2_12_12_1$ space group [31]. The lattice parameters of this $P2_12_12_1$ were found to be $a = 15.886$ (11) Å, $b = 11.408$ (6) Å and $c = 7.803$ (4) Å. The $\delta\text{-Al}_2\text{O}_3$ phase is related to spinel structure and is different from the $\delta^*\text{-Al}_2\text{O}_3$ ($P222$) [32] with lattice parameters $a = 7.936$ Å, $b = 7.956$ Å and $c = 11.711$ Å reported by Fargeot *et. al.* [32]. It is, however, impossible to differentiate the $P222$ and $P2_12_12_1$ structures based on profile fitting. It is possible that the δ^* phase of Fargeot *et. al.* is the δ phase described by Levin and Brandon [31]. On the other hand, 24 h ball-milled AlFeO_3 adopt rhombohedral structure with the space group $R\bar{3}c$ as shown in the profile fitting [Figure 2.31(h)]. The lattice parameters of the rhombohedral AlFeO_3 are, $a = 4.909$ (2) Å and $c = 13.393$ (7) Å. Note that the lattice parameters of $\alpha\text{-Fe}_2\text{O}_3$ are, $a = 5.032$ Å and $c = 13.733$ Å, while those of $\alpha\text{-Al}_2\text{O}_3$ are, $a = 4.760$ Å and $c = 12.993$ Å (JCPDS).

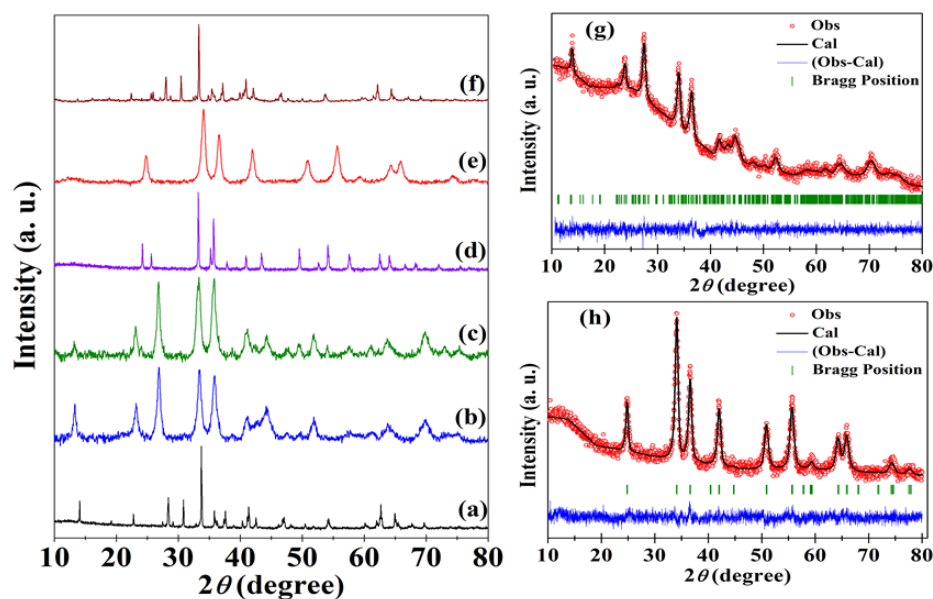


Figure 2.31: X-ray diffraction patterns of (a) orthorhombic ($Pna2_1$) AlFeO_3 sample; (b) ball-milled AlFeO_3 (12 h); (c) 12 h ball-milled AlFeO_3 annealed at 700 °C; (d) mixture of $\alpha\text{-Fe}_2\text{O}_3$ + $\alpha\text{-Al}_2\text{O}_3$ (1:1) and (e) ball-milled AlFeO_3 (24 h); (f) ball-milled AlFeO_3 annealed at 1350 °C; XRD patterns of ball-milled AlFeO_3 in (g) $\delta\text{-Al}_2\text{O}_3$ structure ($P2_12_12_1$) and (h) $R\bar{3}c$ structure along with profile fits, difference patterns and Bragg positions.

2.4.3.1.2 Raman spectroscopic study

Raman spectroscopic study has been carried out to understand the differences in the structural phases upon ball-milling. The Raman spectrum of AlFeO_3 ball-milled for 12 h at 298 K with the $P2_12_12_1$ structure is distinctly different from that of bulk AlFeO_3

with the $Pna2_1$ structure [see Figure 2.32(a) and 2.32(b)]. After annealing ball-milled $AlFeO_3$ at 700 °C, the Raman spectrum did not change significantly [Figure 2.32(c)] except for sharpening of the bands. Figure 2.32(d) shows the Raman spectrum of $AlFeO_3$ ball-milled for 24 h at 298 K. The spectrum is that expected of the $R\bar{3}c$ space group. Thus, XRD and Raman studies of $AlFeO_3$ clearly establish that the orthorhombic structure ($Pna2_1$) first transforms to the orthorhombic $P2_12_12_1$ structure of $\delta-Al_2O_3$ on ball-milling for 12 h and transforms to the rhombohedral $R\bar{3}c$ structure on further ball-milling.

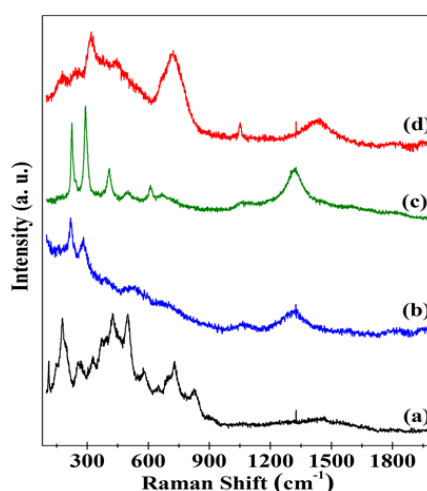


Figure 2.32: Raman spectra of (a) orthorhombic $AlFeO_3$ sample; (b) ball-milled $AlFeO_3$ (12 h); (c) 12 h ball-milled $AlFeO_3$ annealed at 700 °C and (d) ball-milled $AlFeO_3$ (24 h).

2.4.3.1.3 Magnetic property

DC magnetization measurements were carried out to establish the magnetic behavior of $AlFeO_3$ with different structures. The magnetization data of $AlFeO_3$ ball-milled for 12 h has been compared with those of $AlFeO_3$ structure with the $Pna2_1$ space group. In Figure 2.33(a), temperature-dependent FC (field-cooled) and ZFC (zero-field-cooled) magnetization data of ball-milled $AlFeO_3$ in the $P2_12_12_1$ structure are shown. A divergence between the FC and the ZFC data has been realized below 390 K in the $P2_12_12_1$ sample. Furthermore, the nature of the magnetization curves of this sample is quite different from that of the $Pna2_1$ sample which shows a sharp ferrimagnetic transition (T_N) at 250 K [8]. The $P2_12_12_1$ sample shows magnetic hysteresis at 5 K as shown in the inset of Figure 2.33(a). Figure 2.33(b) shows the magnetization data of $AlFeO_3$ in the $R\bar{3}c$ structure obtained by ball-milling for 24 h. The field-cooled data shows a ferrimagnetic transition at a different temperature from that of the $Pna2_1$

structure, with a T_N of 225 K. We observe magnetic hysteresis at 5 K, in the $R\bar{3}c$ sample as well but no saturation. The magnitude of magnetization of both the $P2_12_12_1$ and $R\bar{3}c$ samples are much lower than that of the orthorhombic $Pna2_1$ structure showing a preponderance of antiferromagnetic interaction in these transformed phases.

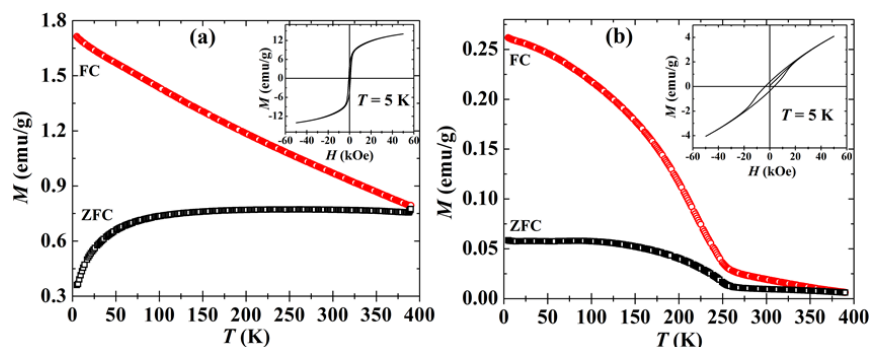


Figure 2.33: Temperature dependent dc magnetization of ball-milled AlFeO_3 in the (a) $P2_12_12_1$ and (b) $R\bar{3}c$ structures under field-cooled (FC) and zero-field cooled (ZFC) conditions. Magnetic hysteresis at 5 K is shown in the inset.

2.4.3.2 GaFeO_3

2.4.3.2.1 X-ray diffraction study

We next examined the effect of ball milling on the structure of GaFeO_3 by performing x-ray diffraction experiment. In Figure 2.34 we show the x-ray diffraction patterns of GaFeO_3 in the $Pna2_1$ structure as well as of the GaFeO_3 ball-milled for 12 h or 6 h at 300 K. In this figure we also show the XRD pattern of GaFeO_3 nanoparticles prepared by the sol-gel route. The XRD pattern of the nanoparticles prepared by the sol-gel route is the same as that of the $Pna2_1$ GaFeO_3 [see Figure 2.34(a) and 2.34(b)] except for line broadening due to the small size. Using the Scherrer formula the crystallite size was found to be 25 nm. The XRD pattern of ball-milled GaFeO_3 [Figure 2.34(c)] is quite different from that of the starting material [Figure 2.34(a)] and it is similar to the XRD pattern of $\alpha\text{-Fe}_2\text{O}_3$ crystallizing in the rhombohedral structure with the space group $R\bar{3}c$. The ball-milled pattern has rather broad reflections due to the small crystallite size, estimated to be 20 nm. On annealing the ball-milled GaFeO_3 at 700 °C the XRD pattern remains the same [Figure 2.34(d)], but with smaller line width due to the increase in the crystallite size (estimated to be 40 nm). Furthermore, the XRD pattern of a 1:1 mixture of Fe_2O_3 and Ga_2O_3 [Figure 2.34(e)] is entirely different from that of ball-milled GaFeO_3 . Interestingly, on heating ball-milled GaFeO_3 sample to 1000 °C, it

transformed back to the orthorhombic chiral ($Pna2_1$) structure as can be seen from the XRD pattern in Figure 2.34(f).

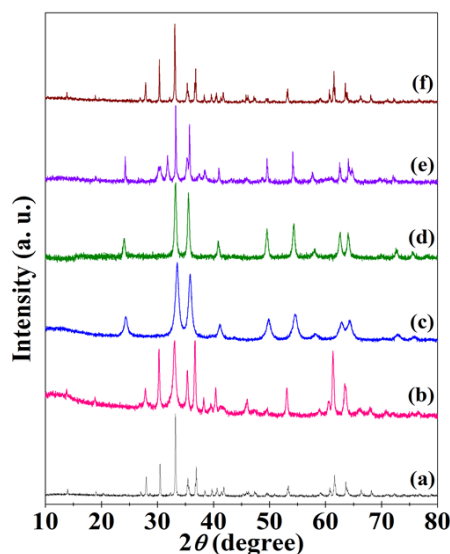


Figure 2.34: X-ray diffraction patterns of (a) orthorhombic GaFeO_3 sample; (b) GaFeO_3 nanoparticles by sol-gel route; (c) ball-milled GaFeO_3 ; (d) ball-milled GaFeO_3 annealed at $700\text{ }^\circ\text{C}$; (e) mixture of $\text{Fe}_2\text{O}_3 + \text{Ga}_2\text{O}_3$ (1:1) and (f) ball-milled GaFeO_3 annealed at $1000\text{ }^\circ\text{C}$.

In Figure 2.35 we show the XRD pattern of ball-milled GaFeO_3 along with profile fit and difference pattern. The lattice parameters of ball-milled GaFeO_3 are, $a = 5.022(2)\text{ \AA}$ and $c = 13.606(5)\text{ \AA}$. Note that the lattice parameters of $\alpha\text{-Fe}_2\text{O}_3$ and rhombohedral Ga_2O_3 are, $a = 5.032\text{ \AA}$, $c = 13.733\text{ \AA}$ and $a = 4.979\text{ \AA}$, $c = 13.429\text{ \AA}$ respectively. In both the ball-milled sample, AlFeO_3 (24 h) and GaFeO_3 (6 or 12 h) the transformed space group is $R\bar{3}c$, rather than $R3c$, was confirmed by the absence of second harmonic generation by these materials.

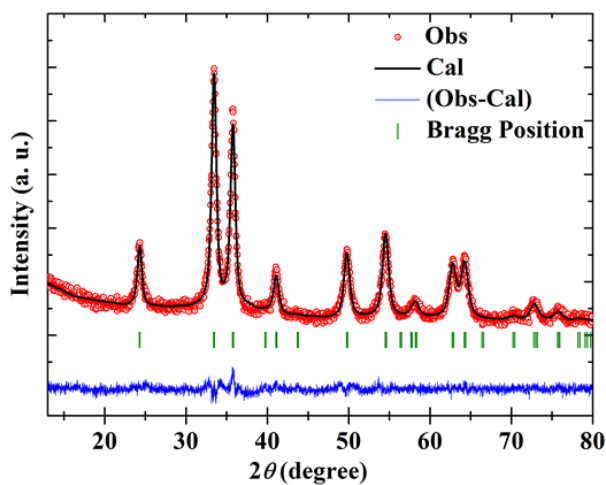


Figure 2.35: XRD patterns of ball-milled GaFeO_3 along with profile fit, difference pattern, and Bragg positions.

2.4.3.2.2 Raman spectroscopic study

The Raman spectrum of ball-milled GaFeO_3 ($R\bar{3}c$) is compared with that of the orthorhombic sample as well as that of the nanoparticles of GaFeO_3 synthesized by the sol-gel route. The Raman spectrum of the starting GaFeO_3 sample [Figure 2.36(a)] is similar to that of the nanoparticles of GaFeO_3 [Figure 2.36(b)], but we see distinct differences in the spectrum of ball-milled GaFeO_3 [Figure 2.36(c)]. After annealing the ball-milled GaFeO_3 at 700 °C, the spectrum remained the same [Figure 2.36(d)] except for sharpening of the bands. The Raman spectrum recorded after annealing the ball-milled sample at 1000 °C [Figure 2.36(e)] is similar to that of the starting GaFeO_3 sample [Figure 2.36(a)]. The XRD and Raman results clearly show that orthorhombic GaFeO_3 ($Pna2_1$) transforms directly to the rhombohedral $R\bar{3}c$ structure when subjected to ball-milling, unlike AlFeO_3 , which goes through an intermediate phase of $P2_12_12_1$ space group.

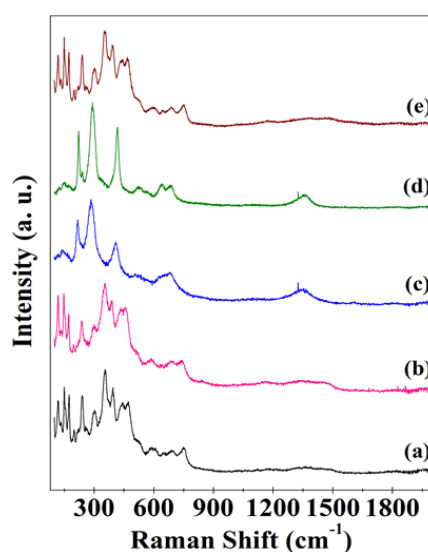


Figure 2.36: Raman spectra of (a) orthorhombic GaFeO_3 sample; (b) GaFeO_3 nanoparticles by sol-gel route; (c) ball-milled GaFeO_3 ; (d) ball-milled GaFeO_3 annealed at 700 °C and (e) ball-milled GaFeO_3 annealed at 1000 °C.

2.4.3.2.3 Magnetic property

In Figure 2.37, the temperature dependence of magnetization data of the $R\bar{3}c$ sample of GaFeO_3 under FC (field-cooled) and ZFC (zero-field cooled) conditions is shown. There is a divergence between the FC and ZFC data below 350 K, and there is no sharp ferrimagnetic transition. Thus, the magnetization curves are quite different from those of the orthorhombic structure GaFeO_3 , which shows a sharp ferrimagnetic transition at

210 K [8,14]. The magnitude of magnetization of the $R\bar{3}c$ sample is much smaller than that of the $Pna2_1$ sample showing the presence of prominent antiferromagnetic interaction. Nanoparticles of $GaFeO_3$ however, show similar magnetic behavior as that of the $Pna2_1$ $GaFeO_3$ sample, but with a higher T_N .

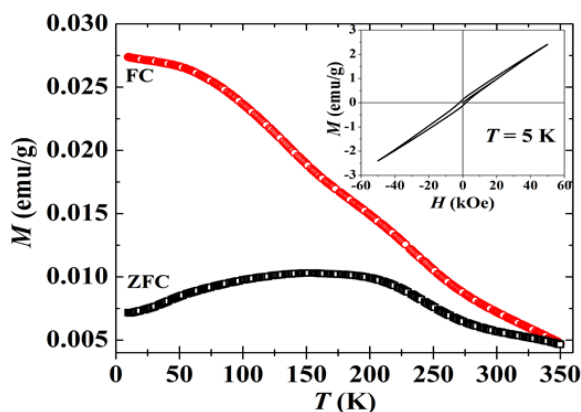


Figure 2.37: Temperature dependent dc magnetization of ball-milled $GaFeO_3$ under field-cooled (FC) and zero-field-cooled (ZFC) conditions. Insets show the magnetic hysteresis at 5 K.

Although $AlFeO_3$ and $GaFeO_3$ show different phase transition characteristics on ball-milling, it is interesting that partial substitution of Al by Ga in $AlFeO_3$ i.e. $Al_{0.5}Ga_{0.5}FeO_3$ favors the direct transformation of the $Pna2_1$ phase to the $R\bar{3}c$ phase [$a = 4.970$ (1) Å; $c = 13.509$ (3) Å] on ball-milling for the duration of 6 to 24 h without arriving at the $P2_12_12_1$ phase. On heating the ball-milled $Al_{0.5}Ga_{0.5}FeO$ to $1200^\circ C$, it reverts to the $Pna2_1$ structure [Figure 2.38]. XRD pattern and Raman spectrum of ball-milled sample of $Al_{0.5}Ga_{0.5}FeO_3$ are consistent with the $R\bar{3}c$ structure. We compare the lattice parameters of different structural phases among these compounds as displayed in Table 2.23.

Table 2.23: Structural data of the various phases of $Al_{1-x}Ga_xFeO_3$ ($x = 0, 0.5, 1$)

AlFeO ₃				
Structure	Space Group	<i>a</i> (Å)	<i>b</i> (Å)	<i>c</i> (Å)
Orthorhombic	$Pna2_1$	4.9806 (3)	8.5511 (6)	9.2403 (6)
Orthorhombic	$P2_12_12_1$	15.886 (11)	11.408 (4)	7.803 (4)
Rhombohedral	$R\bar{3}c$	4.909 (2)		13.393 (7)
GaFeO ₃				
Orthorhombic	$Pna2_1$	5.0814 (2)	8.7436 (3)	9.3910 (2)
Rhombohedral	$R\bar{3}c$	5.022 (2)		13.606 (5)
Al _{0.5} Ga _{0.5} FeO ₃				
Orthorhombic	$Pna2_1$	5.0306 (1)	8.6461 (2)	9.3175 (2)
Rhombohedral	$R\bar{3}c$	4.970 (1)		13.509 (3)

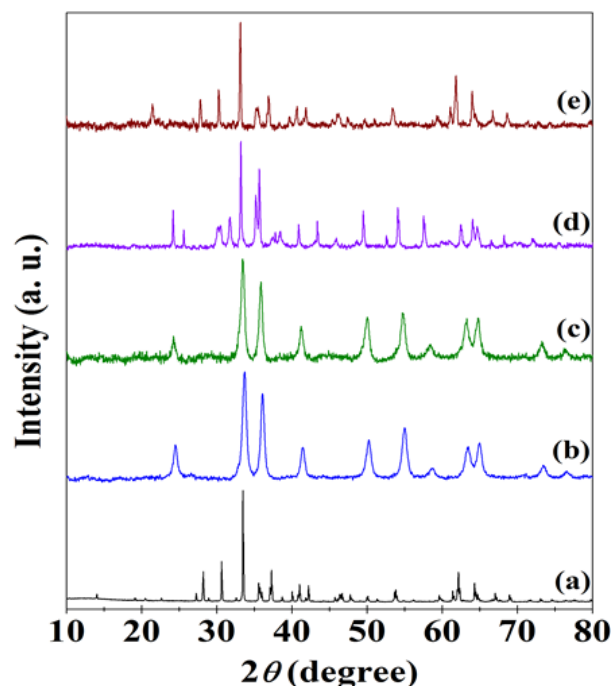


Figure 2.38: X-ray diffraction patterns of (a) orthorhombic $\text{Al}_{0.5}\text{Ga}_{0.5}\text{FeO}_3$ sample; (b) ball-milled $\text{Al}_{0.5}\text{Ga}_{0.5}\text{FeO}_3$ (12 h); (c) ball-milled $\text{Al}_{0.5}\text{Ga}_{0.5}\text{FeO}_3$ annealed at 700 °C; (d) mixture of Fe_2O_3 , Al_2O_3 , Ga_2O_3 (1:0.5:0.5) and (e) ball-milled $\text{Al}_{0.5}\text{Ga}_{0.5}\text{FeO}_3$ annealed at 1200 °C.

Now the structural transformation of AlFeO_3 in the light of the various transformations of Al_2O_3 will be discussed [31]. The most stable structure of Al_2O_3 is the α -form with the space group $R\bar{3}c$. We can view this structure as an HCP sublattice of oxygen anions in which Al^{3+} cations fill the 2/3 of the octahedral interstices in an ordered array. The oxygen anions occupy 18c Wyckoff positions, the coordinates of which are $x, 0, 1/4$ ($x = 0.306$), whereas the aluminium cations located at 12c positions have coordinates $0, 0, z$ ($z = 0.347$). Boehmite on heating to 700 °C and above gives rise to an orthorhombic δ -phase. The δ -phase of Al_2O_3 is different from the δ^* -phase mentioned by Fargeot *et al.* [32] compared to the structure of AlFeO_3 . The δ -phase derived from the spinel structure belongs to the $P2_12_12_1$ space group [33]. The orthorhombic structure found by us in AlFeO_3 and GaFeO_3 are akin to κ -phase of Al_2O_3 which has lattice parameters $a = 4.69 \text{ \AA}$, $b = 8.18 \text{ \AA}$ and $c = 8.87 \text{ \AA}$. The unit cell contains 16 cations ordered in octahedral and tetrahedral sites. The packing of oxygen anions is expected to remain nearly unaffected in Al_2O_3 through the phase transformations. The chemical ordering of cations in the FCC anion structure gives rise to different structures with partly disordered sublattice. While the orthorhombic structures order chemically, there will be considerable disorder in the $R\bar{3}c$ structure. Looking at the Al_2O_3 – Fe_2O_3 phase diagram [34,35], we find that at 50:50 composition

the orthorhombic phase is stable, but decompose to the α -phase of the two component oxides on heating. In our case of phase transformation, we obtain the $Pna2_1$ as the stable room temperature phase which further transforms to δ -phase of Al_2O_3 or $R\bar{3}c$ on ball-milling. It appears that the disorder kinetics favors the phase transformation rather than the relative stability and pressure effects. It is important to note that in our experiment we did not observe any decomposition of the orthorhombic $Pna2_1$ phase.

The important role of disorder kinetics and the change in molar volume is the driving force for the phase transformations which is also evident from the first-principles calculations carried out by Waghmare *et al.* [15]. We summarize the key observations below.

- (a) The minimum energy volume of the crystal cell (see results in Table 2.24) show that the corundum structure has a cell volume about 12 and 6% smaller than that of the orthorhombic structure of $AlFeO_3$ and $GaFeO_3$ respectively, suggesting a possible transition from the orthorhombic to corundum structure upon application of pressure. For the purpose of calculations, lowest energy structure of the orthorhombic phase with $Pna2_1$ space group have been used and but not considered the possibility of anti-site disorder between Al (or Ga) and Fe. On the other hand, for the corundum structure ($R\bar{3}c$ space group) with half the cation sites randomly chosen for occupation with Fe because Al_2O_3 is known to take this structure and there are no distinct cation sites. In the case of corundum structure anti-site disorder have been taken into account.

Table 2.24: Calculated equilibrium volumes (per formula unit), binding energies (per formula unit), bulk modulus for orthorhombic (Ort) and corundum (Cor) structures of $AlFeO_3$ and $GaFeO_3$ and their critical pressures for transition from orthorhombic to corundum structures

Compound	V (Ort) ($\text{\AA}^3/\text{fmu}$)	V (Cor) ($\text{\AA}^3/\text{fmu}$)	E (Ort) (eV/fmu)	E (Cor) (eV/fmu)	B (Ort) (GPa)	B (Cor) (GPa)	P_{crit} (GPa)
$AlFeO_3$	50.1	44.3	-37.59	-37.29	192	259.0	9.0
$GaFeO_3$	53.9	50.9	-33.89	-33.61	186	131.5	12.7

(b) The corundum structure is higher in energy than the orthorhombic one by about 0.3 eV per formula unit for both the compounds. Using the minimum energies, volumes and bulk moduli, and a parabolic approximation to the energy function, our estimates of the pressure of transition from the orthorhombic to corundum structure are quite similar for both AlFeO_3 and GaFeO_3 (slightly higher for GaFeO_3). We should note that the critical pressure for the orthorhombic to corundum structure would reduce with the disorder. We note that the estimated critical pressures for a transition from orthorhombic to corundum structure are relatively small and readily achievable in the laboratory conditions.

2.5 Conclusions

From x-ray and neutron diffraction studies of the $\text{Al}_{1-x}\text{Ga}_x\text{FeO}_3$ family of oxides, it is observed that all these oxides crystallize in the orthorhombic structure with the space group, $Pna2_1$. The unit cell parameters and volume of an $\text{Al}_{1-x}\text{Ga}_x\text{FeO}_3$ family of oxides increase with the Ga content. Interestingly, the temperature dependence of unit cell volume shows a marked increase in the 200-250 K regions along with a small dip around 150 K. The dimension of chemical and magnetic unit cells of these oxides are the same and all these oxides ferrimagnetically order around 200-250 K. Mössbauer spectroscopy gives useful information on site occupancies and the hyperfine field decreases with increasing Ga content. Cr substituted GaFeO_3 showed interesting magnetic properties. We observe that on the substitution of Cr in Fe site leads to a reduction in magnetic transition temperature (T_N) while T_N value slightly increases on Cr substitution at the Ga site as compared with parent GaFeO_3 . First-principles calculations show (1) greater anti-site disorder in GaFeO_3 than in AlFeO_3 due to better matching of ionic radii of Fe and Ga. (2) The weak magnetic moment arises from the difference in effective magnetic moments of Fe^{3+} at Fe1, Fe2 and Al2 sites. (3) The presence of strong spin-phonon coupling resulting from a significant difference in ionic radii of Fe^{3+} in high and low spin states (0.645 and 0.55 Å respectively). Both disorder and magnetic properties are intimately related to the local structure as well as ionic sizes. Raman spectroscopic study on AlFeO_3 establishes the existence of spin-phonon coupling in the magnetically ordered state.

Ball-milling brings about interesting structural transformations of AlFeO_3 and GaFeO_3 from the orthorhombic ($Pna2_1$) structure. The contrast between the structural behavior of AlFeO_3 and GaFeO_3 on ball-milling has been understood by invoking an intermediate phase that facilitates the transformation of AlFeO_3 from the orthorhombic phase. Since Al_2O_3 is known to occur in the δ structure with the $P2_12_12_1$ space group, it is understandable why this occurs as the intermediate structure in the transformation of AlFeO_3 . There is a change in volume in the transformations indicating their first order nature. It is noteworthy that partial substitution of Al by Ga in AlFeO_3 eliminates the $P2_12_12_1$ intermediate phase. While XRD and Raman spectroscopic data suffice to characterize the phase transitions fully, magnetic data also throw light on the transformed phases. The phases with the $Pna2_1$ structure exhibit sharp ferrimagnetic transitions, but the $R\bar{3}c$ phases are antiferromagnetic with much smaller values of magnetization and a high irreversibility temperature. In the case of AlFeO_3 , it is noteworthy that the orthorhombic structure seems to be more stable than the rhombohedral structure unlike in the case of Al_2O_3 .

Bibliography

- [1] W. Eerenstein, N. Mathur, and J. F. Scott, *Nature* **442**, 759 (2006).
- [2] C. N. R. Rao, A. Sundaresan, and R. Saha, *J. Phys. Chem. Lett.* **3**, 2237 (2012).
- [3] T. Kimura, T. Goto, H. Shintani, K. Ishizaka, T. Arima, and Y. Tokura, *Nature* **426**, 55 (2003).
- [4] Y. Yamasaki, S. Miyasaka, Y. Kaneko, J.-P. He, T. Arima, and Y. Tokura, *Phys. Rev. Lett.* **96**, 207204 (2006).
- [5] Y. Tokura and S. Seki, *Adv. Mater.* **22**, 1554 (2010).
- [6] J. Remeika, *J. Appl. Phys.* **31**, 263 (1960).
- [7] T. Arima *et al.*, *Phys. Rev. B* **70**, 064426 (2004).
- [8] R. Saha *et al.*, *J. Solid State Chem.* **184**, 494 (2011).
- [9] P. Kumar *et al.*, *Phys. Rev. B* **85**, 134449 (2012).
- [10] K. Kelm and W. Mader, *Z. Anorg. Allg. Chem.* **631**, 2383 (2005).
- [11] M. B. Mohamed, H. Wang, and H. Fuess, *J. Phys. D: Appl. Phys.* **43**, 455409 (2010).
- [12] R. Saha, A. Shireen, S. N. Shirodkar, U. V. Waghmare, A. Sundaresan, and C. N. R. Rao, *J. Solid State Chem.* **184**, 2353 (2011).

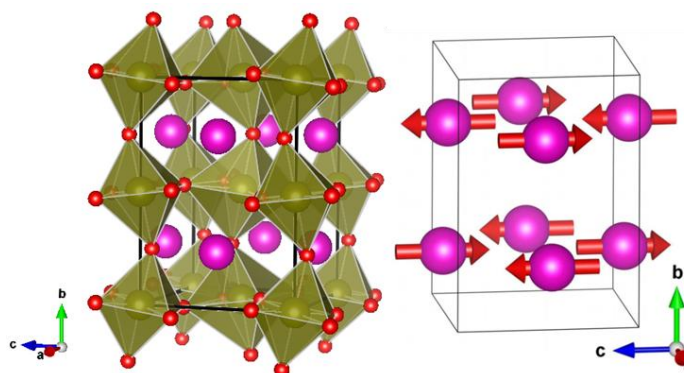
- [13] T. Nagai, D. Hamane, P. S. Devi, N. Miyajima, T. Yagi, T. Yamanaka, and K. Fujino, *The J. Phys. Chem. B* **109**, 18226 (2005).
- [14] R. B. Frankel, N. Blum, S. Foner, A. Freeman, and M. Schieber, *Phys. Rev. Lett.* **15**, 958 (1965).
- [15] R. Saha, A. Shireen, S. N. Shirodkar, M. S. Singh, U. V. Waghmare, A. Sundaresan, and C. N. R. Rao, *Inorg. Chem.* **50**, 9527 (2011).
- [16] M. Villafuerte-Castrejón, E. Castillo-Pereyra, J. Tartaj, L. Fuentes, D. Bueno-Baqués, G. González, and J. Matutes-Aquino, *J. Magn. Magn. Mater.* **272**, 837 (2004).
- [17] J. Rodríguez-Carvajal, *Physica B: Condens. Matter* **192**, 55 (1993).
- [18] F. Bourée, J.-L. Baudour, E. Elbadraoui, J. Musso, C. Laurent, and A. Rousset, *Acta Cryst.* **52**, 217 (1996).
- [19] E. F. Bertaut, in *Magnetism*, edited by G. T. Rado and H. Suhl (Academic Press, New York, 1963), Vol. 3.
- [20] E. Bertaut, *Acta Cryst.* **24**, 217 (1968).
- [21] K. Sharma, V. R. Reddy, D. Kothari, A. Gupta, A. Banerjee, and V. Sathe, *J. Phys.: Condens. Matter* **22**, 146005 (2010).
- [22] J. Laverdiere, S. Jandl, A. Mukhin, V. Y. Ivanov, V. Ivanov, and M. Iliev, *Phys. Rev. B* **73**, 214301 (2006).
- [23] K. Jonason, E. Vincent, J. Hammann, J. Bouchaud, and P. Nordblad, *Phys. Rev. Lett.* **81**, 3243 (1998).
- [24] A. Haldar, K. Suresh, and A. Nigam, *Europhys. Lett.* **91**, 67006 (2010).
- [25] W. Kim, J. H. We, S. J. Kim, and C. S. Kim, *J. Appl. Phys.* **101**, 09M515 (2007).
- [26] J. H. We, S. J. Kim, and C. S. Kim, *Magnetics, IEEE Trans.* **42**, 2876 (2006).
- [27] G. Amthauer, H. Annerste, and S. Hafner, *Z. Krist. Cryst. Mater.* **143**, 14 (1976).
- [28] L. Jianhua and S. Qingchi, *Rare Metals* **27**, 362 (2008).
- [29] Z. Yang, R. Zhang, L. Yang, and Y. Chang, *Mater. Res. Bull.* **42**, 2156 (2007).
- [30] S. W. Lee, S. Y. An, G. Y. Ahn, and C. S. Kim, *J. Appl. Phys.* **87**, 6238 (2000).
- [31] I. Levin and D. Brandon, *J. Am. Ceram. Soc.* **81**, 1995 (1998).
- [32] D. Fargeot, D. Mercurio, and A. Dauger, *Mater. Chem. Phys.* **24**, 299 (1990).
- [33] J. E. Bonevich and L. D. Marks, *J. Mater. Res.* **7**, 1489 (1992).
- [34] C. Levi, *Acta Mater.* **46**, 787 (1998).

-
- [35] A. D. Polli, F. F. Lange, C. G. Levi, and J. Mayer, *J. Am. Ceram. Soc.* **79**, 1745 (1996).

Crystallographic and magnetic structures of the magnetoelectric EuZrO_3 *

Summary

High-resolution temperature dependent synchrotron x-ray and neutron powder diffraction experiments have been carried out to investigate the crystal and magnetic structures of EuZrO_3 . From the neutron diffraction experiment we establish that in the ordered state, Eu^{2+} moments (G -type) in EuZrO_3 are oriented along the crystallographic c -axis while Eu^{2+} moments in EuTiO_3 are reported to lie in the ab -plane. Based on the antiferromagnetic vector direction along c in EuZrO_3 , we arrive at the magnetic space group symmetry ($Pn'm'a'$) which supports linear magnetoelectric effect in this compound. In addition, by applying Landau theory analysis to EuTiO_3 and EuZrO_3 , we are able to contrast the differing magnetoelectric coupling resulting from the different magnetic space groups of the Ti and Zr compounds in the magnetically ordered state. The observed order parameter (β) of EuZrO_3 obtained from the fitting of the temperature dependent integrated intensity of the (110) and (011) reflections is consistent with the asymptotic three dimensional Ising model.



*Paper based on this chapter is published in: Phys. Rev. B 93, 014409 (2016), © (2016) by the American Physical Society.

3.1 Introduction

Magnetoelectric Multiferroic materials enable to control the ferroelectric polarization with a magnetic field and the magnetization by an electric field [1,2]. These fascinating technologically advantageous materials with unique magnetoelectric coupling also allow us to investigate the fundamental interplay between magnetic and electric order parameters. Most commonly known multiferroics are perovskite oxides having a general formula ABO_3 , e.g., $TbMnO_3$ shows unambiguous, strong cross-coupling between the electric field and magnetization or vice-versa [3]. The only known perovskite which shows multiferroicity at room temperature is $BiFeO_3$, where weak ferromagnetism arises from the canting of the antiferromagnetically aligned spins [4,5].

$EuTiO_3$ has a cubic structure with the space group $Pm\bar{3}m$ and the small optical band gap of 0.8 eV while $EuZrO_3$ has an orthorhombic structure with the space group $Pnma$ and has a much higher optical band gap of about 2.4 eV [6,7]. However, these compounds exhibit similar magnetic properties where A -site Eu^{2+} ($S = 7/2$) ion undergoes a paramagnetic-to-antiferromagnetic (AFM) transition in the temperature range of 4-5 K. Neutron scattering and magnetic resonant X-ray diffraction techniques revealed the spin structure of $EuTiO_3$ and $EuZrO_3$ [8,9]. In Eu^{2+} containing perovskite oxides, nearest-neighbour superexchange interactions via the Ti or Zr d -states are antiferromagnetic (AFM) while the interaction with the next-nearest-neighbour is ferromagnetic (FM). In both Ti and Zr compounds G -type AFM ordering takes place below Néel temperature ($T_N = 5.3$ and 4.1 K) with the moments lying within the ab -plane along the plane diagonal and a -axis respectively. The stronger AFM superexchange interaction involving smaller energy gap between Eu $4f$ and Ti $3d$ -states in $EuTiO_3$ leads to the higher T_N in $EuTiO_3$ compared to $EuZrO_3$ where AFM interaction involves larger gap between Eu $4f$ and Zr $4d$ states. In these materials, a delicate balance exists between the AFM and FM states. For example, one can obtain the FM metallic state instead of the AFM insulator state in $EuTiO_3$ by strain [10] and hydride substitution [11].

Perovskite oxides based on divalent europium ions, like $EuTiO_3$ and $EuZrO_3$ having localized spin $S = 7/2$ are also being investigated experimentally and theoretically extensively to understand the intriguing correlation of magnetic and

dielectric properties giving rise to magnetoelectric effects. Figures 3.1 and 3.2 show the experimental demonstration of magnetodielectric effect in EuTiO_3 and EuZrO_3 respectively [12,13].

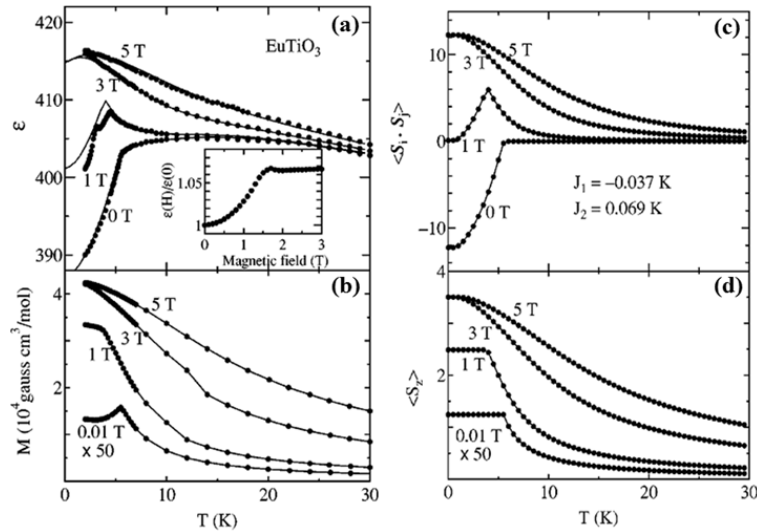


Figure 3.1: (a) Dielectric constants at 1 kHz and (b) magnetization as a function of temperature under several magnetic fields for EuTiO_3 . Solid lines in (a) are the fittings with the spin correlation function [$\epsilon(T, H) = \epsilon_0(T)(1 + \alpha \langle S_i \cdot S_j \rangle)$] where α (2.74×10^{-3}) is the coupling constant between spin correlation and dielectric constants. The inset shows the magnetic field dependence of the dielectric constant (normalized to the value at zero field) at 2 K; (c) spin pair correlation between nearest-neighbor sites $\langle S_i \cdot S_j \rangle$ and (d) the z component (parallel to the magnetic field) of the total magnetization $\langle S_z \rangle$ for the system with $S = 7/2$ on the cubic lattice by a mean-field calculation. The nearest-neighbor interaction J_1 is -0.037 K and the next-nearest-neighbor interaction J_2 is 0.069 K [adapted with permission from ref. 12, © (2001) by the American Physical Society].

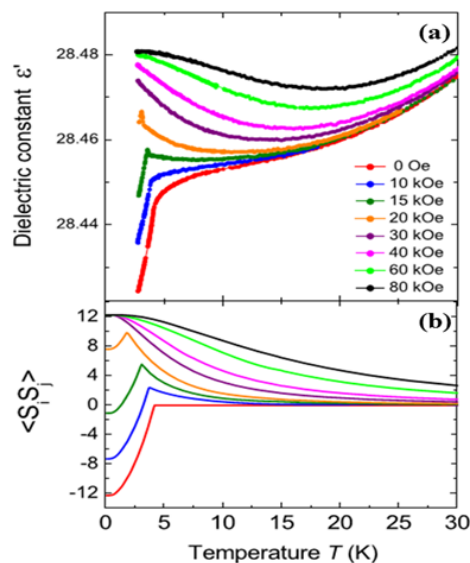


Figure 3.2: Temperature dependent dielectric constant of EuZrO_3 measured at 200 kHz in the presence of different magnetic field and (b) spin correlation function for cubic EuZrO_3 calculated using a mean-field approximation [adapted with permission from ref. 13, © (2010) by the AIP publishing LLC].

Both the compounds show a decrease in dielectric constant with antiferromagnetic ordering while the dielectric constant increases in the presence of a magnetic field due to the ferromagnetic arrangement of the Eu^{2+} moments. The occurrence of magnetodielectric effect in these compounds is understood based on the spin-pair correlation [$\varepsilon(T, H) = \varepsilon_0(T)(1 + \delta \langle S_i \cdot S_j \rangle)$], where $\varepsilon_0(T)$ is the dielectric constant in the absence of spin correlation, δ is the coupling constant between spin correlation and dielectric constants, $\langle S_i \cdot S_j \rangle$ is the spins on Eu sites next to each other; the coupling constant δ is related to the third-order susceptibility tensor in the Landau free energy expansion] between the nearest-neighbor Eu^{2+} spins through the variation of soft phonon mode frequency associated with the Ti or Zr vibrations against the O_6 octahedra [12]. Since the soft phonon mode (Slater) is coupled with localized Eu^{2+} spins which can be controlled by the magnetic fields, therefore on application of external magnetic field Eu-O-Eu superexchange interaction is modified which in turn controls the frequency of soft phonon mode. As a result, the dielectric constants of these materials are also strongly affected by the application of an external magnetic field indicating a strong coupling between magnetization and dielectric constant. The stronger magnetodielectric coupling in EuTiO_3 as compared to EuZrO_3 could be attributed to the stronger covalency of the Ti-O bond as compared to the Zr-O bond (more ionic in nature) favoring the formation of soft phonon mode (T_{1u}) which facilitates the coupling with the low energy magnetic excitations [14]. This result indicates that the spin phonon coupling in EuZrO_3 is smaller than EuTiO_3 . In this context it is also important to mention that the spin dependent hybridization of Eu-4*f* orbital with transition metal *d*-orbital which is the source of spin-lattice coupling actually drives the bulk EuTiO_3 away from ferroelectricity [15]. The increased Eu-Ti hybridization also lowers the energy and stabilizes the rotational lattice distortion in EuTiO_3 as compared to analogous compound SrTiO_3 [16].

3.2 Scope of the present investigation

To investigate the nuclear and magnetic structure of EuZrO_3 , we have carried out temperature dependent synchrotron x-ray and high-resolution neutron powder diffraction (time-of-flight) experiment respectively. High-resolution neutron diffraction allows us to determine the direction of easy axis unambiguously in the ordered state of

EuZrO₃. A proper knowledge of the magnetic easy axis is essential for a correct analysis of magnetic symmetry governing the magnetoelectric coupling. The previous report on neutron powder diffraction experiments in EuZrO₃ revealed *G*-type AFM ordering although the spin direction along the crystallographic axis could not be determined unambiguously. They obtained a better agreement when the magnetic moments were assumed to be aligned parallel to *a*-axis resulting in magnetic space group *Pnm'a* [9] which does not support linear magnetoelectric coupling in EuZrO₃. It has been shown theoretically in a recent paper [17] that the possible magnetic structure of EuZrO₃ could be isotropic *G*-AFM or anisotropic *A*-AFM. It is therefore extremely important to determine the spin-orientation with respect to the crystallographic directions in the orthorhombic perovskite EuZrO₃ as directional spin-orbit coupling play pivotal role in determining magnetoelectric coupling in these materials [4,5]. From the Rietveld analysis of high-resolution neutron powder diffraction pattern below Néel temperature of 4.4 K, we obtained the magnetic moment which is oriented along the *c*-axis corresponding to magnetic symmetry *Pn'm'a'* which allows linear magnetoelectric effect. Based on our analysis we observe that the Eu²⁺ ions attain a moment of 6.40 μ_B along *c*-axis at 1.5 K following the asymptotic three-dimensional (3D) Ising model with order parameter $\beta = 0.29$ [18].

3.3 Experimental details

Polycrystalline sample of EuZrO₃ was prepared by the conventional solid-state reaction in a reducing atmosphere of pure H₂ (99.9995%) starting from the binary oxides namely Eu₂O₃ (Sigma-Aldrich, 99.9%) and ZrO₂ (Fluka Chemika, 97%). Stoichiometric amounts of the precursors were mixed, ground and heated in a reducing atmosphere at 1400 °C for 24 hrs with several intermittent grindings. X-ray diffraction (XRD) patterns of the samples were recorded with a PANalytical monochromatic laboratory x-ray diffractometer ($\lambda = 1.5406 \text{ \AA}$) to confirm the phase purity. We have also recorded synchrotron XRD pattern at 298 and 10 K at ESRF, Grenoble (France). The FULLPROF suite [19] program was used to refine the crystallographic parameters obtained from x-ray diffraction. DC magnetization measurements were carried out using a Superconducting Quantum Interference Device Magnetometer (SQUID, MPMS3, Quantum Design, USA) in the temperature range of 2-390 K under Zero-field-cooled (ZFC) and Field-cooled (FC) conditions in the presence of different

magnetic fields. Isothermal magnetization measurement was carried out in the magnetic field range of ± 70 kOe. Neutron powder diffraction measurements were performed on the high-resolution long wavelength diffractometer (TOF) WISH [20] at the ISIS facility in zero applied magnetic field. To perform the neutron diffraction experiment, the powder sample was loaded in a 3 mm diameter thin walled vanadium can, lightly packed to minimize absorption. The Rietveld analysis of the neutron data was performed with the JANA2006 [21] software using standard scattering length densities and the Eu^{2+} form factor. The effect of neutron absorption was treated in the standard linear absorption coefficient manner and was not found to be significant.

3.4 Results and discussion

3.4.1 Crystal structure:

In Figure 3.3(a) Rietveld refinement of the XRD data of polycrystalline EuZrO_3 collected at room temperature using synchrotron x-ray source is shown. From the Rietveld refinement of XRD pattern, it is confirmed that this compound has an orthorhombic perovskite structure with the space group $Pnma$ at room temperature [9].

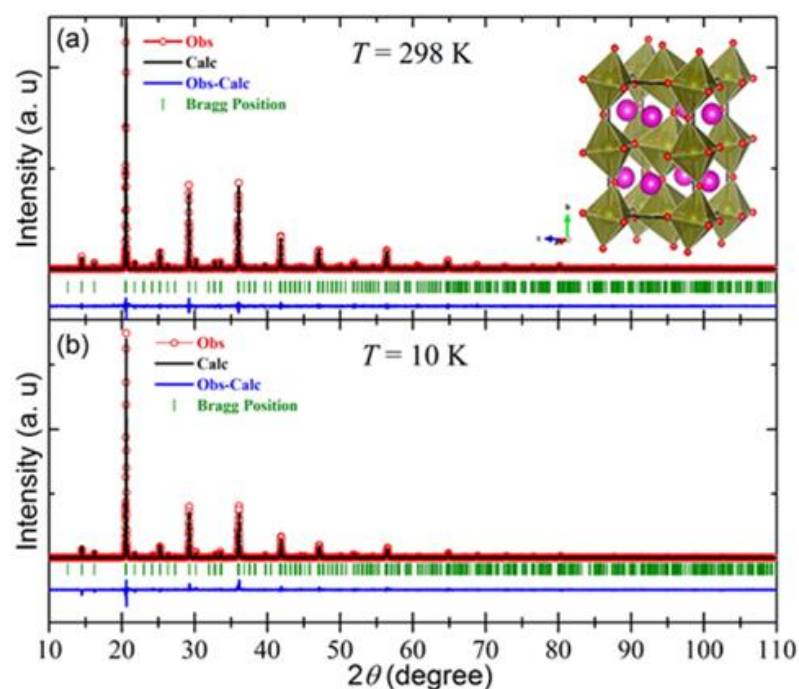


Figure 3.3: Rietveld refinement of XRD pattern of polycrystalline EuZrO_3 acquired at (a) 298 and (b) 10 K using synchrotron x-ray with wavelength = 1.0379 Å. Red open circle and solid black line indicate the experimental data and calculated profile, green ticks indicate the Bragg positions for the space group $Pnma$ and the blue line below is the difference between observed and calculated profile. Inset of (a) shows the schematic of the crystal structure of EuZrO_3 .

The sample contains a small amount of $\text{Eu}_2\text{Zr}_2\text{O}_7$ as an impurity phase. EuZrO_3 does not show any symmetry lowering or structural phase transition down to 10 K [Figure 3.3(b)]. In contrast, EuTiO_3 is known to show a structural phase transition from cubic $Pm\bar{3}m$ to tetragonal $I4/mcm$ structure at 235 K [22]. Neutron diffraction pattern of EuZrO_3 also shows that the compound retains the orthorhombic space group $Pnma$ down to lowest temperature ($T = 1.5$ K) which we will discuss later. For the structural refinement, we have used the $Pnma$ standard settings where Eu, Zr, O1, and O2 are present at $4c$, $4b$, $8d$ and $4c$ Wyckoff sites respectively. The structure of EuZrO_3 consists of corner shared ZrO_6 octahedra forming a perovskite network with the Eu^{2+} ions occupying the interstitial sites as shown in the inset of Figure 3.3(a). In EuZrO_3 the smaller tolerance factor, as compared to EuTiO_3 leads to a rotation of the ZrO_6 octahedra, resulting in GdFeO_3 type structural distortion. Though the octahedral rotation will facilitate the hybridization between the Eu $4f$ and Zr $4d$ states it will occur to a lesser extent in EuZrO_3 as compared to EuTiO_3 as a result of the larger band gap in the former as compared to the latter. The octahedral rotation will also lead to the change in the coordination environment of the Eu-site and alter the covalent bonding strength as well as hybridization between the Eu-O bonds. Importantly, the octahedral rotation has also impact on the strength of superexchange interaction other than optimizing the bonding of two cations [23]. Further, Akamatsu *et al.* in ref. [23] have pointed out that the firm correlation between octahedral rotation and magnetism in EuXO_3 ($X = \text{Ti, Zr, Hf}$) stabilizing the G -AFM ground state rather than FM state when the structure changes from cubic to orthorhombic.

3.4.2 Magnetic properties:

The temperature dependent dc magnetization data of EuZrO_3 at different magnetic fields is shown in Figure 3.4. The temperature dependent Zero-Field-Cooled (ZFC) and Field-Cooled (FC) data recorded in the presence of an applied magnetic field of 50 Oe show a sharp kink at 4.4 K without any divergence between the ZFC and FC data down to lowest temperature as shown in the inset of Figure 3.4(a). The kink at 4.4 K indicates the second order magnetic phase transition from the paramagnetic to the antiferromagnetic state which is also evident from the inverse susceptibility against temperature plot shown in the inset of Figure 3.4(a). Interestingly, the sharp kink gradually becomes broader with increasing magnetic field, and it completely disappears

at about 20 kOe as evident from the temperature dependent magnetization data shown in Figure 3.4 (a).

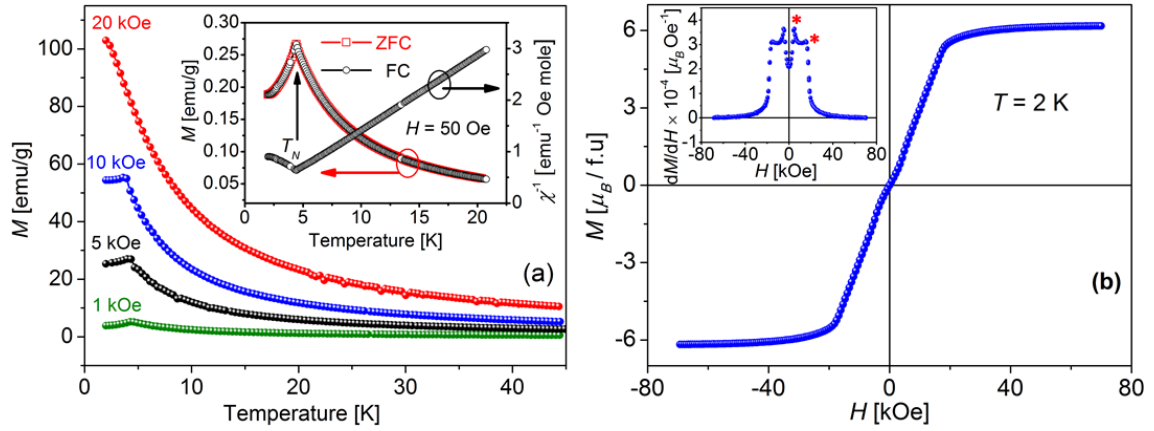


Figure 3.4: (a) Temperature dependent dc magnetization data recorded at various magnetic fields under Field-Cooled (FC) conditions. The inset shows the ZFC and FC magnetization and inverse susceptibility as a function of temperature at $H = 50$ Oe; (b) Isothermal magnetization data recorded at 2 K showing spin-flop behavior at the moderate magnetic field. The inset shows the first derivative of magnetization with respect to magnetic field plotted as a function of magnetic field.

Isothermal magnetization data as a function of magnetic field recorded at 2 K [Figure 3.4 (b)] shows linear behavior up to about 20 kOe. After that the magnetization data tends to be saturated indicating the appearance of ferromagnetic state with the saturation magnetization value around $6.2 \mu_B$ per formula unit which is close to the spin only moment of Eu^{2+} ($7\mu_B$) ion. From Figure 3.4 (b) we see that initially the slope of the M vs. H curve increases with the magnetic field and then the slope changes ~ 5 kOe which is prominent from the inspection of the derivative plot as shown in the inset of Figure 3.4(b). This phenomenon is similar to the spin-flop transition where spins in the antiferromagnetic state start flipping perpendicular to the magnetic field and then gradually changes to the ferromagnetic state with increasing magnetic field. Spin flipping continues with increasing magnetic field up to 20 kOe where all the spins go to the ferromagnetic state. It is consistent with the observation of $M(T)$ data, where the kink in the temperature dependent magnetization data disappears in the presence of a magnetic field of 20 kOe. This spin flop behavior at moderate magnetic fields occurs due to the weak inter sublattice molecular field coefficient (A_{mf}) and a small uniaxial magnetic anisotropy constant (K_u) of Eu^{2+} ion ($S = 7/2$, $L = 0$) [6]. At $T = 0$ K, the spin-flop field is represented as $H_C = (2K_u A_{mf})^{1/2}$. Such a magnetic field induced change in spin configuration also affects the dielectric properties of EuZrO_3 significantly as shown in Figure 3.2.

3.4.3 Magnetic structure:

Now we will discuss the results obtained from the neutron diffraction experiment. From the Rietveld refinement of neutron diffraction pattern [Figure 3.5] recorded in the paramagnetic region ($T = 10$ K) we observe that the compound remains in the orthorhombic structure with the space group $Pnma$, a similar agreement obtained from the synchrotron XRD pattern. In Table 3.1 we report the crystal structure parameters. The refined thermal parameters are consistent with manageable absorption effects for the transmission geometry (used in the experiment) as evident from the absence of a large sloping background in the neutron diffraction data shown in Figure 3.5.

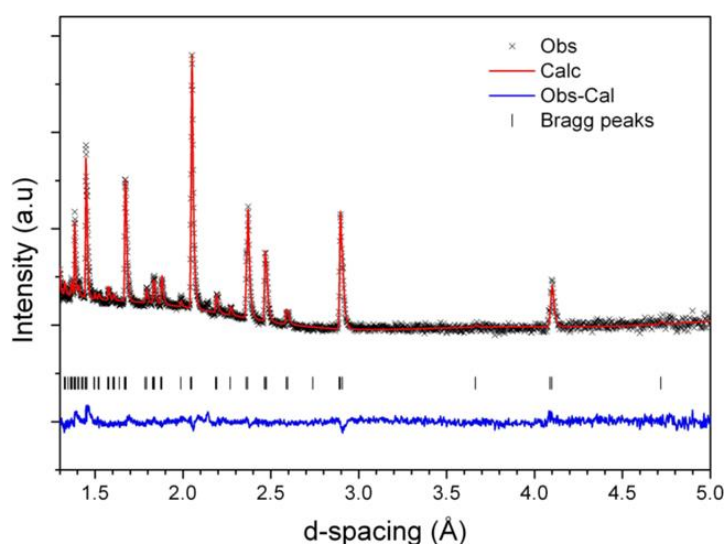


Figure 3.5: The Rietveld refinement of the time-of-flight (TOF) neutron data acquired at $T = 10$ K. The black crosses represent the neutron data, and the red and blue lines represent the calculated profile and its difference to the data respectively. The black lines show the positions of the Bragg peaks.

Table 3.1: Structural parameters of EuZrO_3 at 10 K

EuZrO ₃ (Space Group: $Pnma$)					
$a = 5.8172$ (2) Å, $b = 8.1805$ (2) Å, $c = 5.7833$ (2) Å					
Atom (Position)	x	y	z	U_{iso} (Å ²)	Occupancy
Eu (4c)	0.0237 (11)	0.25	0.4853 (15)	0.002 (1)	1.0
Zr (4b)	0	0	0	0.002 (1)	1.0
O1 (8d)	0.2784 (9)	0.0427 (6)	0.2123 (9)	0.007 (2)	1.0
O2 (4c)	0.4807 (16)	0.25	0.5702 (16)	0.007 (2)	1.0
$R_p = 1.82$ %, $R_{wp} = 2.03$ %, goodness-of-fit = 1.65					

In Figure 3.6 we show the refinement of the neutron diffraction data collected at 1.5 K. As the magnetically ordered phase appears, magnetic contribution in some of the Bragg peaks become apparent, indicating a propagation vector $\vec{k} = (0\ 0\ 0)$ pointing out that the magnetic and chemical unit cells are of the same dimension. Neutron diffraction is an ideal technique for the internal calibration of the magnetic moment as the magnetic scattering contribution gets added to the nuclear scattering as the temperature approaches the AFM transition. From the refinement below, we obtain the collinear G -type antiferromagnetic structure for the Eu^{2+} ions in the $Pn'm'a'$ magnetic space group with a moment of $6.40(2)\ \mu_B$ along the c direction [inset of Figure 3.6]. The obtained magnetic moment is quite close to the theoretically predicted moment of $6.82\ \mu_B$ for the Eu^{2+} ions [24]. There is also agreement with our magnetometry measurements.

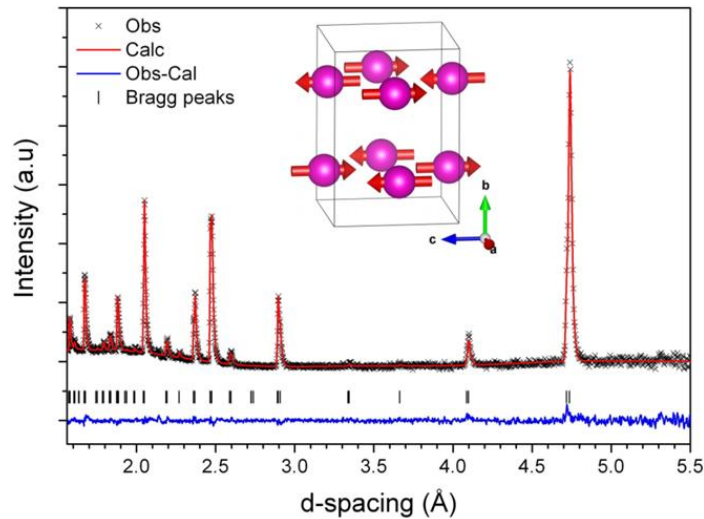


Figure 3.6: The Rietveld refinement of the time-of-flight (TOF) neutron data acquired at $T = 1.5$ K. The black crosses represent the neutron data and the red and blue lines represent the calculated profile and its difference from the data respectively. The black lines show the positions of the Bragg peaks. The inset shows a schematic of the G -type antiferromagnetic structure in the $Pn'm'a'$ Shubnikov group. The agreement factors are $R_p = 1.99\%$, $R_{wp} = 2.25\%$ and goodness-of-fit = 1.62.

Now we focus on the high d -spacing region of the neutron powder diffraction pattern collected at 1.5 K as shown in Figure 3.7. Although the presented data in Figure 3.7 is broadly consistent with the earlier result [9], higher resolution of our time-of-flight (TOF) data allows to distinguish the (110) and (011) reflections and becomes crucial in solving the magnetic structure. The refinement indicates the alignment of spins on the Eu^{2+} ions along the c -axis which results in the magnetic space group, $Pn'm'a'$. The relative intensities of (110) and (011) Bragg reflections were found to be

strongly dependent on the preferred orientation of the spin of Eu^{2+} ions along a particular axis of this orthorhombic structure. In the right panel of Figure 3.7 we have shown the results of our refinements assuming different orientations of the Eu^{2+} magnetic moments, corresponding to the different magnetic space groups. The calculated data agree with the measured intensity profile only when we assume the spins are orientated along c -axis of this G -AFM magnetic structure.

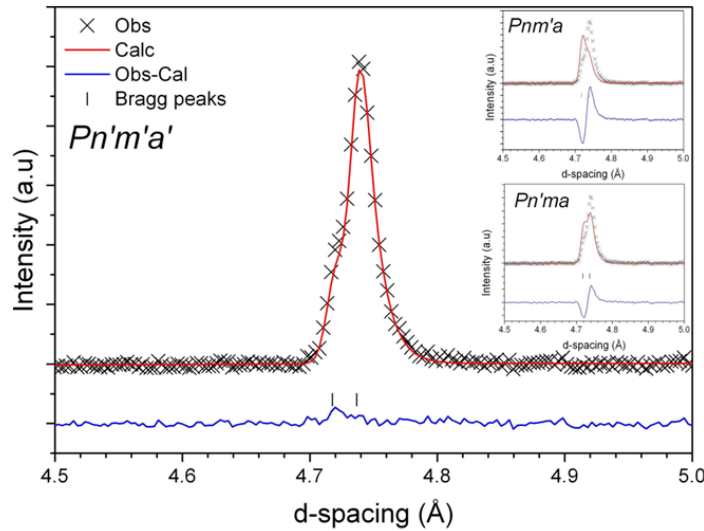


Figure 3.7: The experimental time-of-flight (TOF) neutron data (black) for the (110) and (011) reflections recorded at $T = 1.5$ K. In the main panel of Rietveld refinement, the red and blue lines represent the calculated profile and its difference from the data respectively. The right inset shows the calculated profile assuming that the orientation of spins along a -axis ($Pnm'a$) or b -axis ($Pn'ma$), upper and lower curves respectively. Both of these models fail to accurately represent the data.

It is noteworthy that the closeness of the d spacing (and respective neutron wavelength) for these two reflections minimizes the effect of sample absorption on the subsequent interpretation. It is evident from the calculated profiles that the assumption of spin-orientation along the a -axis ($Pnm'a$) and b -axis ($Pn'ma$) presented in right inset of Figure 3.7 does not reproduce the measured data. It should be mentioned here that in the previous neutron diffraction measurement [9] the R -factors for these three different magnetic structures were fairly similar and authors pointed out that with the Eu moment lying along the a -axis ($Pnm'a$) gives a slightly better fit. However, the better resolution of the data presented here clearly indicates that the moments lie along the c -axis ($Pn'm'a'$) as shown in Figures 3.6 and 3.7. Of these two mentioned magnetic space groups ($Pnm'a$ and $Pn'm'a'$) the second one (as proposed from our refinement) allows a linear magnetoelectric effect while the latter does not [25]. It is important to highlight the difference between the moment direction in the two

compounds EuZrO_3 and EuTiO_3 . In order to avoid misunderstanding due to the different cell choice and space group of the two compounds, it is worthwhile to describe the moment direction with respect to the BO_6 octahedra. In the case of the EuTiO_3 compound the Eu^{2+} moments point towards the void left by the octahedra networks, whereas in the case of the EuZrO_3 the Eu^{2+} moments point towards the apical oxygen of the BO_6 polyhedra.

In Figure 3.8 we have plotted the background corrected integrated intensity of the (110) and (011) peaks as a function of temperature to analyze the magnetic scattering with temperature. We fit the data with a power law (the red curve) of the form $I \propto \left(\frac{T-T_c}{T_c}\right)^{2\beta}$ yielding a T_c of 4.0(1) K and $\beta = 0.29(4)$. The critical exponent $\beta = 0.29(4)$ is consistent with the asymptotic three dimensional (3D) Ising model.

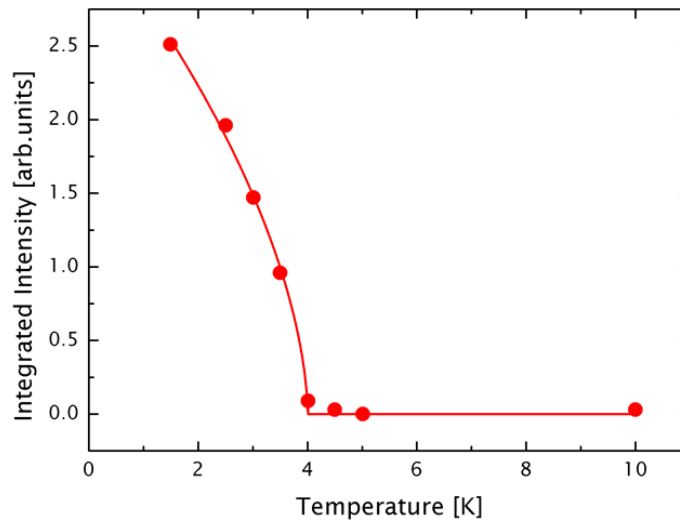


Figure 3.8: The background corrected integrated intensity of the (110) and (011) reflections as a function of temperature. The intensity increases below $T_N \sim 4.1$ K. The solid line is the power-law fit.

Based on the literature report, AFM order of an epitaxial EuTiO_3 film follows either the 3D Heisenberg model with an exponent of $\beta = 0.385$ or larger $\beta = 0.496$, depending upon the strain induced by the substrates [26]. The value of exponent compares with 0.373 in a bulk single crystal [27]. The Eu^{2+} moments in both the Zr [27] and Ti [12] are treated as Heisenberg-like, given their spin only moment. Interestingly, in our zero field data we see evidence of a reduced β consistent with an Ising-like symmetry. The interpretation is in conformity with the weak spin-flop transition as observed in the magnetometry data and implies a weak anisotropy which we easily overcome with an applied field greater than 5 kOe. As reported, this is only a

weak anisotropy given the isotropic nature of the $4f$ electrons and the weak sublattice interactions [6].

3.4.4 Magnetic symmetry analysis:

Based on the obtained result of magnetic easy axis we now analyze the magnetic symmetry. Magnetic anisotropy, which arises primarily due to spin-orbit coupling, plays a major role in determining the magnetoelectric coupling. Based on the symmetry analysis we compare the different nature of the magnetoelectric coupling between Ti and Zr compounds. Based on the reported G -type AFM structure of EuTiO_3 with the magnetic moments aligned along the diagonal of the tetragonal ab -plane, we obtain the magnetic space group ($Fm'mm$) with the help of ISODISTORT software [28]. The magnetic space group of EuZrO_3 is $Pn'm'a'$ obtained based on our neutron diffraction experiment.

By writing the Landau theory of free energy F in terms of the i th component of an applied magnetic field H and an applied electric field E , we can describe the magnetoelectric effect. We write the Landau free energy constructed based on the magnetic point group for both the compounds up to fourth order as:

$$F(E, H) = \varepsilon_{ik} E_i E_k + \chi_{ik} H_i H_k + \alpha_{ik} E_i H_k + \delta_{iklm} E_i E_k H_l H_m \quad (3.1)$$

From the expansion of free energy, it is observed that there is a possibility of linear and biquadratic magnetoelectric coupling in both the Ti and Zr system. In Table 3.2 we summarize the allowed components of α_{ik} and δ_{iklm} in the contracted matrix form [25]. Regarding the linear magnetoelectric tensor α_{ik} , the only allowed coefficients from the magnetic point group ($m'mm$) of EuTiO_3 are the off-diagonal terms α_{23} and α_{32} , while for EuZrO_3 the magnetic point group, $m'm'm'$, allows only the diagonal terms α_{11} , α_{22} and α_{33} . Therefore based on the magnetic symmetry analysis, it becomes apparent that allowed linear magnetoelectric tensors are different in both the materials as a result of different magnetic point group symmetry. Interestingly, the fourth rank tensor δ_{iklm} which is related to the giant magnetocapacitance effect at the magnetic transition [29] has the same internal symmetry for the two materials, though of course, the values of the tensor components may be different.

Table 3.2: Magnetolectric tensor components α_{ik} and δ_{iklm} for EuXO_3 ($X = \text{Ti, Zr}$)

	EuTiO ₃	EuZrO ₃
Magnetic point group	$m'mm$	$m'm'm'$
α_{ik}	$\begin{bmatrix} 0 & 0 & 0 \\ 0 & 0 & \alpha_{23} \\ 0 & \alpha_{32} & 0 \end{bmatrix}$	$\begin{bmatrix} \alpha_{11} & 0 & 0 \\ 0 & \alpha_{22} & 0 \\ 0 & 0 & \alpha_{33} \end{bmatrix}$
δ_{iklm}	$\begin{bmatrix} \delta_{11} & \delta_{12} & \delta_{13} & 0 & 0 & 0 \\ \delta_{21} & \delta_{22} & \delta_{23} & 0 & 0 & 0 \\ \delta_{31} & \delta_{32} & \delta_{33} & 0 & 0 & 0 \\ 0 & 0 & 0 & \delta_{44} & 0 & 0 \\ 0 & 0 & 0 & 0 & \delta_{55} & 0 \\ 0 & 0 & 0 & 0 & 0 & \delta_{66} \end{bmatrix}$	

From the above discussion, it becomes clear that the different nature of magnetolectric coupling in these two systems is caused by the different magnetic space groups of the ordered structure. However, the magnetic symmetry analysis cannot predict the strength of magnetolectric coupling because it depends on the specific microscopic coupling mechanism. For example, the partially covalent Ti-O bond in EuTiO_3 favors a soft phonon mode which then couples to the magnetic excitations [14], in contrast to the more ionic-like Zr-O bond in EuZrO_3 [13]. Improved covalency suggests a larger magnetolectric coupling in the Ti system over the Zr one.

3.5 Conclusions

In conclusion, our results of a high-resolution time-of-flight (TOF) neutron powder diffraction study clearly demonstrates that Eu^{2+} moments direction in the magnetically ordered state of EuZrO_3 is along c -axis. In contrast, in the case of EuTiO_3 , Eu^{2+} spin orientation is along the diagonal of ab -plane. Moreover, by applying Landau theory, we indicate the symmetry allowed magnetolectric coupling in the EuXO_3 ($X = \text{Ti, Zr}$) compounds, and highlight the distinct tensor properties in the two materials induced by the different magnetic groups which describe the differing magnetolectric behaviors. The presented magnetic structure obtained in this perovskite oxide is intriguing given the first principles calculations [15,30] have revealed critically balanced states between the antiferromagnetic and ferromagnetic ordering and shows a spin flop transition at moderate magnetic fields. It will be interesting to study magnetic structure of EuZrO_3 as a function of strain [10] and hydride substitution [11] as demonstrated for EuTiO_3 .

Bibliography

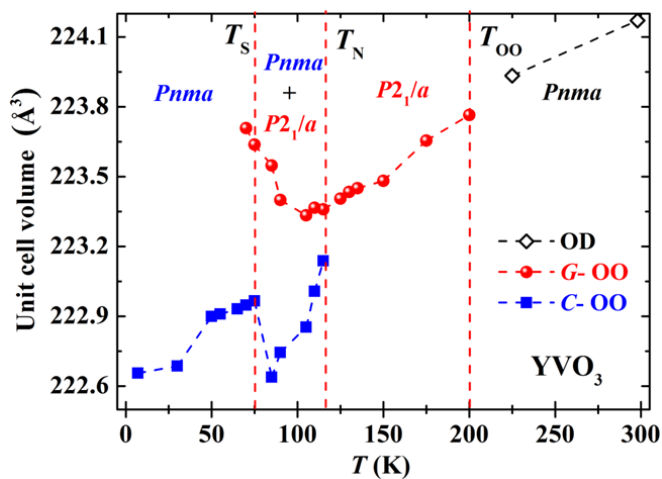
- [1] W. Eerenstein, N. Mathur, and J. F. Scott, *Nature* **442**, 759 (2006).
- [2] C. N. R. Rao, A. Sundaresan, and R. Saha, *J. Phys. Chem. Lett.* **3**, 2237 (2012).
- [3] T. Kimura, T. Goto, H. Shintani, K. Ishizaka, T. Arima, and Y. Tokura, *Nature* **426**, 55 (2003).
- [4] J. Heron *et al.*, *Nature* **516**, 370 (2014).
- [5] I. A. Sergienko and E. Dagotto, *Phys. Rev. B* **73**, 094434 (2006).
- [6] H. Akamatsu *et al.*, *Inorg. Chem.* **51**, 4560 (2012).
- [7] B. J. Kennedy, G. Murphy, E. Reynolds, M. Avdeev, H. E. Brand, and T. Kolodiazhnyi, *J. Phys.: Condens. Matter* **26**, 495901 (2014).
- [8] V. Scagnoli, M. Allieta, H. Walker, M. Scavini, T. Katsufuji, L. Sagarna, O. Zaharko, and C. Mazzoli, *Phys. Rev. B* **86**, 094432 (2012).
- [9] M. Avdeev, B. J. Kennedy, and T. Kolodiazhnyi, *J. Phys.: Condens. Matter* **26**, 095401 (2014).
- [10] J. H. Lee *et al.*, *Nature* **466**, 954 (2010).
- [11] T. Yamamoto, R. Yoshii, G. Bouilly, Y. Kobayashi, K. Fujita, Y. Kususe, Y. Matsushita, K. Tanaka, and H. Kageyama, *Inorg. Chem.* **54**, 1501 (2015).
- [12] T. Katsufuji and H. Takagi, *Phys. Rev. B* **64**, 054415 (2001).
- [13] T. Kolodiazhnyi, K. Fujita, L. Wang, Y. Zong, K. Tanaka, Y. Sakka, and E. Takayama-Muromachi, *Appl. Phys. Lett.* **96**, 252901 (2010).
- [14] V. Goian, S. Kamba, J. Hlinka, P. Vaněk, A. Belik, T. Kolodiazhnyi, and J. Petzelt, *Eur. Phys. J. B* **71**, 429 (2009).
- [15] C. J. Fennie and K. M. Rabe, *Phys. Rev. Lett.* **97**, 267602 (2006).
- [16] T. Birol and C. J. Fennie, *Phys. Rev. B* **88**, 094103 (2013).
- [17] H. Ai-Yuan, Q. Guo-Ping, W. Zhi-Min, and C. Yu-Ting, *Chin. Phys. B* **24**, 067501 (2015).
- [18] R. Saha, A. Sundaresan, M. K. Sanyal, C. N. R. Rao, F. Orlandi, P. Manuel, and S. Langridge, *Phys. Rev. B* **93**, 014409 (2016).
- [19] J. Rodríguez-Carvajal, *Physica B: Condens. Matter* **192**, 55 (1993).
- [20] L. C. Chapon *et al.*, *Neutron News* **22**, 22 (2011).
- [21] V. Petříček, M. Dušek, and L. Palatinus, *Z. Kristallogr.* **229**, 345 (2014).

-
- [22] M. Allieta, M. Scavini, L. J. Spalek, V. Scagnoli, H. C. Walker, C. Panagopoulos, S. S. Saxena, T. Katsufuji, and C. Mazzoli, *Phys. Rev. B* **85**, 184107 (2012).
- [23] H. Akamatsu, Y. Kumagai, F. Oba, K. Fujita, K. Tanaka, and I. Tanaka, *Adv. Fun. Mater.* **23**, 1864 (2013).
- [24] Z.-L. Zhu, J.-H. Gu, Y. Jia, and X. Hu, *Physica B: Condens. Matter* **406**, 3985 (2011).
- [25] R. E. Newnham, *Properties of Materials: Anisotropy, Symmetry, Structure: Anisotropy, Symmetry, Structure* (Oxford University Press, 2005).
- [26] P. Ryan *et al.*, *Nat. commun.* **4**, 1334 (2013).
- [27] J.-W. Kim, P. Thompson, S. Brown, P. S. Normile, J. A. Schlueter, A. Shkabko, A. Weidenkaff, and P. J. Ryan, *Phys. Rev. Lett.* **110**, 027201 (2013).
- [28] B. J. Campbell, H. T. Stokes, D. E. Tanner, and D. M. Hatch, *J. Appl. Crystallogr.* **39**, 607 (2006).
- [29] V. Shvartsman, P. Borisov, W. Kleemann, S. Kamba, and T. Katsufuji, *Phys. Rev. B* **81**, 064426 (2010).
- [30] R. Ranjan, H. S. Nabi, and R. Pentcheva, *J. Phys.: Condens. Matter* **19**, 406217 (2007).

Temperature effects on the structural aspects of YVO_3 *

Summary

A temperature dependent synchrotron x-ray diffraction experiment carried out on polycrystalline YVO_3 showing the distribution of lattice parameters at all temperatures as well as the coexistence of monoclinic (G -type orbital order) and orthorhombic (C -type orbital order) phases in the temperature range, $T_S < T < T_N$. The appearance of C -type orbital-ordered state ($Pnma$) at T_N in the background of G -type orbital-ordered state ($P2_1/a$) is triggered by the magnetic exchange striction, in addition to the increased GdFeO_3 type octahedral distortion. The phase coexistence in YVO_3 in $T_S < T < T_N$, gains additional stabilization from the lattice strain associated with the difference in unit cell volume. The distribution of lattice parameters has also been observed for other orthovanadates. The origin of lattice parameters distribution has been suggested to be due to strain resulting from the fact that $R\text{VO}_3$ (R = rare-earth and Y) is prepared from $R\text{VO}_4$ by hydrogen reduction.



*Paper based on this chapter is submitted for publication.

4.1 Introduction

RVO_3 (R = rare-earth and Y) family of compounds with the perovskite structure provide an interesting and rich playground to explore the complex interplay among spin, charge, orbital and lattice degrees of freedom [1-5]. Importantly, various physical properties of RVO_3 are strongly coupled with the spin and orbital-ordered states which depend on the cationic radii of the A -site ions [6]. In this distorted orthovanadates, $V^{3+}(d^2)$ ions present at the octahedral coordination undergo crystal field splitting resulting in the occupation of two valence electrons in the triply degenerated t_{2g} orbitals. In the low-temperature Jahn-Teller (JT) ordered state, a tetragonal distortion of the V^{3+} octahedra leads to the splitting of the t_{2g} orbitals into a singlet of higher energy and a doublet of lower energy. The doublet contains d_{xy} orbital which remains always occupied, and either d_{zx} or d_{yz} orbital would be occupied alternatively on the neighboring V^{3+} sites giving rise to orbital-ordered (OO) state [3,7]. In RVO_3 , two types of orbital ordering are found to be present, e.g., G - and C -type orbital ordering (OO) which have been observed from many experimental techniques [8-10]. In G -type orbital ordering, the d_{zx} and d_{yz} orbitals are alternately occupied along three orthogonal directions. In C -type orbital ordering, the d_{zx} and d_{yz} orbitals are alternately occupied in the ab plane and similar orbitals (either d_{zx} or d_{yz}) are occupied along the c direction as shown schematically in Figure 4.1 [5]. In RVO_3 , Jahn-Teller active V^{3+} ions undergo antiferromagnetic ordering below the orbital ordering transition ($T_{OO} \sim 180$ -200 K), indicating that the orbital interactions among t_{2g} orbitals are weak. In $RMnO_3$, Mn^{3+} ions with the electronic configuration $t_{2g}^3 e_g^1$ are also Jahn-Teller active. In $LaMnO_3$, the e_g orbital undergoes orbital ordering at very high temperature ($T_{OO} \sim 800$ K) followed by A -type antiferromagnetic ordering at low temperature ($T_N \sim 150$ K) indicating that the orbital interactions among the e_g orbitals are strong [10-12]. In contrast to RVO_3 , in $LaMnO_3$ the orbital order-disorder phase transition involving the e_g orbital, does not change the structural symmetry, not even with the application of pressure [11,13].

The appearance of G -OO state in RVO_3 is accompanied by the change in crystal symmetry from orthorhombic ($Pnma$) to monoclinic symmetry ($P112_1/a$; $\gamma \neq 90^\circ$, c is

unique axis). In the C -OO state the orthorhombic symmetry is preserved except there exists long and short V-O bond lengths which alternate along the $[110]$ and $[1\bar{1}0]$ directions of the ab plane due to Jahn-Teller distortion. On the other hand, in the orbital disordered state with the orthorhombic symmetry, all the V-O distances in the ab -plane are nearly similar [14]. Interestingly, due to the strong coupling between spin and orbital-ordered states [15] and Goodenough-Kanamori-Anderson (GKA) rule [16,17], the G -OO favours C -type spin ordering (C -SO) while C -OO leads to G -type spin ordering (G -SO) as shown in Figure 4.1.

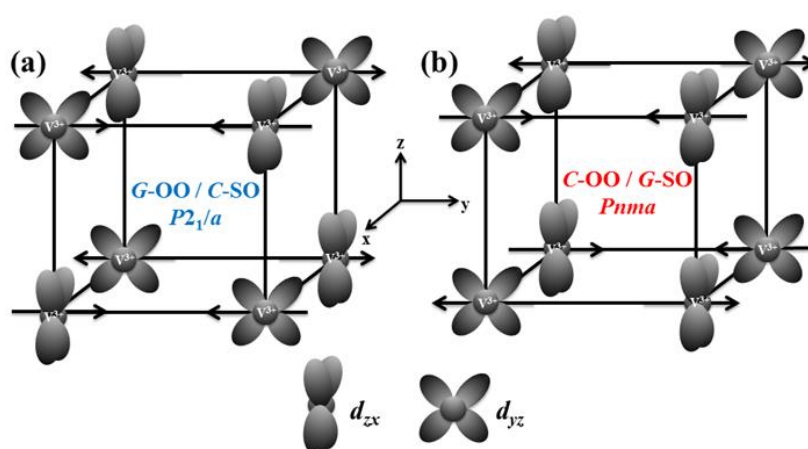


Figure 4.1: Schematic representation of (a) G -type and (b) C -type orbital ordering (OO) in RVO_3 with the nominal cubic perovskite axes, respectively. The arrows indicate the directions of magnetic moment on V^{3+} ion in the magnetically ordered state, where C -SO indicates that spin ordering along c -axis is ferromagnetic, and G -SO indicates that spin ordering along all the three orthogonal directions is antiferromagnetic in nature. For convenience, only occupied d_{zx} and d_{yz} orbitals are shown while d_{xy} orbital remains always filled.

In RVO_3 family of compounds, a series of temperature-induced structural phase transitions between states with a different spin and orbital-ordered configurations have been reported. For $R = \text{La-Tb}$, the ground state configuration of RVO_3 is G -OO/ C -AF (AF - antiferromagnetic), while for $R = \text{Dy-Lu}$ and Y , it undergoes a further phase transition at low temperature from G -OO/ C -AF to C -OO/ G -AF which is the ground state configuration. Later, it is found that in DyVO_3 four transitions occur. G -type orbital ordering at $T_{\text{OO}} = 190$ K, the C -type of antiferromagnetic phase transition at $T_N = 113$ K followed by the orbital phase transition from G -OO/ C -AF to C -OO/ G -AF at $T_{\text{CG1}} \sim 57 - 64$ K, and finally a re-entrant transition to G -OO/ C -AF at $T_{\text{CG2}} \sim 12 - 22$ K [18]. In DyVO_3 , it has been demonstrated using a magnetic field that C -OO can be switched to G -OO with the concomitant result of the change in G -SO to C -SO [19]. In the case of YVO_3 , it shows orbital disordered orthorhombic phase ($Pnma$) in the

temperature range of 300-200 K followed by *G*-type orbital ordered monoclinic phase ($P112_1/a$) in the region of 200-77 K, and finally, *C*-type orbital ordered orthorhombic phase ($Pnma$) below 77 K ($Pnma$) [20].

Interestingly, rare-earth ions having ionic radii larger than Dy^{3+} are known to exhibit a region of phase coexistence of *G*- and *C*-type orbital ordering of different symmetry below antiferromagnetic ordering, driven by magnetic exchange striction which mediates the coupling between orbital and lattice, whereas rare-earth ions which have ionic radii $\leq \text{Dy}^{3+}$ show complete and sharp orbital phase transition due to increasing magnitude of octahedral tilting of VO_6 octahedra [6,21]. It has been reported that in the solid solution, $\text{Dy}_{0.8}\text{Tb}_{0.2}\text{VO}_3$, both *G*- and *C*-type orbital ordered states coexist in the temperature range of 2-60 K where the phase fraction is temperature and magnetic field dependent [18]. On the other hand, independent structural studies performed on single crystalline TbVO_3 and SmVO_3 by employing neutron [4] and synchrotron x-ray diffraction [22] respectively, did not find any evidence of orthorhombic symmetry with *C*-OO state below the magnetic transition. Interestingly, a recent report on TmVO_3 finds coexistence of structural phases of orthorhombic and monoclinic symmetry with *C*- and *G*-type orbital ordered states between $T_N \sim 105$ K and $T_S \sim 75$ K [23]. In TmVO_3 , the formation of orthorhombic phase (*C*-OO) in the background of monoclinic phase (*G*-OO) at T_N indicates that the appearance of orthorhombic phase is triggered by antiferromagnetic transition [23]. Moreover, the effect of hydrostatic pressure on the orbital-ordered states of $R\text{VO}_3$ has also been reported in the literature. It has been observed that in YVO_3 and TbVO_3 ground state orbital configuration completely quenches to *C*-OO state at an applied pressure of 6 and 8 GPa respectively [24]. Therefore, the rich structural diversity in $R\text{VO}_3$ family of compounds is indeed interesting.

4.2 Scope of the present investigation

Motivated by the rich structural features of $R\text{VO}_3$, we have investigated the different structural phases of YVO_3 associated with orbital order/disorder states as a function of temperature by employing synchrotron x-ray diffraction technique. The present study indicates that the phase coexistence is not only limited to $R\text{VO}_3$ with intermediate radii of rare-earth cation or TmVO_3 but could be independent of the size of the rare-earth

ions which requires careful investigation. Careful analysis x-ray diffraction data of YVO_3 collected at room temperature reveals a highly asymmetric nature of some Bragg peaks which could only be modelled with a distribution of lattice parameters with the same orthorhombic symmetry ($Pnma$). Rietveld refinement of the ambient condition x-ray diffraction pattern of rare-earth orthovanadates with the intermediate size rare-earth cations ($R = \text{Sm}, \text{Eu}, \text{Gd}, \text{and Tb}$) also show the existence of multiple lattice parameters. Interestingly, we see that such a lattice parameter distribution is also observed in low-temperature G -type ($P112_1/a$) and C -type ($Pnma$) orbital ordered phases. The origin of lattice parameters distribution has been suggested to be due to strain which could result from the fact that these samples are prepared from $R\text{VO}_4$ by hydrogen reduction. The sample preparation method that involves different temperatures and annealing conditions determine the extent of lattice parameter distribution. We also report the occurrence of phase coexistence of G -type ($P112_1/a$) and C -type ($Pnma$) orbital ordered states in the temperature range between $T_S \sim 77 \text{ K}$ and $T_N \sim 116 \text{ K}$. Below T_S , the coexisting structural phases transform to the C -OO state ($Pnma$) which is in correspondence with the reported literature. The appearance of C -type orbital-ordered state ($Pnma$) at T_N in the background of G -type orbital-ordered state ($P2_1/a$) is triggered by the magnetic exchange striction, in addition to the increased GdFeO_3 type octahedral distortion. The phase coexistence in YVO_3 in $T_S < T < T_N$, gains additional stabilization from the lattice strain associated with the difference in unit cell volume.

4.3 Experimental details

The polycrystalline samples of $R\text{VO}_3$ ($R = \text{Sm}, \text{Eu}, \text{Gd}, \text{Tb}, \text{and Y}$) were prepared by reducing the $R\text{VO}_4$ under a pure H_2 (99.9995 %) atmosphere at $1400 \text{ }^\circ\text{C}$ for 24 hrs with several intermittent grinding to improve the homogeneity of the phase pure $R\text{VO}_3$. The polycrystalline powders of $R\text{VO}_4$ were prepared by the conventional solid-state reaction starting from the stoichiometric amounts of respective binary rare-earth oxides e.g., Sm_2O_3 (Alfa Aesar, 99.9 %), Eu_2O_3 (Alfa Aesar, 99.9 %), Gd_2O_3 (Indian Rare Earths Ltd., 99.99 %), Tb_4O_7 (Alfa Aesar, 99.99 %), Y_2O_3 (Alfa Aesar, 99.99 %) and V_2O_5 (Sigma-Aldrich, 99.99 %). The respective oxides were mixed, ground and heated in air at $1000 \text{ }^\circ\text{C}$ and $1200 \text{ }^\circ\text{C}$ for the duration of 12 hrs with intermediate grinding. Also, we have prepared YVO_3 samples under mild reducing condition in the presence of Ar/H

and lower annealing temperatures (800 and 1000 °C) separately. We confirmed the phase purity of the polycrystalline samples of RVO_4 and RVO_3 by acquiring x-ray diffraction data at room temperature with a PANalytical Empyrean diffractometer using monochromatic $CuK\alpha_1$ radiation with wavelength, $\lambda = 1.5406 \text{ \AA}$. Temperature dependent synchrotron x-ray diffraction on YVO_3 was carried out using x-rays of two different wavelengths $\lambda = 0.32$ and 0.48 \AA at material science powder diffraction beamline (BL04-MSPD) of the ALBA synchrotron facility [25,26]. A software package FULLPROF suite [27] was used for the treatment of diffraction pattern and Rietveld analysis. Temperature dependent dc magnetization and ac magnetic susceptibility measurements of YVO_3 were carried out using Superconducting Quantum Interference Device Magnetometer (SQUID, MPMS3) and Physical Property Measurement System (PPMS), Quantum Design, USA, respectively to determine the magnetic phase transition temperatures. Thermogravimetric Analysis (TGA) was carried out with a Perkin-Elmer Pyris1 instrument. About 20-30 mg sample was loaded into a furnace using a platinum crucible and heated to the target temperature at the rate of $10 \text{ }^\circ\text{C}/\text{min}$.

4.4 Results and discussion

4.4.1 Ambient condition x-ray diffraction study in RVO_3 ($R = Y, \text{Sm}, \text{Eu}, \text{Gd}, \text{Tb}$):

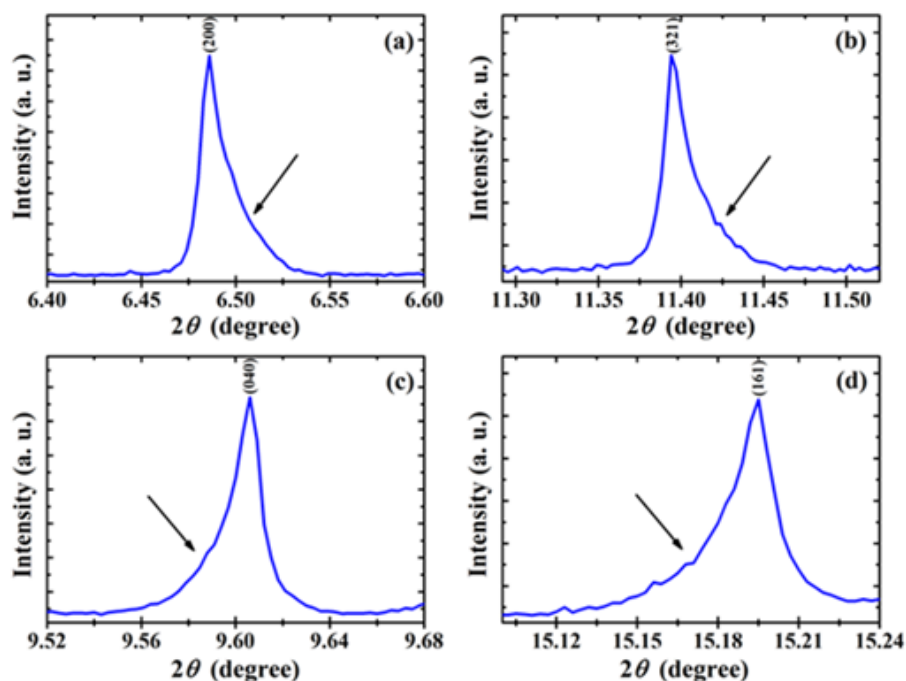


Figure 4.2: Synchrotron x-ray diffraction data of polycrystalline YVO_3 at 298 K using monochromatic x-rays with wavelength $\lambda = 0.32 \text{ \AA}$, showing asymmetric broadening (indicated by an arrow) of selected reflections at (a), (b) higher and (c), (d) lower angle, respectively.

Analysis of synchrotron XRD data of YVO_3 collected at ambient condition confirmed that the compound crystallizes in the orthorhombic structure ($Pnma$) as reported earlier [4]. However, from a careful inspection of ambient condition XRD profile, we found that the profile of the reflections (200, 220, 202, 321) and (022, 040, 042, 004, 161) are highly asymmetric with a Lorentzian tail on the side of higher and lower angles, respectively as shown in Figure 4.2. Secondary phase cannot account such an asymmetric broadening, and we have considered the possibility of lattice parameter distribution with the same orthorhombic structure ($Pnma$) [28].

To analyze the asymmetric broadening of the reflection we have performed Rietveld refinement with two sets of lattice parameters under the consideration of same $Pnma$ space group as shown in Figure 4.3. Inset of Figure 4.3 shows the enlarged view of fitted XRD pattern of YVO_3 across the highest intensity region indicating the goodness of fit to the asymmetric reflections, (200) and (210) as shown by the arrow. The structural parameters obtained from the Rietveld refinement of ambient condition XRD pattern are shown in Table 4.1.

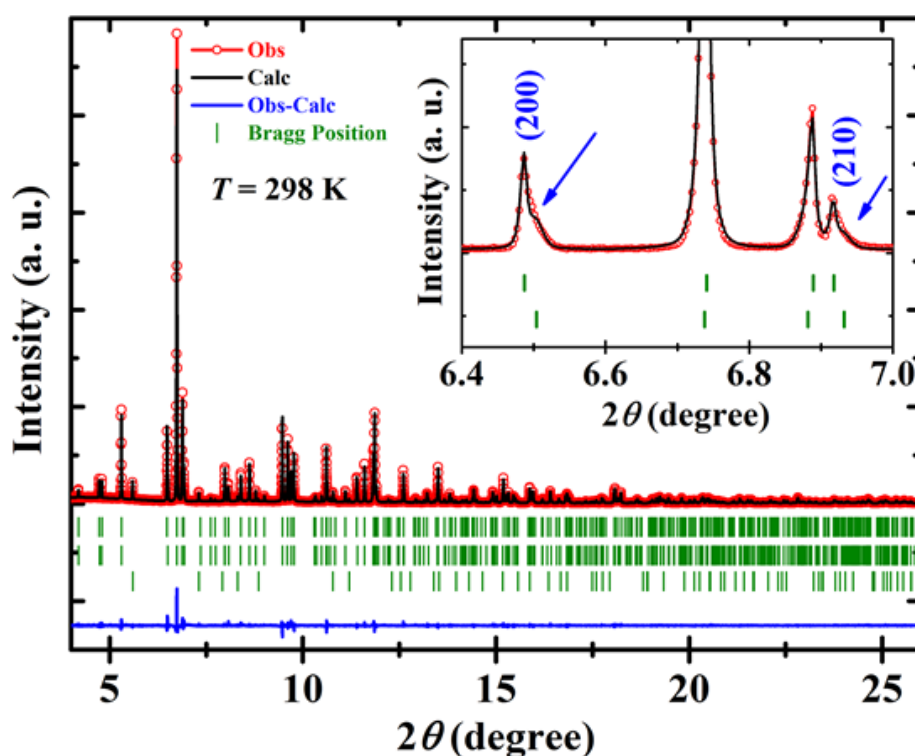


Figure 4.3: The Rietveld refinement of synchrotron x-ray diffraction pattern of polycrystalline YVO_3 at 298 K using a wavelength of $\lambda = 0.32 \text{ \AA}$. The inset shows the enlarged view of Bragg peaks across the highest intensity to reveal the asymmetry in (200) and (210) peaks (indicated by an arrow). First, two Bragg positions are associated with the two different sets of lattice parameters under the space group $Pnma$, and the last Bragg positions are due to the TiO_2 (Rutile phase) originated from the cryostat.

Table 4.1: Structural parameters of YVO_3 at 298 K

Space Group: $Pnma$ (Orthorhombic)					
$a = 5.60413$ (1) Å, $b = 7.57320$ (2) Å, $c = 5.27781$ (1) Å					
Atom (Position)	x	y	z	B_{iso} (Å ²)	Occupancy
Y (4c)	0.0690 (2)	0.25	0.9798 (2)	0.39 (2)	1.0
V (4b)	0	0	0.5	0.31 (3)	1.0
O1 (4c)	0.4538 (12)	0.25	0.1135 (14)	0.42 (5)	1.0
O2 (8d)	0.3028 (9)	0.0595 (8)	0.6907 (11)	0.42 (5)	1.0

$R_B = 3.24$ %, $R_F = 3.59$ %, $\chi^2 = 1.94$ %

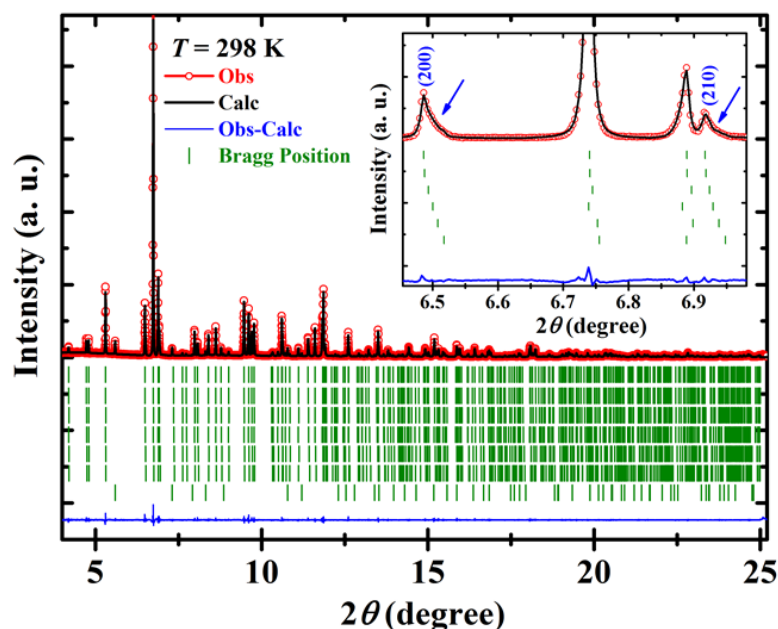


Figure 4.4: The Rietveld refinement of synchrotron x-ray diffraction pattern of polycrystalline YVO_3 at 298 K ($\lambda = 0.32$ Å) fitted with six sets of lattice parameters under the space group $Pnma$ and the 7th Bragg positions are due to the TiO_2 (Rutile phase) originated from the cryostat.

In fact, it is possible to have the better goodness of fit as we introduce more sets of lattice parameters [Figure 4.4]. However, to obtain reasonable structural parameters we limited to only two sets of lattice parameters. Since we prepare the samples under reducing conditions, so to find the oxygen content we performed thermogravimetric analysis (TGA). The experiment shows that the starting compound ($\text{YVO}_{3\pm\delta}$) gains 8.75 % weight while heating in the presence of oxygen resulting in the transformation to YVO_4 , which is confirmed by the x-ray diffraction. From the weight gain, we have calculated the oxygen content of starting compound to be ~ 2.97 [Figure 4.5].

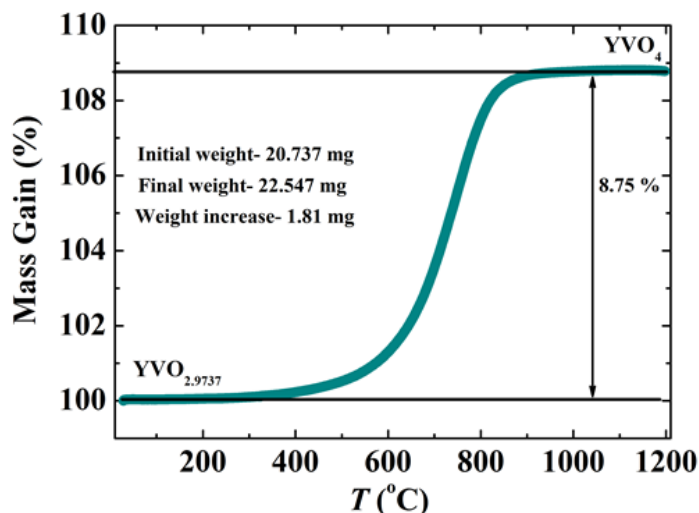


Figure 4.5: TGA curves (weight gain as a function of temperature) of YVO_3 recorded in the presence of oxygen atmosphere to determine the initial oxygen content of the sample.

The distribution of cell parameters in these samples can arise from strain or oxygen distribution which should not be a surprise as these samples are prepared from RVO_4 by reducing under a hydrogen atmosphere. This observation prompted us to check the role of the synthetic condition in controlling the oxygen content and distribution throughout the sample. Therefore, we have synthesized YVO_3 under mild reducing condition (Ar/H) at lower annealing temperature (800 °C) and recorded XRD pattern at room temperature using laboratory monochromatic x-ray.

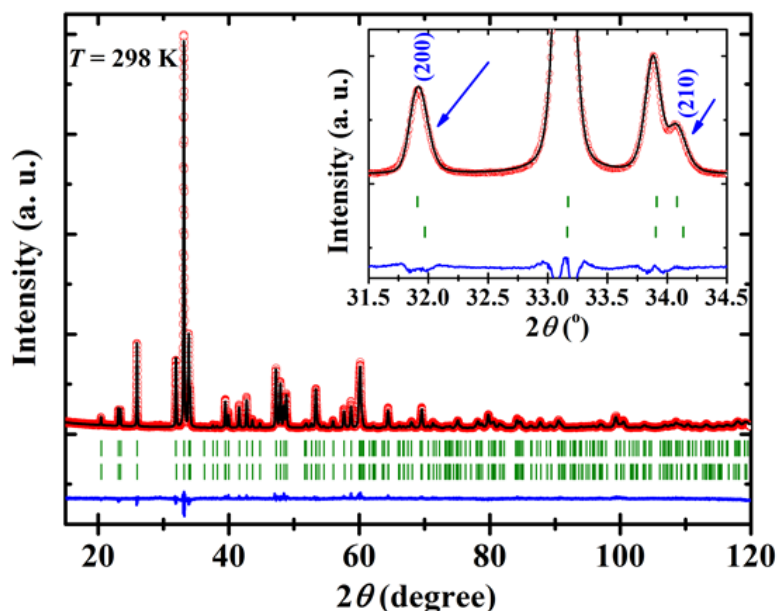


Figure 4.6: The Rietveld refinement of x-ray diffraction pattern of polycrystalline YVO_3 prepared at 800 °C under reducing condition, crystallizing in the orthorhombic perovskite structure ($Pnma$), acquired at 298 K using a monochromatic laboratory x-rays with wavelength $\lambda = 1.5406$ Å. Inset shows the enlarged view of Bragg peaks across the highest intensity to reveal the asymmetry in (200) and (210) peaks (indicated by an arrow).

In Figure 4.6 we show the Rietveld refinement on the XRD pattern which reveals reduced asymmetry in the reflections. The expanded view of the highest intensity region (inset of Figure 4.6) shows that (200) and (210) reflections are more symmetric compared to the sample prepared at higher temperature indicating the vital role of the synthetic condition in controlling the distribution of lattice parameters. The degree of peak asymmetry which strongly depends on the synthetic condition is also evident from Figure 4.7. From this figure, it is seen that mild reducing condition and lower annealing temperature reduce the asymmetric broadening while strong reducing condition and higher annealing temperature enhance the asymmetry in the XRD reflections.

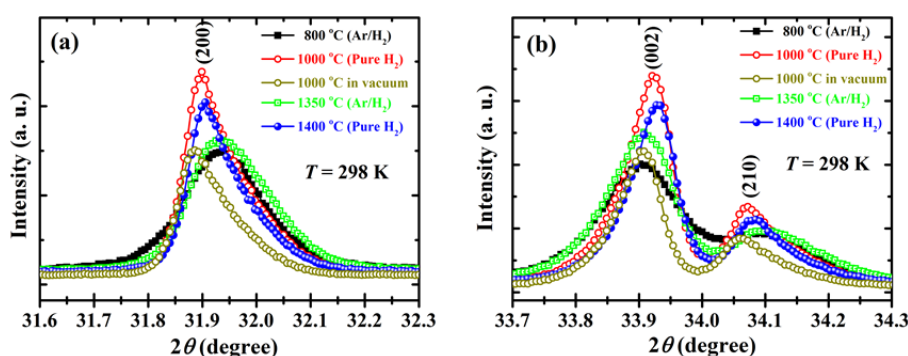


Figure 4.7: Synthetic condition dependence of broadening of XRD peaks of YVO_3 . The XRD data was acquired at 298 K using a monochromatic laboratory x-rays with wavelength $\lambda = 1.5406 \text{ \AA}$.

In the context, we mention here that, we see similar asymmetric reflections in the XRD pattern of other $R\text{VO}_3$ compounds with intermediate size rare-earth ions ($R = \text{Sm}, \text{Eu}, \text{Gd}, \text{and Tb}$) recorded at the ambient condition as shown in Figure 4.8. It is important to mention that all these samples are free of impurities, and therefore the existence of lattice parameter distribution at ambient condition is the intrinsic nature of chemically phase pure YVO_3 and other orthovanadates. Thus, these results demonstrate that $R\text{VO}_3$ prepared from $R\text{VO}_4$ will have different extent of lattice parameter distribution depending on the nature of reducing condition and annealing temperature.

However, such an asymmetric broadening is also reported in the synchrotron data of GdVO_3 collected at 295 K [6]. From ref. [6], we can clearly see the asymmetric broadening of (321) reflection [considering $Pnma$ symmetry]. We see similar asymmetry in the (321) reflection of YVO_3 (as well in GdVO_3) and to account that asymmetric broadening we have modelled the synchrotron XRD data with two phases (both under the consideration of $Pnma$ symmetry) to improve the goodness of fit as shown in Figure 4.9. The requirement of two phases does not mean there is structural

phase separation at room temperature rather it indicates the distribution of lattice parameters which is the main origin of asymmetric broadening.

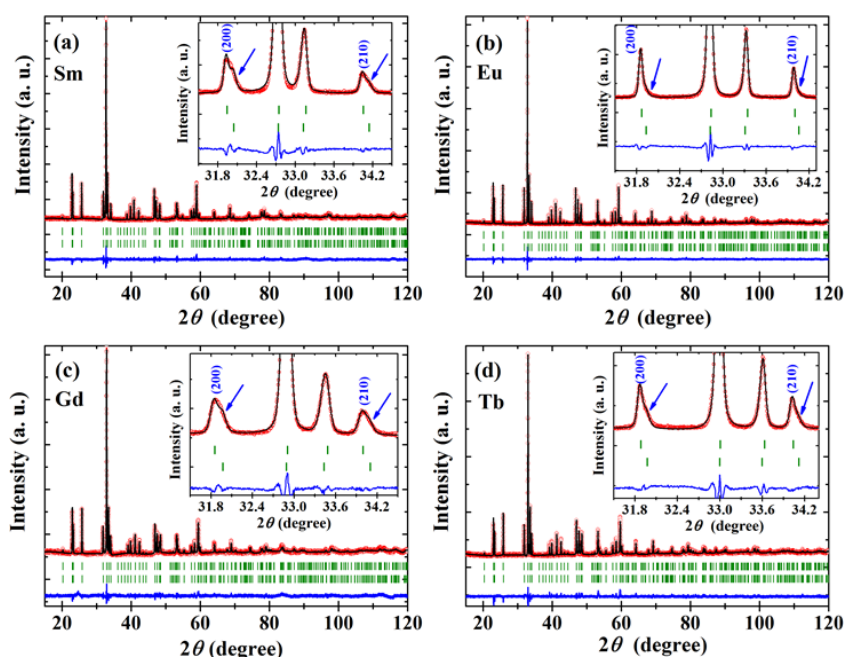


Figure 4.8: The Rietveld refinement of x-ray diffraction pattern of polycrystalline (a) SmVO_3 , (b) EuVO_3 , (c) GdVO_3 and (d) TbVO_3 crystallizing in the orthorhombic perovskite structure ($Pnma$), acquired at 298 K using monochromatic laboratory x-rays with wavelength $\lambda = 1.5406 \text{ \AA}$. Insets of (a), (b), (c) and (d) show the enlarged view of Bragg peaks across the highest intensity to reveal the asymmetry in (200) and (210) peaks (indicated by an arrow). Red open circle and the solid black line indicate the experimental data and calculated profile; green ticks indicate the Bragg positions and the blue line below is the difference between observed and calculated profile.

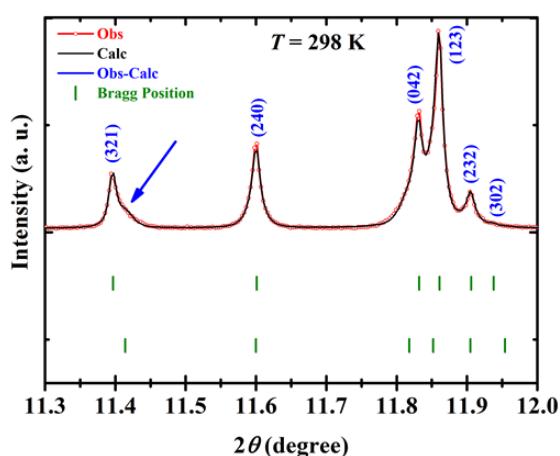


Figure 4.9: The Rietveld refinement of synchrotron x-ray diffraction pattern of polycrystalline YVO_3 at 298 K using a wavelength of $\lambda = 0.32 \text{ \AA}$, showing the asymmetry in (321) reflection which has been fitted well by considering two different sets of lattice parameters.

In ref. [6] authors have explained the occurrence of asymmetry in the ($h00$) and ($0k0$) reflections [considering $Pnma$ symmetry] by linking with the evolution of a and b lattice parameters as a function of temperature at the onset of G -type OO state. The

asymmetric tail represents a range of a and b lattice parameters which has been accounted based on the martensitic-type transition where inside the main matrix (main peak), a fraction of the sample has a range of slightly different lattice parameters (reflected in the asymmetric tail part). However, the observation of peak asymmetry in the reported literature is only limited to the rare-earth ions with larger size and only observable below the orbital ordering temperatures. According to the reported data, as the ionic radius of the rare-earth ions become smaller, this phenomenon appearing at T_{OO} would disappear because the rate of increase in a and decrease in b lattice parameter would be smaller as compared to rare-earth ions with the larger size. In contrast, our observation of asymmetric ($h00$) and ($0k0$) reflection in YVO_3 at room temperature suggests that the asymmetry is due to strain arises from the oxygen distribution controlled by the synthetic conditions as illustrated in Figures 4.6 and 4.7.

4.4.2 Low-temperature x-ray diffraction study in YVO_3 :

Since we observe the distribution of lattice parameters in YVO_3 at ambient conditions, due to the distribution of oxygen content, we were curious to explore the presence of such lattice parameter distribution at low temperatures. With this motivation, synchrotron x-ray diffraction data on YVO_3 were collected at low temperatures and the results of Rietveld refinement are shown for 90 and 7 K XRD data in Figure 4.10. From the analysis of Rietveld refinement of the XRD data of YVO_3 recorded at 90 K [Figure 4.10(a)], we infer that the modeling of XRD pattern requires a mixture of two crystallographic phases with the monoclinic ($P112_1/a$) and orthorhombic ($Pnma$) symmetry. In the previous report, no such phase coexistence has been reported in YVO_3 at this temperature [20]. In YVO_3 , only a short range correlation or fluctuation of C -type orbital order coexisting with the G -type OO state has been suggested based on Raman spectroscopic study [29]. Such an orbital fluctuation can lower the symmetry of G -type OO state from $P112_1/a$ to $P11a$ symmetry where the VO_6 octahedra form a dimerized chain along the c -axis [30,31]. Similar observation was also reported in $HoVO_3$ by Blake *et al.* [31] in the temperature range between T_{OO} and T_S . Since the ionic radii of Y^{3+} and Ho^{3+} are nearly identical, therefore in our sample there is a possibility of reduction of crystallographic symmetry further below to $P11a$ in the G -type OO state. Since our sample is polycrystalline in nature, we could not confirm the existence of any symmetry other than $P112_1/a$ and hence we stick to the monoclinic

space group associated with the G -type OO state. To determine the accurate symmetry, one has to perform diffraction experiment on a single crystalline sample. From the temperature dependent XRD data we observe that this two-phase coexistence arises in the vicinity of magnetic ordering temperature ($T_N \sim 116$ K). A similar observation has been reported in RVO_3 compounds with intermediate size rare-earth ions ($R = \text{Sm}, \text{Eu}, \text{and Gd}$) [6,23] and recently in TmVO_3 [23]. Based on the findings in TmVO_3 , we believe that the second orthorhombic phase of YVO_3 appearing at T_N is C -type orbital ordered ($Pnma$) which coexists with the major G -type orbital ordered ($P112_1/a$) phase.

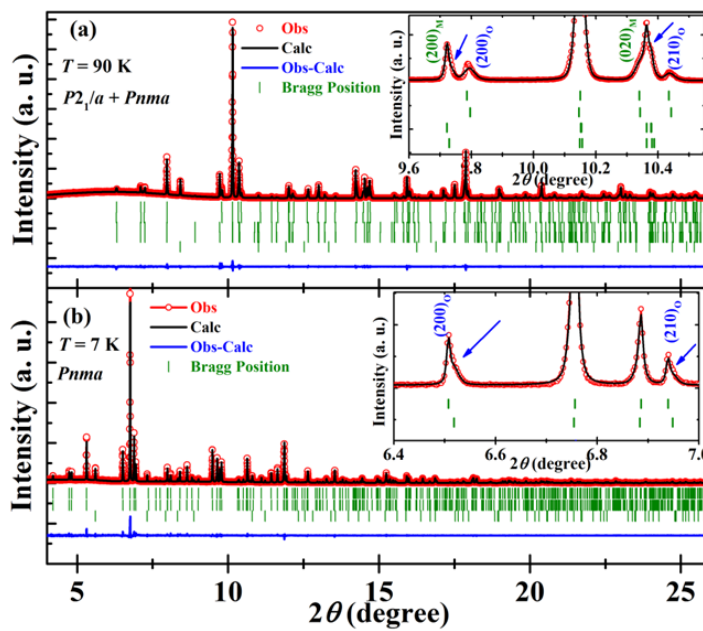


Figure 4.10: (a), (b) The Rietveld refinement of temperature dependent synchrotron x-ray diffraction pattern of polycrystalline YVO_3 at 90 and 7 K respectively using a wavelength of $\lambda = 0.48$ and 0.32 Å respectively. Insets of (a) and (b) show the enlarged view of Bragg peaks across the highest intensity to reveal the asymmetry in (200) and (210) peaks (indicated by an arrow). For each space group, two sets of lattice parameters have been used and hence two Bragg positions. The last Bragg positions in each panel are due to the TiO_2 (Rutile phase) originated from the cryostat. In the insets, the suffix O and M outside the parenthesis stands for orthorhombic and monoclinic symmetry respectively.

The obtained structural parameters from the Rietveld refinement of 90 K data are displayed in Table 4.2. From the Rietveld analysis of temperature dependent diffraction data, we observe that such phase coexistence which arises near T_N remains till the second structural transition at $T_S \sim 77$ K, below that temperature coexisting phases convert to the single orthorhombic phase ($Pnma$) with C -OO state.

Table 4.2: Structural parameters of YVO_3 at 90 K

Space Group: $P 1 1 2_1/a$ (Monoclinic)					
$a = 5.62036 (2) \text{ \AA}, b = 7.53460 (3) \text{ \AA}, c = 5.27336 (2) \text{ \AA}; \gamma = 90.0139 (9)^\circ$					
Atom (Position)	x	y	z	$B_{iso} (\text{\AA}^2)$	Occupancy
Y (4e)	0.0709 (2)	0.2501 (8)	0.9834 (3)	1.63 (3)	1.0
V1 (2c)	0.5	0	0	1.51 (5)	1.0
V2 (2b)	0	0.5	0.5	1.51 (5)	1.0
O1 (4e)	0.4327 (17)	0.2668 (26)	0.1280 (17)	1.00	1.0
O2 (4e)	0.2884 (35)	0.0548 (27)	0.6826 (29)	1.00	1.0
O3 (4e)	0.6920 (38)	0.5619 (26)	0.2627 (32)	1.00	1.0
$R_B = 2.04 \%, R_F = 1.47 \%, \chi^2 = 1.90 \%$					
Space Group: $Pnma$ (Orthorhombic)					
$a = 5.58359 (11) \text{ \AA}, b = 7.55268 (16) \text{ \AA}, c = 5.28533 (15) \text{ \AA}$					
Atom (Position)	x	y	z	$B_{iso} (\text{\AA}^2)$	Occupancy
Y (4c)	0.0680 (11)	0.25	0.9769 (32)	1.63 (3)	1.0
V (4b)	0	0	0.5	1.51 (5)	1.0
O1 (4c)	0.5923 (88)	0.25	0.3979 (98)	1.00	1.0
O2 (8d)	0.2397 (92)	0.0257 (71)	0.7125 (71)	1.00	1.0
$R_B = 2.32 \%, R_F = 2.08 \%, \chi^2 = 1.90 \%$					

In Figure 4.10(b) we show the Rietveld analysis of the XRD data of YVO_3 recorded at 7 K (C -OO state). From Figure 4.10(b), it is evident that the XRD data can be modelled with only single orthorhombic symmetry with two different sets of lattice parameters similar to the room temperature data. The (200) reflection which is the characteristics of the distribution of cell parameters is found to be asymmetric at both the temperatures, 7 and 90 K [insets of Figures 4.10(a) and 4.10(b)]. We show the structural parameters extracted from the refinement of 7 K data in Table 4.3. The phase transitions temperatures of polycrystalline YVO_3 were obtained from the temperature dependent dc and ac magnetization data as illustrated in Figure 4.11.

Table 4.3: Structural parameters of YVO₃ at 7 K

Space Group: <i>Pnma</i> (Orthorhombic)					
$a = 5.58702 (2) \text{ \AA}, b = 7.54766 (2) \text{ \AA}, c = 5.28008 (2) \text{ \AA}$					
Atom (Position)	x	y	z	$B_{iso} (\text{\AA}^2)$	Occupancy
Y (4c)	0.0706 (2)	0.25	0.9781(2)	0.47 (2)	1.0
V (4b)	0	0	0.5	0.46 (3)	1.0
O1 (4c)	0.4568 (15)	0.25	0.1178 (17)	0.74 (4)	1.0
O2 (8d)	0.2991 (12)	0.0579 (9)	0.6905 (14)	0.74 (4)	1.0

$R_B = 4.27 \%, R_F = 2.43 \%, \chi^2 = 1.4 \%$

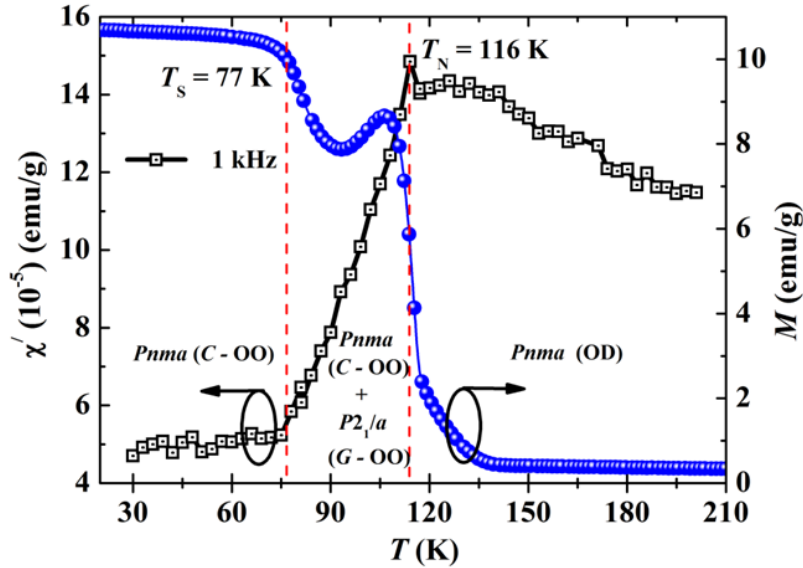


Figure 4.11: (a), (b) Temperature dependent dc magnetization data in the presence of a magnetic field of 100 Oe (right) and real part of ac magnetic susceptibility in the presence of an ac amplitude of 10 Oe (left) for polycrystalline YVO₃.

In Figures 4.12 and 4.13, we show the thermal variation of structural parameters such as lattice parameters, V-O bond lengths and V-O₁-V bond angle (apical) which are indicative of different orbital-ordered states. In Figure 4.12 we show the variation of lattice parameters and unit cell volume as a function of temperature. From this figure, we observe that there is a change in slope in all the three lattice parameters at T_{OO} , T_N and T_S . Temperature dependent volume data [Figures 4.12(d)] shows a monotonous decrease with lowering temperature followed by a jump at $T_N \sim 116$ K, indicating a first order phase transition associated with the coexistence of crystallographic phases of monoclinic ($P112_1/a$) and orthorhombic ($Pnma$) symmetry. Interestingly, both b and c

lattice parameters decrease while a parameter increases with lowering the temperature in the region of 200-116 K. This anisotropic expansion and contraction is understood from the variation of V-O bonding pattern of VO_6 octahedra. The anisotropic lattice parameter suggests that there would be two pairs of short and one pair of long V-O bonds which are an indication of Jahn-Teller ordered state. In $Pnma$ settings, the equatorial ac -plane of the VO_6 octahedra would contain two long and two short V-O₂ bonds. The second pair of the short bond (V-O₁) would be along the apical b -axis.

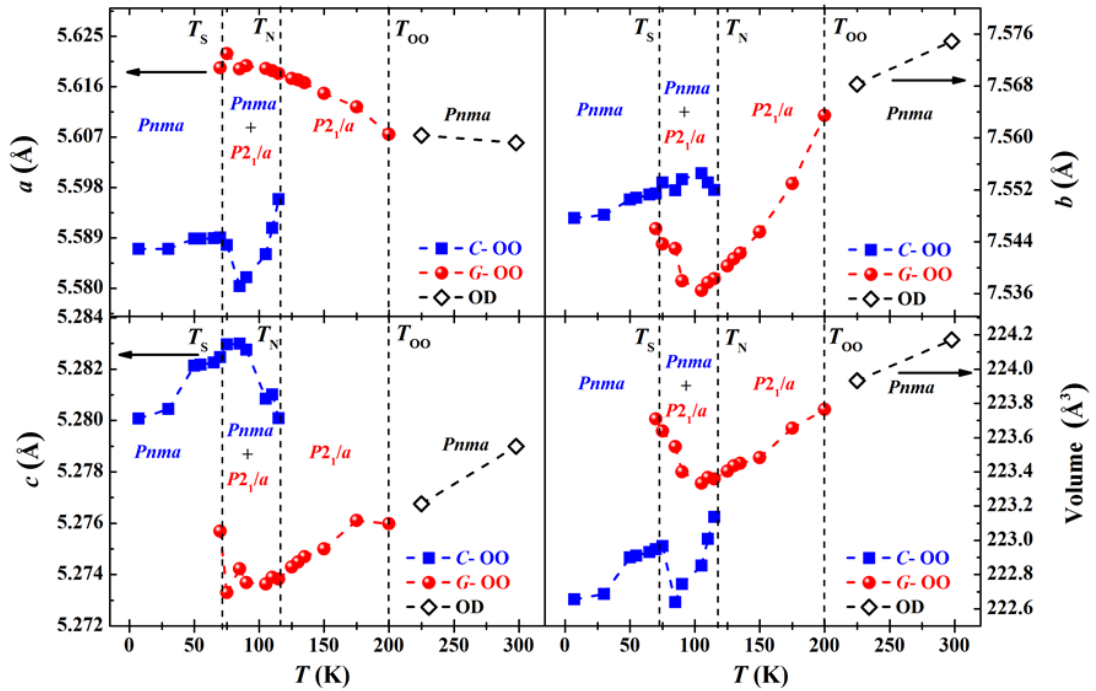


Figure 4.12: Variation of lattice parameters and unit cell volume of polycrystalline YVO_3 as a function of temperature.

In Figure 4.13(a) we have plotted the V-O bond lengths obtained from the Rietveld analysis of synchrotron x-ray diffraction data. Despite the fact that determination of V-O bond length would involve larger standard deviation as compared to the results obtained from neutron diffraction experiment, qualitatively the obtained bond lengths agree with the reported literature [20]. From Figure 4.13(a) it is evident that at the onset of G -type OO state ($T_{00} \sim 200$ K), the six bonds of VO_6 octahedra are split into two short and two long bonds in the ac -plane suggesting that orbital degeneracy of t_{2g} orbital of V^{3+} (d^2) ion is lifted. In contrast, there would be three inequivalent V-O bonds at all the temperature above the Jahn-Teller transition temperature ($T_{00} \sim 200$ K). In Figure 4.13(a) we observe a jump in the apical V-O₁ bond distance around 90 K, which could be due to the sudden change in the tilt of

octahedra. Interestingly, we also see an anomaly around 90 K in the temperature dependent V-O₁-V bond angles data as shown in Figure 4.13(b).

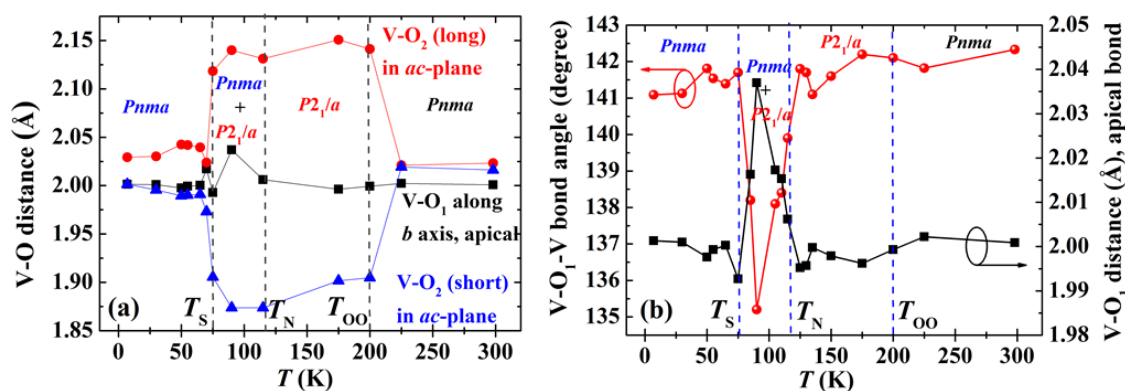


Figure 4.13: Temperature dependent (a) V-O bond distances, (b) V-O₁-V bond angles (bold circle, left) and apical V-O₁ distance (bold square, right) of polycrystalline YVO₃ obtained from the Rietveld refinement of synchrotron x-ray diffraction data. The standard error of the data would be high due to the inability of x-ray diffraction to determine the position of oxygen atom accurately in the presence of dominating scattering from Y³⁺ ion.

Now we turn our discussion on the structural phase coexistence observed in the temperature range of $T_S < T < T_N$. Sage *et al.* have constructed a phase diagram on the stability of *G*- and *C*-type orbital ordered states of *RVO*₃ based on the opposing influence of octahedral distortion and the magnetic exchange interaction [6]. From the phase diagram, it is evident that *C*-OO is preferred with increasing octahedral distortion, while with increasing magnetic exchange striction *G*-OO state would be stabilized. In our study of YVO₃, we find that monoclinic phase with *G*-type OO state appears at 200 K and then with lowering temperature octahedral tilting (*GdFeO*₃-type distortion) increases leading to the appearance of *C*-OO state with *Pnma* symmetry around $T_N \sim 116$ K in the background of monoclinic phase (*P112*₁/*a*) thereby creating phase coexistence. In contrast to the *RVO*₃ compounds with intermediate size rare-earth ions ($R = \text{Sm, Eu, Gd and Tb}$), where the phase coexistence appearing just below T_N remains down to lowest temperature (5 K), the phase coexistence in YVO₃ survives only in the temperature window between T_N and T_S . The occurrence of phase coexistence in these orthovanadates with intermediate size rare-earths has been attributed to the magnetic exchange striction which leads to the change in volume in the vicinity of T_N . Interestingly, we also see a similar change in the temperature dependent volume data at T_N [Figure 4.12] indicating that magnetic exchange striction is playing an important role to nucleate the *Pnma* phase with *C*-type OO state. In YVO₃, we could connect the origin of phase coexistence of *G*- and *C*-type of orbital ordered states based

on recent observation on TmVO_3 [23]. In TmVO_3 , the occurrence of phase coexistence in the temperature region of $T_S < T < T_N$ has been attributed to different coexisting magnetic structures with the nuclear phases $P112_1/a$ (major) and $Pnma$ (minor). In the case of YVO_3 , with lowering temperature octahedral distortion/tilting increases and it becomes maximum around 90 K where the orthorhombic phase starts picking up at the expense of monoclinic phase as shown in Figure 4.14. We have seen from Figure 4.13(a) that apical V-O₁ bond distance (along b axis) of VO_6 octahedra peaks around 90 K and then decreases which indicates a sudden increase in octahedral tilting followed by relief from the octahedral distortion. The abrupt change in V-O₁ bond length is also reflected in the sudden change in V-O₁-V bond angle as shown in Figure 4.13(b). Accordingly our phase coexistence data which nucleates at T_N suggests that probably the upper stability limit to support the octahedral tilting by $P112_1/a$ phase has reached a maximum limit near 90 K and therefore to relieve from that $P112_1/a$ phase gradually converts to the $Pnma$ phase.

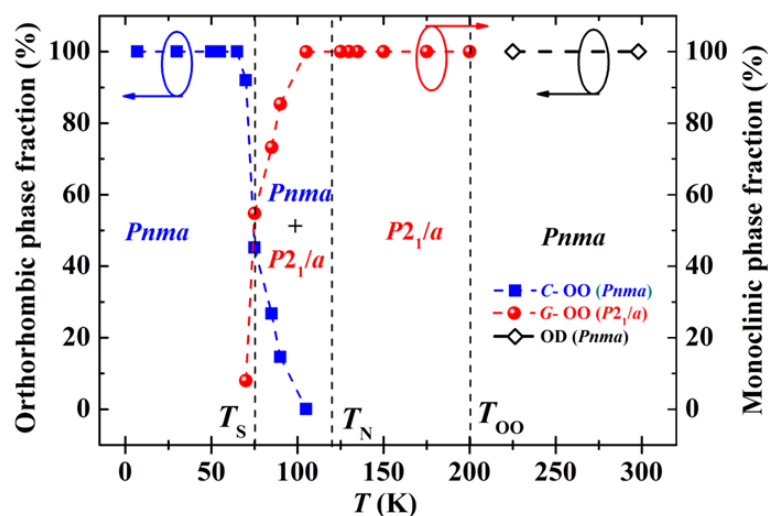


Figure 4.14: Variation of phase fractions of orthorhombic and monoclinic structures of polycrystalline YVO_3 as a function of temperature.

We believe that the phenomenon phase coexistence in these orthovanadates could be independent of the size of the rare-earth ions. It has already been reported that there exists short range correlation of C -type OO state in the G -type OO state [29]. To the best of our knowledge, the occurrence of C -type OO state in the G -type OO state in YVO_3 could not be identified from the diffraction experiment which is very much sensitive to the long-range phenomena. We believe that to establish the long-range order one has to pay attention to the annealing temperature at which the samples are

prepared. We have prepared our sample at 1400 °C which probably helps to establish a long-range order and therefore we could identify the phase coexistence from the synchrotron x-ray diffraction experiment. Most of the YVO_3 samples reported in the literature are prepared at 1000 °C which may not be sufficient to establish the long-range order. In this context, it is important to mention that RVO_3 compounds with intermediate size rare-earth ions ($R = \text{Sm, Eu, Gd, and Tb}$) where phase coexistence has been reported were synthesized at 1400 °C [6]. In these compounds, the occurrence of orbital phase coexistence has been attributed to the lattice strain associated with the difference in unit cell volume of orthorhombic ($C\text{-OO}$) and monoclinic ($G\text{-OO}$) structure and strain present in the system prevents complete phase transformations thereby coexistence prevails till 5 K [6,21].

Such phase separation into orbitally ordered states ($G\text{-}$ and $C\text{-}$ type) of different structural symmetry in $T_S < T < T_N$ is analogous to the phenomenon of electronic phase coexistence between metallic and insulating phases in doped manganites. The origin of this electronic phase separation phenomena in manganites has been attributed to the strong electron-lattice coupling and presence of long-range strain [32]. In magnetically phase separated manganites, ferromagnetic metallic puddles grow on the matrix of an insulating antiferromagnetic background. In comparable fashion, we can say that the competition between the ordering of different orbital states favours the formation of one type of orbital ordering over the background of another orbital ordered state in YVO_3 leading to the orbital phase separation into $G\text{-}$ and $C\text{-}$ type. Since the lattice mediates the coupling between different orbital states, therefore, the change in orbital state would be reflected on lattice symmetry. Now with decreasing temperature due to a reduction in unit cell volume $C\text{-OO}$ state ($Pnma$) evolves in the regime of $G\text{-OO}$ state as a result of increased $GdFeO_3$ -type distortion facilitating to release the strain. In Figure 4.12(d) the relaxation of strain is reflected in the reduction of unit cell volume with decreasing temperature indicating the occurrence of first-order orbital phase transition. $GdFeO_3$ -type structural distortion shifts the $A\text{-}$ site ion facilitating the $A\text{-O}$ covalency which favours the $d\text{-}$ type Jahn-Teller distortion or $C\text{-OO}$ state whereas in the absence of $GdFeO_3$ -type distortion orbital ordering gains the energy in $a\text{-}$ type Jahn-Teller distorted or $G\text{-OO}$ state [5].

4.5 Conclusions

In conclusion, we have demonstrated using high-resolution synchrotron x-ray diffraction that the ambient condition orthorhombic phase of YVO_3 has a distribution of lattice parameters which stems from the possible strain. A similar observation on the rare-earth orthovanadates with the intermediate size rare-earth cations ($R = \text{Sm}, \text{Eu}, \text{Gd}$, and Tb) at ambient condition further generalizes the significant role of oxygen distribution throughout the sample in the existence of multiple lattice parameters. The distributions of lattice parameters are also found to be present in YVO_3 at low temperature as clearly seen in the C - OO state of YVO_3 suggesting that the findings are intrinsic in nature. The appearance of orthorhombic phase with C - OO state near T_N is attributed to the magnetostriction, in addition to the GdFeO_3 -type octahedral distortion. The occurrence of phase coexistence in the temperature range $T_S < T < T_N$ is stabilized by the strain associated with the difference in unit cell volume of orthorhombic and monoclinic structure.

Bibliography

- [1] S. Miyasaka, Y. Okimoto, M. Iwama, and Y. Tokura, *Phys. Rev. B* **68**, 100406 (2003).
- [2] Y. Ren, T. Palstra, D. Khomskii, E. Pellegrin, A. Nugroho, A. Menovsky, and G. Sawatzky, *Nature* **396**, 441 (1998).
- [3] J. B. Goodenough and J.-S. Zhou, *J. Mater. Chem.* **17**, 2394 (2007).
- [4] M. Reehuis *et al.*, *Phys. Rev. B* **73**, 094440 (2006).
- [5] T. Mizokawa, D. Khomskii, and G. Sawatzky, *Phys. Rev. B* **60**, 7309 (1999).
- [6] M. Sage, G. Blake, C. Marquina, and T. Palstra, *Phys. Rev. B* **76**, 195102 (2007).
- [7] J. Goodenough, *Annu. Rev. Mater. Sci.* **28**, 1 (1998).
- [8] D. Bizen, N. Shirane, T. Murata, H. Nakao, Y. Murakami, J. Fujioka, T. Yasue, S. Miyasaka, and Y. Tokura, *J. Phys.: Conf. Series* **150**, 042010 (2009).
- [9] S. Wilkins, P. Spencer, P. Hatton, S. Collins, M. Roper, D. Prabhakaran, and A. Boothroyd, *Phys. Rev. Lett.* **91**, 167205 (2003).
- [10] Y. Murakami *et al.*, *Phys. Rev. Lett.* **81**, 582 (1998).
- [11] J. Rodriguez-Carvajal, M. Hennion, F. Moussa, A. Moudden, L. Pinsard, and A. Revcolevschi, *Phys. Rev. B* **57**, R3189 (1998).

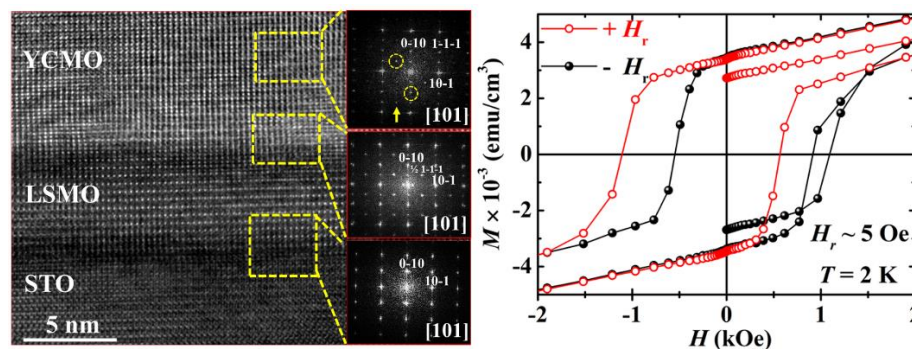
-
- [12] Y. Tokura and N. Nagaosa, *Science* **288**, 462 (2000).
- [13] D. Muthu, A. Midgley, P. Scott, M. Kruger, J. Sahu, A. Sood, and C. N. R. Rao, *J. Phys.: Conf. Series* **377**, 012025 (2012).
- [14] G. R. Blake, T. Palstra, Y. Ren, A. A. Nugroho, and A. Menovsky, *Phys. Rev. Lett.* **87**, 245501 (2001).
- [15] D. Bizen, H. Nakao, K. Iwasa, Y. Murakami, T. Osakabe, J. Fujioka, T. Yasue, S. Miyasaka, and Y. Tokura, *J. Phys. Soc. Jpn.* **81**, 024715 (2012).
- [16] J. Kanamori, *J. Phys. Chem. Solids* **10**, 87 (1959).
- [17] P. W. Anderson, *Solid State Phys.* **14**, 99 (1963).
- [18] J.-Q. Yan, H. Cao, M. A. McGuire, Y. Ren, B. Sales, and D. Mandrus, *Phys. Rev. B* **87**, 224404 (2013).
- [19] S. Miyasaka, T. Yasue, J. Fujioka, Y. Yamasaki, Y. Okimoto, R. Kumai, T. Arima, and Y. Tokura, *Phys. Rev. Lett.* **99**, 217201 (2007).
- [20] G. Blake, T. Palstra, Y. Ren, A. Nugroho, and A. Menovsky, *Phys. Rev. B* **65**, 174112 (2002).
- [21] M. Sage, G. Blake, G. Nieuwenhuys, and T. Palstra, *Phys. Rev. Lett.* **96**, 036401 (2006).
- [22] R. D. Johnson *et al.*, *Phys. Rev. B* **85**, 224102 (2012).
- [23] C. Ritter, S. A. Ivanov, G. V. Bazuev, and F. Fauth, *Phys. Rev. B* **93**, 054423 (2016).
- [24] D. Bizen, K. Nakatsuka, T. Murata, H. Nakao, Y. Murakami, S. Miyasaka, and Y. Tokura, *Phys. Rev. B* **78**, 224104 (2008).
- [25] F. Fauth, I. Peral, C. Popescu, and M. Knapp, *Powder Diffr.* **28**, S360 (2013).
- [26] F. Fauth, R. Boer, F. Gil-Ortiz, C. Popescu, O. Vallcorba, I. Peral, D. Fullà, J. Benach, and J. Juanhuix, *Eur. Phys. J. Plus* **130**, 1 (2015).
- [27] J. Rodríguez-Carvajal, *Physica B: Condens. Matter* **192**, 55 (1993).
- [28] P. Karen, *J. Solid State Chem.* **170**, 9 (2003).
- [29] S. Miyasaka, J. Fujioka, M. Iwama, Y. Okimoto, and Y. Tokura, *Phys. Rev. B* **73**, 224436 (2006).
- [30] A. Tsvetkov, F. Mena, P. Van Loosdrecht, D. Van Der Marel, Y. Ren, A. Nugroho, A. Menovsky, I. Elfimov, and G. Sawatzky, *Phys. Rev. B* **69**, 075110 (2004).

-
- [31] G. Blake, A. Nugroho, M. Gutmann, and T. Palstra, *Phys. Rev. B* **79**, 045101 (2009).
- [32] K. Ahn, T. Lookman, and A. Bishop, *Nature* **428**, 401 (2004).

Exchange bias at the interface between ferromagnetic $\text{La}_{0.7}\text{Sr}_{0.3}\text{MnO}_3$ and charge- ordered antiferromagnetic $\text{Y}_{0.5}\text{Ca}_{0.5}\text{MnO}_3$ *

Summary

Epitaxial thin films of ferromagnetic $\text{La}_{0.7}\text{Sr}_{0.3}\text{MnO}_3$ (LSMO) and charge-ordered, antiferromagnetic $\text{Y}_{0.5}\text{Ca}_{0.5}\text{MnO}_3$ (YCMO) bilayers were deposited on SrTiO_3 (100) substrates by pulsed laser deposition (PLD). The heterostructure undergoes tetragonal distortion due to strong biaxial tensile strain imposed by the underlying STO substrate. In addition to the conventional exchange bias (CEB) in the presence of strong cooling magnetic fields, bilayers of LSMO-YCMO exhibit significant exchange bias (EB) under cooling in the presence of small remnant magnetic field (~ 5 Oe) of the superconducting magnet. The unidirectional exchange anisotropy at the interface is switchable by reversing the polarity of the remnant magnetic field. The occurrence of EB under cooling in the presence of such a low magnetic field is noteworthy.



*Paper based on this chapter is published in: Phys. Status Solidi RRL 10, 622 (2016), © (2016) by John Wiley and Sons.

5.1 Introduction

In perovskite manganites, interactions among spin, lattice, charge and orbital degrees of freedom give rise to interesting physical properties, e.g., high T_C superconductivity [1], colossal magnetoresistance [2,3], metal-insulator transition [4] and magnetoelectric multiferroicity [5,6]. Such interactions also give rise to novel effects at the interfaces of artificially grown heterostructures by modifying the electronic states or through orbital reconstruction [7]. Thus, a ferromagnetic (FM) state has been realized in antiferromagnetic (AFM) BiFeO_3 by interfacing with ferromagnetic $\text{La}_{0.7}\text{Sr}_{0.3}\text{MnO}_3$ (FM-LSMO) as a result of electronic orbital reconstruction [8]. Interfaces between LaAlO_3 and SrTiO_3 undergoes electronic reconstruction that modifies the transport properties [9]. Charge transfer-driven orbital ordering and ferromagnetism exist at the interface between $\text{YBa}_2\text{Cu}_3\text{O}_7$ and $\text{La}_{0.67}\text{Ca}_{0.33}\text{MnO}_3$ [10]. There has been considerable effort to study the magnetic properties of such heterostructure interfaces.

When two magnetically different materials (e.g. antiferromagnet and ferromagnet) are adjoined and allowed to cool across the Néel temperature (T_N), unidirectional exchange anisotropy is realized at the interface, known as exchange bias (EB) [11-13]. Since the pioneering discovery of EB in oxide-coated fine particles of cobalt by Meiklejohn and Bean in 1956, it has been extensively studied due to its applications in ultrahigh-density magnetic recording, giant magnetoresistance and spin valve devices [14,15]. The Meiklejohn and Bean equation is [11],

$$H_E = -J \frac{S_{AFM} S_{FM}}{\mu_0 t_{FM} M_{FM}} \quad (5.1)$$

where, J is the exchange integral across the FM/AFM interface per unit area; S_{AFM} , S_{FM} are the interface magnetization of the AFM and FM layer respectively; M_{FM} is the spontaneous magnetization of FM layer; t_{FM} is the thickness of FM layer. According to the above equation, EB is roughly inversely proportional to the thickness of the ferromagnetic layer. The occurrence of EB is manifested by the shift of the isothermal $M(H)$ loop either along the positive or negative magnetic field (H) axis depending on the strength of the cooling magnetic field and coupling at the magnetic interface [16,17]. The exchange bias field (H_E) and coercive field (H_C) of the shifted $M(H)$ loop are given by $H_E = -(H_L + H_R)/2$ and $H_C = -(H_L - H_R)/2$, where H_L and H_R are the

coercive fields at the left and right sides, respectively. Exchange bias also exists at the interfaces of soft FM - hard FM [18], FM - spin glass (SG) [19], AFM - ferrimagnet [20] and FM - ferrimagnet [21] other than the FM - AFM interface [12].

Recent reports show that EB at the interface between FM-LSMO and AFM-ferroelectric BiFeO₃ can be switched reversibly by changing the polarity of ferroelectric polarization which in turn facilitates electric-field-controlled interface ferromagnetism thereby enabling electrically controllable spintronic devices [22,23]. Electric field control of interface magnetization would provide a new direction towards the realization of strong magnetoelectric coupling essential for technological applications.

5.2 Scope of the present investigation

We have studied the exchange bias at the interface between charge-orbital-ordered [24] (COO) antiferromagnetic Y_{0.5}Ca_{0.5}MnO₃ (YCMO) and ferromagnetic La_{0.7}Sr_{0.3}MnO₃ (LSMO). Interestingly, the charge-order state of bulk YCMO with small A-site cation radius is so robust that it cannot be destroyed even with the application of very high magnetic field of the order of 40 T [25]. In nanoparticles of YCMO with the reduction of particle size, there is a suppression of charge-ordering transition temperature [26]. Such destabilization of charge-ordered state in nanoparticle of Sm_{0.5}Ca_{0.5}MnO₃ give rise to a weak ferromagnetic state followed by spin-glass-like phase at low temperature [27]. The presence of the interface between disordered spin-glass (SG) and AFM core gives rise to an exchange bias effect. Magnetometry measures the average interaction over the whole interface area in the film. Exchange bias is an interface phenomenon which strongly depends on the thickness of the ferromagnetic layer and the interface magnetization. With this motivation, we have grown epitaxial LSMO-YCMO bilayers of different thicknesses and have examined the evolution of EB at the interface. We have also compared the results on bilayers of LSMO-YCMO with those of bare epitaxial YCMO films on SrTiO₃ (STO).

Interestingly, we observe significant EB in the bilayers in the presence of a small remnant magnetic field of ~ 5 Oe present in the superconducting magnet. We find the value of the field-cooled (FC) conventional exchange bias (CEB) to be maximum in the LSMO (2 nm) - YCMO (20 nm) bilayer. In addition we have also studied the interface atomic configuration of LSMO-YCMO bilayer by electron microscopy.

5.3 Experimental details

Single and bilayer of perovskite manganite thin films consists of ferromagnetic $\text{La}_{0.7}\text{Sr}_{0.3}\text{MnO}_3$ and charge-orbital-ordered antiferromagnetic $\text{Y}_{0.5}\text{Ca}_{0.5}\text{MnO}_3$ layers of different thicknesses were grown on (100) oriented SrTiO_3 (STO) substrate using pulsed laser deposition (PLD). To get a bilayer, YCMO layer was grown on top of ferromagnetic LSMO layer immediately after depositing the ferromagnetic layer. Film deposition was carried out using a KrF excimer laser of 248 nm wavelength and 20 ns pulse width. The laser repetition rate and the energy per pulse were 5 Hz and 150 mJ respectively. The distance between the target and substrates was kept constant at 50 mm. During deposition, the substrate temperature and partial pressure of oxygen was maintained at 750 °C and ~ 300 mTorr respectively. To avoid oxygen nonstoichiometry, after depositing the films the substrates were cooled down to room temperature slowly in the presence of ~ 1 atm oxygen pressure. We have prepared a dense ceramic target of LSMO and YCMO by mixing stoichiometric amounts of the binary oxides namely, La_2O_3 (Alfa Aesar, 99.9%), SrCO_3 (Sigma-Aldrich, 99.9%), Mn_2O_3 (Sigma-Aldrich, 99.0%) (for LSMO) and Y_2O_3 (Sigma-Aldrich, 99.99%), CaCO_3 (Sigma-Aldrich, 99.0%), Mn_2O_3 (for YCMO). The mixtures were ground and heated in the temperature range 1000-1300°C in air for 12 h with several intermittent grindings. Finally, after phase confirmation by analyzing the x-ray diffraction data (XRD) collected with PANalytical Empyrean diffractometer using $\text{Cu K}\alpha_1$ monochromatic x-ray radiation, the targets were prepared and sintered in air at 1400°C for the duration of 12 h.

To study the interface atomic configuration, high-resolution transmission electron microscopy (HRTEM) imaging was performed using an aberration-corrected FEI TITAN³™ 80-300 kV TEM with a $C_s \sim -35 \mu\text{m}$ and a $\Delta f \sim 8 \text{ nm}$ [28]. Cross-sectional TEM samples were prepared first by conventional mechanical polishing and then Ar ion milling to generate greater electron transparent area. High angle annular dark field (HAADF) combined with energy dispersive spectroscopy (EDS) was performed to distinguish the chemical homogeneity of the films across the interface.

We have performed magnetic measurements with the superconducting quantum interference device (SQUID) magnetometer (MPMS, Quantum Design) and applied the

magnetic fields parallel to the sample surface. We have carried out temperature dependent dc magnetization measurements at $H = 0.1$ kOe in the temperature range 2-390 K. To study the exchange bias first we cooled the sample from 390 to 2 K in the presence of a magnetic field, and then recorded the $M(H)$ loop while sweeping the magnetic field in the range ± 70 kOe under isothermal condition. We have also recorded isothermal $M(H)$ loop after cooling the sample in the presence of remnant magnetic field of the superconducting magnet. To reduce the effect of remnant-field of the superconducting magnet demagnetization process has been performed by oscillating fields at 390 K where the sample is in the paramagnetic region. However, there still was a small unavoidable positive or negative trapped magnetic field (~ 5 Oe), depending on the polarity of the initial magnetic field, either negative or positive from which demagnetization starts. We have used this small remnant magnetic field of the superconducting magnet present as the source of low magnetic field for our experiment. Two types of $M(H)$ loops, namely P and N type were measured, where P and N indicate the positive ($0 \rightarrow +H$) and negative ($0 \rightarrow -H$) directions of the initial magnetization. Since both the hysteresis loops coincide with each other, we have carried out P type of $M(H)$ loop for positive cooling magnetic field and N-type $M(H)$ loop for the negative cooling magnetic field. In both cases we have recorded closed $M(H)$ loop following the magnetic field ramping sequence as $+70 \rightarrow 0 \rightarrow -70 \rightarrow +70$ kOe or $-70 \rightarrow 0 \rightarrow +70 \rightarrow -70$ kOe. To estimate the exchange bias parameter we have recorded isothermal closed $M(H)$ loop in stable at each magnetic field mode (log scale) with the ramping rate of 0.1 kOe/sec.

5.4 Results and discussion

5.4.1 Structure characterization of LSMO - YCMO bilayer:

To examine the interface atomic configuration, imaging by high-resolution transmission electron microscopy (HRTEM) has been carried out across the film interfaces. The HRTEM image in Figure 5.1(a) shows layers, corresponding to the substrate STO, interlayer LSMO, and the epilayer YCMO. The thickness of the LSMO and YCMO layers are 5 and 20 nm respectively. The interface between the YCMO epilayer and interlayer LSMO is atomically sharp. The additional broad dark contrast at

both the interfaces arises due to the strain. The films have following epitaxial relationship: STO (0-10) || LSMO (0-10) || YCMO (0-10).

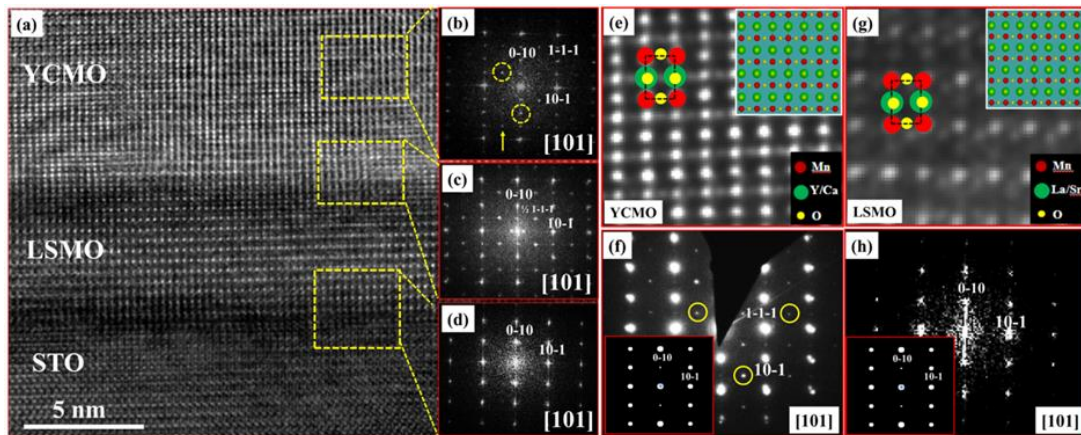


Figure 5.1: (a) HRTEM image of epitaxial YCMO (20 nm) - LSMO (5 nm) thin films on STO substrate. Local Fourier transformation (FT) images of (b) YCMO film with superlattice spots associated with charge ordering at room temperature, (c) LSMO - YCMO interface and (d) epitaxial LSMO film - STO substrate interface. (e) Atomic resolution TEM image of YCMO film with the corresponding (f) ED pattern along [101] zone axis. The simulated projection and ED pattern of YCMO film with tetragonal structure along [101] zone axis are shown in the inset of (e) and (f), respectively. (g) Atomic resolution TEM image with corresponding (h) local FT from LSMO layer along [101] zone axis. The simulated projection and ED pattern of LSMO film with tetragonal structure along [101] zone axis are shown in the inset of (g) and (h) respectively.

Figure 5.1(b) is the Fourier transform (FT) image of the YCMO lattice, showing superlattice spots confirming the presence of charge ordering at room temperature. The superlattice spot at $g = \frac{1}{2} (1-1-1)$ is commensurate with the lattice vector. Figure 5.1(c) shows the FT from LSMO-YCMO along [101] zone axis of STO confirming the epitaxial nature of the thin film. Figure 5.1(d) is the local FT pattern from STO - LSMO, indicating epitaxial growth with in-plane strain. Interestingly, the presence of strong biaxial strain leads to tetragonal distortion of both LSMO and YCMO layers. Atomic resolution TEM projection image as well as electron diffraction (ED) of YCMO [Figures 5.1(e) and 5.1(f)] and LSMO [Figures 5.1(g) and 5.1(h)] shown along the zone axis [101] are found to be identical with the simulated projection [insets of Figures 5.1(e) and 5.1(g)] and ED [insets of Figures 5.1(f) and 5.1(h)] with tetragonal structure along the same orientation. In contrast, the structure of LSMO and YCMO in the bulk state is found to be rhombohedral ($R\bar{3}c$) and orthorhombic ($Pnma$) respectively. A Large area view of the epitaxial thin film with the corresponding SAD (Selected Area Diffraction) along the zone axis [101] from STO, LSMO - YCMO, YCMO is shown in Figure 5.2.

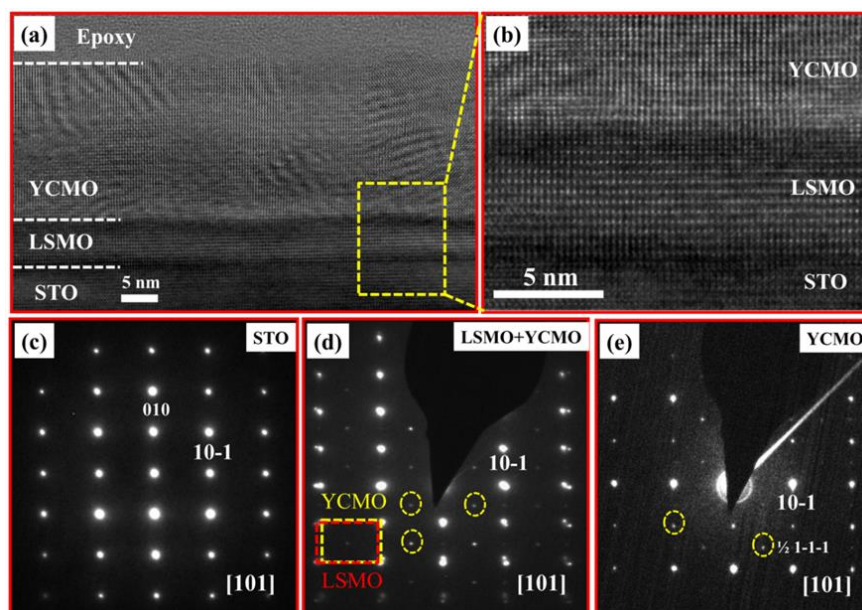


Figure 5.2: (a) Large area view of the bilayer of LSMO - YCMO thin film. The film is grown under tensile strain which has been reflected in the additional strain contrast across the respective interfaces. (b) The magnified view of the film clearly indicates that the interface is atomically sharp and of epitaxial nature. (c) Electron diffraction (ED) pattern from STO. (d) SAD from a bilayer of LSMO - YCMO, where additional superlattice spots represent the charge ordering arising from YCMO layer. Individual lattice plane contribution from LSMO, YCMO is shown in the rectangular box and (e) SAD from YCMO along the [101] zone axis. The commensurate superlattice spots are marked with a circle.

In order to detect the chemical homogeneity across the interlayers of YCMO-LSMO-STO, STEM-EDX (Scanning Transmission Electron Microscopy – Energy-dispersive x-ray Spectroscopy) line scan was performed over ~ 25 nm distance covering both the interfaces. LSMO film appears with brighter contrast because of higher average Z compared to STO and LSMO [Figure 5.3(a)]. HAADF and EDS line scan profile across the layers confirm that there is no interdiffusion of elements between the layers [Figure 5.3(b)].

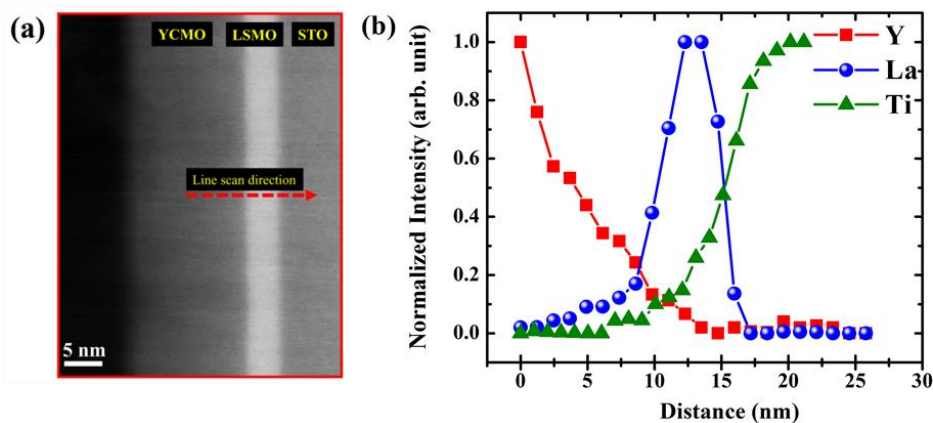


Figure 5.3: (a) STEM-HAADF image used for the STEM-EDS line profile of STO-LSMO-YCMO thin film and (b) STEM-EDX line scan profile. The elemental detection of Y from YCMO, La from LSMO and Ti from STO is plotted with normalized intensity.

The epitaxial nature of the thin films was also confirmed by recording the x-ray diffraction pattern at room temperature [Figure 5.4]. The lattice parameter mismatch between STO - LSMO is 1.18 %, and that between LSMO - YCMO is 2.05 % indicating that the films are grown under biaxial tensile strain imposed by the STO substrate. Analysis of the x-ray diffraction pattern reveal that bare LSMO (~ 20 nm) and YCMO (~ 20 nm) films undergo a shortening of the c -axis, ~ 3.845 (LSMO) and ~ 3.703 Å (YCMO) respectively relative to the bulk value of ~ 3.858 (LSMO) and ~ 3.780 Å (YCMO) indicating that the films are tensile strained on the STO (100) substrate (~ 3.905 Å). The tetragonal distortion is also evidenced by the c/a ratios of 0.95 (~20 nm of YCMO) and 0.98 (~ 20 nm of LSMO) obtained from the monochromatic laboratory x-ray diffraction data.

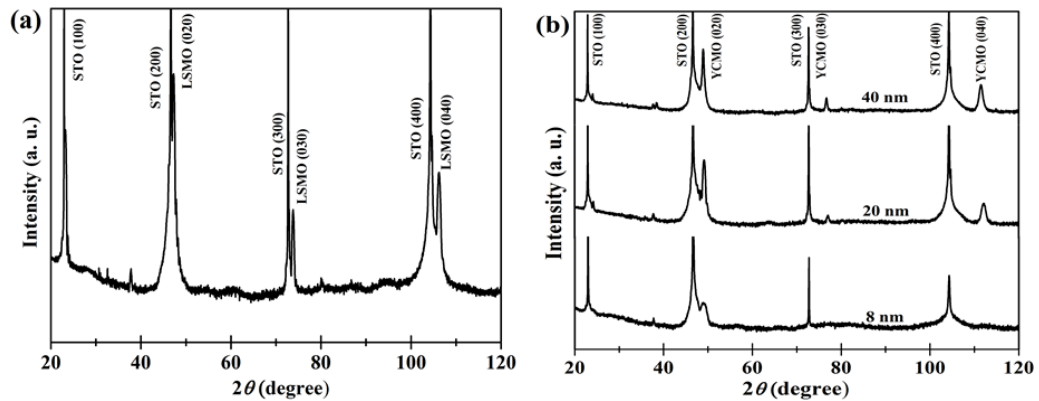


Figure 5.4: Room temperature XRD pattern of (a) $\text{La}_{0.7}\text{Sr}_{0.3}\text{MnO}_3$ (LSMO) film of ~ 20 nm thickness and (b) $\text{Y}_{0.5}\text{Ca}_{0.5}\text{MnO}_3$ (YCMO) films of varying thicknesses grown on (100) oriented SrTiO_3 (STO) substrates, acquired using PANalytical Empyrean diffractometer using $\text{Cu K}\alpha_1$ monochromatic x-ray of wavelength $\lambda = 1.54$ Å.

5.4.2 DC Magnetization as a function of temperature [$M(T)$] and time [$M(t)$]:

Temperature dependent dc magnetization data shows an anomaly at $T_{\text{COO}} \sim 360$ K in the bilayer containing a 2 nm LSMO - 20 nm YCMO layer [Figure 5.5(a)] and at $T_{\text{COO}} \sim 355$ K in 40 nm bare YCMO film [inset of Figure 5.5(d)] due to charge ordering. The charge ordering state [3] is a long range ordering of Mn^{3+} and Mn^{4+} ions associated with e_g orbital ordering of Mn^{3+} ions. It is important to note that the different charge ordering transition temperature (T_{COO}) in the YCMO films of different thickness is associated with the different biaxial strain [29]. The weak antiferromagnetic transition (T_{N}) is generally not visible in films of bilayers or of bare YCMO, but a gradual

increase in the Curie temperature (T_C) is observed in the bilayers with increasing thickness of the ferromagnetic LSMO layer [Figures 5.5(a) - 5.5(c)].

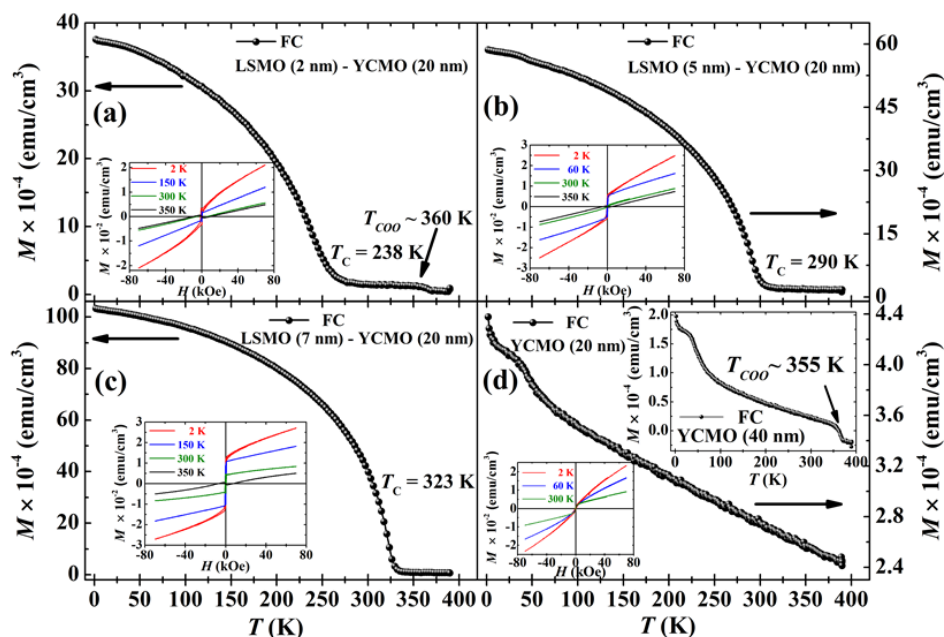


Figure 5.5: $M(T)$ data for (a-c) bilayers of LSMO (varying thickness) - YCMO (20 nm) and (d) 20 nm YCMO film under FC conditions in the presence of a magnetic field of 0.1 kOe. Upper inset of (d) shows the $M(T)$ data of 40 nm YCMO film. Bottom insets of (a-d) show $M(H)$ data of the respective thin films at different temperatures.

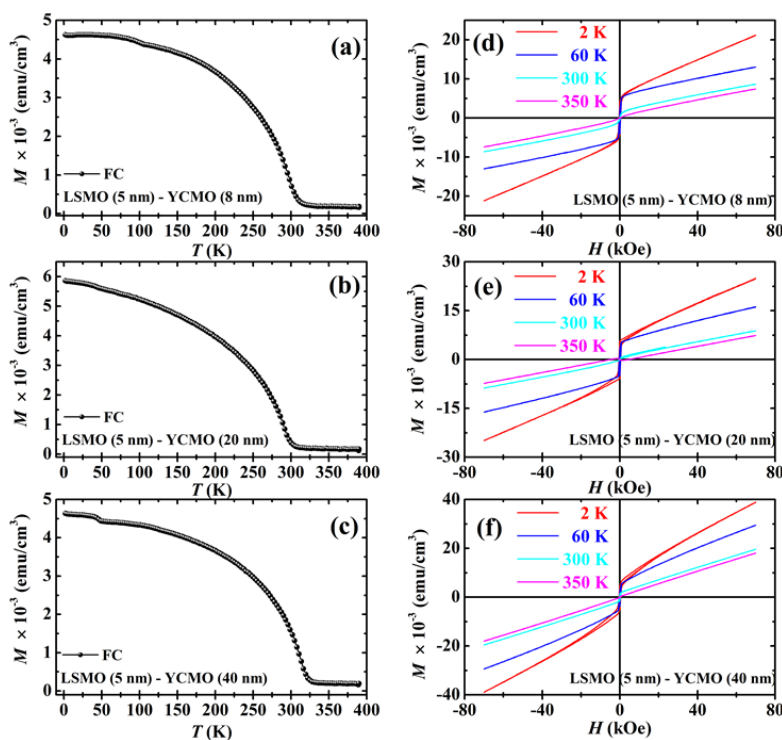


Figure 5.6: (a-c) Temperature dependence of dc magnetization data, $M(T)$, under field-cooled (FC) conditions in the presence of a magnetic field of 0.1 kOe and (d-f) isothermal dc magnetization data as a function of magnetic field, $M(H)$ at various temperatures for bilayers of LSMO (5 nm) - YCMO (varying thickness).

Weak anomaly associated with charge-ordering is also not visible in bilayers containing LSMO of fixed thickness and YCMO of varying thickness as shown in Figure 5.6. Magnetic field dependent isothermal magnetization data, $M(H)$, at different temperatures [insets in Figure 5.5 and Figures 5.6(d) - 5.6(f)] suggest that canted antiferromagnetism coexists with ferromagnetism as a result of electronic phase separation [30].

In the phase separated perovskite manganites it is observed that the glassy phase coexists along with the ferromagnetic (FM) clusters in the background of antiferromagnetic (AFM) matrix and the interface between AFM and SG/FM (spin-glass/ferromagnetic) clusters give rise to exchange bias in manganites [29] and as well as in many other systems, e.g., in NiMnIn_{13} Heusler alloys [31] and $\text{BiFeO}_3\text{-Bi}_2\text{Fe}_4\text{O}_9$ nanocomposites [32]. To verify the presence of the glassy state, we have carried out dc magnetic memory experiment because memory and rejuvenations are the essential characteristics feature for the spin-glass system [33]. We have performed dc memory experiment on bilayer of LSMO (2 nm) - YCMO (20 nm). We performed dc memory experiment by cooling the sample to a particular temperature (T_w , the waiting temperature) under ZFC conditions and then allowed to wait at that temperature for the duration of $\sim 10^4$ sec. After that the sample is cooled to the lowest possible temperature under ZFC conditions and $M(T)$ is measured while warming in the presence of a magnetic field of 0.1 kOe. We must note that under the ZFC conditions there is a small remnant magnetic field of ~ 5 Oe in the superconducting magnet.

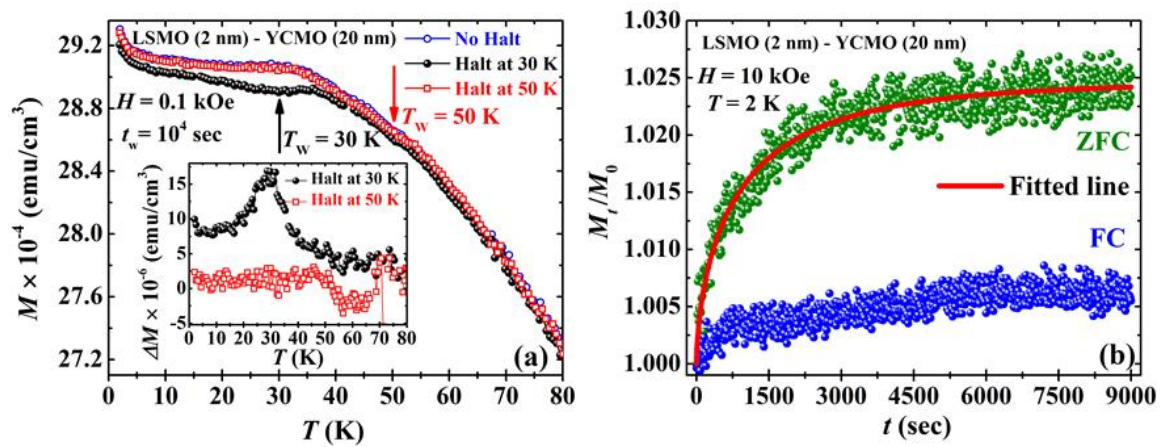


Figure 5.7: (a) DC memory effect experiment carried out with and without halt at 30 and 50 K under ZFC conditions for bilayer of LSMO (2 nm) - YCMO (20 nm). Inset of (a) shows the difference in ZFC magnetization with and without halt as a function of temperature. (b) Time-dependent dc magnetization data at 2 K after zero-field-cooled (ZFC) and field-cooled (FC) conditions at $H = 10$ kOe.

In Figure 5.7(a) we show the ZFC, $M(T)$ data with and without halt at 30 and 50 K respectively. From this figure, it is clearly seen that there is a dip at 30 K, but we do not see any dip at 50 K. In the inset of Figure 5.7(a) we show the difference plot between the ZFC data without and with waiting as a function of temperature, which show a sharp peak feature at 30 K but no such feature at the waiting temperature at 50 K suggesting that the previous temperature is below the glass transition temperature and the other temperature is above the glass transition. This memory effect suggests that in this bilayer metastable glassy state exists.

To study the glassy dynamics, we have examined the time-dependent magnetic relaxation effect at a constant temperature and the effect of magnetic field on the bilayer of LSMO (2 nm) – YCMO (20 nm) following the measurement protocols mentioned in the literature [34]. The sample is cooled under ZFC or FC conditions to the desired measurement temperature, and then the magnetic field is applied for ZFC conditions, or the cooling magnetic field is retained in case of FC mode. After that time dependent magnetization growth is recorded at the measurement temperature in the presence of a steady magnetic field. In Figure 5.7(b) we compare the normalized magnetization data (M_t/M_0) as a function of time (t) at 2 K in both ZFC and FC conditions performed in the presence of a magnetic field of 10 kOe. We do not observe any magnetic relaxation effect either in ZFC or FC mode at low magnetic field (0.1 kOe). Therefore, we have performed the relaxation experiment with the high magnetic field (10 kOe). From Figure 5.7(b) we see that there is an increase in magnetization with time at $H = 10$ kOe under ZFC conditions while the magnetization data remains almost unchanged with time under FC conditions. This experimental observation indicates that there is a field induced isothermal growth of ferromagnetic clusters under ZFC conditions in the presence of a high magnetic field. The evolution of ZFC magnetization as a function of time at constant temperature and magnetic field has been fitted well with the stretched exponential function [35] of the type, $M_t(H) = M_0(H) + [M_\infty(H) - M_0(H)] [1 - \exp\{- (t/\tau)^\alpha\}]$ as shown in Figure 5.7(b), where τ is the characteristic relaxation time, α is the stretching parameter which ranges between 0 and 1. From the fit, we obtain stretching parameter, $\alpha = 0.63$ and the characteristic relaxation time, $\tau = 978$ sec. These experimental results indicate the coexistence of glassy state along with the FM clusters embedded in the AFM matrix which is crucial

in the understanding of exchange interaction phenomena across the interface in the bilayer of LSMO - YCMO.

5.4.3 DC Magnetization as a function of magnetic field, $M(H)$:

5.4.3.1 Field - Cooled (FC) exchange bias

To understand the microscopic exchange interactions at the interface of LSMO - YCMO, we have recorded the $M(H)$ loops at 2 K under FC conditions. The results on the field-cooled (≥ 10 kOe) exchange bias on bilayers of LSMO - YCMO have been compared with that of bare YCMO film. We have performed the experiment by cooling the samples from 390 to 2 K at $H = \pm 10$ kOe and then data was recorded at 2 K while sweeping the magnetic field in the range of ± 70 kOe. The presence of exchange anisotropy at the interface of the LSMO - YCMO bilayer is revealed by the asymmetric shift in the FC $M(H)$ loop along the negative and positive magnetic field axis when the cooling magnetic field is either positive or negative, respectively [Figure 5.8]. Although the bare YCMO film shows a minor shift in the $M(H)$ loop due to intrinsic magnetic phase separation [36,37], the shift is enhanced in the LSMO - YCMO bilayer due to the ferromagnetic moment induced at the interface of YCMO thereby allowing a greater number of pinning centers causing enhanced unidirectional anisotropy.

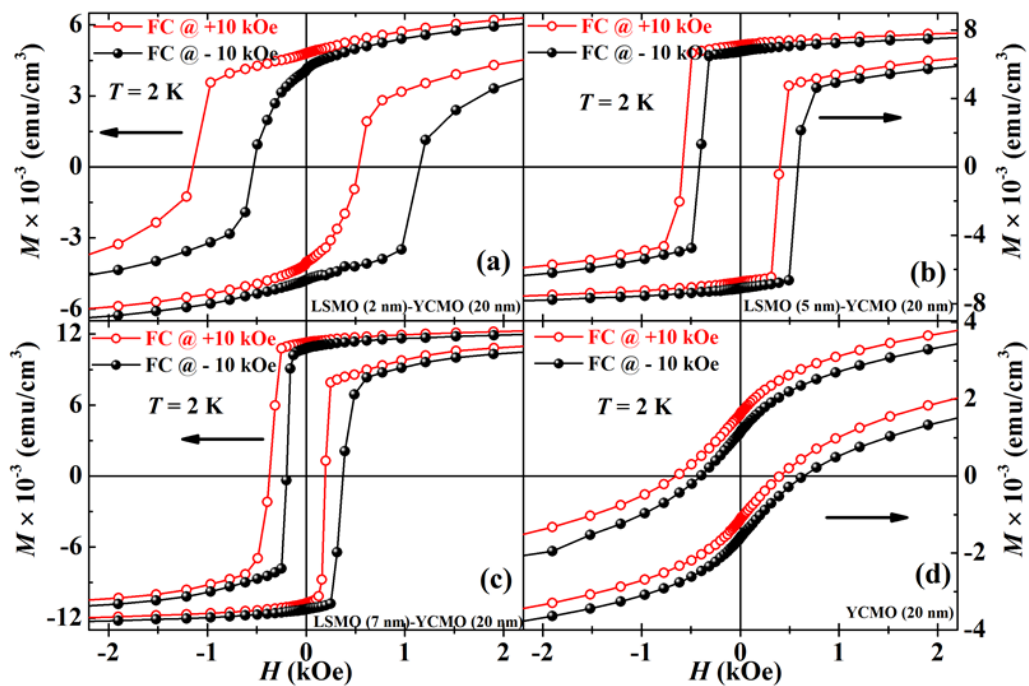


Figure 5.8: $M(H)$ hysteresis loops of (a-c) bilayers of LSMO (varying thickness) - YCMO (20 nm) and (d) YCMO film (20 nm) at 2 K recorded after FC with $H = \pm 10$ kOe.

From the examination of above data, it is evident that in the case of a bilayer of LSMO (varying thickness) - YCMO (20 nm), the asymmetry in the $M(H)$ hysteresis loop gradually reduces with the increasing thickness of ferromagnetic LSMO layer indicating the reduction in exchange bias (H_E) value. This result is consistent with the Meiklejohn and Bean equation [11], which suggests that EB varies inversely with the thickness of the ferromagnetic layer.

We have also compared the various cooling magnetic field dependence of $M(H)$ loops of bilayers of LSMO of different thickness - YCMO of fixed thickness (20 nm) with the bare 20 nm YCMO film at 2 K as shown in Figure 5.9. We performed the measurement after field cooling the sample in the presence of various magnetic fields from 390 to 2 K and then isothermal $M(H)$ data is recorded after each FC at $H = \pm 70$ kOe. Interestingly, these bilayers show non-monotonic behavior of H_E and H_C as functions of the cooling magnetic field at 2 K as shown in the Figures 5.9(e) and 5.9(f).

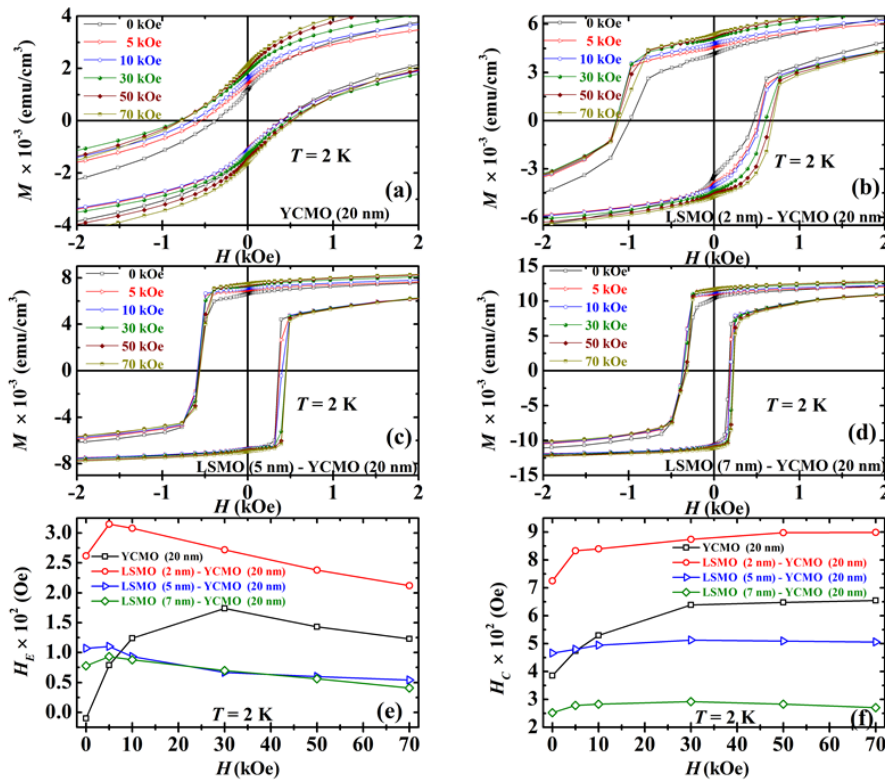


Figure 5.9: Cooling magnetic field dependence of $M(H)$ hysteresis loops at 2 K for (a) bare YCMO film (20 nm) and (b-d) bilayers of LSMO (varying thickness) - YCMO (20 nm). Comparison of (e) exchange bias (H_E) and (f) coercive field (H_C) as a function of the magnetic field between 20 nm bare YCMO film and bilayers of LSMO (varying thickness) - YCMO (20 nm) at 2 K.

From Figure 5.9 it is observed that initially the value of H_E and H_C increases for both bare YCMO film (20 nm) and bilayers up to 30 and 10 kOe respectively and then

it decreases. In Table 5.1 we have summarized the remnant field-cooled (RFC) and FC, H_E and H_C parameters for bare YCMO film (20 nm) and bilayers of LSMO (varying thickness) - YCMO (20 nm).

Table 5.1: Comparison of exchange bias parameters among bilayers of YCMO (20 nm) - LSMO (varying thickness) with respect to bare YCMO film (20 nm) at $T = 2$ K in the presence of different cooling magnetic fields applied at 390 K.

Sample	LSMO (2 nm) - YCMO (20 nm)		LSMO (5 nm) - YCMO (20 nm)		LSMO (7 nm) - YCMO (20 nm)		YCMO (20 nm)	
H (kOe)	H_E (Oe)	H_C (Oe)	H_E (Oe)	H_C (Oe)	H_E (Oe)	H_C (Oe)	H_E (Oe)	H_C (Oe)
~ 0.005	262	725	107	466	78	252	10	385
5	315	833	110	479	93	278	79	474
10	308	840	93	494	88	283	124	530
30	272	874	67	512	70	292	174	639
50	238	898	60	509	56	283	143	648
70	212	899	54	506	41	271	123	654

The variation of H_E and H_C with cooling field can be understood in terms of the competition between Zeeman coupling and interfacial interaction of the LSMO-YCMO bilayer, where the spin-glass phase of YCMO is strongly affected by the strength of cooling magnetic field [38]. With increasing external magnetic field the effective Zeeman energy increases which align more and more ferromagnetic spins from the FM clusters/SG region along a preferential direction thereby leading to the reduction of average anisotropy of the bilayers due to randomness. On the other hand, in bare YCMO film with increasing magnetic field, spins from spin-glass regions interfacing with the FM clusters aligns along the same direction resulting in strong exchange anisotropy. As a result, we see an initial increase in H_E in both bare YCMO and bilayers of LSMO - YCMO with a magnetic field. On further increasing the cooling magnetic field glassy phase fraction reduces resulting in unfreezing the spin-glass regions. Therefore, there is a decrease in the relative proportion of SG regions with respect to FM clusters and therefore, the small amounts of spins from the SG region can no longer exert the pinning force on the relatively larger ferromagnetic moments of the FM clusters resulting in weaker exchange anisotropy which results in lowering of H_E in bare YCMO film. On the other hand, in the bilayer with the increase in magnetic field it

leads to the saturation of ferromagnetic magnetization of LSMO as well as an increment in the growth of ferromagnetic clusters and reduction of frozen ferromagnetic spins in the SG region from YCMO layer. As a result, H_E decreases in the bilayer with magnetic field.

Now we discuss the results on FC $M(H)$ behavior at 2 K after magnetic field cooling with ± 10 kOe for bilayers of LSMO of fixed thickness (5 nm) - YCMO of varying thickness as shown in Figures 5.10(a), 5.10(b) and 5.10(c), respectively. From this experiment, we observe that increasing the thickness of YCMO layer reduces the exchange bias value of the bilayer as a result of growing amount of ferromagnetic clusters at the expense of glassy regions present in the antiferromagnetic matrix of YCMO due to intrinsic magnetic phase separation. Although the previous observation is somewhat opposite to that expected trend because with increasing thickness of antiferromagnetic YCMO layer average anisotropy should increase which will pin the ferromagnetic moments with greater force. Similar experiments have been carried out for the bare YCMO films of varying thickness as shown in Figures 5.11(a), 5.11(b) and 5.11(c), respectively.

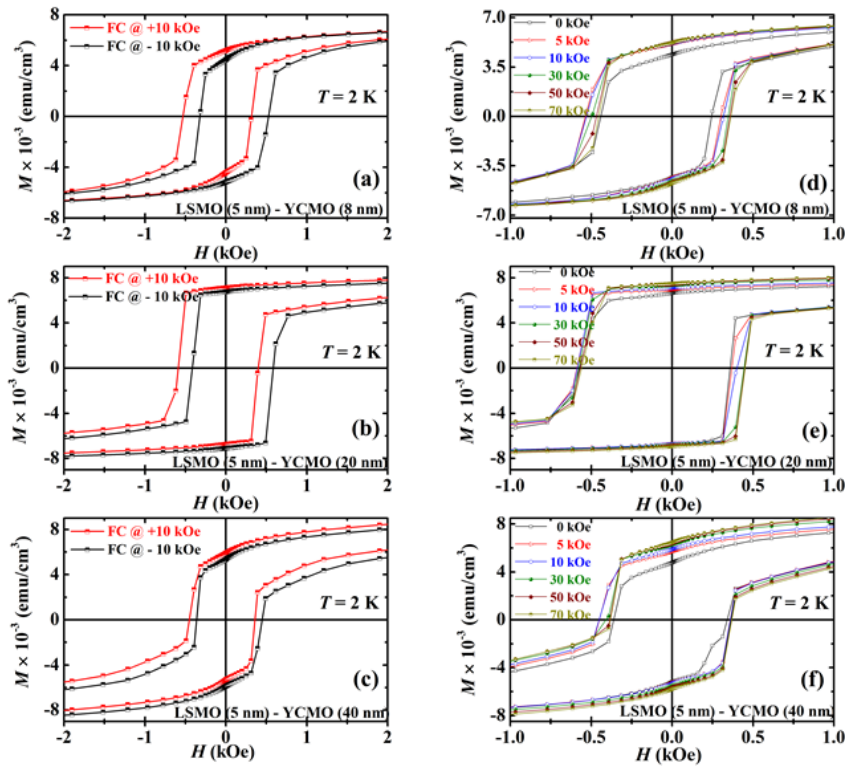


Figure 5.10: $M(H)$ hysteresis loops at 2 K (a-c) under field-cooled (FC) condition at $H = \pm 10$ kOe and (d-f) as a function of various cooling magnetic fields applied at 390 K for bilayers of LSMO (5 nm) - YCMO (varying thickness).

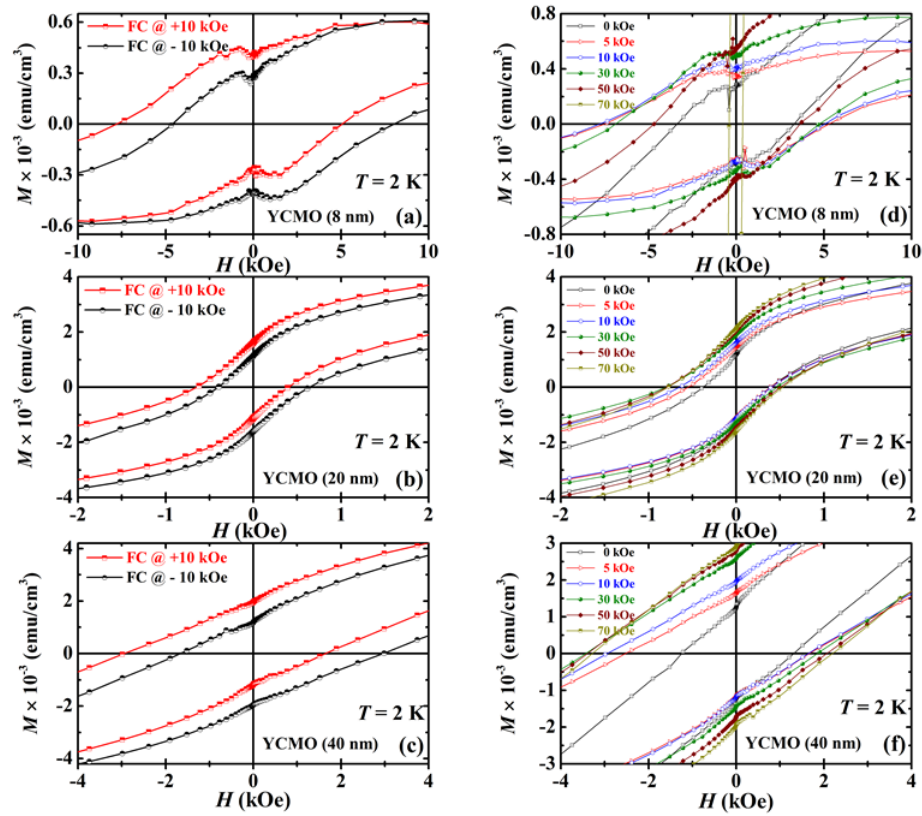


Figure 5.11: $M(H)$ hysteresis loops at 2 K (a-c) under field-cooled (FC) condition at $H = \pm 10$ kOe and (d-f) as a function of cooling magnetic field for bare YCMO films of varying thickness.

We have recorded $M(H)$ loops at 2 K after cooling the sample from 390 K in the presence of different magnetic fields for bilayers of LSMO (5 nm) - YCMO (varying thickness) as well as for bare YCMO film (varying thickness) as shown in Figures 5.10 and 5.11 respectively. Based on the observations as displayed in Figures 5.10 and 5.11, we have compared the cooling magnetic field dependent H_E and H_C of bilayers to that of bare YCMO film at 2 K as shown in Figure 5.12. From this figure we observe that H_E and H_C values are always lower in magnitude in the bilayers of LSMO - YCMO as compared to bare YCMO films which suggest that increased ferromagnetic component in the bilayer leads to the weakening of interfacial exchange anisotropy and therefore reduction in exchange bias.

In the case of bare YCMO film, with lowering the thickness of YCMO, there is an increased magnetic phase separation resulting in more glassy/FM components which create more interfaces with the non-ferromagnetic counterpart thereby leading to the increment in exchange bias. In this context, it is important to mention that in the bare YCMO film of thickness 8 nm, we observe complete ferromagnetic $M(H)$ loop with very low coercivity measured at 2 K after FC with 70 kOe as shown in Figure 5.11(d)

indicating the dominance of ferromagnetic clusters in the YCMO film with lower thickness.

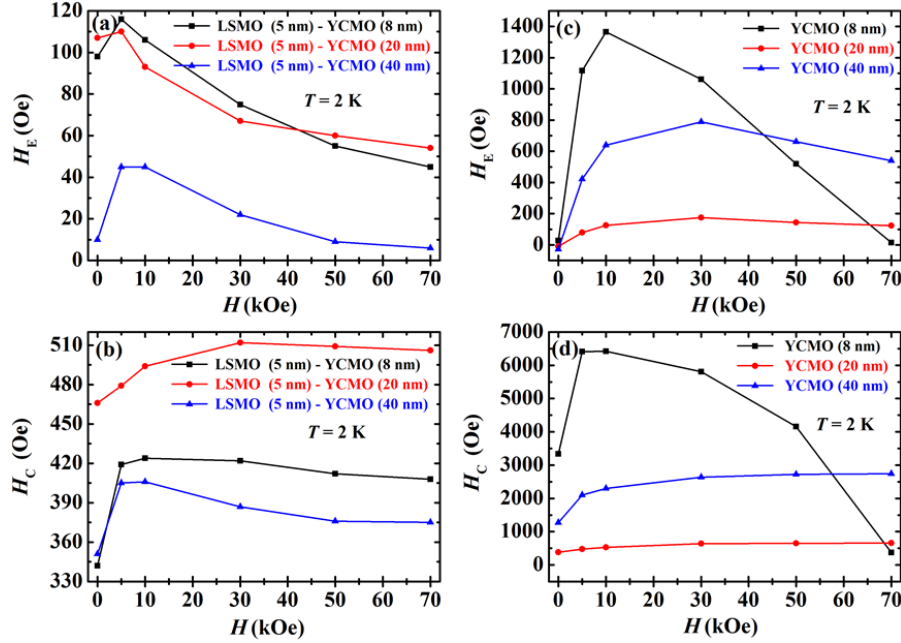


Figure 5.12: Comparison of exchange bias (H_E) and coercive field (H_C) as a function of magnetic field at 2 K between (a-b) bilayers of LSMO (5 nm) - YCMO (varying thickness) and (c-d) bare YCMO films of varying thickness.

5.4.3.2 Training effect

We have studied the training effect in the exchange-biased bilayer of LSMO (2 nm) - YCMO (20 nm). The training effect is the gradual reduction in asymmetry in the isothermal $M(H)$ hysteresis loops as a result of decreased exchange anisotropy at the interface when the exchange coupled magnetic systems undergo continuous field cycling through several hysteresis loops [16]. We have investigated the training effect after field cooling the sample in the presence of a magnetic field of 10 kOe from 390 to 2 K, and then the isothermal $M(H)$ loops are measured consecutively up to 10 cycles in the magnetic field range of ± 70 kOe as shown in Figure 5.13(a). In Figure 5.13(b) we have shown that the value of H_E reduces with increasing number of consecutive field cycling as a result of training effect. The occurrence of training effect in this exchange-biased bilayer can be understood based on the well-known spin configurational relaxation model [39]. Although the observation of thermal training effect is somewhat unusual for a single crystalline system, we attribute the occurrence of training due to the presence of spin-glass phase (in the YCMO layer) which evolves from a non-equilibrium spin-configurations toward an equilibrium configuration with field cycling.

Though there are several potential models [40,41] which can explain the training effect, a complete understanding requires characterization of the interfacial spin configurations. With consecutive magnetic field cycling the ferromagnetic domain of the LSMO and SG-like spins of the YCMO change their direction in a synchronous manner leading to the relaxation of AFM interface spin configuration towards equilibrium. This results in the weakening of exchange interaction at the interface between AFM and FM with the consequence of decreased exchange bias. A similar mechanism has also been found to be operative in the phase separated manganite, $\text{Pr}_{1/3}\text{Ca}_{2/3}\text{MnO}_3$ giving rise to training effect [37].

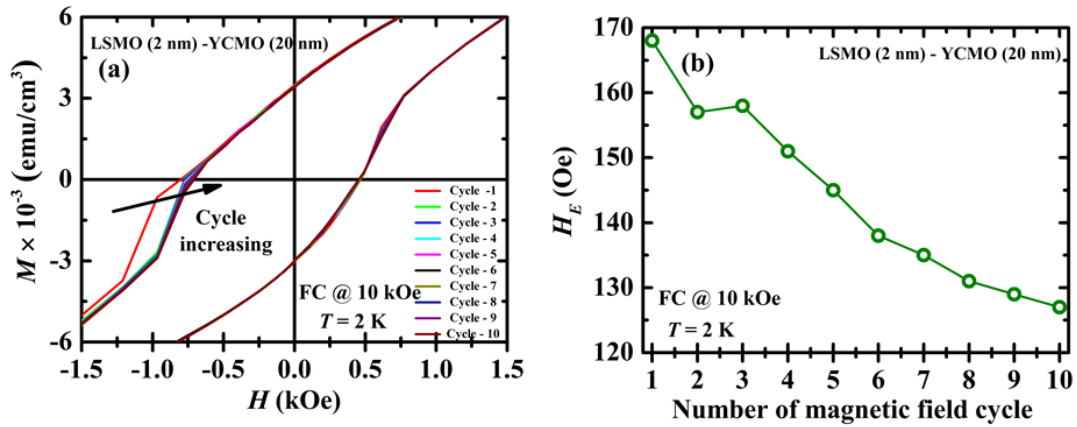


Figure 5.13: (a) Training effect of field-cooled conventional exchange bias (CEB) at 2 K and (b) variation of H_E as a function of increasing number of magnetic field cycle at 2 K for bilayer of LSMO (2 nm) - YCMO (20 nm).

5.4.3.3 Remnant - Field - Cooled (RFC) exchange bias

Now we turn our discussion on the remnant-field-cooled exchange bias on bilayers of LSMO - YCMO. We must note that in the absence of any externally applied magnetic field, a small remnant magnetic field of ~ 5 Oe exists in the superconducting magnet [42]. Interestingly, upon cooling in the presence of remnant magnetic field, we observe an asymmetric shift in the $M(H)$ loop of LSMO (2 nm) - YCMO (20 nm) along the magnetic field (H) axis as shown in Figure 5.14. From this figure, we see that the initial magnetization curve [i.e. the first portion of the $M(H)$ data associated with the sweeping of magnetic field between 0 and $+H$] recorded under RFC condition, starts from a magnetized state ($M \neq 0$ at $H = 0$) suggesting the existence of a remnant magnetic field in the superconducting magnet. It has already been mentioned that we find the existence of a small trapped magnetic field even after demagnetizing the remnant magnetic field of the superconducting magnet by oscillating the magnetic field

before each experiment. In order to examine the effect of the trapped magnetic field on EB, we have carefully performed the $M(H)$ loop measurements after cooling the sample in the presence of a remnant magnetic field. Furthermore, we observe that depending on the polarity of the remnant magnetic field of the superconducting magnet whether positive or negative, $M(H)$ loop is shifted along either negative or positive axis of the magnetic field [Figure 5.14].

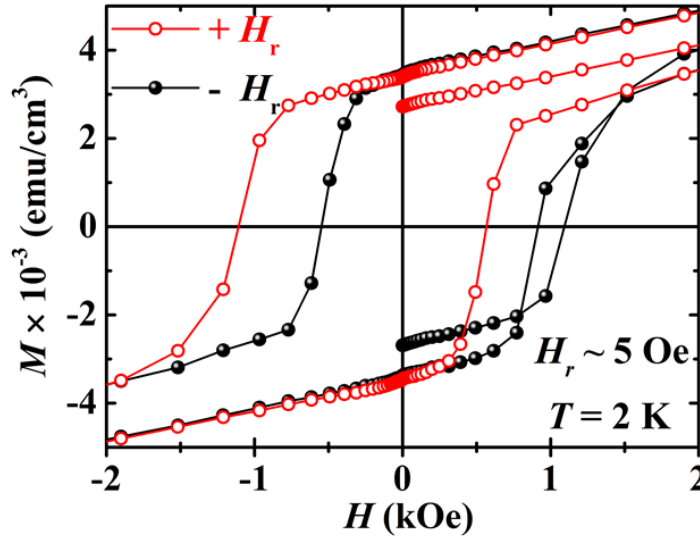


Figure 5.14: $M(H)$ hysteresis loops at 2 K for LSMO (2 nm)-YCMO (20 nm) bilayer under cooling in the presence of small remnant magnetic field.

The observation of significant EB in this bilayer in the presence of such a small remnant magnetic field is noteworthy. In the case of conventional exchange bias as shown in Figure 5.8(a), the sample is cooled in the presence of a magnetic field across the Néel or spin-glass transition temperature to realize the unidirectional magnetic anisotropy at the interface. On the other hand, in the case of RFC experiment exchange interaction across the interface gets locked in while cooling under such a low remnant magnetic field [43], since the ferromagnetic LSMO layer orders at a higher temperature than the antiferromagnetic YCMO layer. It can, therefore, be inferred that such a significant loop shift is associated with the remnant magnetization state of LSMO at $T \geq T_N$ where the small magnetic field of ~ 5 Oe saturates the FM layer due to small anisotropy [44]. In Figure 5.15(a), we compare the P and N, $M(H)$ loops recorded under remnant field-cooled conditions where both the hysteresis loops are shifted along the negative magnetic field axis overlapping with each other without showing any effect of initial magnetization direction (P or N) [21,31]. A similar behavior was

observed for the P and N, $M(H)$ loops recorded after field cooling with ± 10 kOe [Figure 5.15(b)] suggesting that the exchange bias in the former case (RFC conditions) is of conventional type due to the presence of small trapped field and depends only on the direction of the cooling remnant magnetic field. To record the P, N $M(H)$ loop under FC conditions, we have performed the following experiment. The sample was cooled from 390 to 2 K in the presence of a magnetic field of 10 kOe and then switched off the magnetic field to zero followed by ramping of the magnetic field in P and N sequence while recording the $M(H)$ data. EB under such a low remnant magnetic field is also observed in the virgin LSMO-YCMO bilayers not exposed to a magnetic field indicating that low-field EB is independent of any magnetic history of the sample.

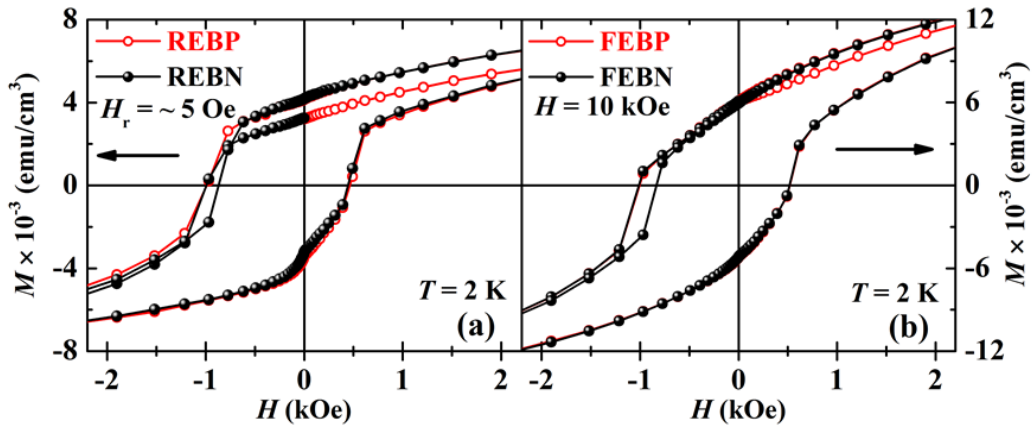


Figure 5.15: P and N-types of $M(H)$ loops at 2 K for LSMO (2 nm) - YCMO (20 nm) bilayer under (a) remnant field-cooled and (b) FC conditions. REB and FEB stands for remnant-field-cooled and field-cooled exchange bias respectively. [P = $0 \rightarrow (+H) \rightarrow (-H) \rightarrow (+H)$; N = $0 \rightarrow (-H) \rightarrow (+H) \rightarrow (-H)$, where $0 \rightarrow (+H)$ or $0 \rightarrow (-H)$ is the initial positive (P) and negative (N) magnetization directions respectively].

5.4.3.4 Temperature-dependent Field - Cooled (FC) exchange bias

We have examined the temperature dependence of interfacial exchange interaction in LSMO (2 nm) - YCMO (20 nm) bilayer, after field cooling the sample in the presence of a magnetic field of 10 kOe from 390 K to the desired temperature and then $M(H)$ loops are recorded at different temperatures [inset of Figure 5.16]. Figure 5.16 shows the variation of H_E and H_C as functions of temperature showing that with increasing temperature H_E gradually decreases and disappears at blocking temperature ($T_B \sim 70$ K). A similar trend observed in H_C indicates a common mechanism for the exchange bias and coercivity. The exchange anisotropy across the magnetic interface becomes weaker resulting in free switching of the ferromagnetic layer while H_E remains zero above the blocking temperature.

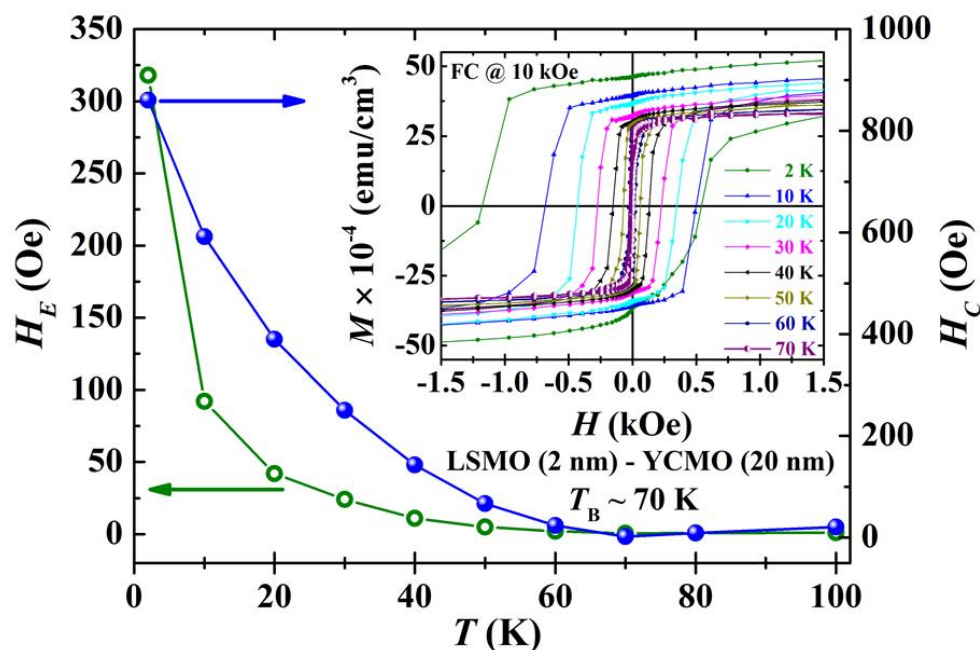


Figure 5.16: Temperature dependence of field-cooled (FC) exchange bias (H_E) and coercive field (H_C) for LSMO (2 nm) - YCMO (20 nm) bilayer. The inset shows the FC $M(H)$ hysteresis loops at different temperatures.

5.5 Conclusions

In conclusion, we observe that LSMO-YCMO bilayers grown on STO substrates undergo tetragonal distortion due to the strong biaxial tensile strain induced by STO. We have studied the magnetic field and temperature dependence of exchange bias and coercivity for the LSMO-YCMO bilayers. In addition, we have compared the EB results on the LSMO - YCMO bilayers with that of bare YCMO films which alone show exchange bias due to intrinsic electronic phase separation.

The observation of exchange bias in LSMO-YCMO bilayers in the presence of a small remnant magnetic field (~ 5 Oe) of the superconducting magnet provides a means to control exchange-coupled interfaces in the heterostructures. Therefore, an investigation of the magnetic configuration across the LSMO-YCMO interface would be of great interest and would throw light on the nature of exchange bias phenomenon.

Bibliography

- [1] J. G. Bednorz and K. A. Müller, *Z. Phys. B Condens. Matter* **64**, 189 (1986).
- [2] A. Ramirez, *J. Phys.: Condens. Matter* **9**, 8171 (1997).

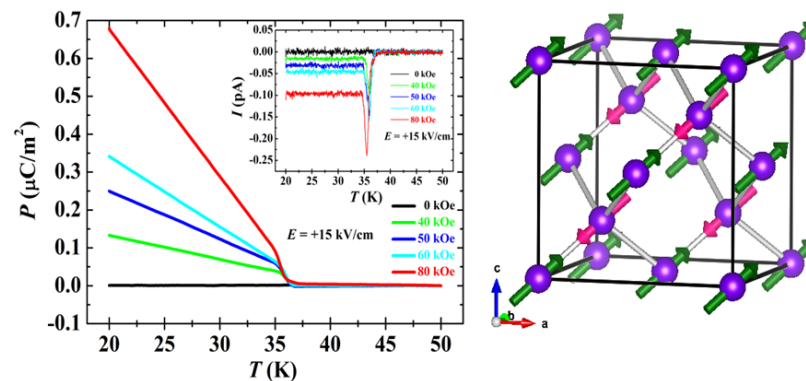
-
- [3] C. N. R. Rao and B. Raveau, Colossal magnetoresistance, charge ordering and related properties of manganese oxides (World Scientific, 1998).
- [4] M. Imada, A. Fujimori, and Y. Tokura, *Rev. Mod. Phys.* **70**, 1039 (1998).
- [5] W. Eerenstein, N. Mathur, and J. F. Scott, *Nature* **442**, 759 (2006).
- [6] C. N. R. Rao, A. Sundaresan, and R. Saha, *J. Phys. Chem. Lett.* **3**, 2237 (2012).
- [7] H. Y. Hwang, Y. Iwasa, M. Kawasaki, B. Keimer, N. Nagaosa, and Y. Tokura, *Nat. Mater.* **11**, 103 (2012).
- [8] P. Yu *et al.*, *Phys. Rev. Lett.* **105**, 027201 (2010).
- [9] A. Ohtomo and H. Hwang, *Nature* **427**, 423 (2004).
- [10] J. Chakhalian *et al.*, *Nat. Phys.* **2**, 244 (2006).
- [11] W. H. Meiklejohn and C. P. Bean, *Phys. Rev.* **102**, 1413 (1956).
- [12] W. H. Meiklejohn and C. P. Bean, *Phys. Rev.* **105**, 904 (1957).
- [13] R. Stamps, *J. Phys. D: Appl. Phys.* **33**, R247 (2000).
- [14] V. Skumryev, S. Stoyanov, Y. Zhang, G. Hadjipanayis, D. Givord, and J. Nogues, *Nature* **423**, 850 (2003).
- [15] J. Nogués, J. Sort, V. Langlais, V. Skumryev, S. Surinach, J. Munoz, and M. Baró, *Phys. Rep.* **422**, 65 (2005).
- [16] J. Nogués and I. K. Schuller, *J. Magn. Magn. Mater.* **192**, 203 (1999).
- [17] A. Berkowitz and K. Takano, *J. Magn. Magn. Mater.* **200**, 552 (1999).
- [18] D. Navas *et al.*, *New J. Phys.* **14**, 113001 (2012).
- [19] M. Ali, P. Adie, C. H. Marrows, D. Greig, B. J. Hickey, and R. L. Stamps, *Nat. Mater.* **6**, 70 (2007).
- [20] G. Salazar-Alvarez, J. Sort, S. Surinach, M. D. Baró, and J. Nogués, *J. Am. Chem. Soc.* **129**, 9102 (2007).
- [21] A. Nayak, M. Nicklas, S. Chadov, C. Shekhar, Y. Skourski, J. Winterlik, and C. Felser, *Phys. Rev. Lett.* **110**, 127204 (2013).
- [22] S. Wu, S. A. Cybart, P. Yu, M. Rossell, J. Zhang, R. Ramesh, and R. Dynes, *Nat. Mater.* **9**, 756 (2010).
- [23] S. Wu, S. A. Cybart, D. Yi, J. M. Parker, R. Ramesh, and R. Dynes, *Phys. Rev. Lett.* **110**, 067202 (2013).
- [24] C. N. R. Rao, A. Arulraj, P. Santosh, and A. K. Cheetham, *Chem. Mater.* **10**, 2714 (1998).
- [25] Y. Tokura and Y. Tomioka, *J. Magn. Magn. Mater.* **200**, 1 (1999).

- [26] P. M. Chowdhury, B. Ghosh, A. Raychaudhuri, S. Kaushik, and V. Siruguri, J. Nanoparticle Research **15**, 1 (2013).
- [27] S. Giri, A. Poddar, and T. Nath, AIP Advances **1**, 032110 (2011).
- [28] R. Datta, S. Kanuri, S. Karthik, D. Mazumdar, J. Ma, and A. Gupta, Appl. Phys. Lett. **97**, 1907 (2010).
- [29] Z. Yang, Y. Zhang, J. Aarts, M. Wu, and H. Zandbergen, Appl. Phys. Lett. **88**, 072507 (2006).
- [30] V. B. Shenoy and C. N. R. Rao, Phil. Trans. R. Soc. (London) **366**, 63 (2008).
- [31] B. Wang, Y. Liu, P. Ren, B. Xia, K. Ruan, J. Yi, J. Ding, X. Li, and L. Wang, Phys. Rev. Lett. **106**, 077203 (2011).
- [32] T. Maity, S. Goswami, D. Bhattacharya, and S. Roy, Phys. Rev. B: Condens. Matter **89**, 140411 (2014).
- [33] K. Jonason, E. Vincent, J. Hammann, J. Bouchaud, and P. Nordblad, Phys. Rev. Lett. **81**, 3243 (1998).
- [34] D. Choudhury *et al.*, Phys. Rev. Lett. **108**, 127201 (2012).
- [35] A. Haldar, K. Suresh, and A. Nigam, Europhys. Lett. **91**, 67006 (2010).
- [36] T. Qian, G. Li, T. Zhang, T. Zhou, X. Xiang, X. Kang, and X. Li, Appl. Phys. Lett. **90**, 2503 (2007).
- [37] D. Niebieskikwiat and M. Salamon, Phys. Rev. B: Condens. Matter **72**, 174422 (2005).
- [38] L. Del Bianco, D. Fiorani, A. M. Testa, E. Bonetti, and L. Signorini, Phys. Rev. B **70**, 052401 (2004).
- [39] C. Binek, Phys. Rev. B: Condens. Matter Mater. Phys. **70**, 014421 (2004).
- [40] E. Menéndez *et al.*, Phys. Rev. B **89**, 144407 (2014).
- [41] A. Hoffmann, Phys. Rev. Lett. **93**, 097203 (2004).
- [42] N. Kumar and A. Sundaresan, Solid State Commun. **150**, 1162 (2010).
- [43] T. Ambrose and C. Chien, J. Appl. Phys. **83**, 7222 (1998).
- [44] P. Miltényi, M. Gierlings, M. Bammig, U. May, G. Güntherodt, J. Nogués, M. Gruyters, C. Leighton, and I. K. Schuller, Appl. Phys. Lett. **75**, 2304 (1999).

Magnetolectric effect in A-site magnetic spinel oxides, MnX_2O_4 (X = Al, Ga)^{*}

Summary

Electric field control of magnetism in materials has received much attention in recent years because of its potential for magnetoelectric devices and technological applications. Several materials exhibiting magnetoelectric effect, i.e. mutual control of electric polarization with the magnetic field or magnetization with an electric field, below the magnetic ordering temperature have been discovered. In this chapter, the discovery of linear magnetolectric effect in this A-site antiferromagnetic spinel family of oxides, MnX_2O_4 (X = Al, Ga) has been discussed. An external magnetic field induces a dielectric anomaly at T_N , accompanied by the generation of electric polarization that varies linearly with magnetic field. Powder neutron diffraction together with magnetic, magnetolectric measurements on single crystal of MnGa_2O_4 and phenomenological theory suggest that the easy axis direction in this compound is [111] with the corresponding magnetic symmetry $R\bar{3}'m'$. According to the proposed theoretical model the magnetolectric effect in these compounds is due to single-ion contribution of magnetic ions located in non-centrosymmetric crystal environment.



^{*}Paper based on this chapter is published in: Phys. Rev. B 94, 014428 (2016), © (2016) by the American Physical Society.

6.1 Introduction

The spinel structure with the chemical formula, $AB_2(O, S, Se)_4$, is one of the most important class of transition metal compounds which have provided a rich variety of phenomena, including ferromagnetism, ferrimagnetism, antiferromagnetism and Jahn-Teller transitions [1]. The spinel structure contains two fundamental building blocks, AO_4 tetrahedra and BO_6 octahedra [Figure 6.1(a)]. There is an edge-sharing between the BO_6 octahedra giving rise to rutile-like array of edge-sharing chains along the $[110]$, $[1\bar{1}0]$, $[101]$, $[10\bar{1}]$, $[011]$ and $[01\bar{1}]$ directions. The B ions themselves form a three-dimensional network of corner-sharing tetrahedra which is known as the pyrochlore lattice [Figure 6.1(b)]. This pyrochlore structure gives rise to strong geometrical frustration. If we look at the pyrochlore lattice from the $[111]$ direction as displayed in Figure 6.1(c) we will see that there are two types of plane with alternate stacking. One is a two-dimensional triangular lattice consisting of apical B ions of the tetrahedra, and the other is a two-dimensional kagomé lattice consists of the B triangles at the base of the tetrahedra. The tetrahedrally coordinated A -ions located in the vacant spaces left by the BO_6 octahedra form a diamond lattice as shown in Figure 6.1(d). In spinel oxides, BO_6 octahedra can be either compressed or elongated along the $[111]$ direction giving rise to a local trigonal symmetry which determines the electronic configuration of the B ions. The trigonal distortion is parameterized by the “ u parameter”, which represents the position of O ions within the cubic cell. For ideal BO_6 octahedra, $u = 3/8$, while a value smaller or larger than $3/8$ corresponds to compression or elongation of the octahedra.

In the presence of cubic crystal field fivefold-degeneracy of the d -orbitals of transition-metal ion is lifted leading to the formation of high-lying, doubly degenerate e_g and low-lying, triply degenerate t_{2g} orbitals. In addition, a local trigonal distortion of the crystal field further leads to the splitting of triply degenerate t_{2g} orbitals into one a_{1g} orbital oriented towards the centre of the B -lattice tetrahedron and two degenerate e_g orbitals (different from the e_g doublet under cubic crystal field) extending perpendicular to the a_{1g} orbital [Figure 6.1(e)]. Moreover, a tetragonal distortion splits the triply degenerate t_{2g} orbitals into d_{xy} and a doubly degenerate d_{yz}/d_{zx} pair at low temperature and the doubly degenerate e_g orbitals into nondegenerate $d_{x^2-y^2}$ and

$d_{3z^2-r^2}$ orbitals. On the other hand, fivefold degenerate d -orbitals of the transition-metal ion located in the tetrahedral A -site undergoes splitting into high-lying, triply degenerate t_2 and low-lying doubly degenerate e orbitals, a reverse situation as compared to the octahedral B -site. The magnetic coupling in spinels usually varies with the number of d -electrons, reflecting changes in orbital character. Most spinel oxides with transition-metal ions are magnetic insulators because of the strong Coulomb repulsion within the narrow d -orbitals. The non-magnetic state could be formed as a result of the formation of a spin singlet state. Metallic nature has also been observed sometimes in mixed-valent spinels but not often. Usually, spinel sulfides are much more conducting than oxides as a result of increased bandwidth due to enhanced $p - d$ hybridization.

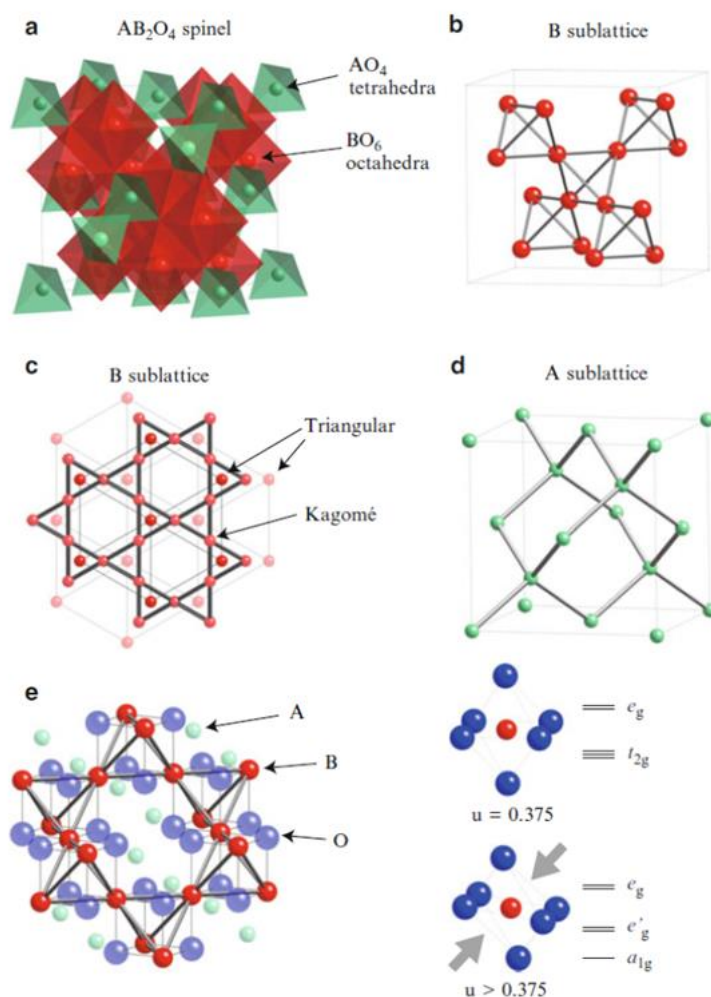


Figure 6.1: (a) Schematic representation of cubic spinel structure consists of fundamental building blocks of AO_4 tetrahedra and BO_6 octahedra, (b) the pyrochlore lattice made of B sublattice, (c) the pyrochlore lattice viewed from the [111] direction, (d) the diamond lattice made of A sublattice and (e) octahedrally coordinated B ions embedded in the cubic spinel structure. The inset shows the trigonal distortion (u) of the BO_6 octahedra [adapted with permission from ref. 2, © (2011) by Springer].

The diversity of magnetic properties of spinels is due to the fact, that both the *A* and *B* sublattice can accommodate magnetic ions with various exchange paths between them [2]. The *A-A* intra-sublattice magnetic interactions are known to be weak and do not influence the type of magnetic order as long as there is a sufficient number of magnetic ions at the *B*-site. However, some spinels with only *A*-site magnetic ions are known to undergo antiferromagnetic ordering at low temperatures [3]. In this chapter, we will discuss the magnetoelectric properties of such *A*-site magnetic spinel oxides.

6.2 Scope of the present investigation

Since the pioneering work of Dzyaloshinskii on the prediction of magnetoelectric effect in Cr_2O_3 followed by its experimental observation by Astrov and Rado, the research on magnetoelectric materials continues to grow [4-7]. In linear magnetoelectric materials the cross coupling between magnetic and electric order parameters ($P_i = \alpha_{ij}H_j$ or $M_i = \alpha_{ji}E_j$) provides an additional degree of freedom, which is promising to design novel devices [8,9]. However, the linear magnetoelectric materials are limited by symmetry requirements, where both spatial inversion and time reversal symmetry needs to be broken simultaneously [10]. There are two classes of materials; one exhibits linear magnetoelectric effects without spontaneous electric polarization as observed in materials such as Cr_2O_3 [11], MnTiO_3 [12], NdCrTiO_5 [13], and $\text{Co}_4\text{Nb}_2\text{O}_9$ [14]. In the second class, a large magnetoelectric effect has been reported in multiferroic materials such as TbMnO_3 [15], RMn_2O_5 [16] and GdFeO_3 [17], where a spontaneous polarization appears upon magnetic ordering. At room temperature the magnetoelectric effect is found only in few materials, e.g. BiFeO_3 and *Z*-type hexaferrite ($\text{Sr}_3\text{Co}_2\text{Fe}_{24}\text{O}_{41}$) [18,19].

Materials having the spinel structure (AB_2O_4) exhibit a rich variety of long-range magnetic ordering, e.g. ferro-, ferri-, and antiferromagnetism, which often occur at high temperatures. The prominent example is the naturally occurring ferrimagnet Fe_3O_4 with $T_c = 860$ K. However, only a few compounds in the spinel family, e.g. CoCr_2O_4 [20] and ZnCr_2Se_4 [21], are known to exhibit magnetoelectric properties, including the celebrated compound Fe_3O_4 [22]. CoCr_2O_4 is magnetoelectric multiferroic, in which conical spin ordering gives rise to spontaneous electric polarization, whereas ZnCr_2Se_4 exhibits a proper screw spin structure without spontaneous polarization, which can be

induced by application of the external magnetic field. Both compounds show magnetoelectric properties at temperatures below approximately 25 K. Therefore, exploring new magnetoelectric materials, especially in such a rich magnetic compounds with crystallographic class as spinels, would help understanding different microscopic mechanisms, which in turn will lead to identify materials with large magnetoelectric coupling. In this chapter, experimental observation of the linear magnetoelectric effect has been discussed following the theoretical prediction on a family of *A*-site collinear antiferromagnetic spinel oxides, MnGa_2O_4 , and MnAl_2O_4 . The symmetry analysis argues that only single-ion effects of magnetic ion located in non-centrosymmetric crystal environment are responsible for the microscopic origin of magnetoelectric coupling in these spinels [23].

6.3 Experimental details

Polycrystalline samples of *A*-site magnetic spinel, MnX_2O_4 ($X = \text{Al}, \text{Ga}$) were prepared by conventional solid state reactions starting from the binary oxides namely MnO (reduced from Mn_2O_3 , Sigma-Aldrich, 99%), Al_2O_3 (Alfa Aesar, 99.99%) and Ga_2O_3 (Sigma-Aldrich, 99.99%). The stoichiometric amounts of precursors were mixed, ground and heated in evacuated quartz ampoules at 900 °C and 1000 °C for 24 hrs. Then the powders were reground, pelletized and sintered in evacuated quartz ampoules at 1100 °C for 24 hrs followed by cooling at the rate of 1 °C/min. Also, MnAl_2O_4 samples under different cooling rates (0.2 and 5 °C/min) were prepared from the sintering temperature of 1100 °C. For all the synthesis we have used a heating rate of 5 °C/min. It is important to mention that the cation inversion can be controlled by different cooling rate and this disorder significantly affects the properties of this *A*-site magnetic spinel. Phase purities of all these samples were confirmed by recording XRD patterns with PANalytical Empyrean diffractometer using $\text{Cu K}\alpha_1$ monochromatic x-ray radiation. The temperature dependent neutron diffraction experiment was carried out on the D2B diffractometer at the Institut Laue-Langevin (ILL) using wavelengths of 1.594 Å. A software package FULLPROF suite [24] was used for the treatment of diffraction pattern and Rietveld analysis.

DC magnetization measurements were carried out using a Superconducting Quantum Interference Device Magnetometer (SQUID, MPMS3, Quantum Design,

USA) in the temperature range of 2-390 K. The specific heat (C_p) was measured while cooling the sample from the temperature above T_N in Physical Property Measurement System (PPMS, Quantum Design, USA). To measure the capacitance and the pyroelectric current an LCR meter (Agilent E4980A) and an electrometer (Keithley 6517A), respectively, were used using a multifunction probe inserted in the PPMS, which allowed accessing the temperature and the magnetic field. The electrode was made by applying conducting Ag paint on both sides of the thin pellets and dried under an infrared lamp. We measured the capacitance in the presence of a magnetic field while warming after performing the magnetic field cooling of the sample from above T_N . Before measuring the pyroelectric current, the sample was poled magnetoelectrically while cooling from a temperature above T_N and then short circuited for 15 min to remove any charges related to the leakage current but the magnetic field was not removed. After that, we measured the magnetoelectric current on warming the sample to a temperature above T_N following the ramping rate of 15 K/min in the presence of an external magnetic field. The electric polarization was obtained by integrating the magnetoelectric current with respect to time and dividing it by the area of the sample after performing required background subtraction. The dc voltage was applied to the samples by using a Radiant Technologies Inc. precision workstation.

6.4 Results and discussion

6.4.1 Structure:

6.4.1.1 X-ray diffraction of MnX_2O_4 ($X = Al, Ga$)

Rietveld refinements performed on the x-ray powder diffraction pattern of polycrystalline samples of $MnAl_2O_4$ and $MnGa_2O_4$ recorded at 298 K with monochromatic laboratory x-ray show that the XRD pattern can be well modeled with the normal spinel structure with the space group $Fd\bar{3}m$. On the other hand, magnetite (Fe_3O_4) crystallizes in the same space group but with inverse spinel structure where one-half of the Fe^{3+} ions occupy the tetrahedral sites ($8a$) and the remaining Fe^{3+} and Fe^{2+} ions occupy octahedral sites ($16d$) and therefore, the formula is written as $Fe^{3+}[Fe^{2+}Fe^{3+}]O_4$ [25]. In the A-site magnetic spinel structure Mn and Al or Ga atoms are located in the non-centrosymmetric Wyckoff positions ($8a$) with tetragonal local symmetry T_d and centrosymmetric Wyckoff positions ($16d$) with rhombohedral

symmetry D_{3d} , respectively. The results obtained based on this refinement show that the experimental sample contains a small amount of anti-site disorder between $8a$ and $16d$ crystallographic sites and the anti-site disorder is more in the MnGa_2O_4 as compared to MnAl_2O_4 . The higher anti-site disorder in MnGa_2O_4 could be attributed to the smaller difference (0.19 Å) between the ionic radii of Mn^{2+} (0.66 Å) and Ga^{3+} (0.47 Å) in tetrahedral coordination as compared to the difference (0.27 Å) between Mn^{2+} and Al^{3+} (0.39 Å) in MnAl_2O_4 .

Table 6.1: Structural parameters of MnX_2O_4 (synthesized at 1100 °C) at 298 K

MnX ₂ O ₄ (Space Group: $Fd\bar{3}m$)				
Compound	MnAl ₂ O ₄ (0.2 °C)*	MnAl ₂ O ₄ (1 °C)*	MnAl ₂ O ₄ (5 °C)*	MnGa ₂ O ₄ (1°C)*
a (Å)	8.20943 (1)	8.20967 (1)	8.20779 (1)	8.45085 (4)
Mn1/Al1(Ga1) ($8a$)				
x	1/8	1/8	1/8	1/8
y	1/8	1/8	1/8	1/8
z	1/8	1/8	1/8	1/8
Al2(Ga2)/Mn2 ($16d$)				
x	1/2	1/2	1/2	1/2
y	1/2	1/2	1/2	1/2
z	1/2	1/2	1/2	1/2
O (32e)				
x	0.26525 (10)	0.26579 (9)	0.26551 (10)	0.26150 (18)
y	0.26525 (10)	0.26579 (9)	0.26551 (10)	0.26150 (18)
z	0.26525 (18)	0.26579 (9)	0.26551 (10)	0.26150 (18)
B_{iso} (Å²)				
Mn	0.74 (2)	0.68 (2)	0.73 (2)	0.49 (5)
Al/Ga	0.62 (3)	0.50 (3)	0.57 (3)	0.18 (2)
O	1.00	1.00	1.00	1.00
Occupancy				
Mn1/Al1(Ga1) ($8a$)	0.920(3)/0.080(3)	0.919(3)/0.081(3)	0.935(3)/0.065(3)	0.835(9)/0.165(9)
Al2(Ga2)/Mn2 ($16d$)	1.920(3)/0.080(3)	1.919(3)/0.081(3)	1.935(3)/0.065(3)	1.835(9)/0.165(9)
O (32e)	1.000	1.000	1.000	1.000

*Cooling rate

The parameter, α defines the degree of cation inversion (or anti-site disorder) present in the spinel structure (AB_2O_4), $A^{2+}_{1-2\alpha}B^{3+}_{2\alpha}(B^{3+}_{2-2\alpha}A^{2+}_{2\alpha})O_4$, where the metal ions outside the bracket belong to the tetrahedral sites ($8a$) and the metal ions within the

bracket, belong to the octahedral sites (16*d*). Since the degree of cation inversion is strongly dependent on the synthetic conditions, we have prepared MnAl₂O₄ samples by different annealing conditions, cooling rates and compared among these samples after performing Rietveld refinements as shown in Table 6.1. Despite our effort, we could see only negligible differences among the MnAl₂O₄ samples due to the small contrast in the x-ray scattering power of Mn and Al. To study the magnetic and electrical properties, all measurements were performed on the samples prepared at 1100 °C with a cooling rate of 1 °C/min.

Table 6.2: Structural parameters of MnAl₂O₄ (synthesized at 1350 °C) at 298 K

MnAl ₂ O ₄ (Space Group: $Fd\bar{3}m$)		
Compound	MnAl ₂ O ₄ (1 °C)*	MnAl ₂ O ₄ (5 °C)*
<i>a</i> (Å)	8.20640 (4)	8.20511 (4)
Mn1/Al1 (8 <i>a</i>)		
<i>x</i>	1/8	1/8
<i>y</i>	1/8	1/8
<i>z</i>	1/8	1/8
Al2/Mn2 (16 <i>d</i>)		
<i>x</i>	1/2	1/2
<i>y</i>	1/2	1/2
<i>z</i>	1/2	1/2
O (32 <i>e</i>)		
<i>x</i>	0.26611 (37)	0.26558 (36)
<i>y</i>	0.26611 (37)	0.26558 (36)
<i>z</i>	0.26611 (37)	0.26558 (36)
<i>B</i> _{iso} (Å ²)		
Mn	0.46 (8)	0.25 (10)
Al	0.39 (12)	0.84 (15)
O	1.00	1.00
Occupancy		
Mn1/Al1 (8 <i>a</i>)	0.927(13) / 0.073 (13)	0.833(11) / 0.167(11)
Al2/Mn2 (16 <i>d</i>)	1.927(13) / 0.073(13)	1.833(11) / 0.167(11)
O (32 <i>e</i>)	1.000	1.000

*Cooling rate

We have studied the effect of annealing temperature on cation distribution by preparing MnAl_2O_4 samples at high temperature ($1350\text{ }^\circ\text{C}$) in the presence of reducing medium (pure H_2 gas, 99.9995 %) and cooled under two different rates, e.g., $1^\circ\text{C}/\text{min}$ and $5^\circ\text{C}/\text{min}$. From the Rietveld refinement of the XRD pattern of these samples, we observe that anti-site disorder is more in these samples compared to the samples prepared at $1100\text{ }^\circ\text{C}$. Moreover, we also observe that between the two samples prepared at $1350\text{ }^\circ\text{C}$, the sample cooled with slow rate contains less cation inversion than the sample cooled with faster rate indicating the importance of both annealing temperature and cooling rate in controlling the cation inversion in the spinel family of oxides. The results are shown in Table 6.2.

6.4.1.2 Neutron diffraction of MnGa_2O_4

Temperature dependent neutron diffraction experiment was carried out on MnGa_2O_4 to study the crystallographic and magnetic structure in detail. The fitted neutron diffraction pattern at 298 and 3.5 K is shown in Figure 6.2.

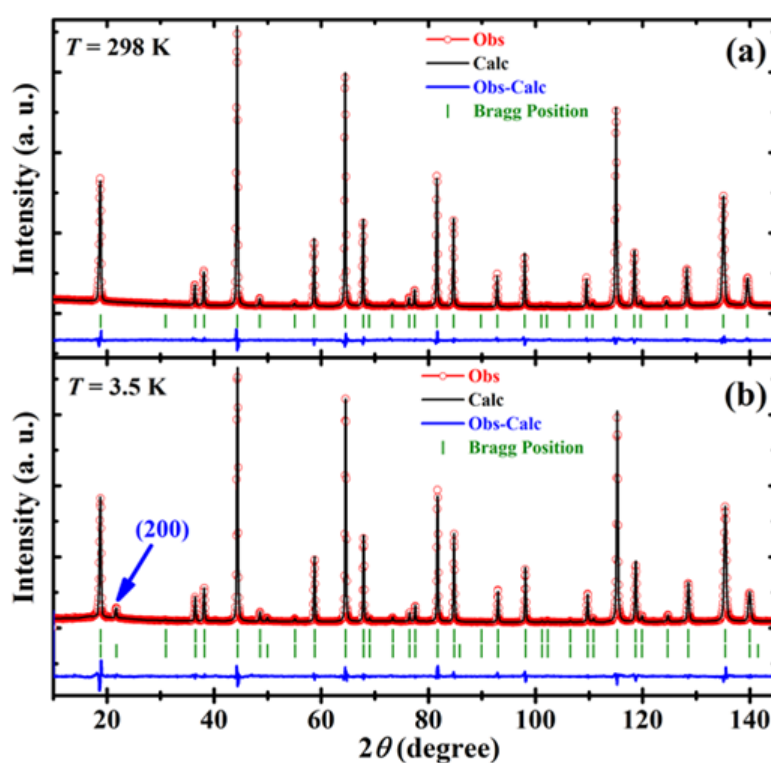


Figure 6.2: (a, b) Rietveld refinements on the neutron diffraction pattern of MnGa_2O_4 acquired at $T = 298$ and 3.5 K with $\lambda = 1.594\text{ \AA}$, respectively. The second Bragg reflections in (b) are associated with magnetic contribution from the compound. The blue arrow on the diffraction pattern at 3.5 K indicates magnetic Bragg peak (200) arises due to antiferromagnetic ordering.

Rietveld refinement of neutron powder data acquired at room temperature allows precise determination of cation inversion as shown in Table 6.3. For the refinement of temperature dependent neutron data, the site occupancy was kept fixed to the room temperature value. From the Rietveld analysis of temperature dependent neutron data, we observe that the structure remains cubic ($Fd\bar{3}m$) down to the lowest temperature. The schematic of the cubic structure obtained from the refinement is shown in Figure 6.3(a).

Table 6.3: Structural parameters of MnGa_2O_4 obtained from the Rietveld refinement of neutron diffraction data acquired at 298 K

MnGa_2O_4 (Space Group: $Fd\bar{3}m$), $\lambda = 1.594 \text{ \AA}$					
Atom	x	y	z	$B_{iso} (\text{\AA}^2)$	Occupancy
Mn1 (8a)	1/8	1/8	1/8	0.49 (4)	0.81
Ga1 (8a)	1/8	1/8	1/8	0.41 (1)	0.19
Ga2 (16d)	1/2	1/2	1/2	0.41 (1)	1.81
Mn2 (16d)	1/2	1/2	1/2	0.49 (4)	0.19
O (32e)	0.26240 (3)	0.26240 (3)	0.26240 (3)	0.78 (1)	1.00

$R_B = 2.60 \%$, $R_F = 3.02 \%$, $\chi^2 = 4.83 \%$

The presence of (200) magnetic Bragg peak in the neutron diffraction pattern of MnGa_2O_4 acquired at 3.5 K [Figure 6.2(b)] confirms the existence of the long-range antiferromagnetic order. Magnetic structure determination has been accomplished following the representation analysis technique of group theory described by Bertaut [26]. The basis vectors associated with each possible magnetic model has been obtained with the SARAh and BasIreps software of the FULLPROF package [24]. A propagation vector, $\vec{k} = (0 \ 0 \ 0)$, accounts the magnetic reflections. Among the possible magnetic modes compatible with the space-group symmetry and the propagation vector, the best agreement with the experimental data corresponds to the irreducible representation (IR) Γ_7 . The irreducible representations and the basis vectors are summarized in Table 6.4. The magnetic structure is shown in Figure 6.3.

Table 6.4: Basis vectors of $\vec{k} = (000)$ and $8a$ site for irreducible representation Γ_7 and Γ_{10}

IR	Basis Vectors	
	Mn1(x,y,z)	Mn2 (y+3/4, x+1/4, -z+1/2)
Γ_7	(0,0,1)	(0,0,-1)
	(1,0,0)	(-1,0,0)
	(0,1,0)	(0,-1,0)
Γ_{10}	(0,0,1)	(0,0,1)
	(1,0,0)	(1,0,0)
	(0,1,0)	(0,1,0)

The coordinate of Mn atom is shifted from (1/8,1/8,1/8) to (0,0,0)

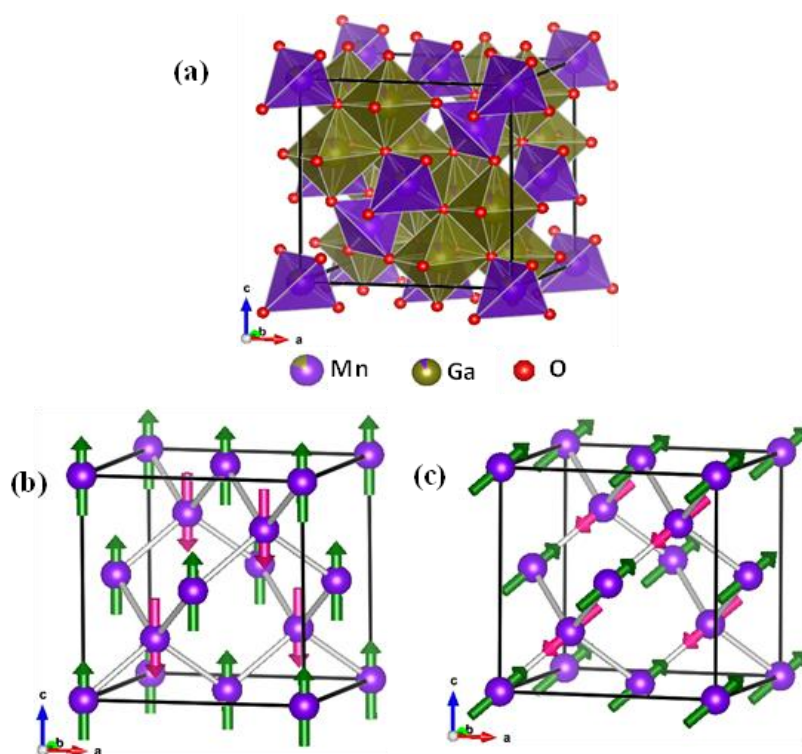


Figure 6.3: (a) Schematic representation of cubic crystal structure of A-site magnetic spinel oxide (AB_2O_4), where magnetic Mn^{2+} is located in the tetrahedral sites, and non-magnetic B- ions (Al^{3+} , Ga^{3+}) are located in the octahedral sites, (b-c) magnetic structure of $MnGa_2O_4$ with spin moments along [001] and [111] respectively. In the magnetic structure, only magnetic ions (Mn^{2+}) are shown in violet.

Rietveld analysis of the powder neutron diffraction pattern [Figure 6.2(b)] of $MnGa_2O_4$ suggest that both moment directions [001] and [111] are equally probable (In the cubic structure six possible antiferromagnetic vectors (L), are possible), and it is not possible to distinguish one from another. From both the magnetic structures [Figures 6.3(a) and 6.3(b)] it is evident that in the antiferromagnetically ordered state, the eight paramagnetic Mn^{2+} ions located at the tetrahedral site ($8a$) are split into two sublattices, $4a$ and $4c$ with opposite spins respectively resulting in chemically equivalent but magnetically non-equivalent atoms. In this structure, each Mn^{2+} ion is tetrahedrally

surrounded by four nearest neighbor Mn^{2+} ions of opposite spins. The determination of actual easy axis of a cubic system unambiguously from the powder neutron diffraction pattern is challenging because the diffraction pattern would look identical. In a cubic crystal, it is impossible to distinguish between moment direction along [001] and [111] by neutron powder diffraction without putting any symmetry breaking uniaxial stress or a magnetic field. It is not just for powder diffraction; it is also so for a single crystal with the cubic structure. Although literature report shows the magnetic easy axis of MnGa_2O_4 to be [111], this is not yet confirmed [27]. The proper knowledge of magnetic easy axis is essential to understand the magnetic symmetry governing the magnetoelectric interaction in this family of oxides. To determine the easy axis of MnGa_2O_4 , magnetic and magnetoelectric measurements are carried out on a single crystalline sample of MnGa_2O_4 , which will be discussed in section 6.4.4. The determination of the easy axis direction is neither possible from magnetic nor magnetoelectric measurements on powder samples. Based on the magnetic and magnetoelectric measurements on single crystalline MnGa_2O_4 , we could distinguish the actual direction of the easy axis to be [111].

6.4.2 Magnetic properties of MnX_2O_4 ($\text{X} = \text{Al, Ga}$):

A-site magnetic spinel compounds exhibit a plethora of magnetic phenomena, such as spin liquid, orbital liquid, or orbital glass, due to frustration pertinent to the A-site diamond lattice with nearest- and next-nearest-neighbor couplings [28-30]. In contrast, MnX_2O_4 spinels show long-range antiferromagnetic order. Temperature dependent dc magnetization data, $M(T)$ for polycrystalline MnGa_2O_4 measured under field cooled condition in the presence of a magnetic field of 1 kOe is shown in Figure 6.4(a). From the magnetization data, it is clear that MnGa_2O_4 undergoes an antiferromagnetic phase transition at 32 K along with an abrupt increase below antiferromagnetic transition. The increase of $M(T)$ below T_N in MnGa_2O_4 is due to a paramagnetic moment of Mn^{2+} arising from anti-site disorder between the A and B-sites as discussed in the preceding section. This observation is consistent with the Rietveld analysis of the room temperature neutron diffraction data where we see an inversion parameter, $\alpha = 0.095$ for the Mn^{2+} ions in the octahedral sites and the corresponding Ga^{3+} ions in the tetrahedral sites [see Table 6.3]. From Figure 6.4(a) we observe that the temperature dependent inverse susceptibility data, $1/\chi(T)$ of MnGa_2O_4 does not show the typical

minimum at the antiferromagnetic transition, rather it shows a rapid decrease at low temperature. To account for this behaviour in MnGa_2O_4 , we have considered the paramagnetic Mn^{2+} spins of the octahedral site [27] and fitted $1/\chi(T)$ curve with the modified Curie-Weiss law ($\chi = \frac{C}{T - \theta_{CW}} + \frac{C'}{T'}$) in the temperature range of 200-390 K as shown in Figure 6.4(a). From the linear fit of $1/\chi(T)$, we obtain the Curie-Weiss temperature (θ_{CW}) as -140 K for MnGa_2O_4 indicating that the average magnetic interaction is antiferromagnetic in nature. Based on the Curie-Weiss fitting we obtain the effective magnetic moment (μ_{eff}) per Mn^{2+} ion as 5.65 and 1.51 μ_B in the tetrahedral and octahedral sites, respectively. Despite the anomalous behaviour in the magnetization data, the specific heat data of MnGa_2O_4 show lambda shape anomaly at the respective magnetic transitions confirming the long-range second-order antiferromagnetic phase transition [Figure 6.4(b)]. Isothermal magnetization data recorded at 2 K [Figure 6.4(c)] confirms the antiferromagnetic nature of MnGa_2O_4 . Further, the $M(H)$ curve shows that there is a change in slope from the initial straight line which was suspected to be spin-flop transition as shown in Figure 6.4(c). In this context it is important to mention that the spin-flop transition cannot be proven unambiguously from the $M(H)$ curve of polycrystalline sample. Measurement of the $M(H)$ curve at 5 K on single crystalline sample of MnGa_2O_4 along different directions show the existence of spin-flop transitions [27] for $H // [001]$ and $H // [111]$, which will be discussed in section 6.4.4.

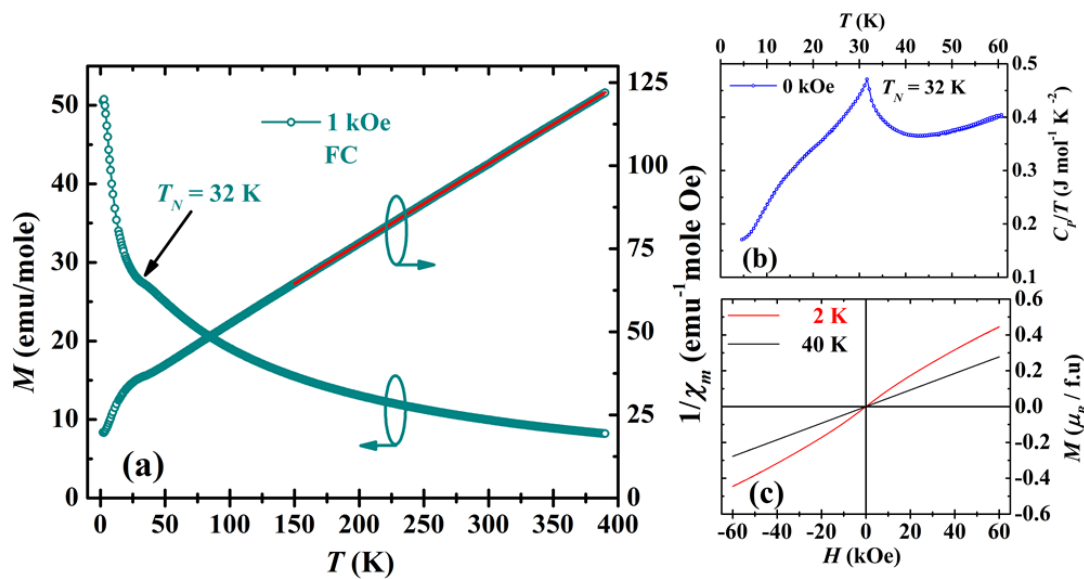


Figure 6.4: (a) Temperature dependence of dc magnetization data, $M(T)$ (left) and inverse susceptibility, $1/\chi(T)$ (right), where the fitted line is shown in red; (b) C_p/T as a function of temperature and (c) isothermal magnetization as a function of magnetic field for polycrystalline MnGa_2O_4 respectively.

Temperature dependent dc magnetization data of MnAl_2O_4 [Figure 6.5] shows a similar behavior but with a higher T_N of 41 K indicating stronger Mn^{2+} - Mn^{2+} interaction in MnAl_2O_4 as compared to MnGa_2O_4 . The stronger antiferromagnetic interaction in MnAl_2O_4 is also evident from the higher Curie-Weiss temperature ($\theta_{CW} = -210$ K). Temperature dependent inverse susceptibility data, $1/\chi(T)$ of MnAl_2O_4 fitted in the temperature range of 200-390 K with the modified Curie-Weiss law, ($\chi = \frac{c}{T-\theta_{CW}} + \frac{c'}{T'}$), shown in Figure 6.5(a) gives the effective magnetic moment (μ_{eff}) per Mn^{2+} ion as 5.66 and $1.84 \mu_B$ in the tetrahedral and octahedral sites, respectively.

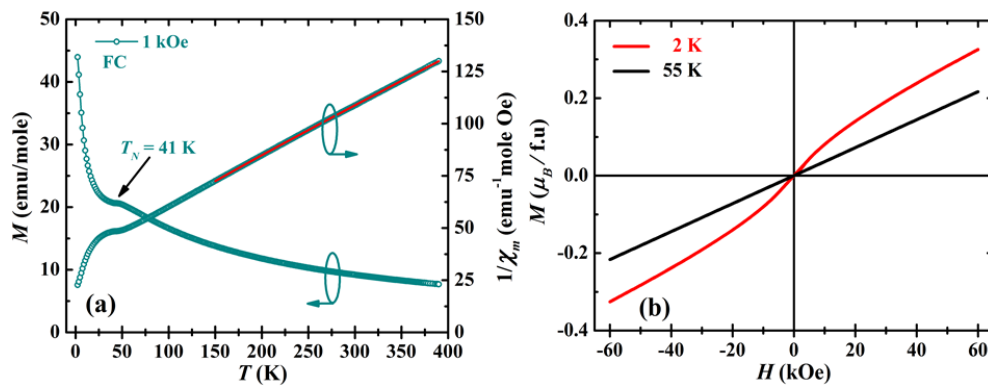


Figure 6.5: (a) Temperature dependence of dc magnetization data, $M(T)$ (left) and inverse susceptibility, $1/\chi(T)$ (right), where the fitted line is shown in red and (b) isothermal magnetization as a function of magnetic field for MnAl_2O_4 respectively.

Table 6.5: Comparison of paramagnetic moments of MnX_2O_4 ($X = \text{Al}, \text{Ga}$) samples

Compound (Prepared at 1100 °C)	(Curie - Weiss + Curie) Fitting ($T = 200$ - 390 K) $H = 1000$ Oe (FC)		
	θ_{CW}	Paramagnetic moment (μ_B/Mn) at tetrahedral site	Paramagnetic moment (μ_B/Mn) at octahedral site
MnAl_2O_4 - 1 °C	-210 K	5.66	1.84
MnGa_2O_4 - 1 °C	-140 K	5.65	1.51

In Table 6.5, we compare the magnetic properties between MnGa_2O_4 and MnAl_2O_4 samples. Interestingly, in both the A -site magnetic spinel compounds significant amount of frustration exists, though it is less as compared to the B -site magnetic spinel compounds, e.g., ZnCr_2O_4 . The strength of frustration is calculated based on the ratio of Curie-Weiss temperature to the magnetic ordering temperature, $f = |\theta_{CW}|/T_N$. The f value for MnGa_2O_4 and MnAl_2O_4 compounds are 4.4 and 5.1 respectively, while for ZnCr_2O_4 the value of f is 28 [see chapter 7].

Now we discuss the origin of frustration in the A -site magnetic spinel compounds, where the magnetic A sublattice forms a diamond lattice. In this configuration, magnetic interactions between A -ions occur through complicated O - B - O paths instead of direct exchange interaction [3]. In the bipartite diamond lattice if only nearest-neighbour magnetic interaction (J_1) exist then there would be no frustration, but due to the O - B - O path the next-nearest-neighbour interaction (J_2) becomes comparable to the former interaction (J_1) giving rise to frustration. It can be understood in an intuitive way by considering the diamond lattice consists of two interpenetrating, face-centered-cubic (fcc) sublattices displaced by $(1/4, 1/4, 1/4)$, as shown in Figure 6.6. The next-neighbour interactions of the diamond lattice are then simply the nearest-neighbour interactions within the fcc sublattice, and hence, give rise to frustration as a result of the antiferromagnetic interaction. The nearest-neighbour interactions of the diamond lattice correspond to the antiferromagnetic interaction between the fcc sublattices giving rise to enhanced frustration within the fcc sublattices.

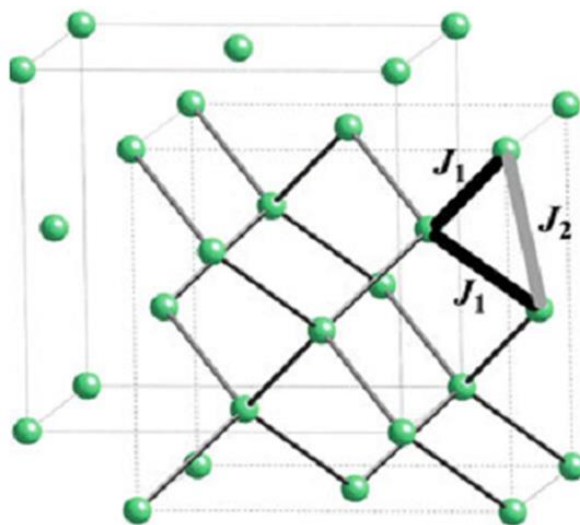


Figure 6.6: Magnetic exchange interaction on nearest-neighbour (J_1) and next-nearest-neighbor (J_2) in the bipartite diamond lattice. FCC sublattice is indicated with cubes marked with dotted lines [adapted with permission from ref. 2, © (2011) by Springer].

6.4.3 Dielectric properties of MnX_2O_4 ($\text{X} = \text{Al}, \text{Ga}$):

The temperature dependence of real part of the dielectric constant measured at 100 kHz is shown in Figure 6.7 for both MnAl_2O_4 and MnGa_2O_4 . At zero magnetic field, the dielectric constant does not show any peak or anomaly at the magnetic transition temperature (T_N). On application of a small magnetic field, a feeble peak feature appears in both the compounds. The intensity of the peak becomes more pronounced

with increasing the magnitude of the magnetic field demonstrating a coupling between magnetism and dielectric polarizability. We have also observed a similar anomaly in the presence of a magnetic field in the vicinity of T_N in the temperature dependent dielectric loss data as shown in the inset of Figure 6.7.

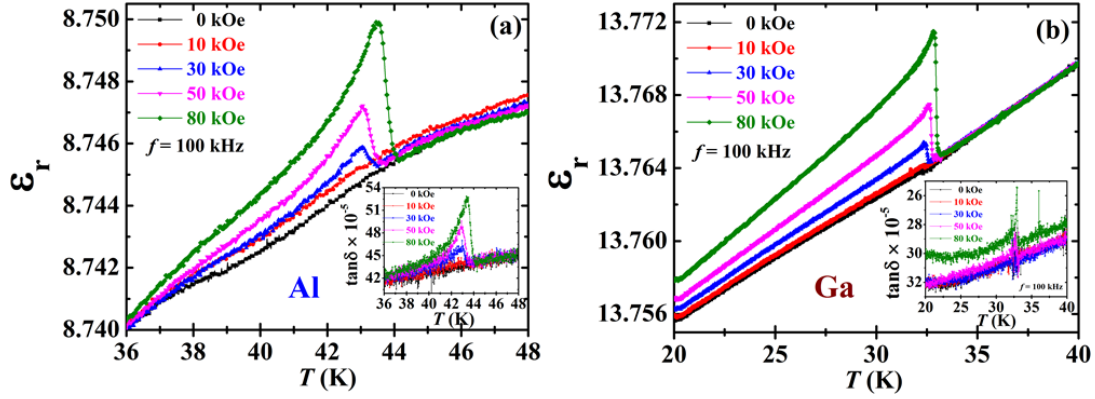


Figure 6.7: Temperature dependence of dielectric constant measured in the presence of different magnetic fields for (a) MnAl_2O_4 and (b) MnGa_2O_4 , respectively. The insets of (a) and (b) show the temperature variation of dielectric loss of MnAl_2O_4 and MnGa_2O_4 , respectively.

To understand the magnetoelectric coupling in these materials, we have measured magnetic field dependent dielectric constant at fixed temperature and the results are shown in Figure 6.8. From this figure, it is evident that the dependence of dielectric constant on the external magnetic field gives rise to isothermal magnetocapacitance effect. The isothermal magnetocapacitance, MC (%) is defined as,

$$\text{MC} (\%) = \left[\frac{C(H) - C(0)}{C(0)} \right] \times 100, \quad (6.1)$$

where $C(H)$ and $C(0)$ are the capacitances with and without magnetic field under isothermal condition. It is interesting to note that the magnetocapacitance becomes maximum in the vicinity of antiferromagnetic ordering temperature where dielectric anomaly appears [Figures 6.8(a) and 6.8(b)]. The occurrence of maximum magnetocapacitance near T_N indicates the origin to be associated with magnetoelectric coupling. In Figures 6.8(c) and 6.8(d), we have plotted the magnetic field dependent magnetocapacitance, MC (%) against changes in magnetic field dependent squared dc magnetization for MnAl_2O_4 and MnGa_2O_4 respectively. From this figure, it is clear that in both the compound the trend of change in square magnetization per Mn^{2+} ion with magnetic field correlates well with the magnetocapacitance change. To emphasize the dependence of MC (%) on the square magnetization per Mn^{2+} ion we have scaled the magnetocapacitance vs. M^2 as shown in the insets of Figures 6.8(c) and 6.8(d) which

shows the linear relationship between the two parameters at all fields near T_N . Hence, the agreement between magnetocapacitance vs. M^2 could be attributed to the magnetoelectric coupling.

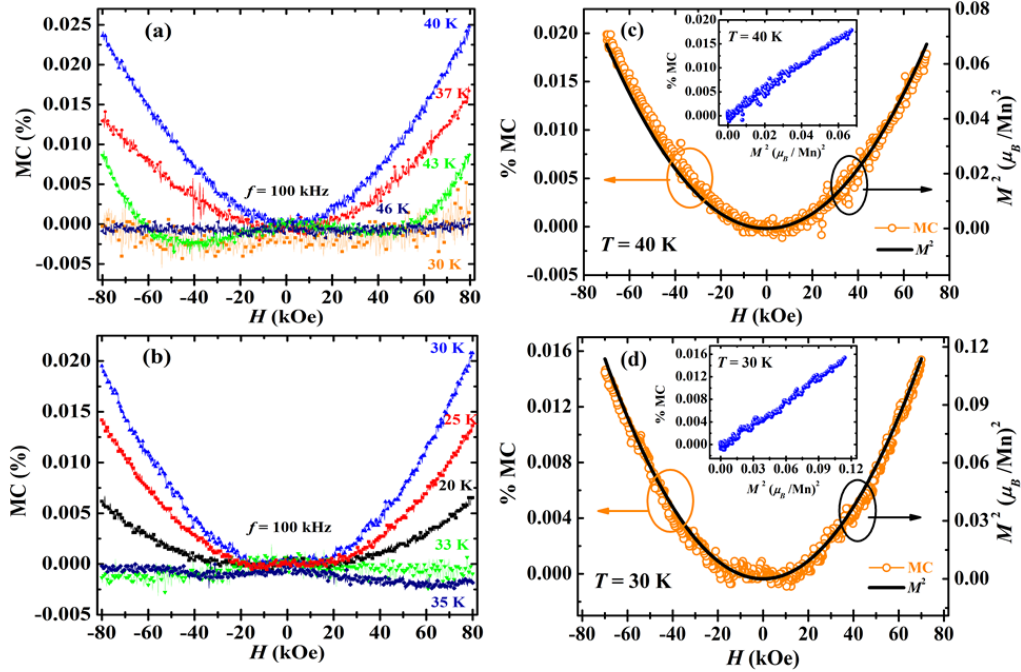


Figure 6.8: (a), (b) Magnetic field dependence of magnetocapacitance at different temperature for MnAl_2O_4 and MnGa_2O_4 , respectively; (c), (d) The relation between MC (%) and square magnetization per Mn^{2+} ion at all magnetic fields near T_N for MnAl_2O_4 and MnGa_2O_4 , respectively. Insets of (c) and (d) show the linear agreement of MC (%) vs. square magnetization per Mn^{2+} ion near T_N for MnAl_2O_4 and (b) MnGa_2O_4 , respectively.

The observation of dielectric anomaly in the presence of a magnetic field in the vicinity of T_N prompted us to investigate the electric polarization of these materials in the presence of magnetic fields. We have carried out pyroelectric current measurements in the presence of various magnetic fields after performing the magnetoelectric poling (both magnetic and electric fields were applied during cooling) from a temperature above T_N . This magnetoelectric (ME) annealing condition is essential to realize a single domain state responsible for exhibiting the electric polarization. In Figure 6.9 we show the temperature-dependent electric polarization for MnAl_2O_4 and MnGa_2O_4 , in the presence of different magnetic fields, obtained by integrating the pyroelectric currents followed by the division of the respective area. From Figure 6.9 we observe that in zero magnetic fields, electric polarization is absent. When magnetic field is applied, the electric polarization appears at the temperature where dielectric anomaly and magnetic transition occur. The onset temperature of magnetoelectric polarization is little higher

compared to the phase transition temperature determined from magnetic or dielectric measurements due to the high ramping rate used while recording the pyroelectric current during warming as mentioned in the experimental section. From this figure, it is clear that electric polarization enhances with increasing magnetic field, which signifies the critical role of the magnetic field in inducing electric polarization. The proportionality between external magnetic field and magnetoelectric polarization indicates the linear nature of the magnetoelectric effect.

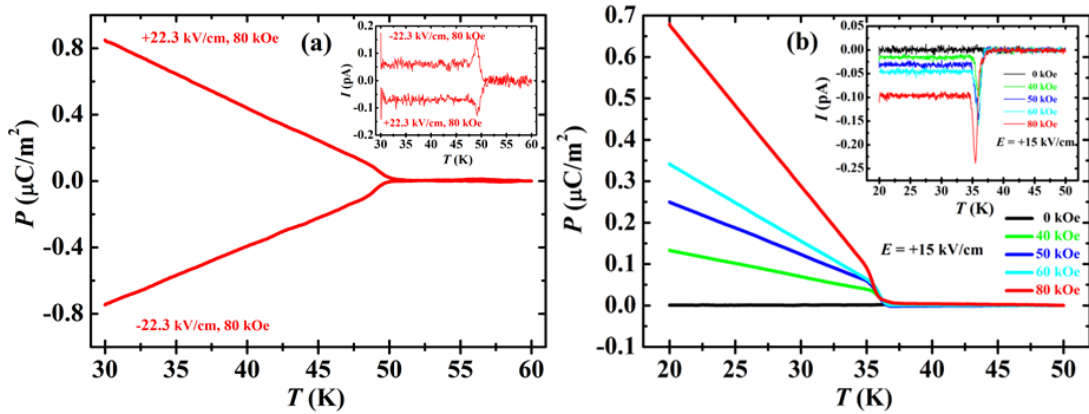


Figure 6.9: Temperature dependence of magnetoelectric polarization induced by a magnetic field for (a) MnAl_2O_4 and (b) MnGa_2O_4 , respectively. Insets of (a) and (b) show the temperature dependence of magnetoelectric current in the presence of magnetic field for MnAl_2O_4 and (b) MnGa_2O_4 , respectively.

To further signify the importance of external magnetic field we performed magnetoelectric poling from a temperature above T_N and then removed the magnetic field at lowest temperature before measuring the pyroelectric current while warming but we could not observe any pyroelectric peak there. This result indicates the importance of external magnetic field in inducing electric polarization. Since MnAl_2O_4 is highly insulating in nature, it is not possible to see magnetoelectric current at the lower magnetic field. Therefore, we have presented only the magnetoelectric polarization data in the presence of a magnetic field of 80 kOe in Figure 6.9(a). From the magnetic field dependent electric polarization data we calculated the magnetoelectric coefficients for MnAl_2O_4 (0.13 ps/m at $E = 22.3 \text{ kV/cm}$, $H = 80 \text{ kOe}$, $T = 30 \text{ K}$) and MnGa_2O_4 (0.17 ps/m at $E = 15 \text{ kV/cm}$, $T = 20 \text{ K}$), which are comparable to the polycrystalline linear magnetoelectric material NdCrTiO_5 (0.54 ps/m at 16 K in the presence of $E = 5.8 \text{ kV/cm}$, $H = 70 \text{ kOe}$) [13]. To demonstrate the polarization reversal with the magnetic field, we have performed following experiment on MnGa_2O_4 . First, the sample was magnetoelectrically poled from above T_N to 20 K in the presence of

negative electric field ($-E$) and positive magnetic field ($+H$) and then at lowest temperature the applied electric field was removed but kept the magnetic field on. Then we measured the magnetoelectric current while warming in the presence of positive magnetic field ($+H$) and obtained the temperature dependent magnetoelectric current profile which is shown in Figure 6.10(a). In the succeeding experiment before measuring the magnetoelectric current, we followed the above-mentioned poling protocol and removed the electric field at 20 K. Also, we changed the polarity of the magnetic field from positive to negative at 20 K. After that, we measured the magnetoelectric current as a function of temperature in the presence of negative magnetic field ($-H$). In this case, we observe that the temperature dependent magnetoelectric current profile is completely reversed as a result of changing the polarity of the applied magnetic field as shown in Figure 6.10(b). This experiment clearly suggests that the applied magnetic field can completely control the magnetoelectric polarization in A -site magnetic spinel oxides.

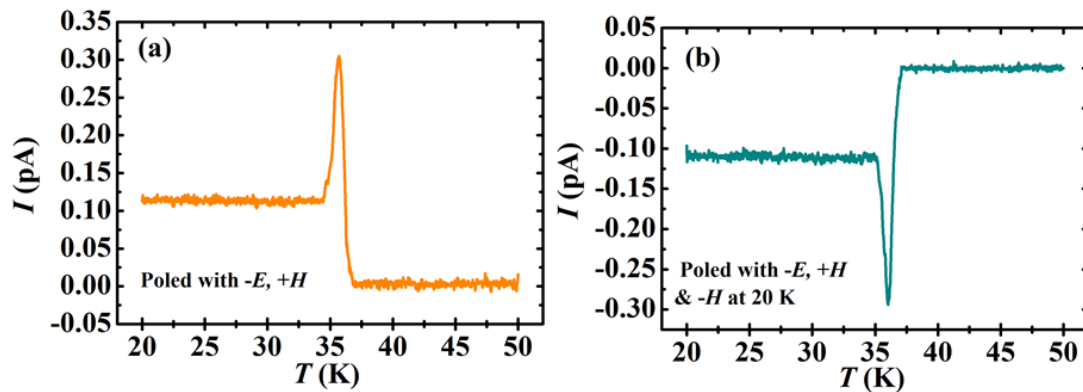


Figure 6.10: Temperature dependence of magnetoelectric current in MnGa_2O_4 under the poling protocol with (a) $-E, +H$ and (b) $-E, +H$ followed by changing the polarity of the magnetic field to $-H$ at 20 K.

6.4.4 Magnetic anisotropy dependent magnetoelectric interaction in MnGa_2O_4 :

In this section, we will discuss the theoretical prediction by N. V. Ter-Oganessian and experimental results on magnetic and magnetoelectric measurements performed on single crystalline MnGa_2O_4 grown by floating zone method by Kee Hoon Kim to determine the magnetic easy axis or antiferromagnetic vector (L) which we could not determine unambiguously from the neutron diffraction experiment of a polycrystalline sample. MnGa_2O_4 and MnAl_2O_4 experience a single second order phase transition to an antiferromagnetic (AF) phase with $\vec{L} \neq 0$. In this case the two possible AF vector

directions [100] and [111] results in the magnetic space group symmetries $I4'_1/a'm'd$ and $R\bar{3}'m'$, respectively. Both magnetic structures allow linear magnetoelectric effect. In earlier studies on polycrystalline $MnAl_2O_4$, Co_3O_4 , and $MnGa_2O_4$ it was not possible to determine the easy axis direction contrary to what is claimed in some works [27,31,32]. Therefore correct determination of magnetic space group requires proper knowledge of magnetic easy axis. In other word, magnetic anisotropy which arises primarily due to spin-orbit coupling plays an important role in determining the magnetoelectric coupling.

6.4.4.1 Magnetic measurements on single crystal of $MnGa_2O_4$

The magnetic and magnetoelectric properties of the studied materials can be understood using the phenomenological theory of phase transitions. The *A*-site collinear antiferromagnetic structure in spinels for $\vec{k} = 0$ corresponds to the irreducible representation Γ^{5-} and can be described by the order parameter (L_x, L_y, L_z) . Here we use the orthogonal axes *x*, *y*, and *z*, which are aligned along the cubic edges. One can write the thermodynamic potential expansion in the form,

$$\Phi_{\text{magn}} = \frac{A}{2}I_1 + \frac{B_1}{4}I_2 + \frac{B_2}{4}I_1^2 + \frac{C}{6}I_1^3 + fI_{ML} + \frac{\alpha}{2}I_M + \frac{\beta}{2}I_M^2 - \vec{H}\vec{M} \quad (6.2)$$

where *A*, *B*₁, *B*₂, *C*, *f*, α , and β are phenomenological coefficients, \vec{M} is the magnetic moment, $I_1 = L_x^2 + L_y^2 + L_z^2$, $I_2 = L_x^4 + L_y^4 + L_z^4$, $I_{ML} = (L_xM_x + L_yM_y + L_zM_z)^2$, and $I_M = M_x^2 + M_y^2 + M_z^2$. The term I_{ML} in the expansion determines the interaction between \vec{L} and \vec{M} favoring their perpendicularity when $f > 0$ and governs the spin-flop behavior as shown below. The easy axis directions [111] or [100] are obtained, when $B_1 > 0$ or $B_1 < 0$, respectively. Performing numerical minimization of the functional (6.2) we obtain the $dM(H)/dH$ dependencies shown in Figures 6.11(a) and 6.11(b). It can be found that the cases of the easy axis along [111] and [001] have qualitatively different $dM(H)/dH$ curves with different spin-flop phase transitions. The behavior of $dM(H)/dH$ curves shown in Figures 6.11(a) and 6.11(b) is explained below.

Case – I : For the direction of the easy axis is along [111] [Figure 6.11(a)] it suggests that the magnetic anisotropy is such that the appearing antiferromagnetic vector wants to have all its components non-zero and equal, i.e. $L_x = L_y = L_z$. Now when we apply a

sufficiently strong magnetic field, the antiferromagnetic vector (i) wants to orient perpendicular to the field and (ii) wants to have as many non-zero and equal components as possible. Now the following three situations can arise depending on the direction of application of magnetic field:

- [1] When the applied magnetic field is along [100] the AF vector would be along [011] (or e.g. [01-1]).
- [2] When the applied magnetic field is along [111] the AF vector would be along [01-1] (or e.g. [10-1]).
- [3] When the applied magnetic field is along [011] the AF vector can remain along [11-1], i.e. along the cubic spatial diagonal.

Therefore, there is a spin flop for two field directions along [100] and [111] and no spin flop for the field along [011] as seen in the magnetic measurements [Figure 6.11(c)].

Case – II : If the easy axis were along [001], [Figure 6.11(b)] then there would be a spin-flop only for $H \parallel [111]$ as the antiferromagnetic axis would flop from [001] to e.g. [1-10]. For other H directions ([001] and [011]) there would be no spin flop since the initial easy axis direction without magnetic field is [100], i.e. perpendicular to the H direction.

Let us now look at the experimental situation performed following the theoretical prediction. For the easy axis along [111] [Figures 6.11(a)] the anomalies of $dM(H)/dH$ curves, which correspond to spin-flops, their amplitudes and succession, as well as the succession of curves at $H = 0$ qualitatively agree with the measurements on single crystal MnGa_2O_4 [Figures 6.11(c)]. In Figure 6.11(c) we show the magnetic field dependence of first order derivative of isothermal magnetization with respect to magnetic field at 5 K measured along three different directions. We see an anomaly in the data at $H \sim 6$ kOe when magnetic field is applied along [001] and another anomaly at ~ 11 kOe on application of a magnetic field along [111]. On the other hand, we do not observe any such anomaly when the magnetic field was applied along the [011] direction. Such behaviour is in accordance with theoretical calculations of Figure 6.11(a) and, therefore, we attribute these anomalies in the dM/dH vs. H plots to the spin-flop transitions, in which the antiferromagnetic vector wants to orient perpendicular to the direction of applied field. In MnGa_2O_4 an anomaly at ~ 6 kOe in

magnetic field dependence of the (200) magnetic reflection in neutron scattering was also found earlier [27], which was also associated with the spin-flop transition.

6.4.4.2 Magnetolectric measurements on single crystal of $MnGa_2O_4$

The measurements of magnetic field-induced polarization can also give a hint at the easy axis direction. Consider the thermodynamic potential with magnetolectric interaction,

$$\Phi = \Phi_{\text{magn}} + \kappa I_{ME} + \frac{a}{2} I_P, \quad (6.3)$$

where a and κ are phenomenological coefficients, \vec{P} is the electric polarization, $I_P = P_x^2 + P_y^2 + P_z^2$ and the magnetolectric interaction can be written in the form [23]

$$I_{ME} = L_x(M_y P_z + M_z P_y) + L_y(M_z P_x + M_x P_z) + L_z(M_x P_y + M_y P_x), \quad (6.4)$$

Due to the presence of spin-flop transitions with rather low critical magnetic field values H_c , at which the AF vector aligns perpendicular to the applied magnetic field, the easy axis directions [100] and [111] in $MnGa_2O_4$ give similar magnetolectric responses for $H > H_c$ for any chosen geometry, whereas for $H < H_c$ induced electric polarization cannot be measured reliably. However, it follows from Eq. 6.3 that at high magnetic fields (i.e. magnetic fields higher than spin-flop magnetic field values) the ratio of $P||[011]$ at $H||[011]$ to $P||[011]$ at $H||[100]$ is different for the easy axis directions [001] and [111]. In the case when the easy axis direction is parallel to [001] the ratio is $2\sqrt{2}$, whereas for the direction parallel to [111] it is $\sqrt{2}$.

Following the aforementioned theoretical arguments, temperature-dependent electric polarization was measured on a single crystal of $MnGa_2O_4$ in the presence of a magnetic field of 90 kOe applied to different directions of the $MnGa_2O_4$ single crystal as shown in Figure 6.11(d). In Figure 6.12 we show the schematics of a cubic crystal which pictorially describes the different direction of application of electric field, magnetic field, and the resultant electric polarization. From this measurement we see that the ratio of $P//[011]$ at $H//[011]$ to $P//[011]$ at $H//[100]$ is 1.3 at 2 K ($E = 1.27$ kV/cm, $H = 90$ kOe), which is close to $\sqrt{2}$. Hence the magnetic and magnetolectric measurements interpreted by phenomenological theory of phase transitions confirm that easy axis of $MnGa_2O_4$ is [111].

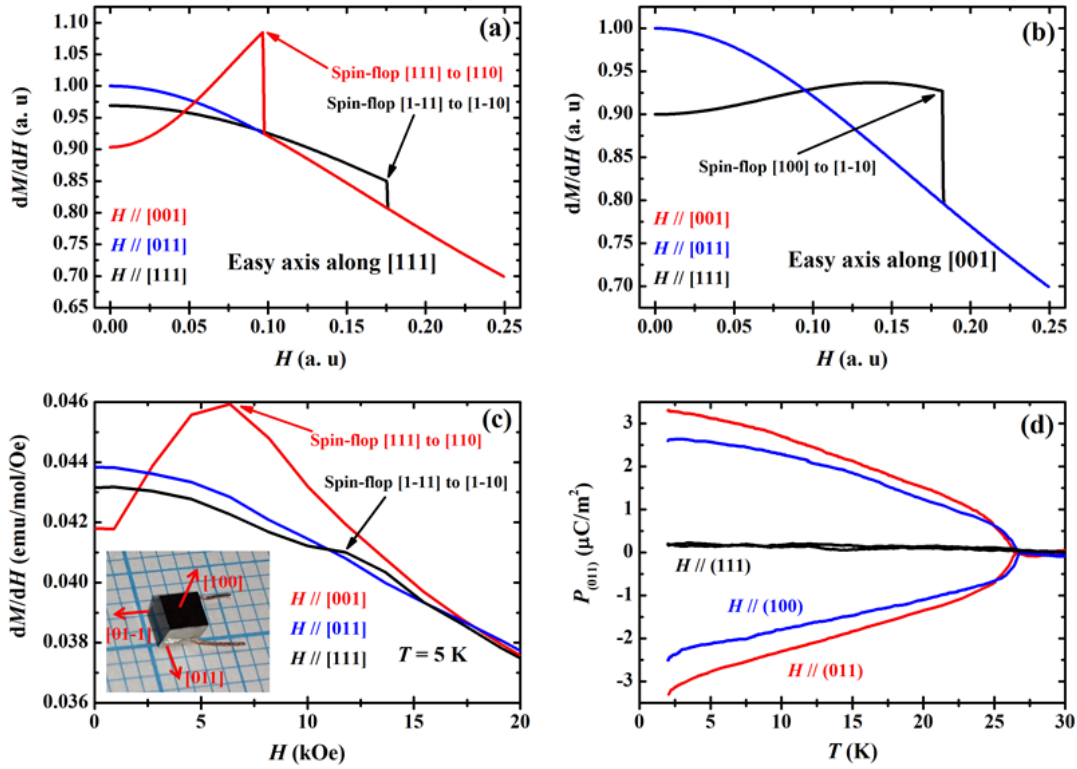


Figure 6.11: (a, b) Theoretically calculated magnetic field dependence of $dM(H)/dH$ in MnGa₂O₄ for the cases of the easy axes along [111] and [001] respectively. (c) Magnetic field dependence of $dM(H)/dH$ measured along [001], [011] and [111] on a single crystal of MnGa₂O₄. Inset of figure (c) shows the single crystal of MnGa₂O₄. (d) Temperature dependencies of magnetic field induced electric polarization at 90 kOe measured along [011] with $H // [100]$, $H // [011]$, $H // [111]$ on single crystal of MnGa₂O₄.

Based on the determination of easy axis of [111] we have obtained the magnetic symmetry $R\bar{3}'m'$ which supports the magnetoelectric components $\alpha_{11}(=\alpha_{22})$ and α_{33} for linear magnetoelectric effect. But in order to measure it we have to apply magnetic fields weaker than the spin flop field 6 kOe along [111], because stronger fields destroy the $R\bar{3}'m'$ structure and there is no α_{33} anymore. Therefore strong fields along [111] should give no polarization along [111], as observed in the experiments [Figure 6.11(d)]. In the presence of strong magnetic field there will be a spin flop of AF vector along [01-1] corresponding to the magnetic symmetry $Im'ma$ ($\vec{k} = 0$) which also supports linear magnetoelectric effect. However it is not correct to say that the symmetry after the spin flop is $Im'ma$, because there is an applied magnetic field (along [111] or [100]) which causes the spin flop. Thus the system is described by two order parameters: an AF vector [01-1] and the ferromagnetic moment along [111] or [100], which determines the symmetry. Moreover the definition of easy axis only holds without magnetic field or in the low magnetic field less than $H_C \sim 6$ kOe.

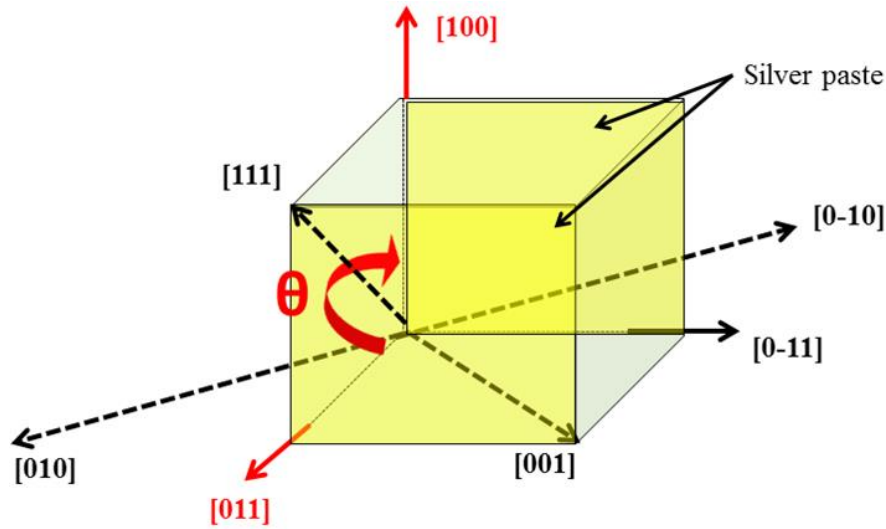


Figure 6.12: Schematics of the cubic single crystal of MnGa_2O_4 showing different axes of the cube, where $P_{[011]}$ at $H//[011]$ and $P_{[011]}$ at $H//[100]$ value can determine the easy axis is. Here in the schematic $\theta = 0^\circ, 45^\circ$ and 90° correspond to $H // (011), H // (111)$ and $H // (100)$ respectively.

The interaction described by Eq. 6.4 results in a linear coupling between \vec{M} and \vec{P} upon a phase transition to the antiferromagnetic phase, which implies the appearance of linear magnetoelectric effect. In case when magnetic field \vec{H} is applied to the crystal, which induces respective magnetic moment \vec{M} , the interaction I_{ME} implies linear coupling between \vec{L} and \vec{P} . This results in the fact that the antiferromagnetic phase transition at T_N under magnetic field becomes proper ferroelectric phase transition with a corresponding divergence in the temperature dependence of the dielectric constant. However, due to the fact that the system is far from the ferroelectric instability and due to the smallness of ME interaction the temperature range of significant increase of the dielectric constant should be very narrow. Likewise, if electric field \vec{E} is applied to the crystal, the antiferromagnetic phase transition becomes proper ferromagnetic, however the appearing ferromagnetic component is weak. Quantitative description of the phase transitions can be performed using the thermodynamic potential (Eq. 6.3).

In both MnAl_2O_4 and MnGa_2O_4 , only the A -sites possess magnetic moments. Based on the phenomenological model the magnetoelectric effect in this family of oxides is due to single-ion contributions of magnetic ions located in the non-centrosymmetric surroundings because spin-orbit coupling modifies the local electric dipole moment of the A -site magnetic ion resulting in spin dependent macroscopic electric polarization [33].

6.5 Conclusions

In conclusion, the occurrence of linear magnetoelectric effect in the *A*-site magnetic spinels, MnX_2O_4 ($X = \text{Al, Ga}$) has been demonstrated. Contrary to many other spinels experiencing structural distortions, these compounds become linear magnetoelectric below a single second order antiferromagnetic phase transition from a highly symmetric cubic structure, which makes them unique. At zero magnetic fields, no dielectric anomaly and electric polarization has been observed. The experimental results clearly demonstrate the gradual evolution of dielectric anomaly and electric polarization with increasing magnetic fields below T_N . The proportionality between electric polarization and magnetic field indicates the linear magnetoelectric behavior. From the magnetic and magnetoelectric measurements on single crystal the easy axis direction of MnGa_2O_4 was determined unambiguously. The easy axis direction in this compound is oriented along $[111]$ with the corresponding magnetic symmetry $R\bar{3}'m'$ which supports linear magnetoelectric coupling. The microscopic symmetry analysis reveals that only single-ion contributions of magnetic ions located in the non-centrosymmetric site are essential to the origin of magnetoelectric effect in these compounds, i.e. electron orbitals of the ions at the *A*-sites have spin-dependent electric dipole moments inducing electric polarization in the antiferromagnetic structure. The magnetoelectricity in *A*-site magnetic spinels is shown to result only from the single-ion effect, which is still relevant in other magnetoelectric spinels with magnetic ion at the *A*-site, such as e.g. CoCr_2O_4 or Fe_3O_4 . This can be used to compare different mechanisms of appearance of electric polarization due to magnetic order. Furthermore, most of the *A*-site magnetic spinels are frustrated magnets. These results potentially open new physics in the study and control of frustrated magnetism by electric field in them due to the spin-dependent electric dipole moments at the *A*-sites. This linear magnetoelectric coupling observed in *A*-site antiferromagnetic spinels provides a new direction to manipulate the dielectric properties of many other magnetic spinels in the presence of magnetic field and may serve as a playground to study the microscopic origins of magnetoelectric coupling.

Bibliography

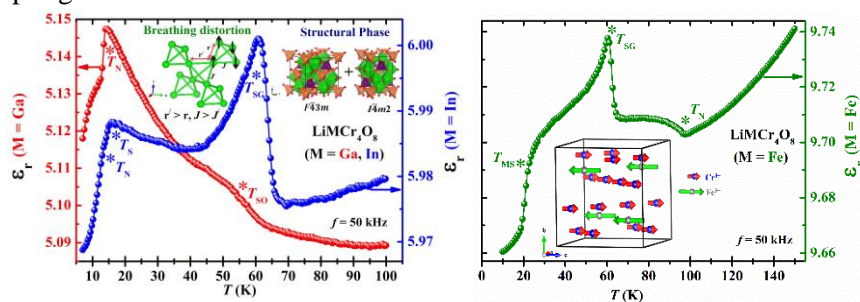
- [1] J. B. Goodenough, *Magnetism and the Chemical Bond* (Interscience, NY, USA, 1963).
- [2] C. Lacroix, P. Mendels, and F. Mila, *Introduction to Frustrated Magnetism: Materials, Experiments, Theory* (Springer Science & Business Media, 2011), Vol. 164.
- [3] W. Roth, *Journal de Physique* **25**, 507 (1964).
- [4] I. E. Dzyaloshinskii, *Zh. Exp. Teor. Fiz.* **37**, 881 (1959) [*Sov. Phys. JETP* **10**, 628 (1960)].
- [5] D. N. Astrov, *Sov. Phys. JETP* **11**, 708 (1960).
- [6] D. N. Astrov, *Sov. Phys. JETP* **13**, 729 (1961).
- [7] G. Rado and V. Folen, *Phys. Rev. Lett.* **7**, 310 (1961).
- [8] M. Fiebig, *J. Phys. D: Appl. Phys.* **38**, R123 (2005).
- [9] J. F. Scott, *J. Mater. Chem.* **22**, 4567 (2012).
- [10] W. Eerenstein, N. Mathur, and J. F. Scott, *Nature* **442**, 759 (2006).
- [11] A. Iyama and T. Kimura, *Phys. Rev. B* **87**, 180408 (2013).
- [12] N. Mufti, G. Blake, M. Mostovoy, S. Riyadi, A. Nugroho, and T. Palstra, *Phys. Rev. B* **83**, 104416 (2011).
- [13] J. Hwang, E. Choi, H. Zhou, J. Lu, and P. Schlottmann, *Phys. Rev. B* **85**, 024415 (2012).
- [14] Y. Fang, Y. Q. Song, W. P. Zhou, R. Zhao, R. J. Tang, H. Yang, L. Y. Lv, S. G. Yang, D. H. Wang, and Y. W. Du, *Sci. Rep.* **4**, 3860 (2014).
- [15] T. Kimura, T. Goto, H. Shintani, K. Ishizaka, T. Arima, and Y. Tokura, *Nature* **426**, 55 (2003).
- [16] N. Hur, S. Park, P. Sharma, J. Ahn, S. Guha, and S. Cheong, *Nature* **429**, 392 (2004).
- [17] Y. Tokunaga, N. Furukawa, H. Sakai, Y. Taguchi, T.-h. Arima, and Y. Tokura, *Nat. Mater.* **8**, 558 (2009).
- [18] J. Wang *et al.*, *Science* **299**, 1719 (2003).
- [19] Y. Kitagawa, Y. Hiraoka, T. Honda, T. Ishikura, H. Nakamura, and T. Kimura, *Nat. Mater.* **9**, 797 (2010).

- [20] Y. Yamasaki, S. Miyasaka, Y. Kaneko, J.-P. He, T. Arima, and Y. Tokura, *Phys. Rev. Lett.* **96**, 207204 (2006).
- [21] H. Murakawa, Y. Onose, K. Ohgushi, S. Ishiwata, and Y. Tokura, *J. Phys. Soc. Jpn.* **77**, 043709 (2008).
- [22] E. Kita, K. Siratori, K. Kohn, A. Tasaki, S. Kimura, and I. Shindo, *J. Phys. Soc. Jpn.* **47**, 1788 (1979).
- [23] N. V. Ter-Oganessian, *J. Magn. Magn. Mater.* **364**, 47 (2014).
- [24] J. Rodríguez-Carvajal, *Physica B: Condens. Matter* **192**, 55 (1993).
- [25] M. S. Senn, J. P. Wright, and J. P. Attfield, *Nature* **481**, 173 (2012).
- [26] E. F. Bertaut, in *Magnetism*, edited by G. T. Rado and H. Suhl (Academic Press, New York, 1963), Vol. 3.
- [27] B. Boucher, A. Herpin, and A. Oles, *J. Appl. Phys.* **37**, 960 (1966).
- [28] A. Krimmel, H. Mutka, M. Koza, V. Tsurkan, and A. Loidl, *Phys. Rev. B* **79**, 134406 (2009).
- [29] V. Fritsch, J. Hemberger, N. Büttgen, E.-W. Scheidt, H.-A. K. von Nidda, A. Loidl, and V. Tsurkan, *Phys. Rev. Lett.* **92**, 116401 (2004).
- [30] R. Fichtl, V. Tsurkan, P. Lunkenheimer, J. Hemberger, V. Fritsch, H.-A. K. von Nidda, E.-W. Scheidt, and A. Loidl, *Phys. Rev. Lett.* **94**, 027601 (2005).
- [31] H. S. Nair, Z. Fu, J. Voigt, Y. Su, and T. Brückel, *Phys. Rev. B* **89**, 174431 (2014).
- [32] W. Roth, *J. Phys. Chem. Solids* **25**, 1 (1964).
- [33] V. P. Sakhnenko and N. V. Ter-Oganessian, *J. Phys.: Condens. Matter* **24**, 266002 (2012).

Magnetostructural coupling and magnetodielectric effects in *A*-site cation-ordered spinel oxides, LiMCr_4O_8 ($M = \text{Ga, In, Fe}$)^{*}

Summary

Structure, magnetism and their correlation with magnetodielectric effect in *A*-site ordered chromate spinel oxides, LiMCr_4O_8 ($M = \text{Ga, In, Fe}$) have been investigated. $\text{LiGa(In)Cr}_4\text{O}_8$ exhibits magnetodielectric effect at $T_N \sim 13\text{-}15$ K, resulting from magnetoelastic coupling through spin Jahn-Teller effect. The Ga compound shows a broad dielectric anomaly at the onset of short-range antiferromagnetic ordering ($T_{SO} \sim 55$ K), whereas the In compound exhibits a sharp change in dielectric constant at the opening of a spin-gap ($T_{SG} \sim 60$ K). The differences in magnetic and dielectric behavior of Ga and In compounds have been understood in terms of breathing distortions of the Cr_4 tetrahedra and compared with that of ZnCr_2O_4 . On the other hand, $\text{LiFeCr}_4\text{O}_8$ shows interesting magnetic phase transitions where three dielectric anomalies have been observed at the ferrimagnetic transition ($T_N \sim 94$ K), spin-gap transition state ($T_{SG} \sim 60$ K) and magnetostructural transition temperatures ($T_{MS} \sim 23$ K) respectively, indicating the occurrence of magnetodielectric effect. The occurrence of magnetostructural transition and evolution of dielectric anomalies in the Fe compound has been discussed in the light of spin-phonon coupling.



^{*}Papers based on this chapter : accepted in Phys. Rev. B 94, 064420 (2016), © (2016) by the American Physical Society and submitted for publication

7.1 Introduction

Chromium containing spinels, ACr_2X_4 ($X = O, S, Se$) have emerged as an important class of materials in the study of magnetoelectric and multiferroic properties because some of them undergo magnetic ordering at low temperatures with complex spin structures which result from their frustrated magnetic interactions [1-4]. One such frustrated magnet is the family of B -site magnetic spinel oxides of general formula ACr_2O_4 crystallizing in a cubic structure with the space group $Fd\bar{3}m$. In these materials, the non-magnetic ions occupying the tetrahedral A -sites form a diamond-like lattice whereas the Cr^{3+} ions located at the octahedral B -sites form a corner sharing network of Cr_4 tetrahedra, the so-called pyrochlore lattice [5,6]. Unlike the ABO_3 perovskite, where the BO_6 octahedra are connected by vertices and the magnetic exchange involves cation-anion-cation superexchange interactions, the magnetic interactions in the B -site magnetic spinels are dominated by direct cation-cation, $Cr^{3+}(3d^3) - Cr^{3+}(3d^3)$, interactions as the CrO_6 octahedra are shared by edges [7]. In spinel compounds, the cation-anion-cation angles differ from 180° . The tetrahedral (A) cation-anion-octahedral (B) cation angle is $\sim 125^\circ$ while octahedral (B) cation-anion-octahedral (B) cation angle is $\sim 90^\circ$ and therefore the indirect exchange mechanism involving the intermediary anion is no more valid [8]. The general hypothesis is that direct cation-cation interactions would be significant when the octahedral site cations have the outer electron configuration $3d^n$ ($n \leq 5$) and the occupied octahedra either share a common face or edge. Depending on the orientation of cation d -orbitals as shown in Figure 7.1 following postulates have been given to account the magnetic interactions in spinel compounds [8].

1. If both the A -site t_2 orbitals and the B -site e_g orbitals are half filled (or less than half filled and degenerate), then the A - B interactions would be strongly antiferromagnetic.
2. If the A -site t_2 orbitals and/or the B -site e_g orbitals are empty, then the A - B interactions would be relatively weak and antiferromagnetic.
3. If the B -site t_{2g} orbitals are half-filled (or less than half filled and degenerate), direct B - B interactions are possible. The strength of these antiferromagnetic interactions depends strongly on inter-cation distance and anion shielding, both of

which are reduced if partial covalency via empty e_g orbital is possible. Therefore, the relatively strong $B-B$ interactions would be compatible with the conditions for weak $A-B$ interactions.

4. If the t_{2g} orbitals of one or both of two cations in neighbouring B -sites are full (or more-than-half-full and degenerate), no direct $B-B$ interactions occur between them.

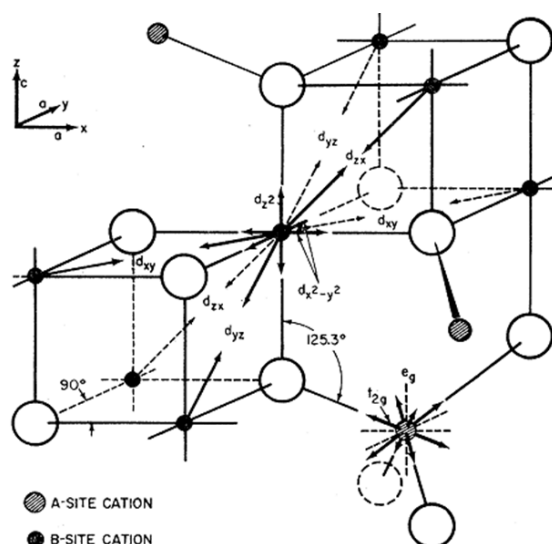


Figure 7.1: Orientation of d -orbitals in spinel structure [adapted with permission from ref. 8, © (1959) by the American Physical Society].

Thus, the antiferromagnetic nearest neighbor interaction between adjacent Cr^{3+} ions located on the pyrochlore sublattice gives rise to a strong geometric magnetic frustration [9,10]. To relieve this frustration, ACr_2O_4 undergoes spin Jahn-Teller effect [11-13] through a magnetoelastic coupling where the structural distortion removes the spin degeneracy cooperatively resulting in the development of long-range antiferromagnetic ordering at low temperatures [5,14]. In other words, in the geometrically frustrated magnetic materials structural distortion is prerequisite which generally makes the magnetic interactions non-uniform thereby facilitating to relieve the geometrical frustration. The magnetostructural transition involving the magnetoelastic coupling leads to the concomitant change in crystallographic and magnetic symmetry which brings about fascinating magnetoelectric properties [15,16].

Spinel oxides offer an enormous amount of scope in the substitution of different cations at both A and B sites and thus enable to tailor various interesting properties. In the conventional B -site chromate spinel oxide, for example in ZnCr_2O_4 , the non-magnetic Zn^{2+} ions are located at the non-centrosymmetric tetrahedral site ($8a$) with

local symmetry T_d and the Cr^{3+} ions are located at the centrosymmetric site (16d) with rhombohedral symmetry D_{3d} . By substituting two inequivalent cations with different oxidation states, Li^+ and Ga^{3+} (In^{3+} , Fe^{3+}), at the A-site, a unique type of frustrated pyrochlore lattice has been made recently [17-19]. Since Li^+ and Ga^{3+} (In^{3+} , Fe^{3+}) ions differ in their valence states, therefore these ions try to order in the equivalent crystallographic sites to minimize the electrostatic energy. This A-site ordering resembles that of the zinc-blende type of order where one Li^+ is surrounded by four Ga^{3+} (In^{3+} , Fe^{3+}), and one Ga^{3+} (In^{3+} , Fe^{3+}) is surrounded by four Li^+ ions on a diamond lattice. These two inequivalent cations exert different amounts of chemical pressures on the Cr_4 tetrahedra resulting in an alternate arrangement of small and large Cr_4 tetrahedra in a corner sharing geometry. This type of arrangement of Cr_4 tetrahedra makes a breathing pyrochlore lattice where both Cr-Cr distance alternation and geometrical frustration coexist [18]. The small and large Cr_4 tetrahedra will give rise to disparate local lattice distortions proportional to their exchange interaction energy. Further, the incorporation of two different ions at the A-site results in the loss of inversion symmetry and thus leads to the reduction of crystal symmetry to $F\bar{4}3m$ where the A-cations, Li^+ and Ga^{3+} (In^{3+} , Fe^{3+}) occupy the 4a and 4d Wyckoff positions respectively and the Cr^{3+} ions are located at the non-centrosymmetric 16e position. In this chapter, we will be investigating the structural, magnetic and dielectric properties of such A-site ordered chromate spinel oxides.

7.2 Scope of the present investigation

In a recent theoretical study, it has been suggested that A-site cation ordering in chromate spinel oxides can give rise to a local electric dipole moment at the B-site magnetic ion, which is located in a local polar non-centrosymmetric surrounding of oxygen ions with the symmetry C_{3v} , contributing to the linear magnetoelectric coupling [20]. According to this theoretical prediction, this effect will result in a single-ion contribution to linear magnetoelectric coupling if the appearing spin structure allows it because spin-orbit coupling modifies the local electric dipole moment of the B-site magnetic ion resulting in spin dependent macroscopic electric polarization [21]. In the previous chapter we have discussed about such linear magnetoelectric effect originating from the local noncentrosymmetry. This motivated us to investigate the detailed structural, magnetic and magnetoelectric properties in the A-site ordered spinel oxides,

LiMCr_4O_8 ($M = \text{Ga, In}$). Also, we have extended our investigation on *A*-site ordered chromate spinel, $\text{LiFeCr}_4\text{O}_8$ containing magnetic ion (Fe^{3+}) at the *A*-site. Detailed investigations on the crystallographic and magnetic structures of $\text{LiGa(In)Cr}_4\text{O}_8$ and $\text{LiFeCr}_4\text{O}_8$ have been carried out by employing high-resolution synchrotron and neutron diffraction experiment as a function of temperature. The difference in the size of *A*-site cations and breathing of Cr_4 pyrochlore network are reflected in the crystallographic and magnetic structures which significantly influence the dielectric properties of these materials.

7.3 Experimental details

Polycrystalline samples of LiMCr_4O_8 ($M = \text{Ga, In, Fe}$) were prepared by conventional solid state reaction method using the starting materials namely, Li_2CO_3 (Aldrich Chemical Company, Inc, 99%+), Ga_2O_3 (Sigma-Aldrich, 99.99%), In_2O_3 (Sigma-Aldrich, 99.99%), Fe_2O_3 (Alfa Aesar, 99.99%) and Cr_2O_3 (Sigma-Aldrich, 99.9%). The stoichiometric amounts of precursors were mixed, ground and heated in air at 900 °C and 950 °C for 24 h. The resulting material was reground, pelletized and sintered in air at 1000 °C for 24 h in the case of $\text{LiGaCr}_4\text{O}_8$ and at 1050 °C for 24 h in the case of $\text{LiInCr}_4\text{O}_8$ followed by cooling at the rate of 5°C/min. Final sintering of $\text{LiFeCr}_4\text{O}_8$ was carried out at 1000 °C for 15 h followed by cooling at the rate of 1°C/min. For all the above synthesis we have added 5-10% of excess Li_2CO_3 because of its loss at a higher temperature. Despite this, $\text{LiInCr}_4\text{O}_8$ contains small amounts of Cr_2O_3 and In_2O_3 as impurity phases. We have prepared ZnCr_2O_4 by heating the stoichiometric mixture of starting materials namely, ZnO (Merck, 99%+) and Cr_2O_3 (Sigma-Aldrich, 99.9%) in air at 900 and 1000 °C for 12 hrs followed by the final sintering at 1100 °C for 24 hrs with a cooling rate of 5°C/min. Phase purities of all these samples were confirmed by analyzing the x-ray diffraction data (XRD) collected with PANalytical Empyrean diffractometer using $\text{Cu K}\alpha_1$ monochromatic x-ray radiation. The FULLPROF suite program was used to perform the Rietveld refinement of diffraction data [22]. The synchrotron x-ray diffraction data of $\text{LiGaCr}_4\text{O}_8$ were collected in the angular range 5-45°, using x-rays of two different wavelengths of 0.4127 and 0.4959 Å at the material science powder diffraction beamline (BL04-MSPD) of the ALBA synchrotron facility [23,24]. Low temperatures were achieved using a recently developed ^4He flow cryostat. The temperature dependent neutron diffraction experiment on $\text{LiGaCr}_4\text{O}_8$ was carried

out at the high-resolution Echidna-ANSTO diffractometer of Australian Nuclear Science and Technology Organisation using two different wavelengths of 1.62 and 2.44 Å [25]. For $\text{LiFeCr}_4\text{O}_8$ variable temperature synchrotron x-ray diffraction data were collected in the angular range of 10-80° using x-rays of wavelength 0.91 Å at the Indian Beamline (BL-18B) of Photon Factory, KEK, Japan. The temperature dependent neutron diffraction experiment of the Fe compound was carried out on the D2B diffractometer at the Institut Laue-Langevin (ILL) using wavelengths of 1.594 and 2.398 Å. Neutron diffraction experiment was performed with ~ 2.5 g sample packed in a vanadium can of diameter 6.2 mm.

DC magnetization measurements of all these samples were carried out using a Superconducting Quantum Interference Device Magnetometer (SQUID, MPMS3, Quantum Design, USA) in the temperature range of 2-390 K. The temperature-dependent specific heat (C_p) was measured between the temperature range of 2-80 K and temperature dependent ac magnetization data was measured in the temperature range of 2-150 K in Physical Property Measurement System (PPMS, Quantum Design, USA). Capacitance and the pyroelectric current measurements were performed with an LCR meter (Agilent E4980A) and an electrometer (Keithley 6517A), respectively using a multifunction probe inserted in the PPMS, which allowed accessing temperature and magnetic field. The electrodes were made by applying conducting Ag paint on both sides of the thin pellets and dried under an infrared lamp. The capacitance was measured with and without an applied magnetic field while warming after performing the magnetic field (or zero magnetic fields) cooling of the sample from above T_N . Before measuring the pyroelectric current, the sample was poled magnetoelectrically (ME) from a temperature above T_N and then cooled to the lowest temperature where the electrodes were short-circuited for 15 minutes to remove any stray charges, but the magnetic field was not removed. Then the magnetoelectric current was measured on warming the sample to a temperature above T_N at a rate of 15 K/min while keeping the magnetic field on. We applied the dc voltage to the samples using a Radiant Technologies Inc. precision workstation. Raman spectroscopy of $\text{LiFeCr}_4\text{O}_8$ has been carried out using a 514.5 nm Argon laser with a power of ~ 0.7 mW at the sample. The scattered light was detected using a triple spectrometer (Jobin-Yvon, T64000) equipped with a confocal microscope in combination with a liquid-nitrogen-cooled multi-channel

charge-coupled device detector. For the temperature dependent studies, the sample was mounted in a vacuum on a cold finger of a Helium flow cryostat.

7.4 Results and discussion

7.4.1 Structure:

7.4.1.1 X-ray diffraction study of $\text{LiGaCr}_4\text{O}_8$ and $\text{LiInCr}_4\text{O}_8$

Rietveld analysis of the room temperature XRD pattern confirmed that the compounds $\text{LiGaCr}_4\text{O}_8$ and $\text{LiInCr}_4\text{O}_8$ have cubic structure with the space group $F\bar{4}3m$. The (200) reflection which was forbidden in $Fd\bar{3}m$ space group is found to be present in these compounds as reported earlier [18], confirming the ordering of Li^+ and $\text{Ga}^{3+}(\text{In}^{3+})$ ions at the A-site of the spinel structure. While there exists only one Cr-Cr distance (2.944 Å) in the conventional ZnCr_2O_4 spinel oxide, the A-site ordered compounds have two distinct Cr-Cr distances, 2.830 (2.891) Å and 2.999 (3.057) Å, which correspond to smaller and larger Cr_4 tetrahedra for the Ga (In) compounds, respectively. From the aforementioned distances it is clear that the Cr-Cr distance in the smaller tetrahedra for both the Ga and In compound is lower than the Cr-Cr distance (2.944 Å) in ZnCr_2O_4 indicating the stronger direct overlap between t_{2g} orbitals of Cr^{3+} ions thereby strengthening the magnetic exchange interaction in the Ga and In compounds as compared to the Zn compound. On the other hand, Cr-Cr distance in the larger tetrahedra for the Ga compound is in between the Cr-Cr distance in ZnCr_2O_4 (2.944 Å) and CdCr_2O_4 (3.035 Å) [26], while the same for the In compound is close to the Cr-Cr distance in HgCr_2O_4 (3.056 Å) [27], which indicates a relatively weaker magnetic interactions among the larger Cr_4 tetrahedra. In other words, the smaller Cr_4 tetrahedra become more isolated in In compound compared to Ga compound, demonstrating that the ordering of cations at the A-site causes breathing distortion of the Cr_4 tetrahedra which depends on the size of the trivalent A-site cations [18]. The existence of large (d) and small (d') Cr_4 tetrahedra gives rise to distortion on the pyrochlore lattice which is expressed by the ratio of (d/d'), where d and d' is the Cr-Cr distance in the large and small tetrahedra.

Analysis of temperature dependent synchrotron XRD data of $\text{LiGaCr}_4\text{O}_8$ revealed that the cubic structure ($F\bar{4}3m$) remains unchanged down to the antiferromagnetic ordering temperature ($T_N \sim 14.5$ K). In Figure 7.2(a) we show the Rietveld refinement of synchrotron XRD pattern of $\text{LiGaCr}_4\text{O}_8$ recorded at 298 K, which is similar to the

laboratory XRD pattern. Analysis of the synchrotron XRD data at 5 K [Figure 7.2(b)] showed the coexistence of two crystallographic phases ($F\bar{4}3m$ and $I\bar{4}m2$) indicating an incomplete structural phase transformation. In contrast, in ZnCr_2O_4 a complete structural phase transition occurs below T_N . However, it has been shown by Kemei *et al.* that below T_N , two different phases, namely, tetragonal ($I4_1/amd$) and orthorhombic ($Fddd$) structures coexist in ZnCr_2O_4 [5]. From the refinement of structural parameters, we see that the transformed phase has c/a ratio of 1.42 which is consistent with the tetragonal distortion of high-temperature cubic phase. Further, it is observed from the XRD pattern at 5 K that the Bragg peaks (400 and 800) are broadened and split, as shown in the insets of Figure 7.2(b), indicating the coexistence of strain and lowering of crystal symmetry to the tetragonal structure. The development of large strain, due to the lattice mismatch between two crystallographic phases, could inhibit complete structural phase transformation and thus results in mixed phase at low temperature [28].

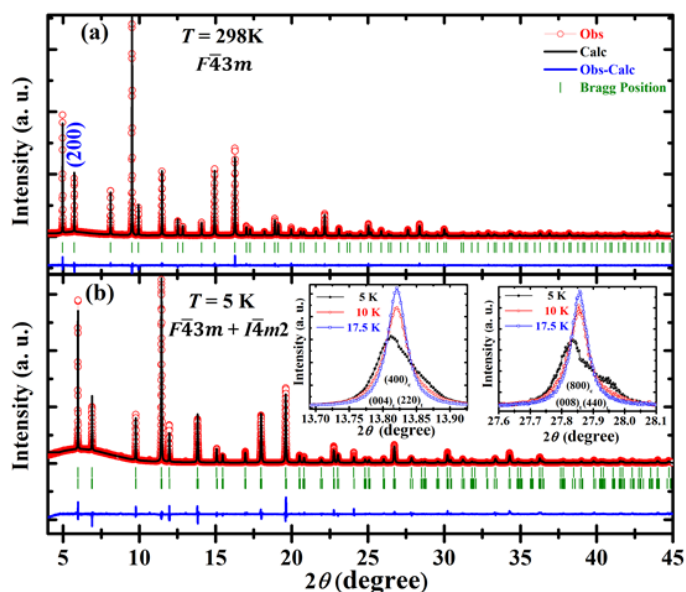


Figure 7.2: (a), (b) The Rietveld refinements on the synchrotron x-ray diffraction pattern of $\text{LiGaCr}_4\text{O}_8$ acquired at 298 and 5 K with $\lambda = 0.4127$ and 0.4959 \AA , respectively. The first and second green vertical bars in (b) correspond to the Bragg reflections for the cubic and tetragonal phases respectively. Insets of (b) show the broadening and splitting of the two cubic Bragg reflections (400) and (800) in the antiferromagnetic state. The XRD patterns in the inset are recorded with $\lambda = 0.4959 \text{ \AA}$. The suffix c and t stands for cubic and tetragonal symmetry respectively. Tiny unrefined peaks visible in the 2θ range of 7-15 degree originate from the cryostat.

7.4.1.2 X-ray diffraction study of $\text{LiFeCr}_4\text{O}_8$

Rietveld analysis of room temperature XRD data of $\text{LiFeCr}_4\text{O}_8$ [Figure 7.3] confirms that it also crystallizes in the cubic $F\bar{4}3m$ space group similar to that found in the case of Ga and In compounds. From the refinement, we find that two kinds of Cr-Cr

distances exist in $\text{LiFeCr}_4\text{O}_8$ such as 2.846 and 3.005 Å, which is nearly similar to the Cr-Cr distance of $\text{LiGaCr}_4\text{O}_8$ (2.830 and 2.999 Å) reflecting the role of A-site cation ordering in $\text{LiFeCr}_4\text{O}_8$. The closeness of the Cr-Cr distance in these two compounds is associated with the similar ionic radii of Fe^{3+} (0.49 Å) and Ga^{3+} (0.47 Å) ion in the tetrahedral coordination. The modulation of Cr-Cr distance in Cr_4 pyrochlore network also confirms the existence of a zinc-blende-type of ordering between Li^+ and Fe^{3+} ions at the A-site.

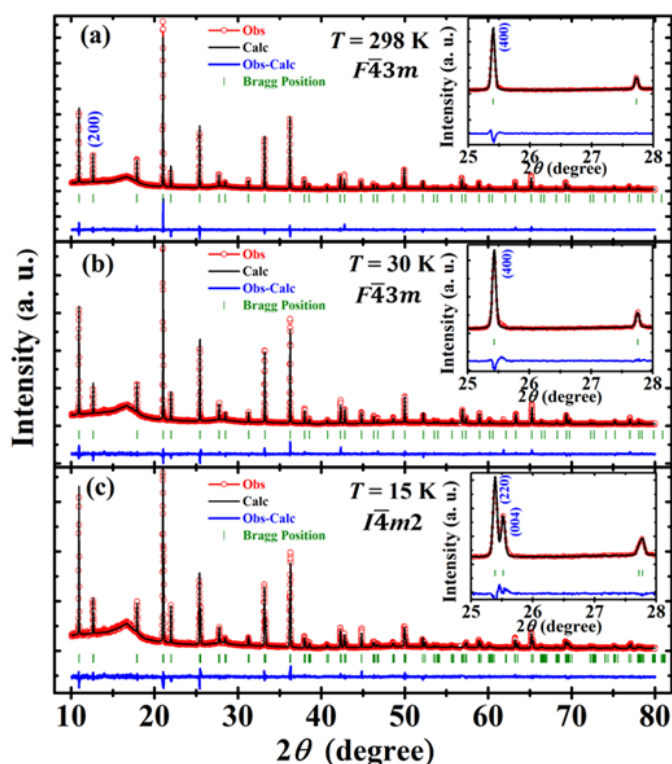


Figure 7.3: (a-c) The Rietveld refinements on the synchrotron x-ray diffraction data of $\text{LiFeCr}_4\text{O}_8$ collected at $T = 298, 30$ and 15 K with $\lambda = 0.91$ Å. Insets of (a-c) show the lowering of symmetry from (a), (b) $F\bar{4}3m$ to (c) $I\bar{4}m2$ upon cooling below the magnetostructural transition (23 K).

Analysis of temperature dependent synchrotron XRD data in $\text{LiFeCr}_4\text{O}_8$ [Figure 7.3] revealed that the cubic structure ($F\bar{4}3m$) remains unchanged down to 23 K and then transforms completely to tetragonal structure with the space group $I\bar{4}m2$, while in the Ga and In compounds the structural phase transformation remain incomplete indicating the importance of magnetic ion at the A-site. In the tetragonal structure, Li^+ and Fe^{3+} ions are present at $2a$ and $2d$ Wyckoff positions respectively, while Cr^{3+} and two O^{2-} ions occupy the $8i$ Wyckoff sites similar to that found in MgV_2O_4 [29]. In the insets of Figure 7.3, it is illustrated how the (400) reflection of cubic phase (298 and 30 K) is split into (220) and (004) reflections in the tetragonal phase (15 K) of $\text{LiFeCr}_4\text{O}_8$.

7.4.1.3 Neutron diffraction study of $\text{LiGaCr}_4\text{O}_8$

To investigate the magnetic and crystallographic structures in detail, we have carried out temperature dependent neutron diffraction experiments on $\text{LiGaCr}_4\text{O}_8$. The magnetic structure determination has been accomplished following the representation analysis technique of group theory described by Bertaut [30]. The basis vectors associated with each possible magnetic model has been obtained with the BasIreps software of the FULLPROF suite package [22].

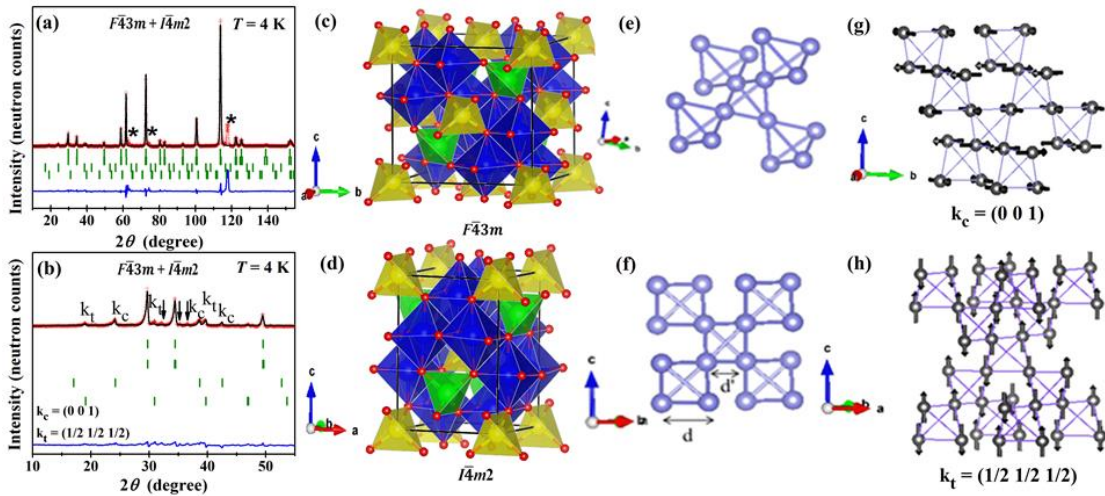


Figure 7.4: (a), (b) The Rietveld refinements on the neutron diffraction pattern of $\text{LiGaCr}_4\text{O}_8$ acquired at 4 K with $\lambda = 2.439 \text{ \AA}$ for the whole region and small region respectively. The red cross and solid black line are the experimental data and calculated patterns, green vertical bars indicate the Bragg reflections and the blue line below is the difference between experimental and calculated pattern. The first series of Bragg reflections correspond to the cubic $F\bar{4}3m$ phase and the second correspond to the tetragonal $I\bar{4}m2$ phase, the third and the fourth series account the magnetic phases for the cubic phase $\vec{k}_c = (0\ 0\ 1)$ and for the tetragonal phase $\vec{k}_t = (\frac{1}{2}\ \frac{1}{2}\ \frac{1}{2})$, respectively. (* aluminium peaks from the cryostat); (c), (d) schematic representation of cubic ($F\bar{4}3m$) and tetragonal ($I\bar{4}m2$) structure of $\text{LiGaCr}_4\text{O}_8$ obtained from the Rietveld refinement on neutron diffraction pattern collected at 4 K, where yellow and green tetrahedra contains the Li^+ and Ga^{3+} ions respectively and blue octahedra contains the Cr^{3+} ions; (e), (f) pyrochlore network consists of Cr_4 tetrahedra embedded in the cubic structure and breathing distortion in a three dimensional network of corner sharing Cr_4 tetrahedra forming pyrochlore sublattice ($d > d'$); (g) The \vec{k}_c magnetic structure associated with cubic symmetry where alternating spin chains on the ab plane. Every second ab plane is rotated 90° with respect to the first one; (h) The \vec{k}_t magnetic structure associated with tetragonal symmetry with chains of spins with two-up and two-down arrangement along the $[100]$ and $[010]$ directions.

The value of lattice parameter of $\text{LiGaCr}_4\text{O}_8$ obtained from the Rietveld analysis of the room temperature neutron data is $a = 8.2457 \text{ \AA}$ and we obtain two distinct Cr-Cr distances (2.824 and 3.006 \AA) which are in agreement with those obtained from the analysis of XRD pattern. Based on Rietveld refinement against the room temperature neutron data we see full occupancy of Li and Ga ions at their respective sites. Consequently, we fixed the occupancy for the refinements against the low temperature

(4 K) neutron data, which is shown in Figure 7.4(a). Though we do not see a clear peak splitting in the low temperature (4 K) neutron diffraction data due to the relatively poorer resolution compared to synchrotron x-ray diffraction data, it could be modeled considering the mixture of two different space groups, $F\bar{4}3m$ and $I\bar{4}m2$ as inferred from the analysis of synchrotron XRD pattern. It should be mentioned here that such a phase coexistence has been reported recently in $\text{LiInCr}_4\text{O}_8$ from the analysis of neutron diffraction pattern at 2 K [17]. The lattice parameters for $\text{LiGaCr}_4\text{O}_8$ obtained from the refinement of neutron data at 4 K are $a = 8.2401(3) \text{ \AA}$ for the cubic phase and $a = 5.8123(3) \text{ \AA}$, $c = 8.2661(3) \text{ \AA}$ for the tetragonal phase. The weight fraction of tetragonal phase obtained from the refinement for $\text{LiGaCr}_4\text{O}_8$ is 28(6) % at 4 K while it is reported to be 70% for $\text{LiInCr}_4\text{O}_8$ at 2 K [17]. The presence of different amount of phase fractions could be attributed to the difference in ionic radii of Ga^{3+} (0.47 \AA) and In^{3+} (0.62 \AA), exerting different amounts of chemical pressure, leading to a structural distortion and lowering of crystallographic symmetry to a different extent. The structural parameters obtained from the refinements of neutron diffraction data at room temperature and 4 K are summarized in Tables 7.1 and 7.2 respectively.

Table 7.1: Structural parameters of $\text{LiGaCr}_4\text{O}_8$ obtained from the Rietveld refinement of neutron diffraction pattern acquired at 298 K.

LiGaCr ₄ O ₈ (Space Group: $F\bar{4}3m$), $\lambda = 1.62 \text{ \AA}$					
Atom	<i>x</i>	<i>y</i>	<i>z</i>	<i>B</i> _{iso} (\AA^2)	Occupancy
Li (4 <i>a</i>)	0	0	0	0.96 (11)	1.0
Ga (4 <i>d</i>)	0.75	0.75	0.75	0.17 (2)	1.0
Cr (16 <i>e</i>)	0.3711 (2)	0.3711 (2)	0.3711 (2)	0.13 (2)	1.0
O1 (16 <i>e</i>)	0.1358 (1)	0.1358 (1)	0.1358 (1)	0.46 (3)	1.0
O2 (16 <i>e</i>)	0.6187 (1)	0.6187 (1)	0.6187 (1)	0.22 (2)	1.0

$R_{\text{Bragg}} = 2.06 \%$, $R_{\text{f}} = 1.74 \%$, $\chi^2 = 3.10 \%$

Table 7.2: Structural parameters of $\text{LiGaCr}_4\text{O}_8$ obtained from the Rietveld refinement of neutron diffraction pattern acquired at 4 K

LiGaCr ₄ O ₈ (Space Group: $F\bar{4}3m$), $\lambda = 2.44 \text{ \AA}$					
Cubic Phase Fraction = 72 (7) %					
Atom	<i>x</i>	<i>y</i>	<i>z</i>	$B_{iso} (\text{\AA}^2)$	Occupancy
Li (4 <i>a</i>)	0	0	0	2.3 (5)	1.0
Ga (4 <i>d</i>)	0.75	0.75	0.75	0.2 (1)	1.0
Cr (16 <i>e</i>)	0.3728 (7)	0.3728 (7)	0.3728 (7)	0.94 (9)	1.0
O1 (16 <i>e</i>)	0.1360 (3)	0.1360 (3)	0.1360 (3)	0.05 (6)	1.0
O2 (16 <i>e</i>)	0.6175 (3)	0.6175 (3)	0.6175 (3)	0.05 (7)	1.0
LiGaCr ₄ O ₈ (Space Group: $I\bar{4}m2$), $\lambda = 2.44 \text{ \AA}$					
Tetragonal Phase Fraction = 28 (6) %					
Atom	<i>x</i>	<i>y</i>	<i>z</i>	$B_{iso} (\text{\AA}^2)$	Occupancy
Li (2 <i>a</i>)	0	0	0	2.3 (5)	1.0
Ga (2 <i>d</i>)	0.0	0.5	0.75	0.2 (1)	1.0
Cr (8 <i>i</i>)	0.264 (3)	0	0.873(3)	0.94 (9)	1.0
O1 (8 <i>i</i>)	0.284(1)	0	0.634(8)	0.05 (6)	1.0
O2 (8 <i>i</i>)	0.251(1)	0	0.108(1)	0.05 (7)	1.0

From the structural parameters obtained from the refinement of neutron diffraction pattern we have drawn the schematics of cubic and tetragonal crystal structures as shown in Figures 7.4(c) and 7.4(d) respectively. In Figures 7.4(e) and 7.4(f), we have shown respectively, the schematics of pyrochlore network made of Cr atoms and two different sizes of the tetrahedral units of the pyrochlore block tuning the magnetic frustration.

Magnetic structures associated with both the cubic and tetragonal phases of $\text{LiGaCr}_4\text{O}_8$ have been identified based on the indexing of the magnetic Bragg peaks in the low angle neutron diffraction pattern [Figure 7.4(a)]. The irreducible representations and the basis vectors are summarized in Table 7.3. A propagation vector, $\vec{k}_c = (0 \ 0 \ 1)$, accounts the magnetic reflections due to the cubic phase. Among the possible magnetic modes compatible with the space-group symmetry and the

propagation vector, the best agreement with the experimental data corresponds to the irreducible representation Γ_1 . As seen in Figure 7.4(g), the magnetic structure can be described as having alternating spin chains along the [110] direction with every second ab plane rotated by 90 degrees with respect to the first one. The magnetic moment of the Cr^{3+} cations in the cubic phase is $0.77(2) \mu_B$. The lower value of magnetic moment may be due to stronger geometrical frustration in the cubic phase (see Table 7.4), which remains even below the magnetic ordering temperature.

Table 7.3: Basis vectors for (a) $\vec{k}_c = (001)$ and the $16e$ site of the cubic S.G.: $F\bar{4}3m$ and (b) $\vec{k}_t = (\frac{1}{2}\frac{1}{2}\frac{1}{2})$ and the $8i$ site of the tetragonal S.G.: $I\bar{4}m2$. ($\text{LiGaCr}_4\text{O}_8$)

(a)	Cr1(x x x)	Cr2(-x -x x)	Cr3(-x x -x)	Cr4(x -x -x)
Γ_1	(1,-1,0)	(-1,1,0)	(-1,-1,0)	(1,1,0)
Γ_2	(1,1,0)	(-1,-1,0)	(-1,1,0)	(1,-1,0)
	(0,0,1)	(0,0,1)	(0,0,-1)	(0,0,-1)
Γ_3	(1,-1,0)	(-1,1,0)	(1,1,0)	(-1,-1,0)
Γ_4	(1,1,0)	(-1,-1,0)	(1,-1,0)	(-1,1,0)
	(0,0,1)	(0,0,1)	(0,0,1)	(0,0,1)
Γ_5	(1,0,0)	(1,0,0)	(-1,0,0)	(-1,0,0)
	(0,1,0)	(0,1,0)	(0,1,0)	(0,1,0)
	(0,0,1)	(0,0,-1)	(0,0,-1)	(0,0,1)
	(0,-1,0)	(0,-1,0)	(0,1,0)	(0,1,0)
	(-1,0,0)	(-1,0,0)	(-1,0,0)	(-1,0,0)
	(0,0,-1)	(0,0,1)	(0,0,-1)	(0,0,1)
(b)	Cr1(x 0 z)	Cr2(-x 0 z)	Cr3(0 -x -z)	Cr4(0 x -z)
Γ_1	(1,0,0)	(-1,0,0)	(0,1,0)	(0,-1,0)
	(0,1,0)	(0,-1,0)	(-1,0,0)	(1,0,0)
	(0,0,1)	(0,0,1)	(0,0,1)	(0,0,1)
Γ_2	(1,0,0)	(-1,0,0)	(0,-1,0)	(0,1,0)
	(0,1,0)	(0,-1,0)	(1,0,0)	(-1,0,0)
	(0,0,1)	(0,0,1)	(0,0,-1)	(0,0,-1)
Γ_3	(1,0,0)	(1,0,0)	(0,-i,0)	(0,-i,0)
	(0,1,0)	(0,1,0)	(i,0,0)	(i,0,0)
	(0,0,1)	(0,0,-1)	(0,0,-i)	(0,0,i)
Γ_4	(1,0,0)	(1,0,0)	(0,i,0)	(0,i,0)
	(0,1,0)	(0,1,0)	(-i,0,0)	(-i,0,0)
	(0,0,1)	(0,0,-1)	(0,0,i)	(0,0,-i)

The magnetic structure of the tetragonal phase is described by the propagation vector $\vec{k}_t = (\frac{1}{2} \frac{1}{2} \frac{1}{2})$ as reported in $\text{LiInCr}_4\text{O}_8$ [17]. After testing the different solutions given in Table 7.3, the best spin arrangement compatible with the tetragonal space group $I\bar{4}m2$ is provided by the basis vector 3 of Γ_2 . The obtained magnetic moment of the Cr^{3+} cations, aligned along the c -axis, is $2.33(9) \mu_B$. The reduction of this value with

respect to the expected magnetic moment ($S = 3/2$) might be due to covalence effects. Figure 7.4(h) shows the magnetic structure of the tetragonal phase of the $\text{LiGaCr}_4\text{O}_8$ spinel, consisting of chains of spins with two-up and two-down arrangement along $[100]$ and $[010]$ directions.

7.4.1.4 Neutron diffraction study of $\text{LiFeCr}_4\text{O}_8$

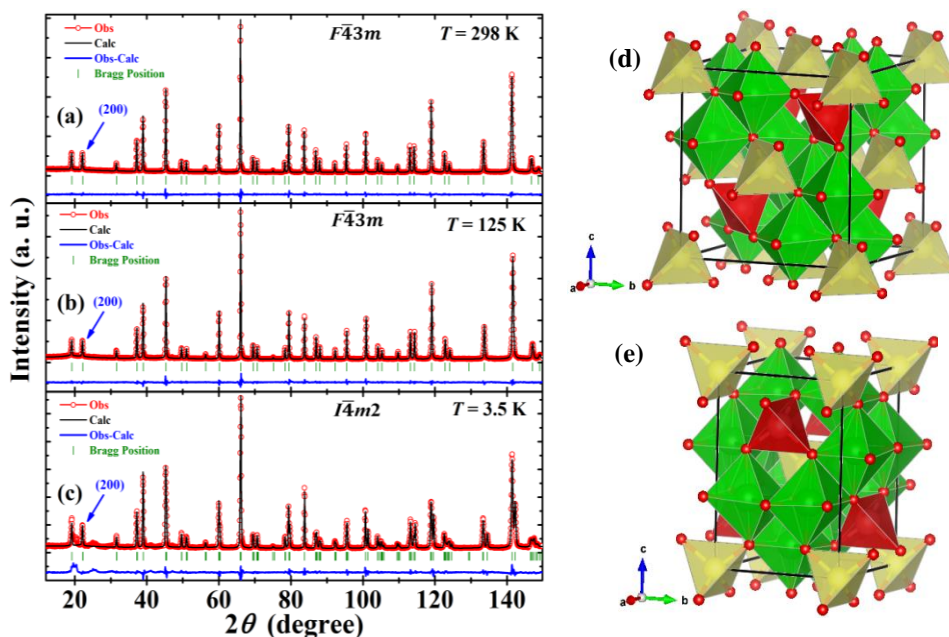


Figure 7.5: (a-c) The Rietveld refinements on the neutron diffraction pattern of $\text{LiFeCr}_4\text{O}_8$ collected at $T = 298, 125$ and 3.5 K with $\lambda = 1.594\text{ \AA}$; Schematic representation of (d) cubic ($F\bar{4}3m$) and (e) tetragonal ($I\bar{4}m2$) structure of $\text{LiFeCr}_4\text{O}_8$ obtained from the Rietveld refinement on neutron diffraction pattern collected at 298 and 3.5 K . The polyhedra with yellow, red and green contain the Li, Fe and Cr atoms respectively. (Unindexed peak at 3.5 K corresponds to the reflections associated with magnetic contribution)

Now we discuss the results obtained from the neutron diffraction experiments on $\text{LiFeCr}_4\text{O}_8$. From the Rietveld analysis of room temperature neutron data, we observe that the compound crystallizes in the cubic structure with the space group $F\bar{4}3m$ as shown in Figure 7.5(a). From the analysis of temperature dependent neutron data, we observe that the compound remains in the cubic structure down to 23 K . Based on the Rietveld refinement performed on the 3.5 K data we find that the diffraction pattern could be fitted well with the tetragonal structure with the space group $I\bar{4}m2$ as shown in Figure 7.5(c). Neutron diffraction patterns recorded at all temperatures contain the (200) reflection which is a signature of ordering between Li^+ and Fe^{3+} ions located at the A-site. This structural information is consistent with the observations obtained from the synchrotron x-ray diffraction study. To model the nuclear structures we have used

the diffraction pattern collected with $\lambda = 1.594 \text{ \AA}$. In Figures 7.5(d) and 7.5(e), we show the schematics of cubic (298 K) and tetragonal (3.5 K) nuclear structures respectively obtained from the refinement. Based on the Rietveld refinement on room temperature neutron data collected with $\lambda = 1.594 \text{ \AA}$, we find that two kinds of Cr-Cr distances are present such as 2.983 and 2.870 \AA which are associated with large and small Cr_4 tetrahedra, respectively reflecting the role of A-site cation ordering in $\text{LiFeCr}_4\text{O}_8$. On the other hand, we have observed four inequivalent Cr-Cr distances in the tetragonal structure ($I\bar{4}m2$), 2.895 and 2.869 \AA (small Cr_4 tetrahedra), 2.963 and 2.973 \AA (large Cr_4 tetrahedra). The relative difference between the long and short bonds in the small and large tetrahedra is 0.026 and 0.01 \AA respectively. Note that in the cubic structure ($F\bar{4}3m$) there was no difference in the Cr-Cr distances of individual (either small or large) tetrahedra. From the refinement of neutron data, we obtain the distortion value (d/d') of tetrahedra as 1.04 (298 K) and 1.03 (3.5 K).

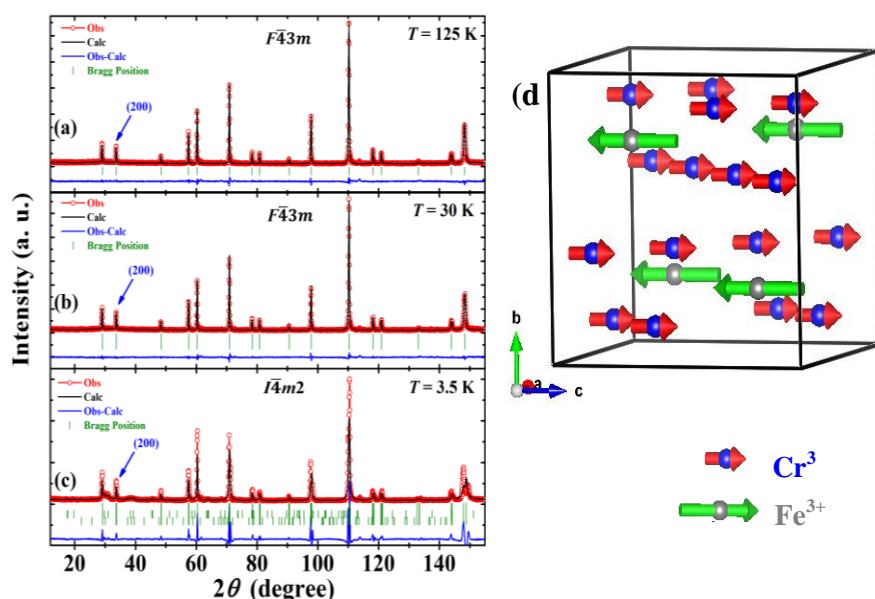


Figure 7.6: (a-c) The Rietveld refinements on the neutron diffraction pattern of $\text{LiFeCr}_4\text{O}_8$ collected at $T = 125, 30$ and 3.5 K with $\lambda = 2.398 \text{ \AA}$; Schematic representation of (d) the ferrimagnetic structure of $\text{LiFeCr}_4\text{O}_8$ obtained from the Rietveld refinement on neutron diffraction pattern collected at 30 K . The second Bragg positions in Fig. 7.6(b) correspond to the magnetic reflection. In Fig. 7.6(c) the second and third Bragg reflections correspond to the magnetic contribution associated with \vec{k}_1 and \vec{k}_2 propagation vectors.

We have investigated the magnetic structures of $\text{LiFeCr}_4\text{O}_8$ by performing the Rietveld analysis on the neutron powder pattern collected at low temperature with $\lambda = 2.398 \text{ \AA}$ as shown in Figure 7.6. Since we do not observe any new reflection other than an increase in intensity on top of some nuclear reflection [Figure 7.6(a)] in the

temperature range $30 \leq T \leq 100$ K, we considered the propagation vector $\vec{k} = (0, 0, 0)$ for the cubic phase. We have found that the refinement of the magnetic structure by considering the representation Γ_4 gives the best fit to the observed diffraction patterns at $30 \leq T \leq 100$ K, i.e., below the magnetic ordering temperature. The fitted pattern at 30 K is shown in Figure 7.6(b) and the corresponding magnetic structure is shown in Figure 7.6(d). The magnetic structure is a collinear ferrimagnetic (Fe^{3+} and Cr^{3+} ions are aligned antiparallel) in nature. The direction of the ordered magnetic moment of Fe^{3+} and Cr^{3+} at 30 K is aligned along the crystallographic c direction with a magnitude of 2.351 and $0.36 \mu_B$ respectively.

We have attempted to determine the magnetic structure associated with the tetragonal phase ($I\bar{4}m2$) which appears below 23 K. Preliminary modelling on the neutron powder pattern [Figure 7.6(c)] collected at 3.5 K shows the presence of two different propagation vectors $\vec{k}_1 = (0.4960 \ 0.4378 \ 1/2)$ and $\vec{k}_2 = (1/4 \ 1/4 \ 0.2360)$ respectively, indicating that the spin structure probably adopts complex spin arrangement. To solve this magnetic structure accurately, we require high-resolution neutron diffraction pattern.

7.4.2 Magnetic properties of LiMCr_4O_8 (M = Ga, In, Fe):

7.4.2.1 Magnetization and heat capacity study of $\text{LiGaCr}_4\text{O}_8$ and $\text{LiInCr}_4\text{O}_8$

Figures 7.7(a) and 7.7(b), show the temperature dependence of dc magnetization data, $M(T)$ for $\text{LiGaCr}_4\text{O}_8$ and $\text{LiInCr}_4\text{O}_8$, respectively. In both compounds, a broad maximum is observed around 55-60 K followed by a decrease in the magnetization value near T_N , similar to that seen in ZnCr_2O_4 . However, the origin of this maximum has been suggested to differ in these A-site ordered compounds [18]. In $\text{LiGaCr}_4\text{O}_8$, the maximum around 55 K is associated with a short-range antiferromagnetic correlation in the paramagnetic phase, similar to that observed in the uniform pyrochlore lattice, e.g. in ZnCr_2O_4 [31]. On the other hand, the maximum in magnetization around 60 K in $\text{LiInCr}_4\text{O}_8$ was initially attributed to the opening of a spin gap (SG) [32] and later it was suggested, using time-of-flight neutron spectroscopy, that the spin-gap is filled with magnetic states thereby forming a pseudogap [17]. It is important to mention that though the features of the temperature dependent magnetization curves for both Ga and

In compounds around 55-60 K region looks apparently similar, there is tiny difference - the maximum is much more rounded in the In compound than in the Ga.

Spin-gap antiferromagnets possess spin-disordered ground states, i.e. the spin-spin correlations in the ground state are short-ranged. Quantum fluctuations favor formation of gapped states. The effect of quantum fluctuations is prominent in low dimensions and for low values of the spin [33]. A gapped state typically arises because one has some form of local singlet covering, i.e. dimers on the Shastry-Sutherland lattice [34] or indeed the singlet ground state on isolated tetrahedra [35]. The formation of a spin gap in a magnetic material where singlet ground state ($S = 0$) is separated from the triplet excited state ($S = 1$) would be manifested as the behavior of nonmagnetic materials at low temperature. The gap arises because the system is a quantum object with only a few spins and hence has discrete energy levels. In experiments, the presence of such gap Δ is confirmed through measurement of properties like susceptibility, χ , which goes to zero exponentially at low temperature as $\chi \sim \exp\left(-\frac{\Delta}{k_B T}\right)$ [33]. Some well-known examples of SG antiferromagnets are Spin-Peierls (SP) systems [36], antiferromagnetic compounds consisting of weakly coupled spin dimers, frustrated spin systems, spin ladders and Haldane gap (HG) antiferromagnets [37]. Antiferromagnetic short range order is rather different because here one starts from the classical limit.

In the case of $\text{LiInCr}_4\text{O}_8$, the gap arises as a result of strong breathing distortion. Breathing distortion is the degree of distortion from the ideal pyrochlore lattice (e.g. ZnCr_2O_4 , where all Cr-Cr distances are equivalent) and it is expressed as the ratio of the bond lengths in the large and small tetrahedra, (d/d') where d and d' is the Cr-Cr distance in the large and small tetrahedra. Therefore two inequivalent bond lengths (d and d') would lead to the existence of different nearest neighbour exchange interaction for the larger (J) and smaller tetrahedra (J') [$J' > J$], where the ratio (J/J'), is called as breathing factor (B_f) [17] which determines the nature of ground state magnetic phase. The isolated tetrahedron with $B_f = 0$ and uniform pyrochlore lattice with $B_f = 1$ possess tetramer singlet and spin liquid ground states, respectively [38,39]. The breathing factor (B_f) is inversely related to the breathing distortion of the pyrochlore lattice. The breathing distortion exists down to the lowest temperature in

both the tetragonal and cubic phases of Ga and In compound. The experimental temperature dependent susceptibility data (χ vs. T) could be fitted with classical Monte Carlo simulation to determine the values of J' and J as shown for the Ga and In compounds in the literature [18]. In ref. 18 it is shown that the isolated tetrahedron model fits the susceptibility data of In compound much better than the Ga data. For this calculation, the energy levels are usually calculated by exact diagonalization of the spin Hamiltonian and the susceptibility calculated from the thermal occupation of the states.

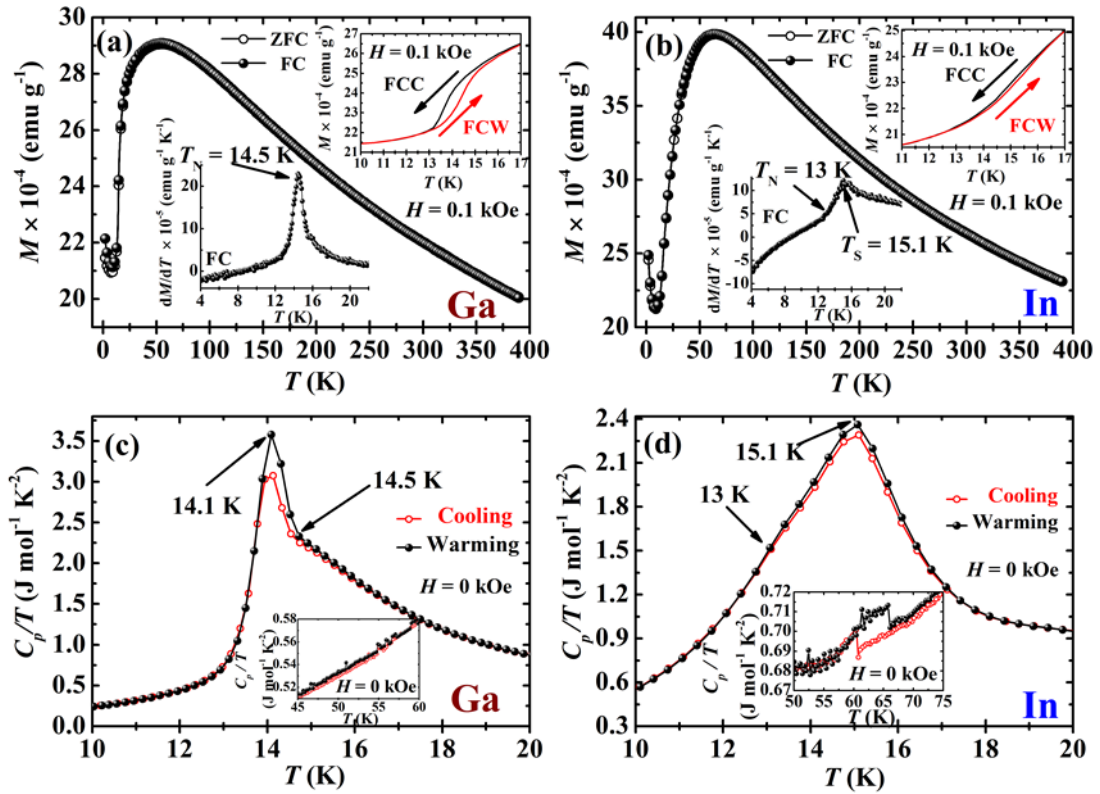


Figure 7.7: (a), (b) Temperature dependence of dc magnetization data of $\text{LiGaCr}_4\text{O}_8$ and $\text{LiInCr}_4\text{O}_8$ respectively under zero-field-cooled (ZFC) and field-cooled (FC) conditions in the presence of a magnetic field of 0.1 kOe. Upper inset of (a) and (b) shows the temperature dependent field-cooled-cooling (FCC) and field-cooled-warming (FCW) magnetization data at 0.1 kOe, while the bottom inset of (a) and (b) shows the first derivative of magnetization with respect to temperature as a function of temperature at 0.1 kOe; (c), (d) temperature dependence of specific heat divided by temperature (C_p/T) for $\text{LiGaCr}_4\text{O}_8$ and $\text{LiInCr}_4\text{O}_8$ across T_N respectively. Inset of (c) and (d) show the C_p/T data across the short-range antiferromagnetic ordering ($T_{SO} \sim 55$ K) of Ga compound and spin-gap opening temperature ($T_{SG} \sim 60$ K) of In compound respectively.

In the case of $\text{LiGaCr}_4\text{O}_8$, a first order long range antiferromagnetic transition occurs at 14.5 K while a second order long-range antiferromagnetic ordering takes place around 13 K in $\text{LiInCr}_4\text{O}_8$ as evident from the first derivative of magnetization with respect to temperature as shown in the bottom inset of Figures 7.7(a) and 7.7(b), respectively. In ZnCr_2O_4 , the first order long-range antiferromagnetic ordering coupled

with the structural transition occurs around 13 K [Figure 7.8(a)]. The first order nature of the antiferromagnetic ordering ($T_N \sim 14.5$ K) in Ga compound is supported by thermal hysteresis in the temperature dependent field-cooled-cooling (FCC) and field-cooled-warming (FCW) magnetization data as shown in the upper inset of Figure 7.7 (a). In the case of Ga compound, the magnetic ordering and the structural transition occur at the same temperature. A similar thermal hysteresis has been observed in $\text{LiInCr}_4\text{O}_8$ at the structural phase transition temperature $T_S \sim 15.1$ K [upper inset of Figure 7.7(b)] rather than at the magnetic phase transition temperature ($T_N \sim 13$ K). The decoupled phase transition temperatures indicate that the antiferromagnetic ordering in In compound is a conventional second order phase transition consistent with a previous report [19]. The low-temperature upturn in the magnetization data is associated with the paramagnetic contribution from orphan spins [40].

The temperature-dependent specific heat divided by temperature (C_p/T) measured on $\text{LiGaCr}_4\text{O}_8$ in zero magnetic field shows a lambda shape anomaly at 14.1 K with a step-like feature at 14.5 K [Figure 7.7(c)]. The two distinct features in C_p/T indicate that the structural and the magnetic transitions occur at different temperatures. On the contrary, a previous report on this compound showed that the antiferromagnetic transition is coupled with the structural distortion, which is first order in nature [19]. In the present study, the proximity of the two peak feature observed in the C_p/T data with an interval of 0.4 K, makes it difficult to ascertain their origin. However, from the temperature dependent derivative of dc magnetization [bottom inset Figure 7.7(a)] and the thermal hysteresis in the C_p/T data [Figure 7.7(c)], we suggest that the anomaly at 14.5 K could be due to structural transition, and the magnetic ordering occurs at 14.1 K. To confirm this suggestion, we require further structural investigation across this temperature region. In a recent report by Lee *et al.*, it has been shown that the Ga compound undergoes magnetostructural and magnetic transitions at different temperatures, within an interval of 2.3 K [40]. The absence of any strong features in the C_p/T data around 55 K suggests that the entropy associated with the short-range spin-spin correlations in $\text{LiGaCr}_4\text{O}_8$ is small.

In the case of $\text{LiInCr}_4\text{O}_8$, a sharp peak at 15.1 K and a change in slope at 13 K in the temperature dependent C_p/T data is evident in Figure 7.7(d). In this compound, an interval of almost 2 K between the two anomalies makes it possible to distinguish the

structural and magnetic transitions. Thermal hysteresis across the peak at 15.1 K [Figure 7.7(d)] indicates the occurrence of structural phase transformation at that temperature while the change in slope around 13 K in the temperature dependent C_p/T data can be associated with the second order antiferromagnetic phase transition. This is further supported from the temperature dependent derivative of the dc magnetization data [bottom inset of Figure 7.7(b)] of the $\text{LiInCr}_4\text{O}_8$, which shows a peak at 15.1 K along with a small anomaly at 13 K. Contrary to $\text{LiGaCr}_4\text{O}_8$, which does not show any peak in the C_p/T data in the vicinity of temperature where the short-range antiferromagnetic ordering sets in [inset of Figure 7.7(c)], the compound $\text{LiInCr}_4\text{O}_8$ shows an anomaly and thermal hysteresis across the spin-gap opening temperature ($T_{\text{SG}} \sim 60$ K) as evident from the inset of Figure 7.7(d). This unique observation is probably associated with the stronger breathing distortion in the In compound indicating the presence of strong spin-lattice coupling. No significant effect of the magnetic field on the temperature dependent C_p/T data was observed in these compounds indicating the robustness of the phase transition.

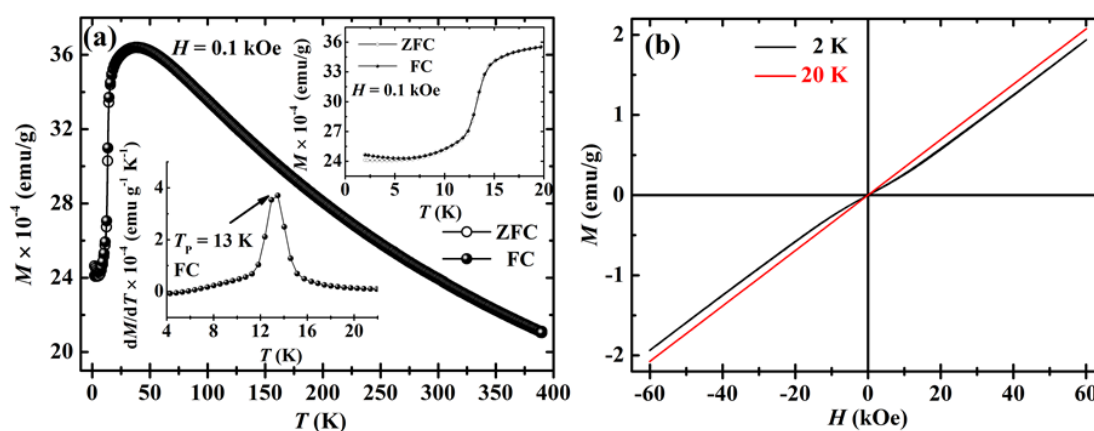


Figure 7.8: (a) Temperature dependent dc magnetization data of ZnCr_2O_4 under zero-field-cooled (ZFC) and field-cooled (FC) conditions in the presence of a magnetic field of 0.1 kOe. The upper inset shows the zoom in view of bifurcation between ZFC and FC data and the bottom inset shows the first derivative of magnetization with respect to temperature as a function of temperature at 0.1 kOe. (b) Isothermal magnetization data of ZnCr_2O_4 measured as a function of magnetic field at 2 K (below T_N) and 20 K (above T_N).

Isothermal magnetization data, $M(H)$ recorded at 2 K [shown in Figure 7.9(a) and 7.9(b)] confirms the antiferromagnetic nature of these compounds. Further, the $M(H)$ curves show that there is a change in slope from the initial straight line, starting at around 2.4 kOe for $\text{LiGaCr}_4\text{O}_8$ and 20 kOe for $\text{LiInCr}_4\text{O}_8$, which is prominent from the first derivative of magnetization with respect to magnetic field shown in the insets of Figure 7.9(a) and 7.9(b). Similar nonlinear behavior is observed in the isothermal

magnetization data of ZnCr_2O_4 [Figure 7.8 (b)]. Although the nonlinear behavior in the antiferromagnetically ordered state (2 K) has previously been explained based on spin flop transition [18], we attribute the behavior of isothermal magnetization data at 2 K to the presence of two different magnetic structures, as revealed by the low-temperature neutron diffraction data on $\text{LiGaCr}_4\text{O}_8$. The different onset value of the magnetic field for the nonlinear behavior of these two compounds could be associated with the coexistence of two different magnetic phases associated with the two different crystallographic phases which are present to a different extent in the Ga and In compounds. This suggestion is supported by the behaviour of the temperature dependence of the zero-field-cooled (ZFC) and field-cooled (FC) magnetization data ($H = 0.1$ kOe), which shows a divergence below the Néel temperature in $\text{LiGaCr}_4\text{O}_8$ while there is negligible divergence for $\text{LiInCr}_4\text{O}_8$ [Figures 7.7(a) and 7.7(b)].

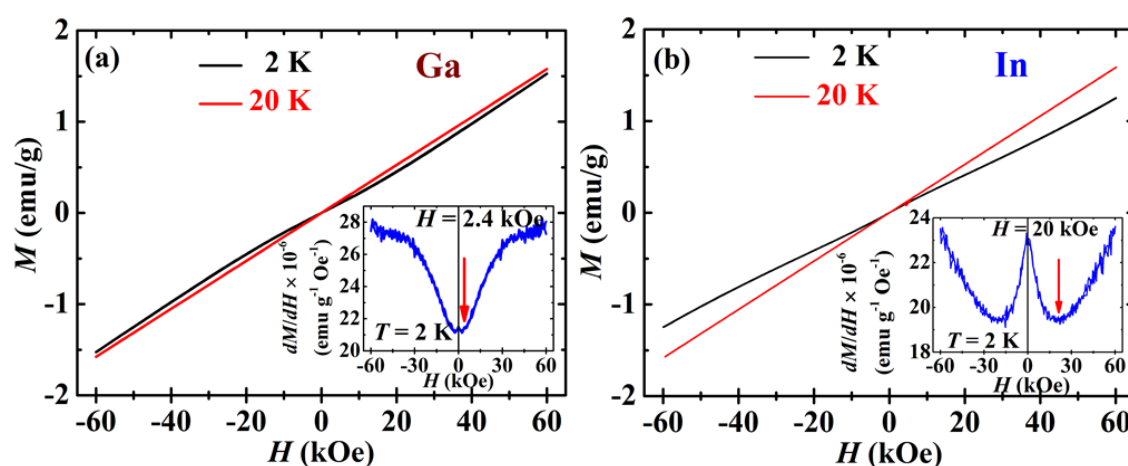


Figure 7.9: Isothermal magnetization data measured as a function of magnetic field at 2 K (below T_N) and 20 K (above T_N) is shown for (a) $\text{LiGaCr}_4\text{O}_8$ and (b) $\text{LiInCr}_4\text{O}_8$. Inset of (a) and (b) shows the first order derivative of magnetization with respect to the magnetic field as a function of magnetic field at 2 K.

To understand the origin of the bifurcation, the temperature dependent ZFC and FC magnetization data for both compounds were measured at various magnetic fields as shown in Figure 7.10. The Ga compound shows an initial increase in the magnitude of divergence between the ZFC and FC magnetization data up to an applied magnetic field of 30 kOe although it decreases at higher fields but the irreversibility persists up to the highest applied magnetic field (70 kOe) [Figures 7.10(a) - 7.10(d)]. The effect of magnetic field on the dc magnetization data of $\text{LiInCr}_4\text{O}_8$ is comparatively small [Figures 7.10(e) - 7.10(h)].

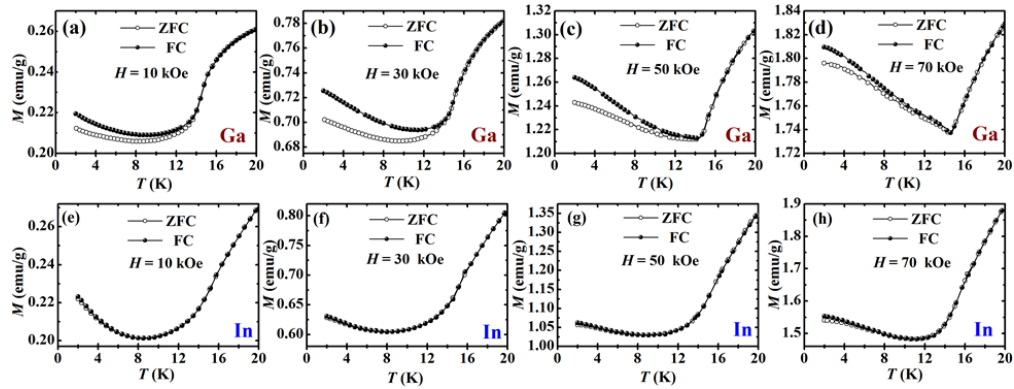


Figure 7.10: Temperature dependent dc magnetization data of (a-d) LiGaCr₄O₈ and (e-h) LiInCr₄O₈ under zero-field-cooled (ZFC) and field-cooled (FC) conditions in presence of different magnetic fields of 10, 30, 50 and 70 kOe, respectively.

It is to be noted that a similar divergence between ZFC and FC behavior has been observed in polycrystalline samples of LiGa_{1-x}In_xCr₄O₈ where such divergence has been attributed to the freezing of spin-glass-like phase [18,32]. In general, the bifurcation between ZFC and FC data is considered to be an indication of spin-glass-like state. Very often spin-glass systems are characterized by measuring temperature dependent ac susceptibility where the maximum temperature of χ' , corresponding to the spin freezing temperature usually varies with the measuring frequency. Temperature dependent ac susceptibility measurements on LiGaCr₄O₈ did not display either a maximum in χ' or the frequency dependence as shown in Figure 7.11 indicating that the origin of bifurcation is not associated with a conventional spin-glass state.

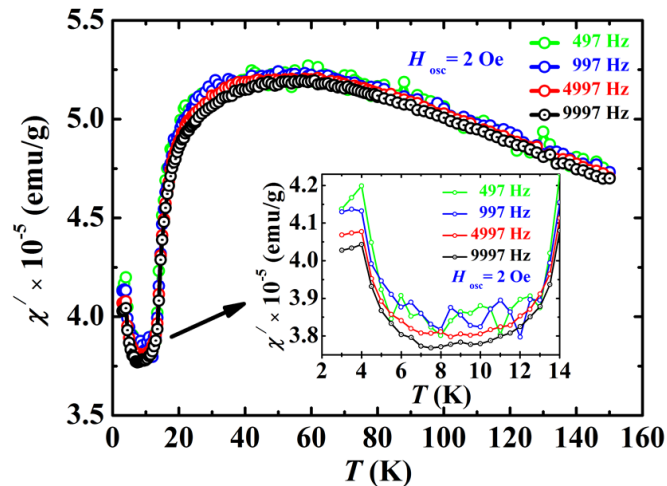


Figure 7.11: Temperature dependent ac magnetic susceptibility data (real part) of LiGaCr₄O₈ measured at different frequencies in the presence of an ac magnetic field of 2 Oe. The inset shows the zoom in view of the data (real part) in the low-temperature region only for clarity.

To investigate whether the divergence is related to any glassy state, we performed dc magnetization measurements employing isothermal waiting under ZFC conditions

below the Néel temperature, because very often the non-equilibrium dynamics of a real spin glass state shows aging, rejuvenation and memory effect [41,42]. We performed dc memory experiment after cooling the sample to the desired temperature under ZFC condition and then allowed to wait at that temperature for some time. After that the sample was cooled to the lowest possible temperature under ZFC condition and then $M(T)$ was measured while warming in the presence of a magnetic field. We have performed two separate waiting experiments with two different halting durations of 6000 and 12000 sec respectively, at 5 K, which is below the Néel temperature where bifurcation between ZFC and FC magnetization starts. On warming the sample in the presence of two different magnetic fields ($H = 0.01$ and 0.1 kOe), we have not observed either any anomalous behavior at the waiting temperature or any difference between the ZFC magnetization data with and without isothermal waiting as shown in Figure 7.12.

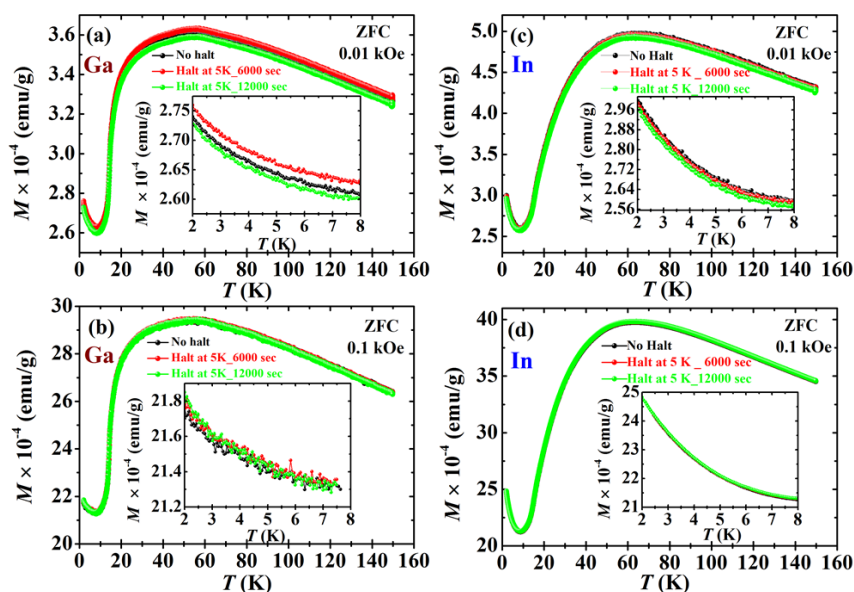


Figure 7.12: Temperature dependent dc magnetization data of (a-b) $\text{LiGaCr}_4\text{O}_8$ and (c-d) $\text{LiInCr}_4\text{O}_8$ measured at 0.01 and 0.1 kOe under zero-field-cooled (ZFC) conditions with an isothermal halt at 5 K for different durations. Insets show the enlarged view across the waiting temperature (5 K) showing superimposing curves with each other without any presence of memory effect at the waiting temperature.

Based on the above experimental results the possibility that a conventional spin-glass or spin-glass-like state is the source of bifurcation between the temperature dependent ZFC, and FC data is discounted. Similar to A-site ordered chromate spinel, we have observed divergence between the ZFC and FC magnetization data in ZnCr_2O_4 at different magnetic fields as shown in Figure 7.13. These results indicate that coexistence of two magnetic phases associated with two distinct crystallographic phases in the Ga and In compounds could be the source of the bifurcation between the

temperature dependent ZFC and FC magnetization data rather than being associated with the spin-glass-like state. Moreover, it is important to study the spin structures of Ga and In compounds under high magnetic fields. It has been reported that the application of a very high magnetic field changes the initial spin configuration of CdCr_2O_4 and HgCr_2O_4 to a collinear three up and one down arrangements for each Cr_4 tetrahedron thereby leading to the reduction in the magnetic frustration [43,44].

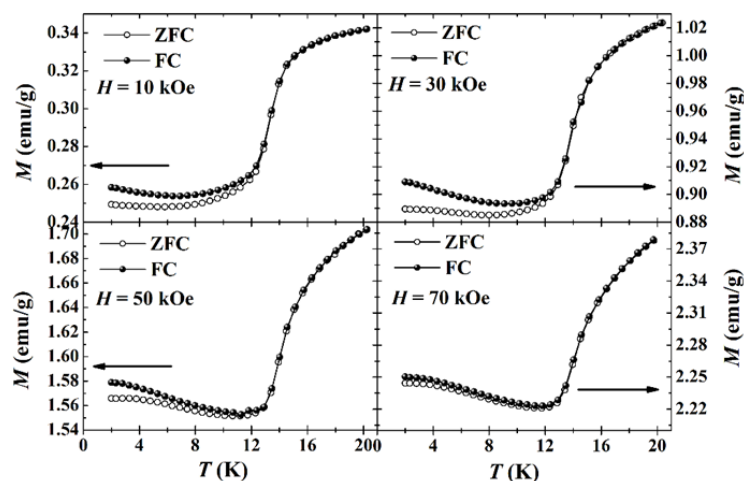


Figure 7.13: Temperature dependent dc magnetization data of ZnCr_2O_4 under zero-field-cooled (ZFC) and field-cooled (FC) conditions in the presence of different magnetic fields of 10, 30, 50 and 70 kOe, respectively.

The temperature dependent inverse susceptibility data of Ga and In compounds, recorded under an applied magnetic field of 0.1 kOe, was fitted with the Curie-Weiss law, $\chi = \frac{C}{T - \theta_{CW}}$ in the temperature range of 200-390 K, where θ_{CW} is the Curie-Weiss constant. The parameters obtained from the linear fit are summarized and compared with that of ZnCr_2O_4 in Table 7.4. The frustration parameters obtained from the Table 7.4 are consistent with the fact that Ga compound orders magnetically at a higher temperature ($T_N \sim 14.5$ K) than the In compound ($T_N \sim 13$ K) to release the geometric magnetic frustration.

Table 7.4: Magnetic parameters of the A-site ordered chromate spinels, LiMCr_4O_8 (M = Ga, In) and ZnCr_2O_4 at $H = 0.1$ kOe.

(Curie-Weiss fitted region: 200-390 K)					
Compound	θ_{CW} (K)	T_N (K)	$f = \theta_{CW} /T_N$	C (emu mole ⁻¹ Oe ⁻¹ K)	μ_{eff} ($\mu_B \text{Cr}^{-1}$)
ZnCr_2O_4	-369	13.0	28	1.872	3.89
$\text{LiGaCr}_4\text{O}_8$	-607	14.5	42	2.062	4.08
$\text{LiInCr}_4\text{O}_8$	-331	13.0	26	1.905	3.92

7.4.2.2 Magnetization and heat capacity study of $\text{LiFeCr}_4\text{O}_8$

Now we discuss the magnetic properties of $\text{LiFeCr}_4\text{O}_8$. In Figure 7.14(a) we show the temperature dependent dc magnetization data recorded in the presence of a magnetic field of 0.1 kOe under zero-field-cooled (ZFC) and field-cooled (FC) conditions. From this data, we observe that $\text{LiFeCr}_4\text{O}_8$ orders magnetically at 94 K indicating that the dominant magnetic interactions between Fe^{3+} and Cr^{3+} ions are antiferromagnetic in nature. It is important to note that in *A*-site ordered chromate spinel, LiMCr_4O_8 ($M = \text{Ga, In}$) the absence of magnetic ions at the *A*-site does not allow long range magnetic order at high temperature because of strong geometrical frustration at the *B*-site. Following the ferrimagnetic transition in $\text{LiFeCr}_4\text{O}_8$, it undergoes two other magnetic transitions at 60 and 23 K as seen from the temperature dependent magnetization data [Figure 7.14(a)]. In the temperature dependent C_p/T data, we also observe three anomalies at 94, 60 and 23 K as shown in Figure 7.14(b).

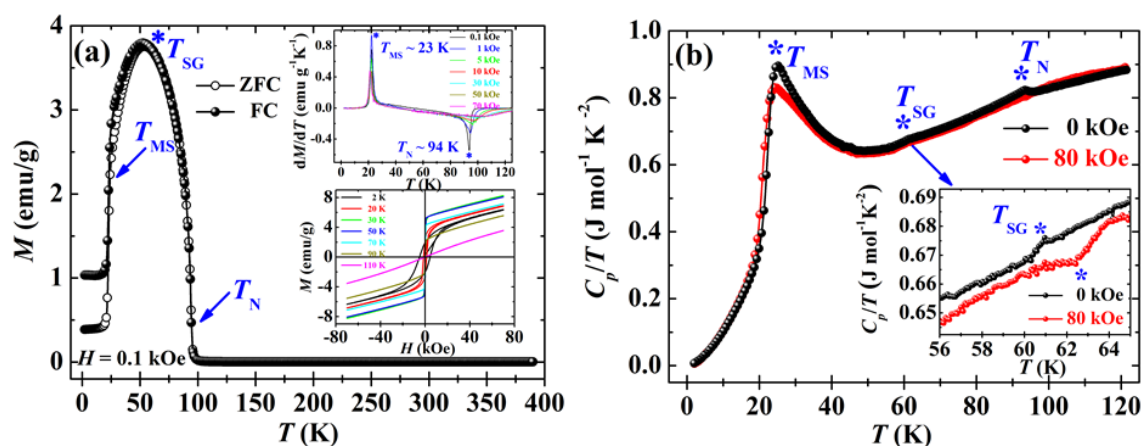


Figure 7.14: (a) Temperature dependent dc magnetization data of $\text{LiFeCr}_4\text{O}_8$. The upper inset of (a) shows the first order derivative of magnetization with respect to temperature (dM/dT) as a function of temperature in the presence of various magnetic fields, and bottom inset of (a) shows the isothermal magnetization data as a function of magnetic field at different temperatures. (b) Temperature dependence of specific heat divided by temperature (C_p/T) for $\text{LiFeCr}_4\text{O}_8$. T_{MS} , T_{SG} , T_{N} stands for magnetostructural, spin-gap state and ferrimagnetic transition temperatures respectively.

The magnetic anomaly at 23 K is attributed to the magnetostructural phase transition (T_{MS}) because it involves an accompanying change in magnetic and crystallographic structures as discussed in the preceding section. In the temperature dependent dM/dT data [upper inset of Figure 7.14(a)], the magnetic transitions at 23 and 94 K are clearly visible, which get suppressed with the application of magnetic field. A similar suppression with magnetic field has been observed in temperature dependent C_p/T data [Figure 7.14(b)]. The origin of a magnetic anomaly at 60 K could

be attributed to the spin-gap state (T_{SG}) arising from modulation of Cr-Cr distances as found in $\text{LiInCr}_4\text{O}_8$ [17]. To confirm the existence of spin-gap state we need to carry out inelastic neutron scattering experiment across the onset of spin-gap transition. Even in the magnetically ordered state, significant geometrical frustration exists and this frustration may be the driving force for the change in magnetic structure from ferrimagnetic to the complex spin structure along with concomitant structural transition at 23 K as discussed in the neutron diffraction study. Isothermal magnetization data recorded as a function of magnetic field at different temperatures [bottom inset of Figure 7.14(a)] shows clear magnetic hysteresis at all temperature below ferrimagnetic ordering. It is important to note that above 20 K the coercive field of the loop decreases drastically as compared to the low temperature hysteresis consistent with the fact that the magnetic structures are different below and above 23 K. From the Curie-Weiss fitting ($\chi = \frac{C}{T - \theta_{CW}}$) of the temperature dependent inverse susceptibility data at 0.1 kOe in the temperature range of 250-390 K, we obtain $\theta_{CW} = -1156$ K indicating that the average magnetic interaction is strongly antiferromagnetic in nature. From the linear fit the obtained effective magnetic moment (μ_{eff}) per formula unit is $10.69 \mu_B$ which is little higher than theoretical value $9.74 \mu_B$.

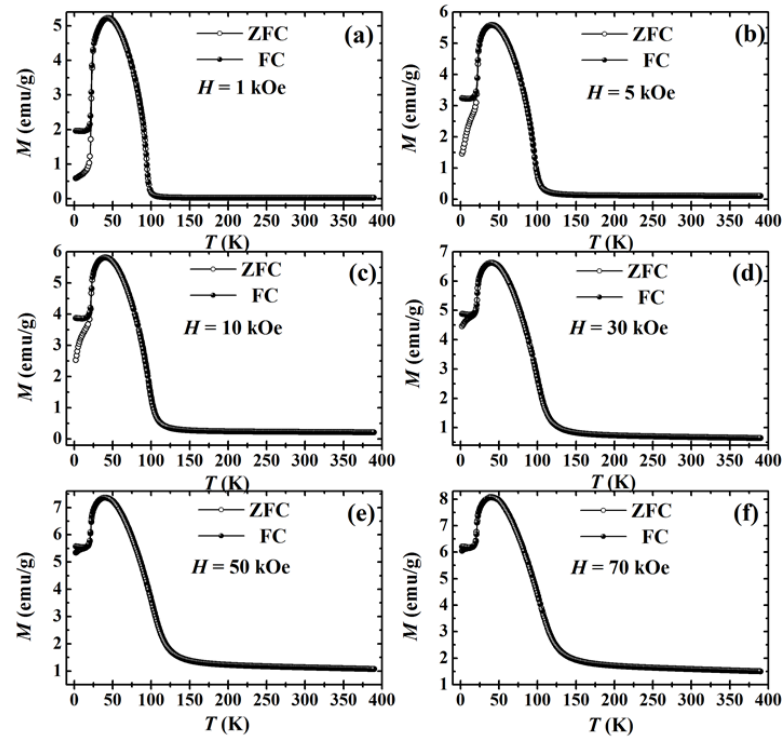


Figure 7.15: (a-f) Temperature dependent dc magnetization data of $\text{LiFeCr}_4\text{O}_8$ under zero-field-cooled (ZFC) and field-cooled (FC) conditions in the presence of various magnetic fields.

Below the magnetostructural transition temperature ($T_{MS} \sim 23$ K) we see a small divergence between ZFC and FC magnetization data in the presence of a magnetic field of 0.1 kOe [Figure 7.14(a)]. With increasing magnetic field the divergence initially increases and then decreases as shown in Figure 7.15. To check whether any glassy state leads to the bifurcation between ZFC and FC magnetization data we have performed additional dc magnetization measurements employing isothermal waiting under ZFC mode below the Néel temperature, because very often the non-equilibrium dynamics of a real spin glass state shows aging, rejuvenation and memory effect [41,42]. From that experiment, we do not observe either any anomalous behavior at the waiting temperature or any difference between the ZFC magnetization data with and without isothermal waiting. Therefore, the occurrence of bifurcation in the low magnetic field indicates the existence of some amount of magnetic frustration which reduces at high magnetic field as a result of changing spin configuration.

7.4.3 Dielectric properties of LiMCr_4O_8 (M = Ga, In, Fe):

7.4.3.1 Dielectric study of $\text{LiGaCr}_4\text{O}_8$ and $\text{LiInCr}_4\text{O}_8$

First, we discuss the temperature dependent dielectric properties for the Ga and In compounds, measured in the temperature range of 7-100 K. For comparison, similar measurements were undertaken on ZnCr_2O_4 which shows a sharp dielectric anomaly in zero magnetic field at the first order antiferromagnetic phase transition ($T_N \sim 13$ K) [inset of Figure 7.16]. The appearance of a dielectric anomaly in the vicinity of the Néel temperature in zero magnetic field has been associated with a magnetostructural coupling induced by a spin Jahn-Teller effect [45]. The temperature dependent dielectric constant, measured in zero magnetic field for $\text{LiGaCr}_4\text{O}_8$ shows a sharp dielectric anomaly at the magnetostructural phase transition temperature ($T_{MS} \sim 14.5$ K) and a broad anomaly in the vicinity of the short-range antiferromagnetic ordering temperature ($T_{SO} \sim 55$ K) [Figure 7.16 (a)]. In the case of $\text{LiInCr}_4\text{O}_8$, dielectric anomalies appear both at the structural phase transition ($T_S \sim 15.1$ K) and spin-gap opening temperature ($T_{SG} \sim 60$ K) where the dielectric anomaly is very sharp [Figure 7.16(b)]. Both Ga and In compounds show anomalies in the temperature dependent dielectric loss data at the above temperatures as shown in the bottom inset of Figures 7.16(a) and 7.16(b) respectively.

It is important to note that the sharp feature of a dielectric anomaly at the spin-gap strongly depends on the synthetic condition. $\text{LiInCr}_4\text{O}_8$ prepared at higher annealing temperature (≥ 1100 °C) as well as repeated heating lead to the loss of Li. In such samples, no dielectric anomaly appears at the spin-gap indicating that dielectric anomaly at the spin-gap is sensitive to Li non-stoichiometry and disorder. Therefore, the present sample was prepared at lower annealing temperature (1050 °C). In this context, we mention here that in a recent paper it has been shown that a broad feature appears in the temperature dependent dielectric data across the onset of spin-gap transition [40].

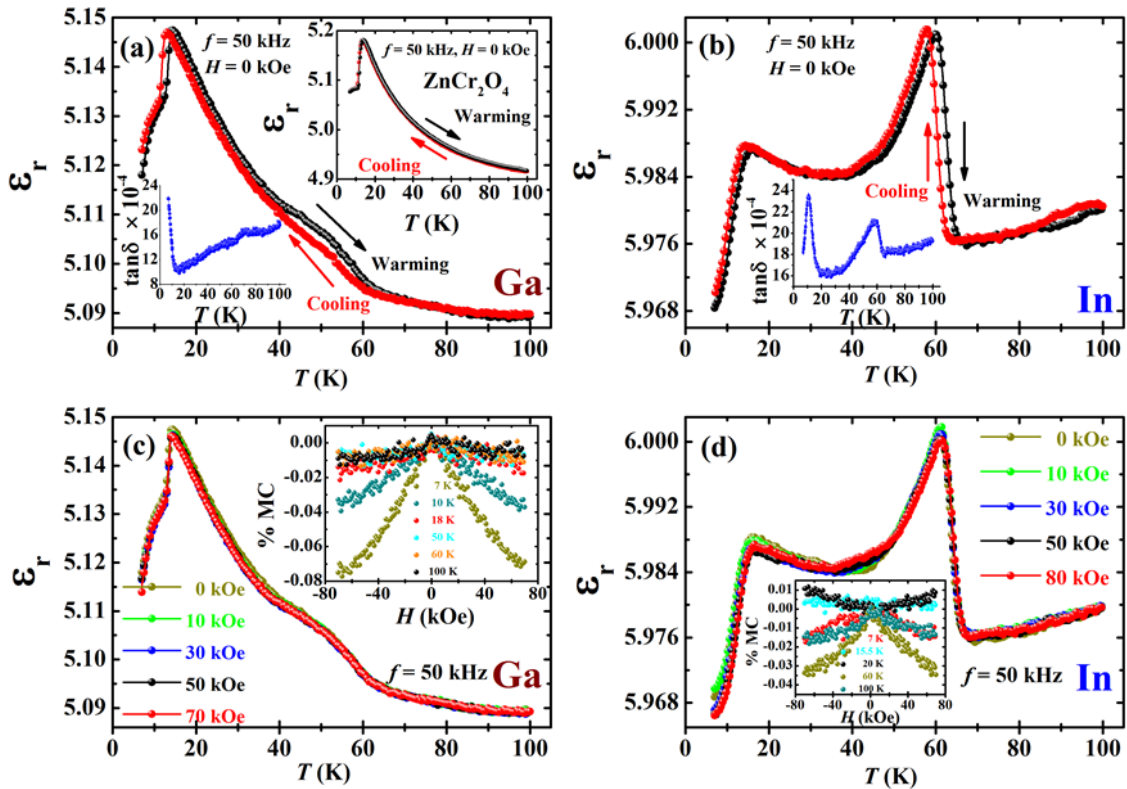


Figure 7.16: (a), (b) Temperature dependence of dielectric constant of $\text{LiGaCr}_4\text{O}_8$ and $\text{LiInCr}_4\text{O}_8$ respectively in zero magnetic fields at 50 kHz. Inset of (a) shows the variation of dielectric constant of ZnCr_2O_4 as a function of temperature in zero magnetic fields at 50 kHz. The bottom inset of (a) and (b) shows the temperature dependent dielectric loss for Ga and In compounds respectively; (c), (d) temperature dependence of dielectric constant of $\text{LiGaCr}_4\text{O}_8$ and $\text{LiInCr}_4\text{O}_8$ respectively in the presence of different magnetic fields at 50 kHz. Insets of (c) and (d) show the magnetic field dependence isothermal magnetocapacitance (%MC) at 50 kHz for the Ga and In compound respectively.

Structural distortion in these compounds at low temperature leads to the coexistence of two crystallographic phases which induces strain in the system due to lattice mismatch [28]. The occurrence of a dielectric anomaly in both compounds in the vicinity of the Néel temperature, in zero magnetic fields, could be attributed to the

combined effect of structural phase coexistence and spin-lattice coupling via a magnetoelastic effect [46,47]. The presence of structural phase coexistence and magnetoelastic effect gives rise to strain which mediates the coupling between magnetization and the dielectric properties. The dielectric anomalies that appeared in the Ga and In compounds do not show frequency dependence. Both the Ga and In compounds show thermal hysteresis in the temperature dependent dielectric data measured across the magnetostructural ($T_{MS} \sim 14.5$ K) and structural phase transition ($T_S \sim 15.1$ K) temperatures respectively, as shown in Figures 7.16(a) and 7.16(b). The occurrence of thermal hysteresis in the temperature dependent dielectric data indicates the first order nature of the phase transition associated with structural distortion. We also observe thermal hysteresis in the temperature dependent dielectric data across the short-range antiferromagnetic ordering ($T_{SO} \sim 55$ K) and the spin-gap opening temperature ($T_{SG} \sim 60$ K) in the Ga and In compounds respectively.

The difference between the dielectric anomalies in Ga and In compounds across T_{SO} or T_{SG} can be understood by considering the Cr_4 breathing distortion, which is unique in these A-site ordered chromate spinels. The breathing factors ($B_f = J/J'$) are 0.1 for $LiInCr_4O_8$ and 0.6 for $LiGaCr_4O_8$ at room temperature, where J and J' correspond to the exchange integral on the large and small Cr_4 tetrahedra respectively [18]. The higher breathing distortion in the In compound gives rise to a pseudogap in the magnetic excitation spectrum [17]. The existence of a gapped state in the In compound, due to stronger breathing distortion, yields an additional contribution over the already existing spin-lattice coupling, thereby enhancing the dielectric anomaly in $LiInCr_4O_8$ at the spin-gap opening temperature ($T_{SG} \sim 60$ K).

Although there is no change in the average structure across the spin gap, it is intriguing to note that, we observe an anomaly in the temperature dependent cell volume of In compound across the spin-gap as well as magnetic and structural transitions as shown in Figure 7.17. The temperature dependent cell volume was modelled with a function of the type $V_0 = V_1 + V_2 \theta_{S1} \text{Coth} \frac{\theta_{S1}}{T}$, where θ_{S1} is the saturation temperature for the thermal expansion of the cubic structure [48]. The volume anomaly indicates a local structural change induced by the opening of spin gap. Conversely, in $LiGaCr_4O_8$, the origin of broad dielectric anomaly that accompanies the

short-range antiferromagnetic ordering ($T_{SO} \sim 55$ K) can only be associated with spin-lattice coupling, due to the weak breathing distortion. The importance of the breathing distortion in inducing a dielectric anomaly in LiMCr_4O_8 ($M = \text{Ga, In}$) at T_{SO} or T_{SG} is further supported by the absence of a dielectric anomaly [inset of Figure 7.16(a)] in the conventional chromate spinel (ZnCr_2O_4) where a breathing distortion is absent due to equivalent Cr-Cr distance. The dielectric anomaly at the spin gap temperature has seldom been reported in the literature. It may be mentioned here that a dielectric anomaly has been observed in NaV_2O_5 at the spin gap opening temperature in the high-frequency region and this anomaly has been attributed to the antiferroelectric charge ordering in the form of a zigzag arrangement of V^{4+} ions [49].

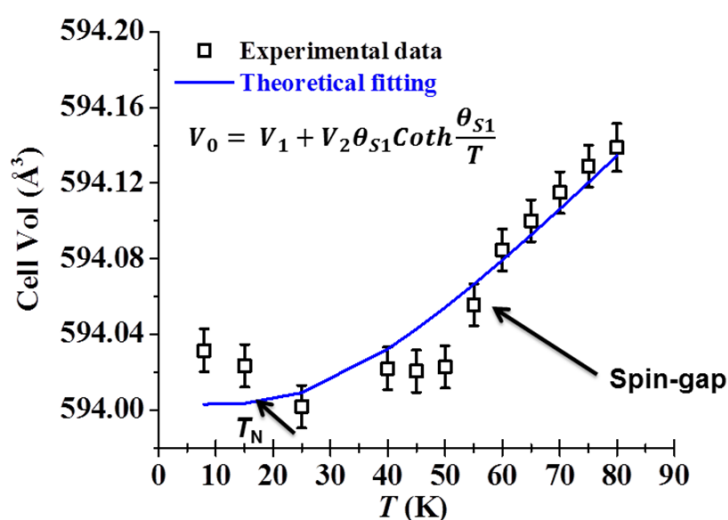


Figure 7.17: Temperature dependent cell volume of In compound fitted with a function of the type $V_0 = V_1 + V_2\theta_{s1}\text{Coth}\frac{\theta_{s1}}{T}$. The experimental data (square symbol) shows a discontinuity from the theoretical fit (blue line) at the spin-gap as well as magnetic and structural transitions (~ 13 - 15 K).

To probe the effect of magnetic field on the dielectric properties of A-site ordered chromate spinel, temperature dependent dielectric constant was measured in the presence of various magnetic fields [Figures 7.16(c) and 7.16(d)]. There is no significant effect of magnetic field on the overall dielectric constant of $\text{LiGaCr}_4\text{O}_8$ except for a small shift of the dielectric peak to the higher temperature with increasing magnetic field, as evident from Figure 7.16(c). Measurement of the isothermal magnetocapacitance (%MC) as a function of magnetic field on the Ga compound shows that below the Néel temperature ($T_N \sim 14.5$ K) the magnetocapacitance (%MC) has reached the maximum value of 0.08% at 7 K and it remains low above the magnetic ordering temperature as shown in the inset of Figure 7.16(c). Application of a magnetic

field has little impact on the dielectric behavior of $\text{LiInCr}_4\text{O}_8$, other than a small shift of both the dielectric peaks to higher temperature with increasing magnetic fields, as shown in Figure 7.16(d). The inset of Figure 7.16(d) illustrates that near the spin-gap opening temperature ($T_{SG} \sim 60$ K) the magnetocapacitance (%MC) reaches a maximum value of 0.04% while it remains almost negligible at other temperatures. The observed values of the magnetocapacitance (%MC) in these two compounds are comparable to those observed in other chromate spinel oxides containing magnetic ions at the A-site [50]. The observed shift in the dielectric peak with magnetic field could be attributed to the coupling between the dielectric response and q -dependent spin-spin correlation where spin-spin correlation, softens the optical phonon frequency giving rise to a shift in the dielectric peak according to the Lyddane-Sachs-Teller relation [51-53].

7.4.3.2 Dielectric study of $\text{LiFeCr}_4\text{O}_8$

Now we will discuss the dielectric properties of $\text{LiFeCr}_4\text{O}_8$. The temperature dependent dielectric data shows three anomalies at 94, 60 and 23 K as illustrated in Figure 7.18. We see a thermal hysteresis across the spin-gap transition ($T_{SG} \sim 60$ K) and magnetostructural transition ($T_{MS} \sim 23$ K) [insets (a) and (b) of Figure 7.18] indicating the first order nature of the phase transition.

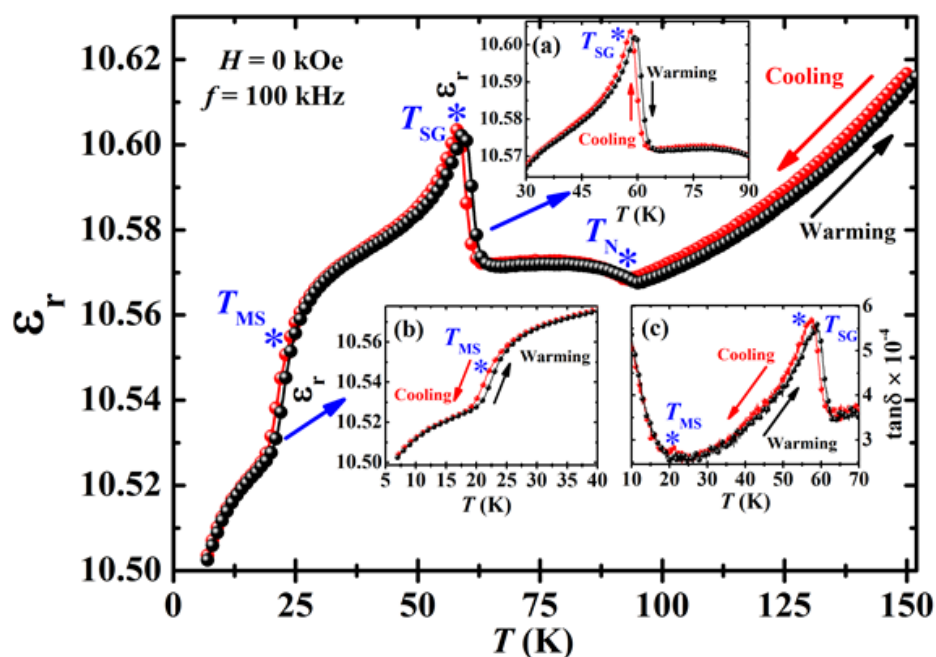


Figure 7.18: Temperature dependence of dielectric constant of $\text{LiFeCr}_4\text{O}_8$ in zero magnetic fields at 100 kHz. Inset (a) and (b) show the zoom in view of thermal hysteresis across the spin-gap state (T_{SG}) and magnetostructural transition (T_{MS}) respectively; inset (c) shows the temperature dependence of dielectric loss in zero magnetic fields at 100 kHz showing thermal hysteresis across T_{SG} and T_{MS} .

A similar thermal hysteresis has been observed at the spin-gap transition temperature of $\text{LiInCr}_4\text{O}_8$ [see Figure 7.16(b)]. Interestingly, temperature dependent dielectric loss also shows two peaks at 23 and 60 K [inset (c) of Figure 7.19] as well as thermal hysteresis across those temperatures indicating that the anomalies in the dielectric data are related to the phase transition.

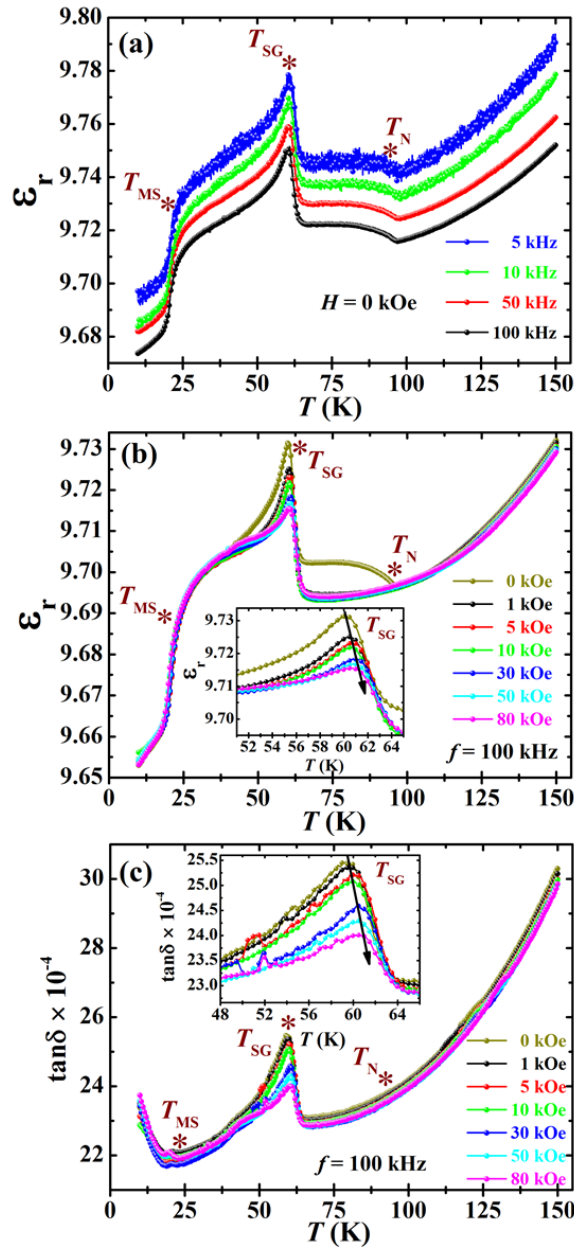


Figure 7.19: (a) Temperature dependence of dielectric constant at various measuring frequency in zero magnetic fields; (b) temperature dependence of dielectric constant and (c) dielectric loss in the presence of different magnetic fields at 100 kHz. Inset of (b) and (c) shows the zoom in view of dielectric constant and loss across $T_{SG} \sim 60$ K respectively.

From Figure 7.19 we observe that the dielectric anomalies do not vary with different measuring frequencies [Figure 7.19(a)] indicating the robust and long range

nature of the phase transitions. To understand the response of dielectric constant to an external magnetic field we have carried out temperature dependent dielectric constant measurement in the presence of different magnetic fields as shown in Figures 7.19(b) and 7.19(c). From this figure, we see find there is a suppression of dielectric anomalies with increasing magnetic field indicating that there is a coupling between the electric polarization and external magnetic field. Moreover, we observe a shift in the dielectric peak at $T_{SG} \sim 60$ K [inset of Figure 7.19(b)] to a higher temperature with increasing magnetic field which could be attributed to the Lyddane-Sachs-Teller effect [51-53] as discussed for the Ga and In compounds. The temperature dependent dielectric loss in the presence of different magnetic fields also shows suppressed feature as well as the shift of loss peak to a higher temperature with increasing magnetic fields [inset of Figure 7.19(c)].

Being observed the effect of magnetic field on the dielectric constant we have investigated the isothermal magnetodielectric effect or magnetocapacitance (% MC) as a function of the magnetic field as shown in Figure 7.20(a) - 7.20(f). From this figure, we observe that there is a magnetodielectric hysteresis with the magnetic field at all temperatures below ferrimagnetic transition. Since below ferrimagnetic ordering temperature there exists isothermal magnetic hysteresis as a function of the magnetic field [Figure 7.20(g) – 7.20(l)] the hysteretic behavior of magnetocapacitance (% MC) could be associated with the magnetization data. Interestingly, we notice that the width of the magnetodielectric hysteresis also changes with changing temperature similar to that happened with the magnetic hysteresis indicating that spin-spin interactions are the driving force for magnetodielectric effect. More surprisingly, we see from Figure 7.20(a) and 7.20(b) that there is a reversal in the direction of magnetodielectric hysteresis as compared to the magnetocapacitance data recorded at $T \geq 23$ K. As we have already mentioned that the magnetic structure of $\text{LiFeCr}_4\text{O}_8$ changes from ferrimagnetic to the complex spin configuration at 23 K, therefore, we believe that the reversal could be associated with the difference in spin structure. The increased width of magnetodielectric hysteresis near the spin-gap state [Figure 7.20(c)] is noteworthy and it could be associated with the increased cation off-centering as a result of stronger breathing distortion facilitating to form the gapped state [54]. Interestingly, it is observed that at 10 K, the trend of change in square magnetization per formula unit

with magnetic field correlates well with the magnetocapacitance change below 7 kOe, while above T_{MS} no such correlation has been observed between %MC and M^2 as evident from Figure 7.21.

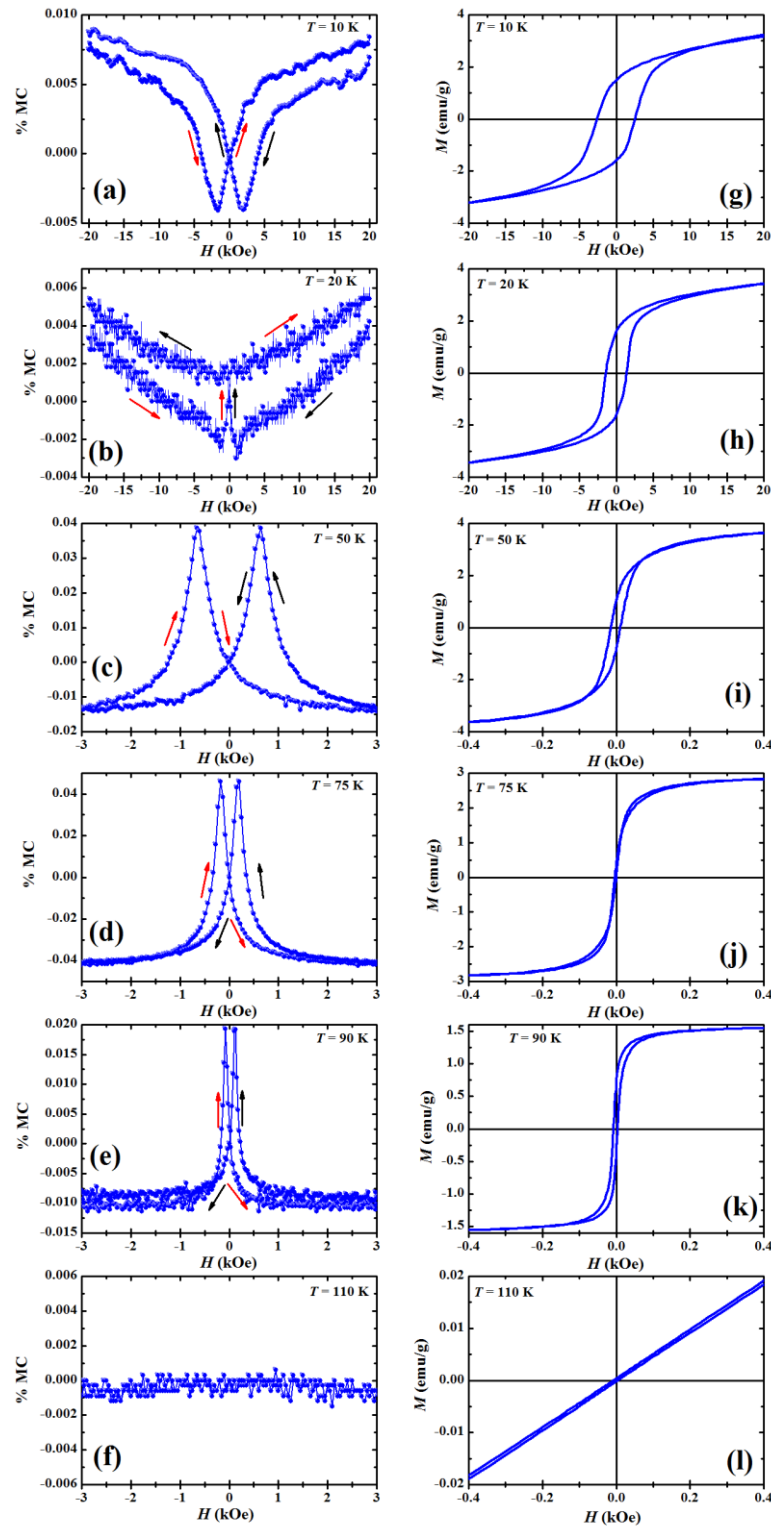


Figure 7.20: (a-f) Magnetocapacitance (%MC) hysteresis and (g-l) isothermal magnetization hysteresis of $\text{LiFeCr}_4\text{O}_8$ as a function of magnetic field at different temperatures.

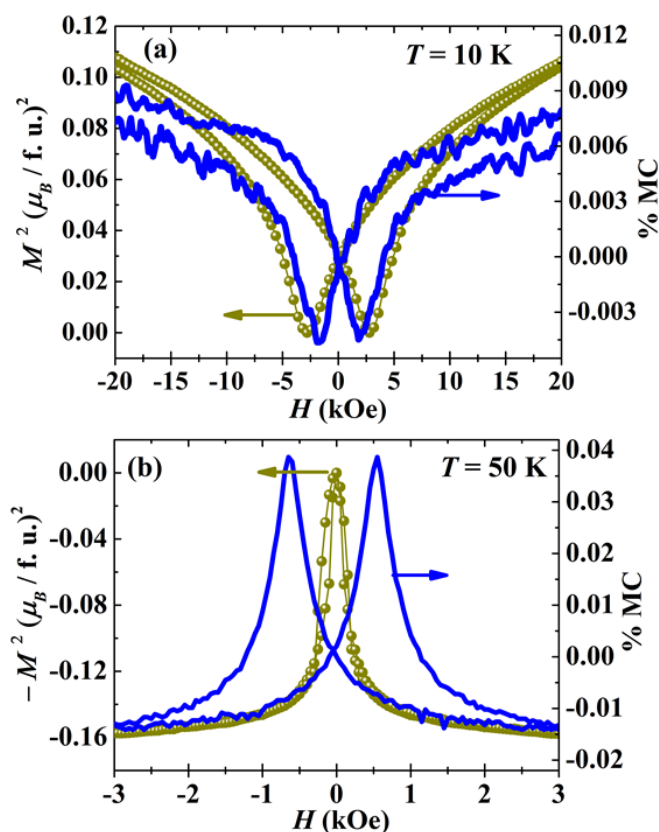


Figure 7.21: The relation between magnetic field-dependent MC (%) and field-dependent square magnetization per formula unit at (a) 10 K and (b) 50 K for $\text{LiFeCr}_4\text{O}_8$.

The dependence of MC (%) on the square magnetization per f.u. below magnetostructural transition ($T_{\text{MS}} \sim 23$ K) could be attributed to the fact that the coupling between spin-spin correlation and lattice distortion becomes stronger due to concurrent change in magnetic and crystallographic structures at T_{MS} . Therefore, based on Figure 7.21(a) it can be inferred that the magnetostructural coupling is the main source of magnetodielectric effect in $\text{LiFeCr}_4\text{O}_8$. On the other hand, above 7 kOe probably the spin structure of the compound changes resulting in weakening of magnetostructural coupling thereby a deviation between field-dependent MC (%) and field-dependent the square magnetization per formula unit is established. Figure 7.21(b) clearly indicates that above magnetostructural transition the coupling between dielectric constant and spin-spin correlation in the collinear ferrimagnetic state is weak. Therefore, no linear scaling behavior between field-dependent MC (%) and field-dependent the square magnetization per formula unit. The dielectric anomaly appeared at 94 K in $\text{LiFeCr}_4\text{O}_8$ is associated with the ferrimagnetic ordering. The occurrence of dielectric anomaly at 23 K, where a concomitant change in crystal and magnetic structures occur through magnetoelastic effect as a result of strong spin-lattice coupling

[15]. It is to be noted that the magnetostructural transition point in the Fe compound is reached from a magnetically ordered state, unlike the Ga or In compound. Despite the fact that $\text{LiFeCr}_4\text{O}_8$ orders magnetically at high temperature (94 K), the magnetic frustration among Cr_4 tetrahedra drives structural transition (23 K) which is accompanied by a change in the magnetic structure. The evolution of dielectric anomalies at the three magnetic transition temperatures as well as the response towards external magnetic field indicates the occurrence of magnetodielectric effect.

7.4.4 Raman spectroscopic study of $\text{LiFeCr}_4\text{O}_8$

Raman measurements have been carried out on $\text{LiFeCr}_4\text{O}_8$ in the temperature range 5-130 K to understand the coupling between spin and lattice modes. The Raman spectrum of $\text{LiFeCr}_4\text{O}_8$ collected at 22 K is shown in Figure 7.22(a). $\text{LiFeCr}_4\text{O}_8$, which consists of LiO_4 , FeO_4 tetrahedra, and CrO_6 octahedra, exhibits a Raman spectrum which is comparable to that of normal spinels. Compared to the Raman spectrum of a spinel structure, few peaks of $\text{LiFeCr}_4\text{O}_8$ have been found to be split into two peaks. For example, the A_1 mode (which corresponds to symmetric Cr-O stretching in the CrO_6 octahedra) is a singlet in the Raman spectra of spinels, has been split into two peaks at 689 and 692 cm^{-1} in $\text{LiFeCr}_4\text{O}_8$ [55]. This could be attributed to the different Cr-O bond lengths present within CrO_6 octahedra. Another prominent Raman peak occurs at ~ 618 cm^{-1} (T_2). Both A_1 and T_2 modes can be attributed to the symmetric stretching of the Cr-O bonds in the CrO_6 octahedra [55]. The temperature dependence of these two modes (692 cm^{-1} and 618 cm^{-1}) is shown in Figure 7.22(b) and 7.22(c) respectively. Usually, frequencies of bond stretching modes increase with a decrease in temperature due to anharmonicity which is the case with the both A_1 and T_2 modes between 130-100K. However, the modes frequencies deviate from the usual anharmonic behavior around T_{MS} , T_{SG} and T_{N} . While lowering the temperature, the Raman mode hardens below T_{MS} and T_{SG} and softens below T_{N} . At T_{N} , the sudden softening of stretching peaks implies that the Cr-O bond length increases probably indicating a release of strain at this point. Since there is an onset of magnetic interactions across these transition temperatures, the anomalous softening/hardening of stretching modes around T_{MS} , T_{SG} and T_{N} can be attributed to spin-phonon coupling [2, 3]. However, the linewidths of the modes which are related to the phonon relaxation times have not shown any observable changes within our experimental resolution, across these transitions. The changes in linewidth

may [56,57] or may not [58] be observed during the spin-phonon coupling. The absence of any changes in linewidth may be attributed to magnetostriction [59]. Nevertheless, the changes observed in the Cr-O stretching modes indicate that all the transitions involve changes in Cr-O bond length which intern indicates that the octahedral distortions play an important role in the magneto-dielectric properties in this material.

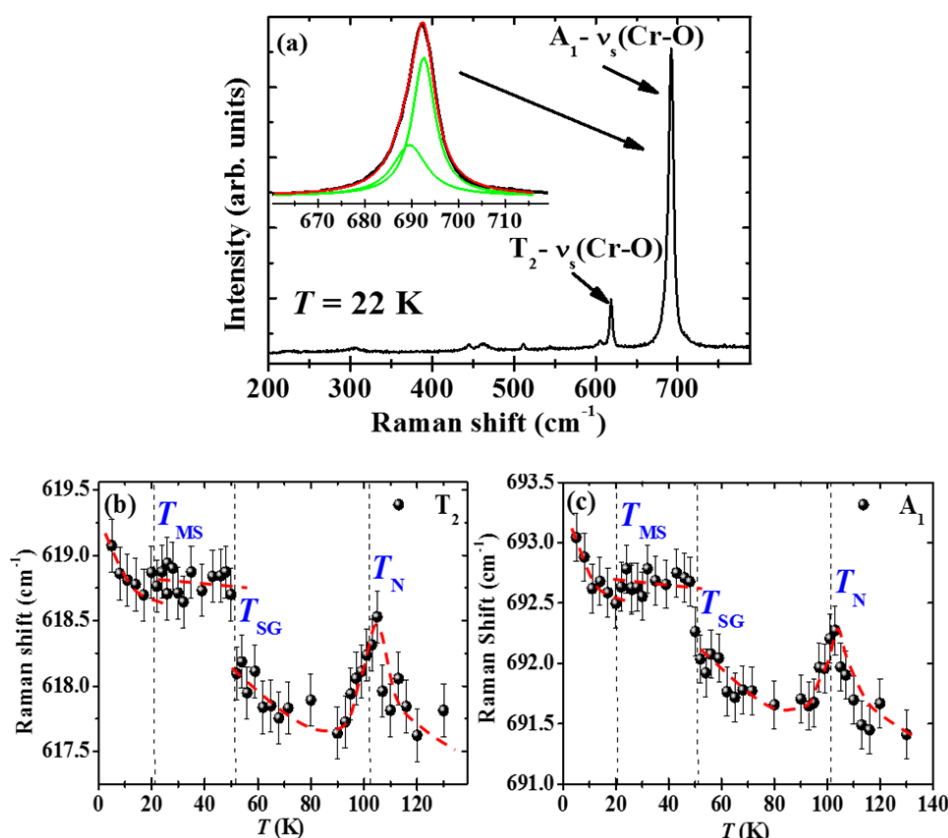


Figure 7.22: (a) Raman spectra of LiFeCr₄O₈ at 22 K. The inset shows the deconvolution of the Cr-O stretching mode (A₁); (b-c) the temperature dependence of the T₂ (left panel) and A₁ (right panel) modes. The dashed lines correspond to the transition temperatures, and the red lines are the guide to the eyes. T_{MS}, T_{SG}, and T_N correspond to the magnetostructural transition, the onset of spin-gap state and Néel transition temperatures respectively.

We have measured the pyroelectric currents of all these compounds (Ga, In and Fe) in zero as well as in the presence of different magnetic field across the aforementioned dielectric anomalies to see whether there exists any polar state or not. However, none of the compounds reveal any pyroelectric peak across those dielectric anomalies. Moreover, since we observe a weak effect of magnetic fields on the dielectric constant of these compounds, therefore, we suggest that the effect of magnetic field in inducing a linear magnetoelectric effect, if any, would be subtle. The absence of linear magnetoelectric polarization is consistent with the observed magnetic structures of LiGaCr₄O₈, which do not allow linear magnetoelectric effect. However since these

crystals are piezoelectric, they should possess second order magnetoelectric effect irrespective of magnetic ordering, which is probably quite small. We also clarify the point that since we do not observe any ferroelectric state based on the temperature dependent pyroelectric measurement, it would be more appropriate to associate these phenomena with magnetodielectric coupling rather than magnetoelectric effect.

7.5 Conclusions

In conclusion, our present investigations clearly demonstrate the magnetodielectric effect in the *A*-site ordered chromate spinel where dielectric anomalies appear in the vicinity of long range as well as short range (or spin-gap) antiferromagnetic ordering temperatures. The origin of a dielectric anomaly in the Ga and In compounds near T_N has been attributed to the combined action of spin Jahn-Teller effect via strong spin-lattice coupling and strain that arises due to structural phase coexistence signifying the role of complex magnetostructural effect. In addition to the already existing spin-lattice interaction, the existence of gapped state enhances the feature of a dielectric anomaly at a higher temperature in the In compound as compared to the Ga compound without any gapped state at higher temperature. In $\text{LiFeCr}_4\text{O}_8$, a unique magnetostructural ground state has been observed where the exchange interaction between the magnetic ions at the *A* and *B* site plays an important role. The origin of magnetodielectric coupling in Fe compound has been attributed to the spin-phonon coupling as evidenced from Raman spectroscopic measurements. Therefore, the introduction of breathing distortion provides additional degrees of freedom in the geometrically frustrated pyrochlore lattice to explore many interesting properties.

Bibliography

- [1] W. Eerenstein, N. D. Mathur, and J. F. Scott, *Nature* **442**, 759 (2006).
- [2] Y. Tokura and S. Seki, *Adv. Mater.* **22**, 1554 (2010).
- [3] J. Scott, *J. Mater. Chem.* **22**, 4567 (2012).
- [4] C. N. R. Rao, A. Sundaresan, and R. Saha, *J. Phys. Chem. Lett.* **3**, 2237 (2012).
- [5] M. C. Kemei, P. T. Barton, S. L. Moffitt, M. W. Gaultois, J. A. Kurzman, R. Seshadri, M. R. Suchomel, and Y.-I. Kim, *J. Phys.: Condens. Matter* **25**, 326001 (2013).

-
- [6] M. Matsuda *et al.*, Phys. Rev. B **75**, 104415 (2007).
- [7] J. B. Goodenough, Phys. Rev. **117**, 1442 (1960).
- [8] D. Wickham and J. Goodenough, Phys. Rev. **115**, 1156 (1959).
- [9] S.-H. Lee, C. Broholm, W. Ratcliff, G. Gasparovic, Q. Huang, T. Kim, and S.-W. Cheong, Nature **418**, 856 (2002).
- [10] A. Ramirez, Annu. Rev. Mater. Sci. **24**, 453 (1994).
- [11] Y. Yamashita and K. Ueda, Phys. Rev. Lett. **85**, 4960 (2000).
- [12] O. Tchernyshyov, R. Moessner, and S. L. Sondhi, Phys. Rev. Lett. **88**, 067203 (2002).
- [13] S. Bordács, D. Varjas, I. Kézsmárki, G. Mihály, L. Baldassarre, A. Abouelsayed, C. A. Kuntscher, K. Ohgushi, and Y. Tokura, Phys. Rev. Lett. **103**, 077205 (2009).
- [14] M. C. Kemei, S. L. Moffitt, L. E. Darago, R. Seshadri, M. R. Suchomel, D. P. Shoemaker, K. Page, and J. Siewenie, Phys. Rev. B **89**, 174410 (2014).
- [15] V. Kocsis, S. Bordács, D. Varjas, K. Penc, A. Abouelsayed, C. A. Kuntscher, K. Ohgushi, Y. Tokura, and I. Kézsmárki, Phys. Rev. B **87**, 064416 (2013).
- [16] S. Lee *et al.*, Nature **451**, 805 (2008).
- [17] G. J. Nilsen, Y. Okamoto, T. Masuda, J. Rodriguez-Carvajal, H. Mutka, T. Hansen, and Z. Hiroi, Phys. Rev. B **91**, 174435 (2015).
- [18] Y. Okamoto, G. J. Nilsen, J. P. Attfield, and Z. Hiroi, Phys. Rev. Lett. **110**, 097203 (2013).
- [19] Y. Tanaka, M. Yoshida, M. Takigawa, Y. Okamoto, and Z. Hiroi, Phys. Rev. Lett. **113**, 227204 (2014).
- [20] N. V. Ter-Oganessian, J. Magn. Mater. **364**, 47 (2014).
- [21] V. P. Sakhnenko and N. V. Ter-Oganessian, J. Phys.: Condens. Matter **24**, 266002 (2012).
- [22] J. Rodríguez-Carvajal, Physica B: Condens. Matter **192**, 55 (1993).
- [23] F. Fauth, I. Peral, C. Popescu, and M. Knapp, Powder Diffr. **28**, S360 (2013).
- [24] F. Fauth, R. Boer, F. Gil-Ortiz, C. Popescu, O. Vallcorba, I. Peral, D. Fullà, J. Benach, and J. Juanhuix, Eur. Phys. J. Plus **130**, 1 (2015).
- [25] K.-D. Liss, B. Hunter, M. Hagen, T. Noakes, and S. Kennedy, Physica B: Condens. Matter **385**, 1010 (2006).
- [26] E. Verwey and E. Heilmann, J. Chem. Phys. **15**, 174 (1947).

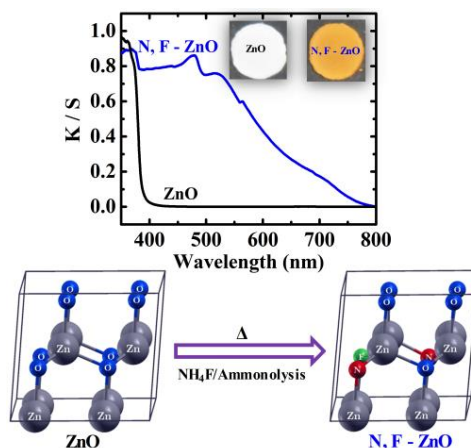
- [27] M. Weil and B. Stöger, *Acta Cryst.* **62**, i199 (2006).
- [28] M. C. Kemei, J. K. Harada, R. Seshadri, and M. R. Suchomel, *Phys. Rev. B* **90**, 064418 (2014).
- [29] E. M. Wheeler, B. Lake, A. N. Islam, M. Reehuis, P. Steffens, T. Guidi, and A. H. Hill, *Phys. Rev. B* **82**, 140406 (2010).
- [30] E. F. Bertaut, *Magnetism*, Eds.: G. T. Rado and H. Shull, (Academic Press, New York, 1963), vol. III, ch. 4.
- [31] H. Martinho *et al.*, *Phys. Rev. B* **64**, 024408 (2001).
- [32] Y. Okamoto, G. J. Nilsen, T. Nakazono, and Z. Hiroi, *J. Phys. Soc. Jpn.* **84**, 043707 (2015).
- [33] I. Bose, *Curr. Sci.* **88**, 62 (2005).
- [34] B. S. Shastry and B. Sutherland, *Physica B* **108**, 1069 (1981).
- [35] O. Tchernyshyov, R. Moessner, and S. Sondhi, *Phys. Rev. B* **66**, 064403 (2002).
- [36] M. Hase, I. Terasaki, and K. Uchinokura, *Phys. Rev. Lett.* **70**, 3651 (1993).
- [37] A. Vasil'ev, M. Markina, and E. Popova, *Low Temperature Phys.* **31**, 203 (2005).
- [38] B. Canals and C. Lacroix, *Phys. Rev. B* **61**, 1149 (2000).
- [39] R. Moessner and J. Chalker, *Phys. Rev. Lett.* **80**, 2929 (1998).
- [40] S. Lee *et al.*, *Phys. Rev. B* **93**, 174402 (2016).
- [41] M. Hakim, M. M. Haque, M. Huq, and P. Nordblad, *Physica B: Condens. Matter* **406**, 48 (2011).
- [42] K. Jonason, E. Vincent, J. Hammann, J. Bouchaud, and P. Nordblad, *Phys. Rev. Lett.* **81**, 3243 (1998).
- [43] H. Ueda, H. A. Katori, H. Mitamura, T. Goto, and H. Takagi, *Phys. Rev. Lett.* **94**, 047202 (2005).
- [44] K. Penc, N. Shannon, and H. Shiba, *Phys. Rev. Lett.* **93**, 197203 (2004).
- [45] I. Kagomiya, H. Sawa, K. Siratori, K. Kohn, M. Toki, Y. Hata, and E. Kita, *Ferroelectrics* **268**, 327 (2002).
- [46] C. Dela Cruz, F. Yen, B. Lorenz, Y. Wang, Y. Sun, M. Gospodinov, and C. Chu, *Phys. Rev. B* **71**, 060407 (2005).
- [47] T. Suzuki and T. Katsufuji, *J. Phys.: Conf. Series* **150**, 042195 (2009).
- [48] B. J. Kennedy, I. Qasim, and K. S. Knight, *J. Phys.: Condens. Matter* **27**, 365401 (2015).

- [49] A. Smirnov, M. Popova, A. Sushkov, S. Golubchik, D. Khomskii, M. Mostovoy, A. Vasil'ev, M. Isobe, and Y. Ueda, *Phys. Rev. B* **59**, 14546 (1999).
- [50] N. Mufti, A. Nugroho, G. Blake, and T. Palstra, *J. Phys.: Condens. Matter* **22**, 075902 (2010).
- [51] T. Katsufuji and H. Takagi, *Phys. Rev. B* **64**, 054415 (2001).
- [52] U. Adem *et al.*, *Phys. Rev. B* **82**, 064406 (2010).
- [53] G. Lawes, A. Ramirez, C. Varma, and M. Subramanian, *Phys. Rev. Lett.* **91**, 257208 (2003).
- [54] T. D. Sparks, M. C. Kemei, P. T. Barton, R. Seshadri, E.-D. Mun, and V. S. Zapf, *Phys. Rev. B* **89**, 024405 (2014).
- [55] Z. M. Stanojević, N. Romčević, and B. Stojanović, *J. Eur. Ceram. Soc.* **27**, 903 (2007).
- [56] P. Mandal, V. S. Bhadram, Y. Sundarayya, C. Narayana, A. Sundaresan, and C. N. R. Rao, *Phys. Rev. Lett.* **107**, 137202 (2011).
- [57] V. S. Bhadram, B. Rajeswaran, A. Sundaresan, and C. Narayana, *Europhys. Lett.* **101**, 17008 (2013).
- [58] E. Granado, A. Garcia, J. Sanjurjo, C. Rettori, I. Torriani, F. Prado, R. Sanchez, A. Caneiro, and S. Oseroff, *Phys. Rev. B* **60**, 11879 (1999).
- [59] A. Nonato, B. Araujo, A. Ayala, A. Maciel, S. Yanez-Vilar, M. Sanchez-Andujar, M. Senaris-Rodriguez, and C. Paschoal, *Appl. Phys. Lett.* **105**, 222902 (2014).

Effect of aliovalent anion (N, F) substitution on the properties of ZnO^*

Summary

ZnO co-substituted with nitrogen and fluorine, has been synthesized for the first time by solid state reaction by using ammonia gas and ammonium fluoride as sources of nitrogen and fluorine respectively. Also, we have synthesized the N, F- co-substituted ZnO by decomposing NH_4ZnF_3 in a flowing ammonia gas medium. From both the synthesis, we have achieved the substitution level of N and F in ZnO lattice in the ratio of 2:1. Substitution of both N and F results in new absorption features in the visible range centered around 500 nm, the edge of this visible band being ~ 1.77 eV. The remarkable change in band gap in N, F- ZnO is reflected in the bright orange color compared to unsubstituted ZnO, which is white in color with the corresponding band gap of ~ 3.4 eV. The reduction in the band gap leads to the increment of dielectric constant of N, F- ZnO as compared to ZnO by two to three-fold. Interestingly, both N, F- ZnO prepared by different routes show the occurrence of room temperature ferromagnetism which is a universal feature of nonmagnetic nanoparticles.



8.1 Introduction

ZnO is one of the foremost and simple material which finds applications in diversified directions. It finds applications in spintronics [1], transparent conducting oxides [2], laser diodes, light emitting diodes [3], transparent thin film transistors [4], liquid crystal displays [5], field emitters [6], medicine [7,8], pigment [9], ceramic industry [10] and many more area [11]. ZnO crystallizes in two structures namely, hexagonal wurtzite ($P6_3mc$) and cubic zinc-blende ($F\bar{4}3m$). Hexagonal wurtzite structure is the most stable form of the ambient condition, and the cubic zinc-blende is stable in a thin film form of ZnO grown on a cubic substrate. At ~ 10 GPa pressure ZnO takes the rock salt configuration ($Fm\bar{3}m$) [12]. The Zn-O bond is highly ionic in nature which makes the bond polar, and it shows piezoelectric property [11]. ZnO is an *n*-type semiconductor with a direct band gap of 3.37 eV and a high concentration of native defects such as oxygen vacancies and zinc interstitials [13]. The existence of high band gap allows it to withstand high electrical voltage and also useful in high-temperature operation. The wide band gap as well as high abundance, nontoxicity, high chemical and photostability makes ZnO an ideal candidate as a catalyst. However, unfortunately, it cannot be used in the visible region of the solar spectrum. Therefore, the band structure of ZnO has been engineered in many different ways to make it useful in the visible region.

It has been a common trend for a long time to substitute the cations in metal oxides to modify the electronic structure thereby tuning the related physical properties [12]. However, such efforts show marginal changes in the electronic structure and hence exhibit a limited effect on the physical properties. Also, separate strategy to substitute the anions of metal oxides or chalcogenides with the isovalent anion has also been adopted to achieve the same goal [14]. The second strategy is found to be more successful because isovalent anion substitution affects the valence band markedly thereby facilitating to modify the electronic structure. There have been efforts to substitute ZnO with other elements to modify its electronic properties [15-21]. In particular, nitrogen substitution brings about significant changes in the Raman spectrum [22-24] and affects the band gap as well as photocatalytic activity [25]. Fluorine substitution marginally changes the electronic properties because halogen atoms give rise to deep-lying levels [20,21]. On the other hand, nitrogen substitution in TiO₂ extends the absorption band to the visible region and creates a band top of the valence

band thereby narrowing the band gap. Fluorine substitution in TiO_2 is also found to be less effective in altering the band gap which lies in the ultraviolet region.

Furthermore doping with nitrogen atom gives rise to oxygen vacancies which give rise to room temperature ferromagnetism in nanoparticles and shows the reduction in band gap suitable for the photocatalytic activity. On the other hand, the oxygen vacancy created from the nitrogen doping also facilitates electron-hole recombination which is a major obstacle for reducing the efficiency of photocatalytic activity. Although the p orbital of fluorine is lower in energy thereby not affecting the band gap of metal oxides, but fluorine doping reduces the recombination of photogenerated electrons and holes due to strong electron withdrawing ability of M-F group present on the surface of fluorine doped metal oxides. Fluorine doped metal oxides are catalytically active only in the ultraviolet region. Therefore, the combination of nitrogen and fluorine could be used to recover one's disadvantage in exchange for others advantage or vice-versa. With this motivation co-substitution of aliovalent anions in metal oxides is found to be one of the most successful strategies. It is because one N^{3-} and one F^- are equivalent to two oxide ions. Moreover N^{3-} , O^{2-} and F^- are isoelectronic and have similar ionic radii. Therefore the ionic radius of O^{2-} is the average of the radii of N^{3-} and F^- . The aliovalent anion substitution in TiO_2 improves the photocatalytic activity significantly due to greater absorption of visible radiation [26]. Aliovalent N, F- co-substitution also affects the magnetic properties of antiferromagnetic-magnetoelectric Cr_2O_3 [27], ferroelectric properties of BaTiO_3 significantly [28].

8.2 Scope of the present investigation

In most of the studies reported so far, the concentrations of N and F in either N- ZnO or F-ZnO have been small. There was no report on the experimental study of the effects of co-substitution of nitrogen and fluorine in ZnO. A theoretical study has predicted the appearance of a sharp peak in the electronic function in the low-energy region [29]. We have synthesized ZnO substituted with both N and F (N, F- ZnO) for the first time by two independent methods and have investigated their properties along with those of ZnO substituted with N or F alone [30]. In one method of preparation, nanoparticles of ZnO were used as the starting material, whereas the second approach involves the

decomposition of NH_4ZnF_3 under suitable conditions. A remarkable property of N, F-ZnO is found to be its bright orange color and the associated long-wavelength visible absorption centered around 500 nm, the edge of this visible band being ~ 1.77 eV [30]. Furthermore N, F-co-substituted ZnO showed reduced oxygen vacancy concentration and increased dielectric constant. The present study also indicates that the presence of fluorine enhances the effect of nitrogen substitution which helps in the reduction of the band gap. The combination of electrostatic and covalent interactions is the stabilizing factor for O-Zn-N/F ordering. First-principles calculations shed light on the understanding of electronic structures and properties of N, F- co-substituted ZnO.

8.3 Experimental details

We have prepared ZnO nanoparticles (NP) by mixing zinc acetate and potassium hydroxide and heated at 60°C for 2 hrs. We heated the so obtained ZnO nanoparticles in flowing ammonia gas at 600°C for 2 hrs to obtain N- ZnO. Heating with ammonium fluoride in air at 600°C for 2 hrs yielded F- ZnO. N, F- co-substituted ZnO was prepared by heating the mixture of ZnO-NP and NH_4F in flowing ammonia gas at 600°C for 2 hrs, followed by annealing at 400°C for 2 hrs in air. We also prepared the F-ZnO and N, F- ZnO by the decomposition of NH_4ZnF_3 . To prepare the NH_4ZnF_3 , commercially available ZnO was mixed with NH_5F_2 and heated at 100°C for 20 hrs followed by 150°C for 24 hrs. Phase pure NH_4ZnF_3 was heated in air at 350°C for 3 hrs to obtain F-ZnO and in flowing NH_3 at 600°C for 2 hrs followed by annealing in air at 400°C for 2 hrs to obtain N, F- ZnO. To check the phase purities of all the unsubstituted ZnO as well as N, F- substituted ZnO samples we recorded x-ray diffraction data with a Bruker D8 Advance x-ray diffractometer. We used a software package FULLPROF suite for performing Le Bail fitting of the XRD patterns to obtain the lattice parameters [31]. X-ray photoelectron (XP) spectra were recorded in an Omicron Nanotechnology Spectrometer with the Mg-K_α (1253.6 eV) as x-ray source to analyze the composition of the samples. Transmission electron microscopy (TEM) images were obtained in JEOL JEM-3010, fitted with Gatan CCD camera operating at an accelerating voltage of 300 kV. We recorded Raman spectra on powdered samples using a LabRAM HR 800 high-resolution Raman spectrometer (HORIBA-Jobin Yvon) in the presence of Ar ion laser (514.5 nm). UV-Vis absorption spectra were recorded using a Perkin-Elmer Lambda 650 (UV/VIS/NIR spectrometer) and PL measurements

were carried out with a Horiba Jobin Yvon Spectrometer (iHR 320) at room temperature. DC magnetization measurements were carried out at room temperature using a Superconducting Quantum Interference Device Magnetometer (SQUID, MPMS3, Quantum Design, USA).

8.4 Results and discussion

8.4.1 X-ray diffraction:

X-ray diffraction data of the N-, F- and N, F- co-substituted ZnO samples correspond to the hexagonal wurtzite structure as can be seen from the XRD patterns in Figure 8.1. Compared to pure ZnO [$a = 3.2486$ (2) Å; $c = 5.2031$ (3) Å], there is a decrease in the cell parameters in both N-ZnO [$a = 3.2464$ (2) Å; $c = 5.1998$ (4) Å] and F-ZnO [$a = 3.2456$ (6) Å; $c = 5.1995$ (10) Å] prepared by the nanoparticle route. The N, F- co-substituted ZnO shows even a greater decrease in the lattice parameters [$a = 3.2355$ (7) Å; $c = 5.1879$ (10) Å]. The lattice parameters of the samples prepared by the complex (NH_4ZnF_3) decomposition route are $a = 3.2541$ (12) Å; $c = 5.2137$ (20) Å for F-ZnO, and $a = 3.2456$ (4) Å; $c = 5.2014$ (6) Å for N, F- ZnO. The crystallite sizes of the samples obtained by the nanoparticle route calculated from the Scherrer formula are 17 (ZnO), 30 (N-ZnO), 30 (F-ZnO) and 27 (N, F- ZnO) nm.

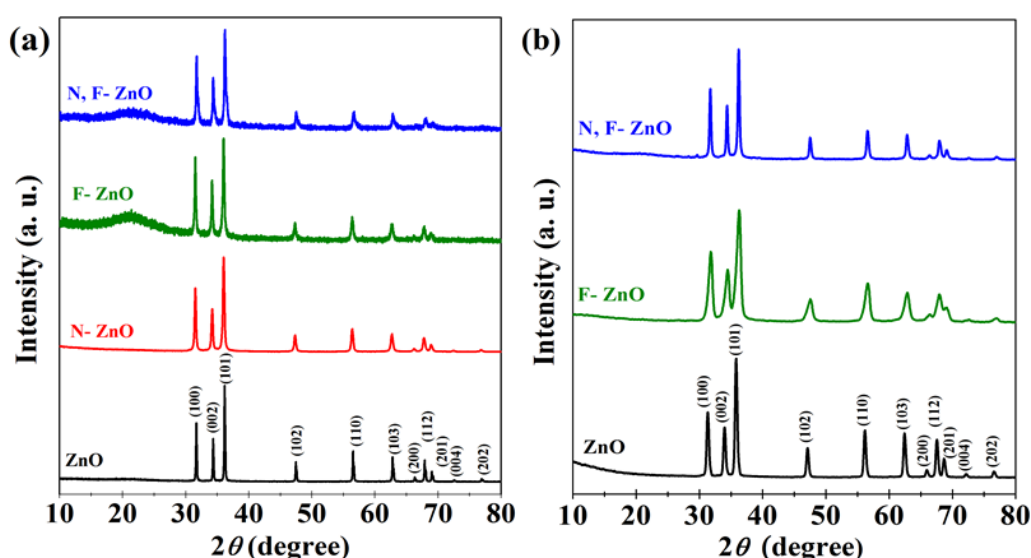


Figure 8.1: XRD patterns of ZnO and anion-substituted ZnO prepared by the (a) nanoparticle and (b) complex decomposition routes respectively.

In the case of samples obtained by the complex decomposition route, the crystallite sizes are 12 (F-ZnO) and 33 (N, F- ZnO) nm. The decrease in crystallite size

of F-ZnO is due to the increasing amount of F atoms occupying the interstitial site of ZnO resulting in a large density of dislocations [32].

8.4.2 X-ray photoelectron and IR spectroscopy:

To analyze the composition of N-, F- and N, F- co-substituted ZnO samples prepared by the two routes, they were subjected to x-ray photoelectron (XP) spectroscopic investigations. The F signals of F-ZnO prepared by nanoparticle and complex decomposition routes appear at 687.9 and 687.6 eV respectively as shown in Figures 8.2(a) and 8.2(b). The co-substituted sample prepared by the complex decomposition route shows the F 1s signal as an asymmetric peak centered at 687.1 eV which we could deconvolute into two peaks, centered at 685.3 and 688.2 eV while the F 1s signal for N, F- ZnO obtained by the nanoparticle route appears at 685.4 eV. The F 1s peak at the lower binding energy arises due to O-Zn-F while the peak at the higher energy originating due to interstitial F. It seems that substitutional fluorine is favored in the presence of nitrogen as evident from the XP spectra. From the spectra, we see that F 1s peak in N, F- ZnO appears at a lower binding energy compared to the F 1s peak position in F-ZnO.

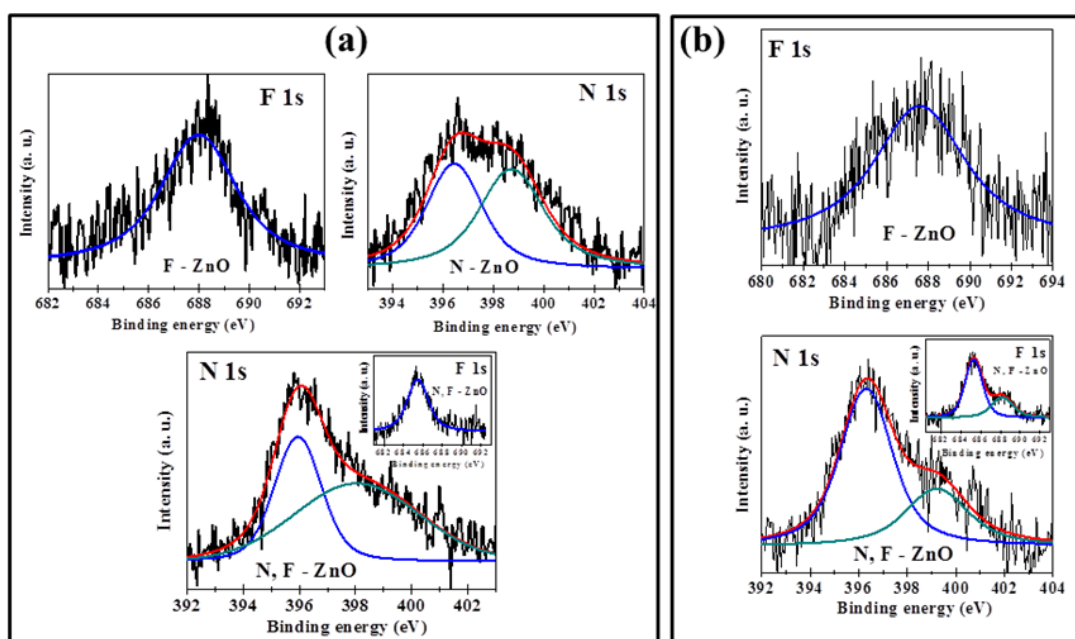


Figure 8.2: X-ray photoelectron spectra of ZnO and anion-substituted ZnO prepared by the (a) nanoparticle and (b) complex decomposition routes respectively.

N- ZnO sample synthesized by the nanoparticle route show a broad feature centered at 398.5 eV which we could deconvolute into peaks centered at 398.7 and

396.4 eV as shown in Figure 8.2(a). We assign the N 1s peak at the lower binding energy to the substitution of nitrogen at the oxygen site (O-Zn-N) [33]. The peak at higher binding energy to the N-H group located at the oxygen site or surface [15] which decreases in intensity on annealing in air at 400 °C as shown in Figure 8.3.

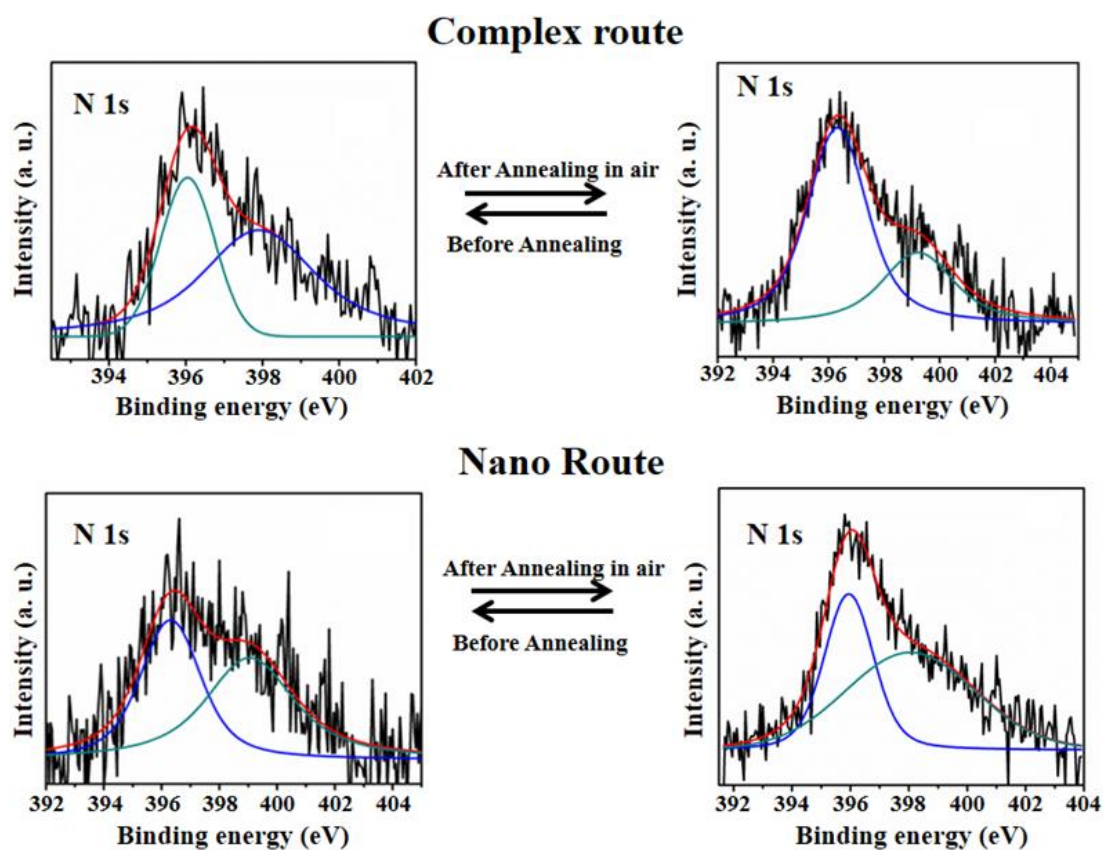


Figure 8.3: Comparison of N 1s peak intensity in the XP spectra of N, F- ZnO samples before and after annealing in air. We show the N, F- ZnO samples prepared by the complex decomposition and nanoparticle routes.

We have not heated the sample to a high temperature to avoid damaging the sample. We have also confirmed the presence of the N-H species from IR spectroscopy which shows a band at 3440 cm^{-1} due to N-H stretching as shown in Figure 8.4. N, F-co-substituted ZnO obtained by the nanoparticle route shows the N signals at 398.2 and 395.9 eV. N, F- ZnO prepared by complex route shows similar two N 1s peaks in the XP spectra. We also see that in the case of F 1s peak which appears at higher binding energy associated with the interstitial F atoms that decrease in intensity on annealing in the air [Figure 8.5]. We have calculated the nitrogen or fluorine contents of the samples only based on the signals due to nitrogen or fluorine substituted at the oxygen site (O-Zn-N/F).

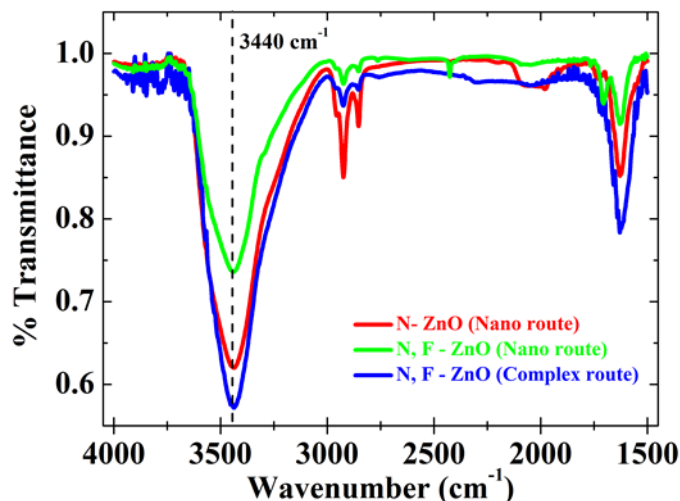


Figure 8.4: IR spectra of N- ZnO and N, F- ZnO samples prepared by the nanoparticle and complex decomposition routes.

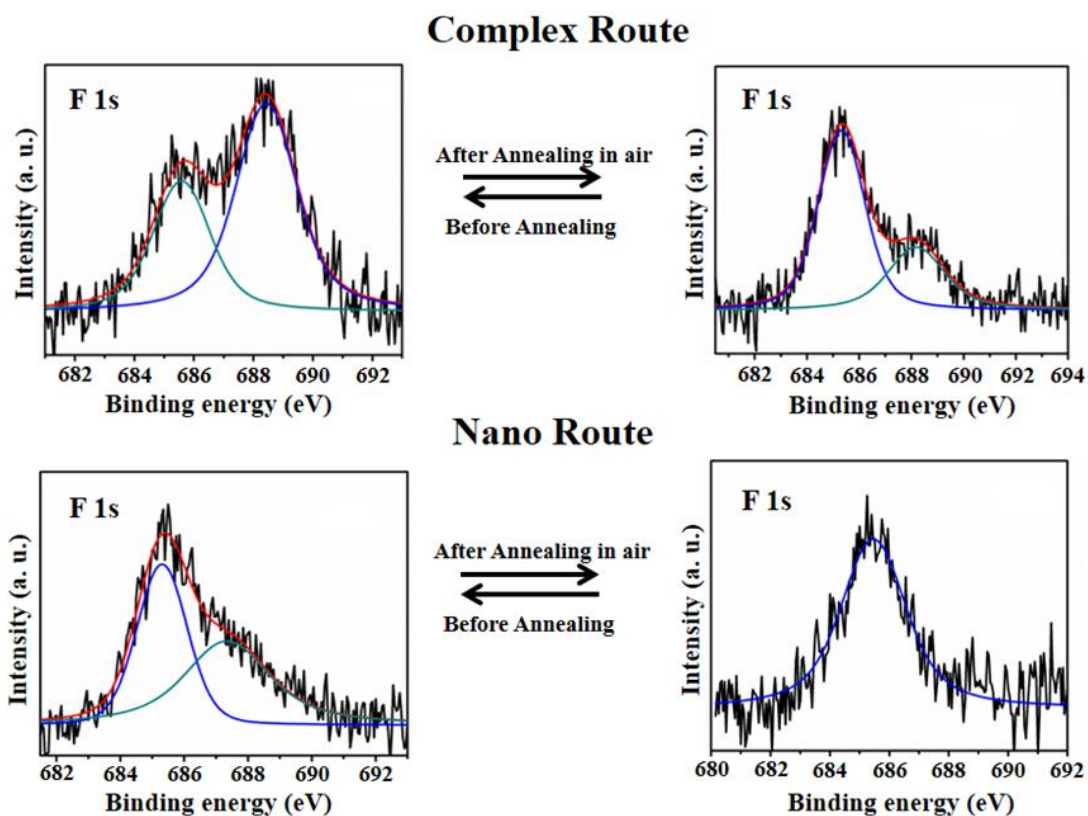


Figure 8.5: Comparison of F 1s peak intensity in the XP spectra of N, F- ZnO samples before and after annealing in air. We present the N, F- ZnO samples prepared by complex decomposition, and nanoparticle routes.

The compositions (in atomic percent) of the samples obtained by the nanoparticle route are N- ZnO (13% N), F- ZnO (14% F), N, F- ZnO (17%N, 9%F). The higher concentration of N in N, F- co-substituted ZnO compared to N- ZnO is due to the presence of fluorine [29]. The compositions of the samples prepared by the complex decomposition route are F- ZnO (20% F) and N, F- ZnO (24% N, 12% F).

8.4.3 Raman spectroscopy:

In Figure 8.6(a), we show the room-temperature Raman spectra of the various samples prepared by the nanoparticle route. F- ZnO shows no significant changes in the Raman spectrum compared to that of ZnO. In N- ZnO nitrogen related Raman bands appear at 272, 505, 575 and 638 cm^{-1} [22-24]. These vibrational modes occur in ZnO co-substituted with N and F along with the phonon modes due to ZnO, confirming the incorporation of nitrogen. The Raman spectra of N, F- ZnO and other samples prepared by the complex decomposition route show similar features as shown in Figure 8.6(b).

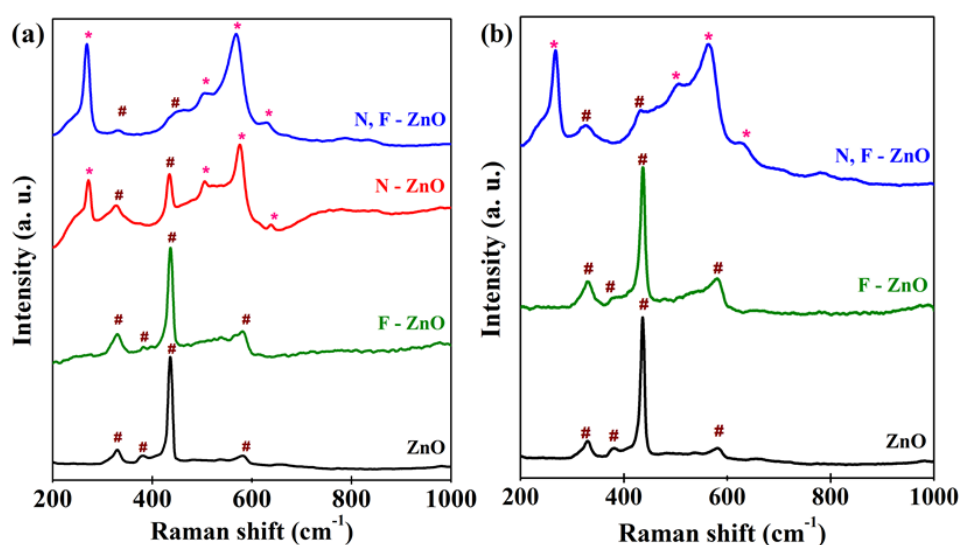


Figure 8.6: Raman spectra of ZnO and anion-substituted ZnO prepared by the (a) nanoparticle and (b) complex decomposition routes respectively.

8.4.4 UV-Visible, Photoluminescence and Electron Energy Loss Spectroscopy (EELS):

The chemical bonds of the constituent elements present in the structure highly influence the optical band gap of material. Substitution of F in ZnO prepared by the nanoparticle route has negligible effect on the UV absorption spectrum showing band-edge absorption at 3.04 eV, compared to pure ZnO at 3.21 eV [Figure 8.7(a)]. N substitution in ZnO also shows a similar feature with the band-edge absorption at 3 eV. Substitution of both N and F results in new absorption features in the visible range centered around 500 nm, the edge of this visible band being around 1.77 eV.

We calculate the band gap of both direct and indirect semiconductor by extrapolating the absorption edge onto the energy axis (x). The $[F(R)hv]^2$ versus hv plot

for a direct transition (in case of ZnO) and the $[F(R)hv]^{1/2}$ versus hv plot for an indirect transition, where $F(R)$ is the Kubelka - Munk (K-M) function $[F(R) = \frac{K}{S} = \frac{(1-R)^2}{2R}]$, $hv = \frac{1240}{\lambda}$ eV is the photon energy, K is the absorption coefficient, S is the scattering coefficient, R is the reflectance, λ is the wavelength (nm). The empirical relation in the parenthesis is often used to convert the reflectance data into absorbance. The value of hv extrapolated to $F(R) = 0$ gives an absorption energy, which corresponds to a band gap E_g [34].

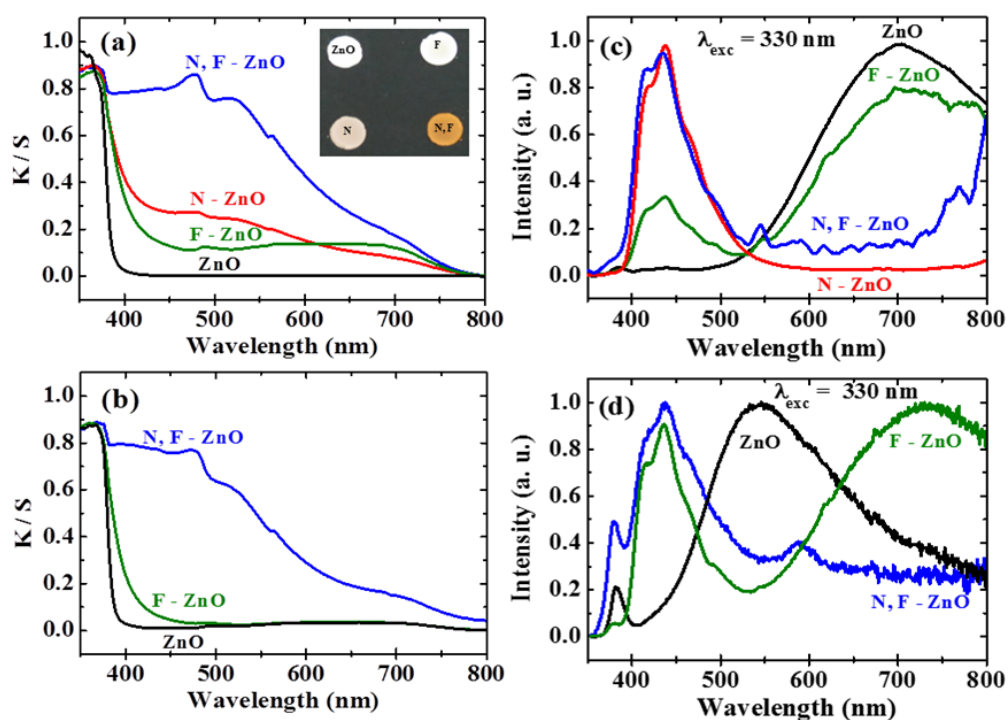


Figure 8.7: (a), (b) UV-Vis spectra of ZnO and anion-substituted ZnO prepared by the nanoparticle and complex decomposition routes respectively. Inset of (a) shows the color of the samples in visible light. (c), (d) PL spectra of ZnO and anion-substituted ZnO prepared by the nanoparticle and complex decomposition route respectively.

The absorption spectra of the samples obtained by complex route [Figure 8.7(b)] are similar to those achieved by the nanoparticle route. The long-wavelength absorption in the visible region upon N, F co-substitution in ZnO causes a change in the color of ZnO from white to bright orange as shown in the inset of Figure 8.7(a). N- ZnO has salmon color while F- ZnO is pale yellow. Electron energy loss spectra (EELS) also demonstrate the presence of local energy states at ~ 1.73 eV corresponding to the optical absorption bands of N, F- ZnO as shown in Figure 8.8 (a). In addition to the characteristics band gap of ZnO at ~ 3.4 eV [Figure 8.8(b)] we observe another two states at ~ 2.18 and 2.68 eV associated with the oxygen vacancy or defect-related states.

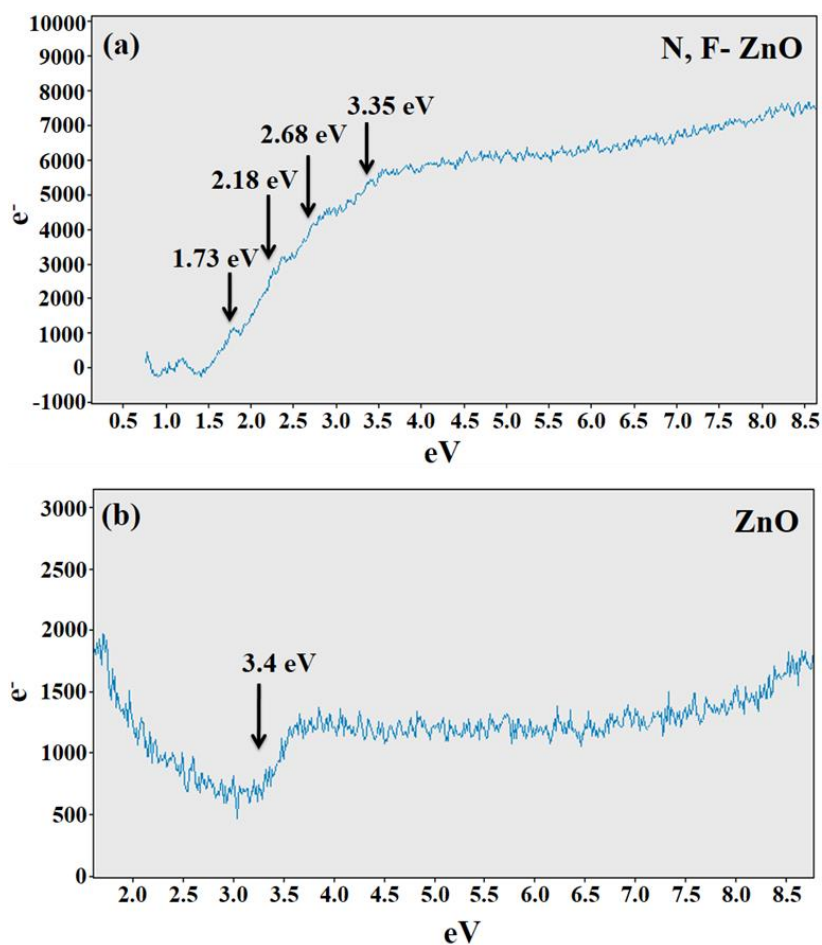


Figure 8.8: EELS data of (a) pure ZnO nanoparticles and (b) N, F- ZnO prepared by the nanoparticle route at room temperature showing the existence of local energy states at different energy.

Photoluminescence (PL) spectroscopy is very much useful to study the defects in oxides. In Figures 8.7(c) and 8.7(d), we show the PL spectra at an excitation wavelength of 330 nm for the N-, F- and N, F- co-substituted samples prepared by the nanoparticle and complex decomposition routes respectively. The PL spectrum shows a weak band-edge emission at 384 nm and a major visible emission at ~ 700 nm due to electron transfer from the singly ionized oxygen vacancies to the photoexcited hole [35]. Both N- and F-substituted ZnO show emission bands at 419 and 438 nm, ascribed to the presence of Zn interstitials [36]. N substitution in ZnO wipes out the emission band at ~ 700 nm due to oxygen vacancies, but F substitution does not [Figure 8.7(c)]. The N, F- co-substituted sample shows peaks in the 410-450 nm range, but almost no absorption around 700 nm. The samples prepared by the complex decomposition route show similar features [Figure 8.7(d)]. From this figure, it is clear that co-substitution with N and F drastically reduces the emission band at ~ 540 nm in ZnO. The defects related band in the emission spectra of ZnO originates from the transition between the

electron near conduction band and the deeply trapped hole sitting at the vacant oxygen center having no electron.

8.4.5 Isothermal magnetization data:

Room temperature ferromagnetism is a universal feature of otherwise non-magnetic inorganic nanoparticles [37,38]. The origin of the ferromagnetism has a connection to the presence of defects such as cation or anion vacancies in the nanoparticles.

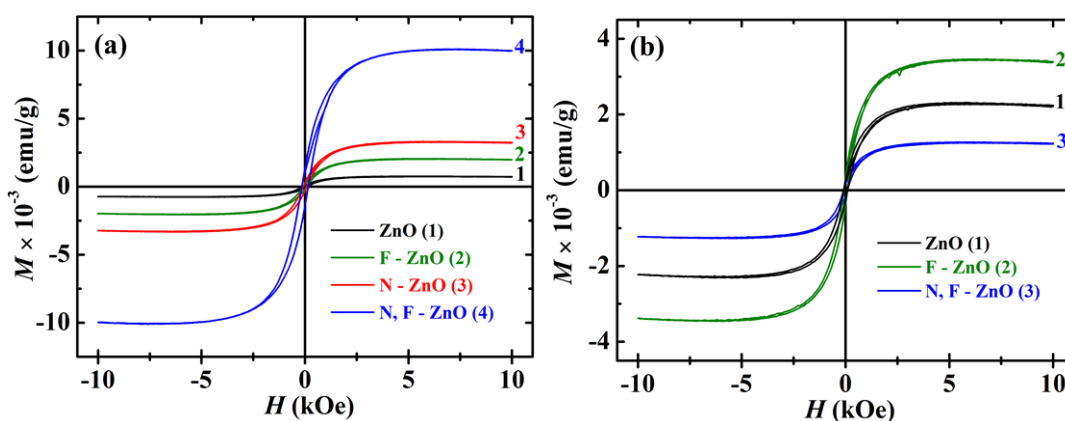


Figure 8.9: Isothermal magnetic hysteresis, $M(H)$, of ZnO and anion-substituted ZnO at room temperature prepared by the (a) nanoparticle and (b) complex decomposition routes respectively.

In Figure 8.9 we show the room temperature magnetization data for ZnO and anion substituted ZnO. We observe that all the samples show saturated magnetic hysteresis, $M(H)$, at room temperature indicating the occurrence of room temperature ferromagnetism. From this figure, we find that saturation magnetization value of N, F - ZnO is relatively lower in the sample prepared by complex decomposition route ($M_S = 0.001$ emu/g) than that obtained from the nanoparticle path ($M_S = 0.01$ emu/g). This result indicates that the defects associated with the N-, F-, co-substitution and particle size effects are relatively less in the N, F- ZnO synthesized by the complex decomposition route than that prepared by the nanoparticle path. This observation is consistent with the PL study.

The observed magnetization data on the samples prepared by the nanoparticle route is also consistent with the N and F compositions obtained from XPS. Since our co-substituted sample contains excess N as compared to F (N: F = 2: 1), therefore that will lead to the creation of oxygen vacancy. Therefore, the gradual increase of saturation magnetization [Figure 8.9(a)] with the introduction of anion substituent could be attributed to the increasing vacancy generated due to inequivalent numbers of N and

F in the sample. Of course in all the samples other cation defects (Zn interstitials) and size effects will also contribute into the ferromagnetism. Here unsubstituted ZnO nanoparticles show the lowest value of saturation magnetization because the as-prepared sample was annealed at 600 °C thereby reducing the defect states and increasing the agglomeration. In Figure 8.10 we show the TEM images of unsubstituted and anion substituted ZnO samples prepared by the nanoparticle route. From the TEM image, it is seen that substitution of anion increases particle agglomeration because of high synthesis temperature (600 °C). The average crystallite size of the anion substituted ZnO is ~ 30 nm, which is consistent with the XRD results.

On the other hand, in the samples prepared by the complex decomposition route we observe that F substitution enhances the saturation magnetization as compared to ZnO indicating that F substitution creates oxygen vacancy. However, in N, F- ZnO the saturation magnetization decreases which mean that there is a reduction in oxygen vacancy related states which is in agreement with the PL study [see Figure 8.7(d)]. Therefore, the study of magnetization data and PL spectra is extremely useful to have information on the defect-related states.

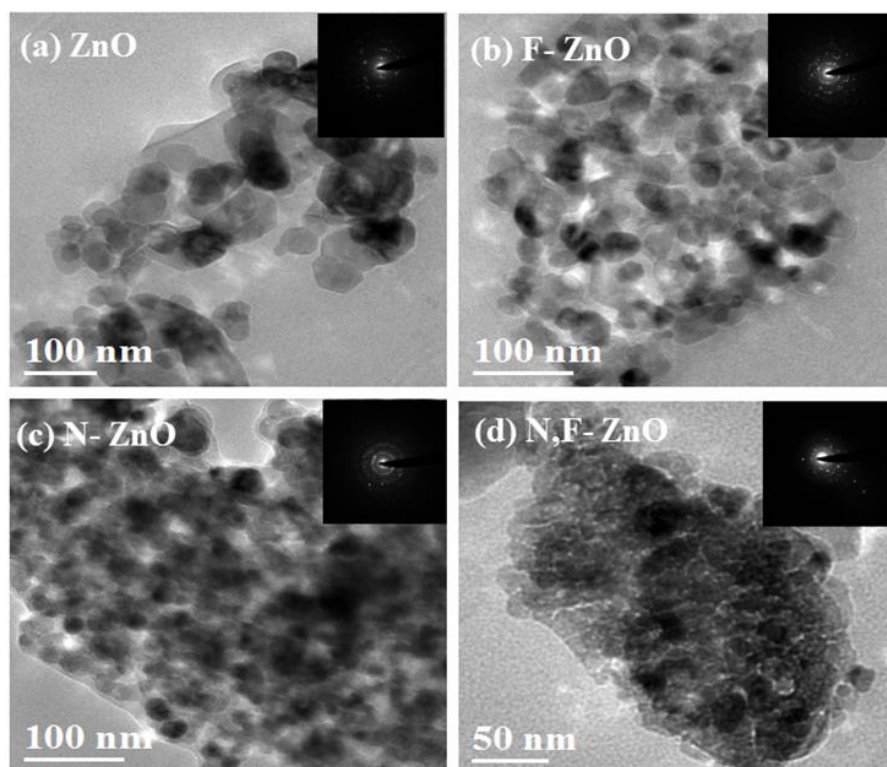


Figure 8.10: TEM images of (a) ZnO nanoparticles annealed at 600 °C, (b) F- ZnO, (c) N- ZnO and (d) N, F- ZnO prepared by the nanoparticle route. The inset shows the electron diffraction (ED) pattern of the respective samples.

8.4.6 Important interpretations from first-principles calculations:

First-principles calculations carried out by Waghmare *et al.* [30] provide significant microscopic insight on the stability of anion co-substitution and electronic structures of N, F- ZnO. The main findings are:

- (1) The analysis of the energetics of F- ZnO, N- ZnO, and N, F- ZnO reveals that co-substitution of N and F is preferable over individual substitution with N or F, with a lowering of energy by 1.97 eV. Further substitution of N in N, F- ZnO is also favorable with a lowering of energy by 0.61 eV.
- (2) The energies of distinct chemically ordered configurations of N, F- ZnO reveals that, N and F preferentially occupy nearest neighbor sites bonded via Zn^{2+} cation. Secondly, configurations with N anions occupying the nearest neighbor sites are not energetically favorable. Thus, the tendency of N and F to cluster together is evident. The co-substitution of aliovalent anions are stabilized due to the combined action of electrostatic and covalent interactions would favor this ordering.

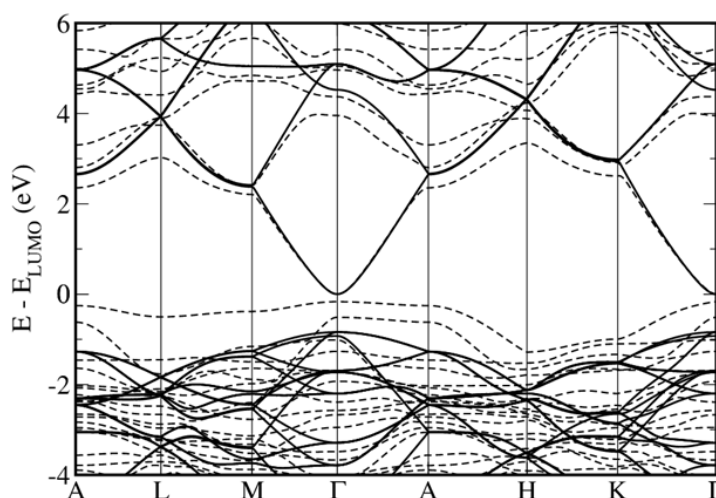


Figure 8.11: Comparison of the electronic band structures of bulk (solid line) and a representative configuration of N, F - ZnO (dashed line), obtained from DFT-based calculations.

- (3) From the band structure calculation (Figure 8.11) it is observed that the uppermost valence bands are most affected by the N, F substitution, with the N $2p$ -derived states arising as a sub-band at the top of the valence band (with minor contributions from the Zn $3d$ and O $2p$ -derived states), effectively reducing the band gap.
- (4) The p -states of the strongly electronegative F are deep down in energy, and less electronegative N is concentrating at the top of the valence band. The p -states of

additional N (in N, F- ZnO) form the sub-band just above the valence band. Thus, the reduction in the gap is indeed an effect of the co-substitution of F and N, as F enhances the effect of N-substitution. The lowest energy conduction bands with Zn 4s-character are essentially unaffected by the substitution.

- (5) The optical absorption spectra of N, F- co-substituted ZnO determined from electronic structure clearly show the effect of the N sub-band at energies below the band gap of bulk ZnO [Figure 8.12(a)]. Changes in the electronic structure with N, F- co-substitution, particularly the reduction in the band gap, is reflected in the changes in properties such as dielectric constant. The electronic dielectric constant (ϵ^∞) estimated using DFT-based linear response calculations show two to three-fold increments with N, F- co-substitution (from about 8.9 to 20.3). In Figure 8.12(b) we show the experimental data on the dielectric constant of ZnO and N, F- ZnO measured as a function of frequency at room temperature. Interestingly N, F- ZnO exhibits a higher dielectric constant than ZnO at all frequencies.

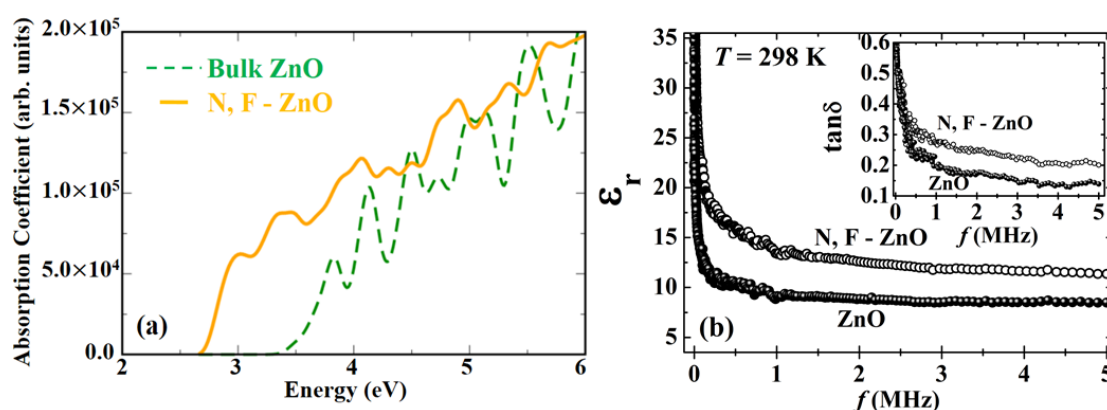


Figure 8.12: (a) Comparison of the absorption coefficients of bulk and N, F- ZnO, obtained from DFT-based calculations and (b) experimental observation of the variation of dielectric constant of ZnO and N, F- ZnO as a function of frequency at 298 K. Inset of (b) shows the dielectric loss as a function of frequency.

8.5 Conclusions

In conclusion, our investigation clearly demonstrates that co-substitution of N and F in ZnO brings about extraordinary changes in the electronic structure. The change in the optical spectrum is remarkable in that there is intense visible absorption imparting bright orange color to the oxide. The disappearance of oxygen vacancies and the increase in dielectric constant are also noteworthy. First-principles calculations show that co-substitution of N and F for O in ZnO is favorable over individual substitution by

N or F. This is because of the pairing of N and F at neighboring sites, with the resulting bonds being stiffer than those of pure ZnO. The *p*-orbitals of nitrogen are the most active states in altering the electronic structure of ZnO by giving rise to a sub-band of about 0.6 eV bandwidth at the top of the valence band, effectively reducing the band gap of ZnO. This effect is enhanced significantly by the presence of fluorine. While the first principles calculations underestimate the gap and the changes in it, they provide a clear picture of the effect of N and F substitution on the electronic structure of ZnO. The properties found by us may indeed result in the useful application of N, F- ZnO. Therefore, the strategy of anion co-substitution provides a new direction to modify the electronic structure of different semiconductors in a better way for desired properties.

Bibliography

- [1] A. C. Mofor *et al.*, Appl. Phys. Lett. **87**, 062501 (2005).
- [2] A. Bakin, A. Behrends, A. Waag, H.-J. Lugauer, A. Laubsch, and K. Streubel, Proc. IEEE **98**, 1281 (2010).
- [3] A. Bakin, A. El-Shaer, A. C. Mofor, M. Al-Suleiman, E. Schlenker, and A. Waag, Phys. Status Solidi (C) **4**, 158 (2007).
- [4] K. Nomura, H. Ohta, K. Ueda, T. Kamiya, M. Hirano, and H. Hosono, Science **300**, 1269 (2003).
- [5] B.-Y. Oh, M.-C. Jeong, T.-H. Moon, W. Lee, J.-M. Myoung, J.-Y. Hwang, and D.-S. Seo, J. Appl. Phys. **99**, 124505 (2006).
- [6] Y. Li, Y. Bando, and D. Golberg, Appl. Phys. Lett. **84**, 3603 (2004).
- [7] G. Hughes and N. McLean, Arch. Emer. Med. **5**, 223 (1988).
- [8] M. Ågren, Dermatology **180**, 36 (1990).
- [9] M. De Liedekerke, Ullmann's Encyc. Ind. Chem. (2006).
- [10] A. Moezzi, A. M. McDonagh, and M. B. Cortie, Chem. Eng. J. (Lausanne) **185**, 1 (2012).
- [11] C. F. Klingshirn, A. Waag, A. Hoffmann, and J. Geurts, Zinc oxide: from fundamental properties towards novel applications (Springer Science & Business Media, 2010), Vol. 120.
- [12] Ü. Özgür, Y. I. Alivov, C. Liu, A. Teke, M. Reshchikov, S. Doğan, V. Avrutin, S.-J. Cho, and H. Morkoç, J. Appl. Phys. **98** (2005).

- [13] H. Zeng, G. Duan, Y. Li, S. Yang, X. Xu, and W. Cai, *Adv. Func. Mater.* **20**, 561 (2010).
- [14] C. N. R. Rao, *J. Phys. Chem. Lett.* **6**, 3303 (2015).
- [15] X. Yang, A. Wolcott, G. Wang, A. Sobo, R. C. Fitzmorris, F. Qian, J. Z. Zhang, and Y. Li, *Nano Lett.* **9**, 2331 (2009).
- [16] S. Xie, X. Lu, T. Zhai, W. Li, M. Yu, C. Liang, and Y. Tong, *J. Mater. Chem.* **22**, 14272 (2012).
- [17] B. Panigrahy and D. Bahadur, *RSC Adv.* **2**, 6222 (2012).
- [18] B. Y. Geng, G. Z. Wang, Z. Jiang, T. Xie, S. H. Sun, G. W. Meng, and L. D. Zhang, *Appl. Phys. Lett.* **82**, 4791 (2003).
- [19] Y.-G. Lin, Y.-K. Hsu, Y.-C. Chen, L.-C. Chen, S.-Y. Chen, and K.-H. Chen, *Nanoscale* **4**, 6515 (2012).
- [20] H. Y. Xu, Y. C. Liu, R. Mu, C. L. Shao, Y. M. Lu, D. Z. Shen, and X. W. Fan, *Appl. Phys. Lett.* **86**, 123107 (2005).
- [21] R. Gonzalez-Hernandez, A. I. Martinez, C. Falcony, A. A. Lopez, M. I. Pech-Canul, and H. M. Hdz-Garcia, *Mater. Lett.* **64**, 1493 (2010).
- [22] A. Kaschner *et al.*, *Appl. Phys. Lett.* **80**, 1909 (2002).
- [23] L. L. Kerr, X. Li, M. Canepa, and A. J. Sommer, *Thin Solid Films* **515**, 5282 (2007).
- [24] N. Varghese, L. S. Panchakarla, M. Hanapi, A. Govindaraj, and C. N. R. Rao, *Mater. Res. Bull.* **42**, 2117 (2007)..
- [25] H. Qin, W. Li, Y. Xia, and T. He, *ACS Appl. Mater. Interfaces* **3**, 3152 (2011).
- [26] N. Kumar, U. Maitra, V. I. Hegde, U. V. Waghmare, A. Sundaresan, and C. N. R. Rao, *Inorg. Chem.* **52**, 10512 (2013).
- [27] J. Pan, U. V. Waghmare, N. Kumar, C. Ehi-Eromosele, and C. N. R. Rao, *Chem Phys Chem* **16**, 1502 (2015).
- [28] N. Kumar, J. Pan, N. Aysha, U. V. Waghmare, A. Sundaresan, and C. N. R. Rao, *J. Phys.: Condens. Matter* **25**, 345901 (2013).
- [29] J. Wen, C. Y. Zuo, M. Xu, C. Zhong, and K. Qi, *Eur. Phys. J. B - Condens. Matter and Complex Systems* **80**, 25 (2011).
- [30] R. Saha, S. Revoju, V. I. Hegde, U. V. Waghmare, A. Sundaresan, and C. N. R. Rao, *Chem Phys Chem* **14**, 2672 (2013).
- [31] J. Rodríguez-Carvajal, *Physica B: Condens. Matter* **192**, 55 (1993).

-
- [32] F. Yakuphanoglu, Y. Caglar, S. Ilican, and M. Caglar, *Physica B: Condens. Matter* **394**, 86 (2007).
- [33] C. Shifu, Z. Wei, Z. Sujuan, and L. Wei, *Chem. Eng. J.* **148**, 263 (2009).
- [34] V.-H. Nguyen, H.-Y. Chan, and J. C. Wu, *J. Chem. Sci. (Bangalore, India)* **125**, 859 (2013).
- [35] K. Vanheusden, W. L. Warren, C. H. Seager, D. R. Tallant, J. A. Voigt, and B. E. Gnade, *J. Appl. Phys.* **79**, 7983 (1996).
- [36] A. B. Djurišić and Y. H. Leung, *Small* **2**, 944 (2006).
- [37] A. Sundaresan, R. Bhargavi, N. Rangarajan, U. Siddesh, and C. N. R. Rao, *Phys. Rev. B* **74**, 161306 (2006).
- [38] A. Sundaresan and C. N. R. Rao, *Nano Today* **4**, 96 (2009).

List of Publications

From the thesis

1. "Structure and magnetic properties of the $\text{Al}_{1-x}\text{Ga}_x\text{FeO}_3$ family of oxides: A combined experimental and theoretical study."
Rana Saha, A. Shireen, A. K. Bera, S. N. Shirodkar, Y. Sundarayya, N. Kalarikkal, S. M. Yusuf, U. V. Waghmare, A. Sundaresan, and C. N. R. Rao, *J. Solid State Chem.* 184 (2011) 494.
2. "Effect of Cr and Mn ions on the structure and magnetic properties of GaFeO_3 : Role of the substitution site."
Rana Saha, A. Shireen, S. N. Shirodkar, U. V. Waghmare, A. Sundaresan, and C. N. R. Rao, *J. Solid State Chem.* 184 (2011) 2353.
3. "Phase transitions of AlFeO_3 and GaFeO_3 from the chiral orthorhombic ($Pna2_1$) structure to the rhombohedral ($R\bar{3}c$) structure."
Rana Saha, A. Shireen, S. N. Shirodkar, M. S. Singh, U. V. Waghmare, A. Sundaresan, and C. N. R. Rao, *Inorg. Chem.* 50 (2011) 9527.
4. "Coupled phonons, magnetic excitations, and ferroelectricity in AlFeO_3 : Raman and first-principle studies."
P. Kumar, A. Bera, D. V. S. Muthu, S. N. Shirodkar, **Rana Saha**, A. Shireen, A. Sundaresan, U. V. Waghmare, A. K. Sood, and C. N. R. Rao, *Phys. Rev. B* 85 (2012) 134449.
5. "Remarkable Properties of ZnO Heavily Substituted with Nitrogen and Fluorine, $\text{ZnO}_{1-x}(\text{N}, \text{F})_x$."
Rana Saha, S. Revoju, V. I. Hegde, U. V. Waghmare, A. Sundaresan, and C. N. R. Rao, *Chem. Phys. Chem.* 14 (2013) 2672.
6. "Neutron scattering study of the crystallographic and spin structure in antiferromagnetic EuZrO_3 ."
Rana Saha, A. Sundaresan, M. K. Sanyal, C. N. R. Rao, F. Orlandi, P. Manuel, and S. Langridge, *Phys. Rev. B* 93 (2016) 014409.
7. "Magnetodielectric effects in A-site ordered chromate spinels, LiMCr_4O_8 (M = Ga and In)."
Rana Saha, F. Fauth, M. Avdeev, P. Kayser, B. J. Kennedy, and A. Sundaresan, *Phys. Rev. B* 94 (2016) 064420.

8. “Magnetoelectric effect in simple collinear antiferromagnetic spinels.”
Rana Saha, S. Ghara, E. Suard, D. H. Jang, K. H. Kim, N. V. T. Oganessian, and A. Sundaresan *Phys. Rev. B* **94** (2016) 014428.
9. “Phase coexistence in YVO₃: A temperature dependent synchrotron X-ray diffraction study.”
Rana Saha, F. Fauth, V. Caignaert, and A. Sundaresan ([Communicated](#)).
10. “Magnetostructural coupling and magnetodielectric effects in A-site ordered LiFeCr₄O₈.”
Rana Saha, E. Suard, J. R. Carvajal, R. Dhanya, C. Bellin, K. Béneut, A. Shukla, C. Narayana, and A. Sundaresan ([Communicated](#)).
11. “Exchange bias at low fields exhibited by the interface between epitaxial layers of ferromagnetic and charge-ordered rare-earth manganites.”
Rana Saha, K. Vasu, D. S. Negi, R. Datta, A. Sundaresan, and C. N. R. Rao *Phys. Status Solidi RRL* **10** (2016) 622.

Reviews

12. “Multiferroic and magnetoelectric oxides: The emerging scenario.”
C. N. R. Rao, A. Sundaresan, and **Rana Saha**, *J. Phys. Chem. Lett.* **3** (2012) 2237.
13. “Novel features of multiferroic and magnetoelectric ferrites and chromites exhibiting magnetically driven ferroelectricity.”
Rana Saha, A. Sundaresan, and C. N. R. Rao, *Mater. Horiz.* **1** (2014) 20.

Miscellaneous

14. “Multiferroic and magnetodielectric properties of the Al_{1-x}Ga_xFeO₃ family of oxides.”
A. Shireen, **Rana Saha**, P. Mandal, A. Sundaresan and C. N. R. Rao, *J. Mater. Chem.* **21** (2011) 57.
15. “Ferroelectricity Induced by Cations of Non-equivalent Spins Disordered in the Weakly Ferromagnetic Perovskites, YCr_{1-x}M_xO₃ (M= Fe or Mn).”
B. Rajeswaran, P. Mandal, **Rana Saha**, E. Suard, A. Sundaresan, and C. N. R. Rao, *Chem. Mater.* **24** (2012) 3591.

16. “Multiferroic and magnetoelectric nature of GaFeO₃, AlFeO₃ and related oxides.”
Rana Saha, A. Shireen, S. N. Shirodkar, U. V. Waghmare, A. Sundaresan, and C. N. R. Rao, *Solid State Commun.* 152 (2012) 1964.
17. “Synthesis and Magnetic Properties of β-KVOF₃.”
M. D. Donakowski, H. Lu, R. Gautier, **Rana Saha**, A. Sundaresan, and K. R. Poeppelmeier, *Z. Anorg. Allg. Chem.* 640 (2014) 1109.

